vol 22 / 2022

JOURNAL OF ELECTICAL ENGINEERING

University "Politehnica"
Timi oara Romania
Faculty of Electrical and Power Engineering

"Politehnica" Publishing House
ISSN 1582-4594

No 1

CONTROL AND SIMULATION OF HYBRID POWER GENERATION SYSTEM OPERATING IN GRID CONNECTED AND STAND ALONE MODE

Ridha BENADLI[1,2] **Brahim KHIARI**[1]
[1]LANSER Laboratory, *CRTEn, B.P.95 Hammam-Lif 2050, Tunis-Tunisia*
[2]National Higher Engineering School of Tunis, EED, BP 56, Montfleury 1008, Tunis, Tunisia
Anis SELLAMI
[2]National Higher Engineering School of Tunis, EED, BP 56, Montfleury 1008, Tunis, Tunisia

Abstract: *This paper presents the modelling, analysis, performance and the synthesis of control of Hybrid Renewable Energy System (HRES), with Battery Energy Storage System (BESS). This HRES can also be connected to the grid and capable to be, with a storage device, a stand-alone operation. The Photovoltaic (PV) generator is controlled via DC-DC boost converter by using Incremental Conductance (InCond) method to search optimum operating point of this source. The BESS is used to maintain the DC bus voltage at a constant value by charging or discharging this storage using a bidirectional DC-DC converter. The wind generator is controlled via AC-DC converter with an MPPT method that allows optimal transfer of wind power for a wide range of wind speeds. The control for the wind generator is based on an indirect vector control by the Filed Orientation Control (FOC) where one makes it possible to perfectly follow the optimum characteristic of the wind turbine. In a Stand-Alone Mode (SAM) operation, the Voltage Source Converter (VSC) is used for the controlled output voltage in terms of amplitude and frequency delivered to the AC load. In Grid Connected Mode (GCM) operation, the VSC is used to control the electrical grandeurs on the grid. Performed validations by simulation in Matlab/Simulink have clearly demonstrated the effectiveness and performance of the control strategies developed for the control of power converters.*

Key words: *Control, Grid-connected, Stand-alone, Hybrid Renewable Energy System, Wind turbine, Photovoltaic; Battery energy storage system.*

1. Introduction

A hybrid system interconnected by a set of renewable energy sources and storage systems help to ensure greater energy availability and optimize maximum power generation systems, both from technical and economic point of view. This type of system is widely used in low power applications; isolated sites or connected to the grid. The common DC bus interconnected various sources of production and storage system is used before converting this energy into alternating current. Among renewable energy sources, we chose wind and PV. The combination of these two sources can help to achieve a more continuous electricity production. This study is directed to PV/ wind systems connected to the grid and able to work in SAM through the BESS. This storage is used as a backup source to power the system when the renewable energy source is unavailable. Other backup sources can be used for the production of renewable sources of hollow periods with or without BESS such as fuel cells [4, 8, and 18], supercapacitors, the energy storage flywheel [19], diesel generators [14]. Conversely, when the energy produced is greater than the energy consumed, the excess electricity is stored in the BESS [5], supercapacitors [13] and with an electrolyzer hydrogen tank [4]. However, fuel cells are very expensive and the diesel generator operate at a mediocre performance with high power consumption grows with their request. This energy management is difficult to achieve but it may be necessary in applications in isolated site to ensure the balance between the power consumed by the user and the power produced by the sources.

Several studies have investigated the hybrid production system. This study concerns the modeling, analysis and synthesis of control and management strategies of the hybrid system. In [15], a management algorithm in a PV/ wind hybrid system with BESS powering a housing loads in parallel with the grid is described. In [2, 3] authors shows the modeling, the analysis and the control of energy from a PV /wind power system with BESS powering the AC load in parallel with the grid. [18], provides the control of a PV/ wind system/ fuel cell for supplying only DC load. In reference [5], authors proposed a control of a PV/wind system operating in both SAM and GCM, but this system is valid only for a single phase. In reference [1], authors presented a control of PV/ wind power, but this system needs an energy storage system to ensure continuity of supply local loads AC islanding mode. Also, in reference [10], the authors are silent about the use of an energy storage device of a hybrid system to supplying AC loads in parallel to the grid.

Different strategies proposed for the control of the bidirectional buck-boost converter to ensure a balance of

power through charging /discharging of the battery. Reference [6] presents the control and quality of wind power with battery pack. The Reference [7], develops the control and management of a PV /battery system connected to the grid. In references [6, 17], a control strategy by a single control loop of the voltage with the Proportional Integral (PI) is proposed. Reference [10] proposes a control strategy with two regulation loop; a voltage loop with the PI and a current control by hysteresis and a voltage regulation loop. Similarly in Reference [4, 9], but the current control with the PI. This strategy is used in our study to the control of the bidirectional converter. It ensures dynamic meshing performance higher than other technology cited above through the internal loop current.

Several standalone converter control strategies have been proposed to set the amplitude and frequency delivered to AC loads off grid. In references [16, 17], a control strategy with six PI controllers in a photovoltaic/wind power the fuel cell proposed. Another strategy to control with a single PI controller in a PV/ battery /supercapacitors was proposed in [13]. In [6, 9] propose a control strategy by two control loop (current / voltage) with four PI controllers in a wind hybrid system. This latter strategy is used in our study to the control of the bidirectional converter in operation out electric grid.

Different strategies proposed in the literature to control the three-phase PWM voltage converter in a renewable energy based production system connected to the electrical grid [1, 4, 19]. All these strategies aim to achieve the same objectives, namely: a power factor near the unit, sinusoidal current is absorbed in phase with the voltage. The most popular is the technique known as the Voltage Oriented Control (VOC) [15]. This technique is used in our study to control the electrical grandeur of the grid becauce ensures high dynamic and static performance through third by the loop current internal regulations.

The developed HRES as shown in Fig.1 constitutes of wind subsystem 10 kW equipped of a direct driven permanent-magnet synchronous generator (PMSG), a PV array 7.625 kW, a BESS, a DC bus (650V), power interfaces and a set of control system. This figure also shows the power balance of the renewable energy conversion system in the two modes operation of HRES.
. This paper is organized as follows: In Section 2, proposed architecture of grid-connected with wind and PV resources. The modeling components of the proposed hybrid system in Section 3. The control strategies of hybrid system in Section 4. Simulation results and discussion are given in Sections 5. Conclusion is addressed in the last section.

2. Proposed hybrid system architecture

Fig. 1 shows the overall architecture of the proposed grid-connected hybrid system with wind and PV resources. The two energy sources are connected in parallel to a common dc bus line through their individual dc-dc converters. Combining multiple renewable resources via a common dc bus of a power converter has been prevalent because of convenience in integrated monitoring and control and consistency in the structure of controllers as compared with a common ac type [12]. The wind subsystem involves a turbine is a small power wind equipped with a PMSG, a diode rectifier and a boost converter for the tracking of the maximum power point using a perturbation and observation (P&O) method, a three-phase inverter. The solar subsystem consists of a PV array controlled by another boost converter used for the maximum power point tracking (MPPT). The PLL is used to detect the phase angle of the grid voltage for the control. The simple inductors L are used as a filter interfacing inverter and mains. The LCL filter provides advantages in costs and dynamics since smaller inductors can be used. However, in a grid-connected system, an LCL filter may cause resonance, which is a disaster for the system's stability [5]. For the inverter, an integral sliding mode controller has been used for the current controller because can eliminate the steady-state error by adding integral sliding surface. The SMC presents attractive features such as robustness to parametric uncertainties of the wind turbine and the generator as well as to electrical grid disturbances [13]. The current-controlled SVPWM inverter is adapting to three-phase PV/WT grid-connected system.

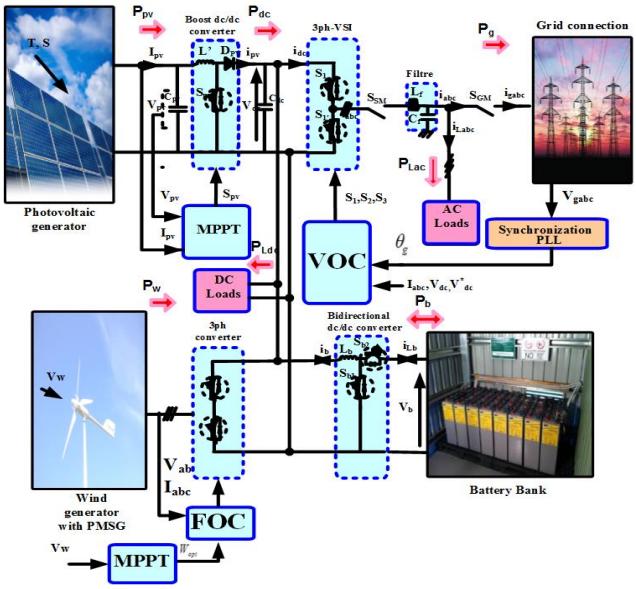

Fig.1. Control Structure of a PV-Wind hybrid system

2. Modeling the different components of the hybrid system.

2.1. PV array model

There are two types of photovoltaic PV modules: electrical model with a diode or two diodes. Among which we chose to model a diode because it is the simplest to implement and most used in the literature. This model is composed of a parallel current generator with a diode in parallel and two resistors (R_s series / shunt R_{sh}) as illustrated

in Fig.2. The two resistors R_s and R_{sh} represent respectively the various contact resistances and connections and leakage currents.

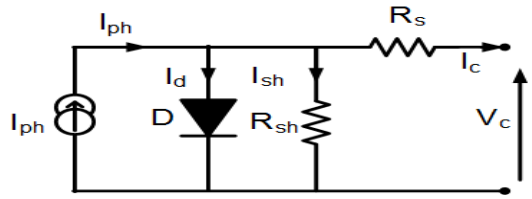

Fig. 2. Electrical model equivalent of a PV cell

The current generated by the PV array is given by [17]

$$I_{pv} = N_p I_{ph} - N_p I_s \left\{ \exp\left[q\left(\frac{V_{pv} + R_s I_{pv}\left(N_s / N_p\right)}{N_s nKT} \right) - 1 \right] \right\}$$

$$- N_p \frac{\left(V_{pv} + R_s I_{pv}\left(N_s / N_p\right)\right)}{R_{sh} Ns} \qquad (1)$$

Where I_{ph} is the photocurrent, I_s is the reverse saturation current of the diode, n is the ideality factor of the diode, q is the electron charge (q = 1.6.10^{-19}), k is the Boltzmann's constant (k = 1.38.10^{-23}), and T is the solar array panel temperature.

In order to get the desired electrical power which is 7,625 kW peak power, we placed 5 modules connected in series (N_s=5) and 5 modules connected in parallel (N_p=5).

The output power and current of PV array delivered by the PV array in function of voltage for different irradiance levels is shown in Fig.3, this allows us to easily observe the influence of solar irradiation on the Maximum Power Point (MPP) and short circuit current (I_{sc}).

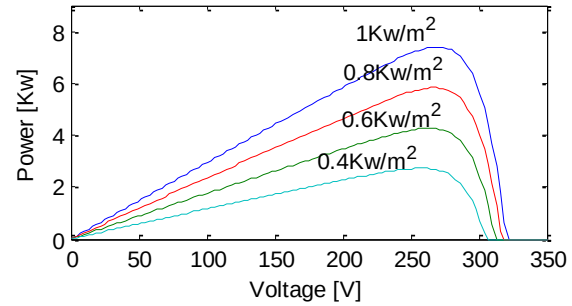

(a)

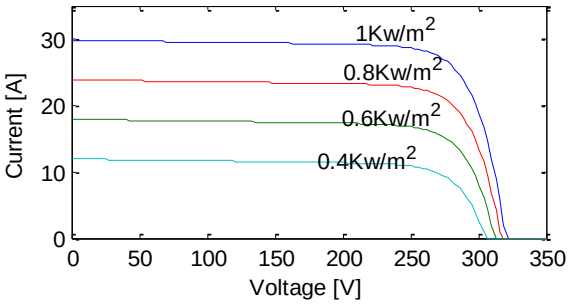

(b)

Fig. 3. P-V and I–V output characteristics of the PV array

2.1. Wind turbine model

The mechanical power captured by the blades of a wind turbine is given by [12]

$$P_w = \frac{1}{2}\rho C_p\left(\lambda,\beta\right)\pi R^2 v_w^3 \qquad (2)$$

Where, ρ is the air density (kg/m^3), R is the rotor radius of wind turbine,v_ω is the wind speed in m/s, C_p is the turbine rotor power coefficient, which is a function of tips speed ratio λ and pitch angle β.

$$\lambda = \frac{R w_m}{v_w} \qquad (3)$$

Where w_m is the rotor speed of the wind turbine.

The maximum power generated by the wind turbine is given by

$$P_w = k_{opt} {w_m}^2 \qquad (4)$$

Where, $k_{opt} = \frac{1}{2}\rho.A.C_{p_{opt}}\left(\frac{R}{\lambda_{opt}}\right)^2$ (5)

The justification for Eq.(4) as shown in Fig.4, on which it is noted that for each value of the wind speed was a maximum power point correspond to different speeds of rotation of the turbine. The idea for adapting the power extracted in the rotational speed of the turbine.

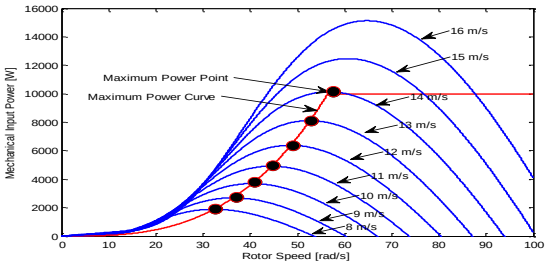

Fig. 4. Output power generated by a turbine for different wind speeds

2.3. Battery storage model

In order to guarantee the availability of energy in the DC and AC loads even in unfavorable weather conditions and in both mode of the bidirectional converter, we use the battery as energy storage dispostif. The modeling of this battery is implemented in Ref [16, 17]. It can be illustrated by the equivalent circuit as shown in a Fig.5. This model consists of a source votage E_0 in series with a resistor R_b, where the voltage source is described by

$$E = E_0 - K\frac{Q}{Q - \int i\,dt} + A\exp\left(-B\int i\,dt\right) \qquad (6)$$

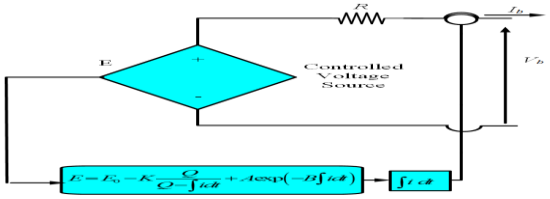

Fig. 5. Lead-acid battery model.

2. Control of power converters

3.1 Photovoltaic MPPT control

The control of the DC/DC boost converter allows both elevateing the value of the PV array to obtain the desired DC bus voltage and searching for the MPP. The principle of any MPPT methods is to act on the duty cyclic of the converter to ensure that the generator is operating at its maximum value no matter how the climatic conditions will be. In our study, we chose the InCond method [2,3]. The principle of this method is based on the conductance G and calculates its incremental ΔG, if the conductance $G > \Delta G$, the operating point is left of MPP, it is right if $G < \Delta G$. The flow chart of this method is illustrated in the Fig. 6.

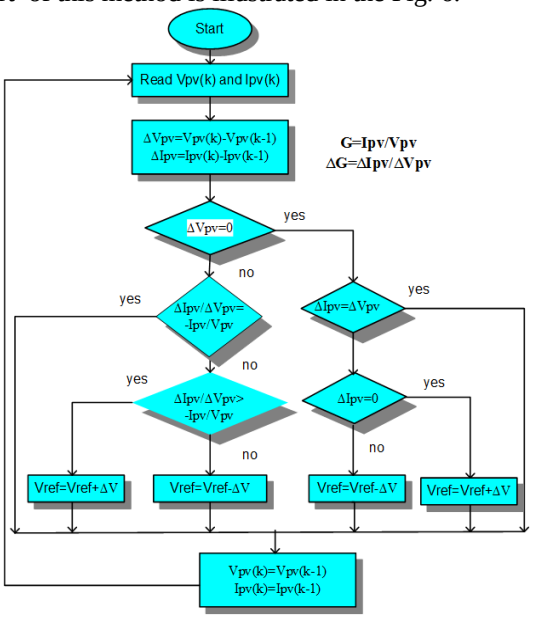

Fig. 6. Flow chart of InCond method

3.1 control of bidirectional buck-boost converter

Fig. 7 shows the block diagram of the proposed control of bidirectional buck-boost DC-DC converter using PI controller. This converter works in boost mode when the switch S_1 is ON (discharging the battery) and buck mode when the switch S_2 is ON (charging the battery).

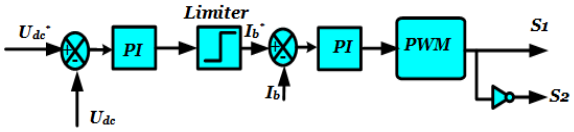

Fig. 7. Control of bidirectional buck-boost converter

3.3 Generator side control

The control of generator side converter enables the search of maximum power point in such a manner to minimize the error between the operating power and maximum power. The Fig.8 shows the principle of control installed for the wind source. The three-phase voltages generated by PMSG will be adjusted of space vector modulation (SVM) vector modulation receiving the reference voltages of control at speed imposed by the maximum extraction power MPPT device.

The reference speed imposed by MPPT is given by

$$w_{m-opt} = \frac{\lambda_{opt} V_w}{R} \quad (7)$$

Where λ_{opt} is the maximum torque coefficient.

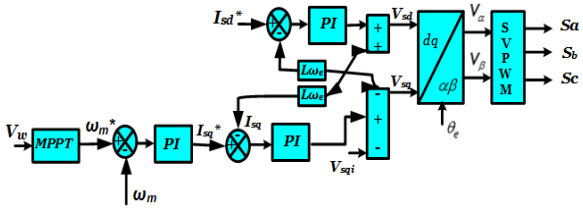

Fig. 8. Control of generator side converter

3.1 Grid side control

The hybrid production system can also be connected to the grid and capable, with a storage device, a standalone operation. In an SAM, the VSC is used in a voltage control mode control strategy for regulating autonomously the amplitude and frequency of the AC loads. Fig. 9 shows the block diagram of the VSI control strategy in d-q coordinates described in [9]. The line voltage and frequency are set to 230 V rms and 50 Hz respectively.

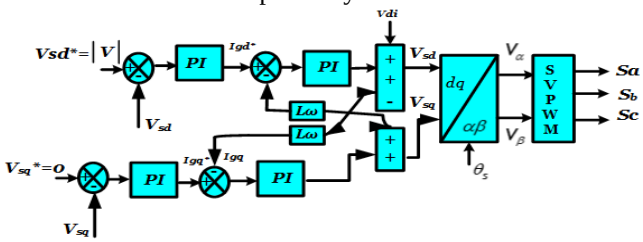

Fig. 9. Control for stand-alone mode

In a GCM, we chose a control structure based on two cascaded control loops, an external voltage loop and an inner loop current in a synchronous d-q frame. Fig. 10 shows the block diagram of proposed control strategy in this mode. The reference voltages generated at the output of the current regulators (V_α, V_β) and the location information of the grid voltage from Phase locked loop (PLL) block will be sent to a Space Vector Pulse Width Modulation SVPWM.

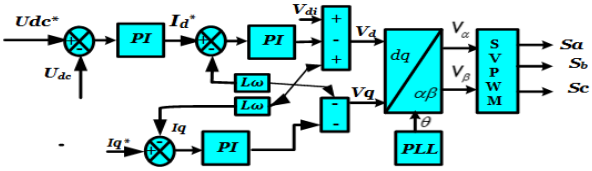

Fig. 10. Control for grid-connected mode

4. Results and discussion

Different simulations results are used to analyze the dynamic performance HRES both GCM and SAM are represented in this work. The overall configuration is shown in Fig. 1 of HRES were simulated by using the Simulink/ Matlab. An option of this system is to connect the sources with the DC, AC load and to the grid via an AC, DC bus. Second option proposed in this study is to connect the sources by only to the DC load via a DC bus.

4.1 Isolated operation with a local DC loads (off grid)

The system is tested for only DC load connected to the DC bus in isolated operation. Fig. 11 illustrate the distribution powers of the HRES with variable input source and load power conditions. Specifically, the wind speed decreases from 12 m/s to 14 m/s at t=1.5s and increases from 12 m/ s to 14 m /s at t=3s, respectively. The solar irradiation varies is increased from 0.8 to 1kW/m^2 at t=1.5 s and decreased from 1kW/m^2 to 0.8 kW/m^2 at t=3s, respectively. The basic power balance equation for the generation sources and the DC load demand is given by

$$P_{pv} + P_w \pm P_b = P_{Ldc} \quad (8)$$

Where P_w is the wind turbine power, P_{pv} is the power generated by the PV array, P_{Ldc} is the DC load demand.

For the first period $t \in [0 \quad 0.8]$, the total generated power from PV and wind is around 12.2kW, the P_{Ldc} is around 8.4kW. The power demand by the load is less than the power produced by the sources. Therefore, the battery is charged with a negative current. For the second period $t \in [0.8 \quad 2]$, the sum of wind and PV generated power is not sufficient to supply the resistive load demand. Under this situation, the battery discharge with a positive current to supply the power loads as shown in Fig. 12.

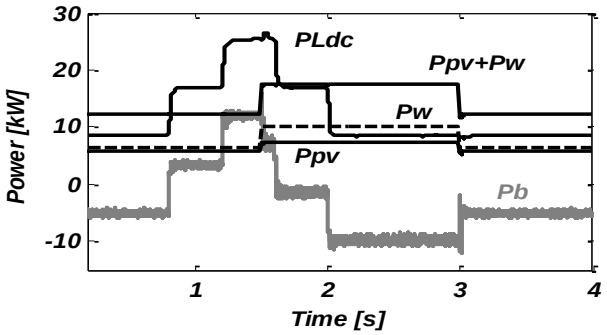

Fig. 11. Various power of the hybrid system (**Case1**)

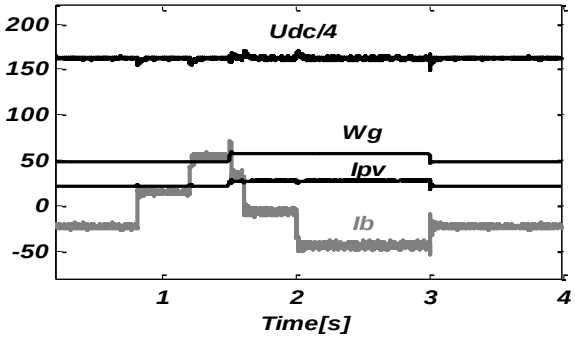

Fig. 12. Hybrid system variables evolution (**Case 1**: U_{dc} is the DC bus voltage [V], W_g is the rotor speed of PMSG [rad/s], I_{pv} is the output current of PV [A], I_b is the battery current [A])

4.2 Isolated operation with a local DC and AC loads (off grid)

The system is simulated in SAM of operation to validate the dynamic performance under varying the load condition, wind speed and in irradiance. Exactly, the irradiance decreases from 1kW/m^2 to 0.7 kW/m^2 at t=1.5s and the wind speed from 14 m/ s to 10 m /s at t=1.5s. The power loads demand P_{Lac} and P_{Ldc} is varied between 15 kW to 19kW and 0 to 4 kW respectively. In this mode, the power difference between the generation sources and the total load demand is calculated as

$$P_{pv} + P_w \pm P_b = P_{Ldc} + P_{Lac} \quad (9)$$

Where P_{Ldc} is the DC load demand.

At period $t \in [0 \quad 0.8]$, the load demand is more than the wind and solar power production. Therefore the required energy is supplied by the battery (positive current and power) as shown in Fig.13 and Fig.14. The VSC is able to regulate the voltage level of local AC load at 230 V and the frequency at 50 Hz as shown in Fig.15.

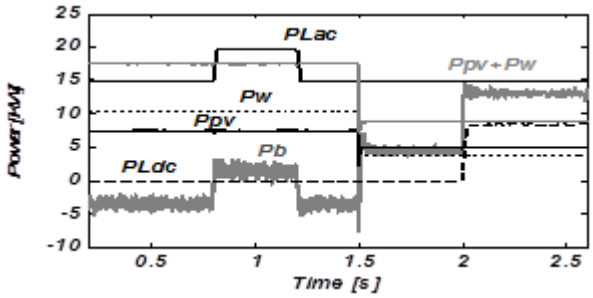

Fig. 13. Various power of the hybrid system (**Case 2**)

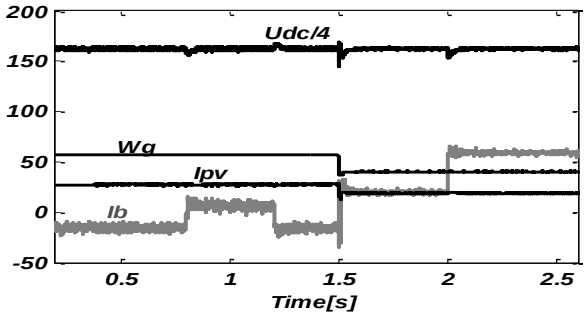

Fig. 14. Hybrid system variables evolution (**Case 2**: U_{dc} is the DC bus voltage [V], W_g is the rotor speed of PMSG [rad/s], I_{pv} is the output current of PV [A], I_b is the battery current [A])

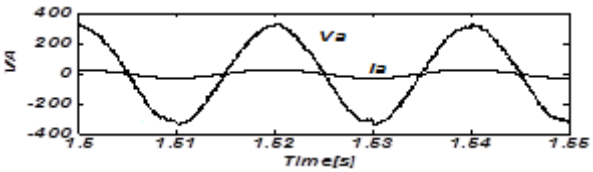

Fig. 15. AC load voltage and current (**Case 2**)

4.3 Grid connected operation

Now consider the system hybrid in GCM. Consider the step change in the DC load power while keeping other variables constant, wile the PV and Wind at their rated power 7.46 kW and 10kW respectively. The AC load demand is fixed at 2kW. In this mode, the exchange power through the grid-side converter and the grid is calculated as

$$P_{inv} = P_{pv} + P_w \pm P_b - P_{Ldc} \quad (10)$$

Where P_{inv} is the real output power from the bidirectional DC-AC converter, the positive value represents means the power flow from the DC bus the AC bus and vice versa.

The exchange power between inverter to the grid can be expressed as

$$P_g = -\left(P_{inv} - P_{Lac}\right) \quad (11)$$

Where P_g *i*s the real power injected into the grid. The negative value represents the injected power to the grid and vice versa.

The power balance equation given in Eq(9) can be written as:

$$P_{net} = P_b = \pm\left(P_{inv} + P_{Lac} - P_{pv} - P_w\right) \quad (12)$$

Fig. 16 shows the control performance of the hybrid system under variable DC load condition. At period $t \in [0 \quad 0.8]$, the sum of power from PV and Wind system (P_{pv}+P_w) is around 17.5 kW, while the value of power DC load demand is set at zero. During this period, the real output power from the bidirectional DC-AC converter is positive (+7 kW). Hence, the DC bus supplies the energy to AC bus. In addition the extra power between P_{inv} and P_{Ldc} is will be injected the grid (P_g=-5 kW). The battery starts charging with a negative limit current as shown in Fig.17. At period $t \in [1.2 \quad 1.8]$, the DC load demand increases to 56 kW, which more than the power net P_{net}. At this moment, the battery turned the discharging mode (positive current I_b).

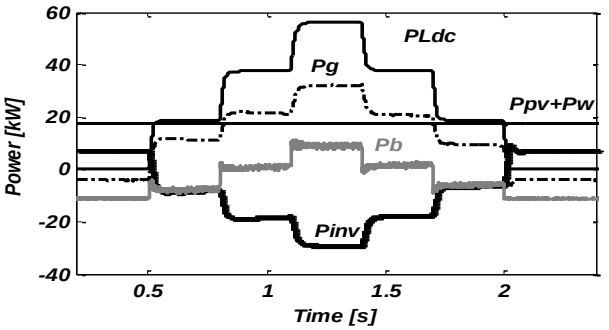

Fig.16. Various power of the hybrid system (**Case 3**)

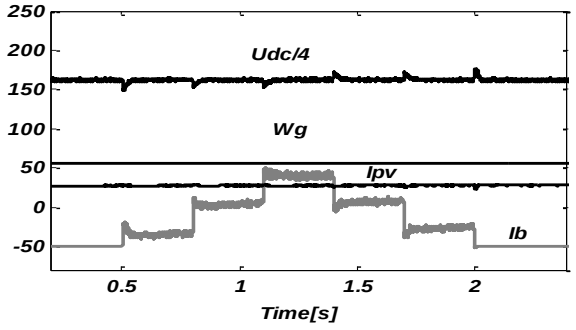

Fig. 17. Hybrid system variables evolution (**Case 3**: U_{dc} is the DC bus voltage [V], W_g is the rotor speed of PMSG [rad/s], I_{pv} is the output current of PV [A], I_b is the battery current [A]).

5. Conclusion

This paper presents a contribution to the analysis of comprtement and mastery of performance of HRES composed of a variable wind speed turbine with PMSG, PV and battery storage system capable of working in stand-alone mode and in grid-connected mode**.** A model for each component of the hybrid system was realised. These models have been interconnected to analyze the dynamic behavior of the complete production system. Validations were performed by simulation in Matlab/Simulink clearly demonstrated the effectiveness of the strategies proposed for the control of converters under different operation using the load demand profile and the real weather data (wind speed, solar irradiance).

Reference

1. Remus Teodorescu, and Frede Blaabjerg . Flexible Control of Small Wind Turbines With Grid Failure Detection Operating in Stand-Alone and Grid-Connected Mode, Power Electronics, IEEE Transactions on, vol . 19, no. 5, 1323 – 1332, 2004.

2. Seul-Ki Kim, Jin-Hong Jeon, Chang-Hee Cho, Jong-Bo Ahn, and Sae-Hyuk Kwon.. Dynamic Modeling and Control of a Grid-Connected Hybrid Generation System With Versatile Power Transfer. Sustainable Energy, IEEE Transactions on Industrial Electronics , Vol. 55, no. 4,July, 2008.

3. Sungwoo Bae, and Alexis Kwasinski. Dynamic Modeling and Operation Strategy for a Microgrid With Wind and Photovoltaic Resources," IEEE Transactions on smart grid. vol. 3, no. 4, pp.1867 – 1876, 2012.

4. Pablo García-Triviño , Antonio José Gil-Mena , Francisco Llorens-Iborra , Carlos Andrés García-Vázquez, Luis M. Fernández-Ramírez, Francisco JuradoPower. Control based on particle swarm optimization of grid-connected inverter for hybrid renewable energy system, Energy Conversion and Management, Vol 91 , Pages 83-92, 2015.

5. Mehdi Dali, Jamel Belhadj and Xavier Roboam. Hybrid solare-wind system with battery storage operating in grid–connected and standalone mode: Control and energy management Experimental investigation, Energy journal, 2587-2595, 2010.

6. Riad Kadri, Jean-Paul Gaubert, and Gerard Champenois. An Improved Maximum Power PointTracking for Photovoltaic Grid-Connected Inverter Based on Voltage- Oriented Control. IEEE Transations On Industrial Electronics, Vol.58, No.1: 66-75, 2011.

7. Kai Sun, Li Zhang, Yan Xing, Josep M. Guerrero. A Distributed Control Strategy Based on DC Bus Signaling for Modular Photovoltaic Generation Systems With Battery Energy Storage. IEEE Transations On Industrial Electronics, Vol.26, No.10: 66-75, 2011.

8. Nabil A. Ahmed MasafumiMiyatake, A.K. Al-Othman. Power fluctuations suppression of stand-alone hybrid generation combining solar photovoltaic/wind turbine and fuel cell systems. Energy Conversion and Management, Vol 49, No. 10:2711–2719, 2008.

9. Nahidul HoqueSamrat, Norhafizan Bin Ahmad, Imtiaz Ahmed Choudhury, and Zahari Bin Taha. Modeling, Control, and Simulation of Battery Storage Photovoltaic-Wave Energy Hybrid Renewable Power Generation Systems for Island Electrification in Malaysia. Hindawi Publishing Corporation, The Scientific World Journal, Article ID 43637, 2014.

10. Chih-Ming Hong, Ting-Chia Ou, Kai-Hung Lu. Development of intelligent MPPT (maximum power point tracking) control for a grid-connected hybrid power generation system. Energy, Vol 50, No.1: 270-279, 2013.

11. Chih-Ming Hong, Chiung-Hsing Chen. Intelligent control of a grid-connected wind photovoltaic hybrid power systems. International Journal of Electrical Power & Energy Systems , Vol 55: 554-56, 2014.

12. Mahmoud M. Amin, Osama A. Mohammed. Development of High-Performance Grid-Connected Wind Energy Conversion System for Optimum Utilization of Variable Speed Wind Turbines. IEEE Transactions On Sustainable Energy, Vol. 2, no. 3, 2011.

13. Jayalakshmi N. S, D. N. Gaonkar, Pramod Bhat Nempu. Power Control of PV/Fuel Cell/Supercapacitor Hybrid System for Stand-Alone Applications. International Journal of Renewable Energy Research, Vol.6, No.2, 2016.

14. Chih-Ming Hong , Ting-Chia Ou , Kai-Hung Lu. Development of intelligent MPPT (maximum power point tracking) control for a grid-connected hybrid power generation system Vol.50: 270-279, 2013.

15. Abderrezzak Bouharchouchel, EI Madjid Berkouk, Tarrak Ghennaml. Control and Energy Management of a Grid Connected Hybrid Energy System PV -Wind with Battery Energy Storage for Residential Applications", 8th International Conference and Exhibition on Ecological Vehicles and Renewable Energies, pp.1-11.

16. G. Malla, C.N. Bhende. Voltage control of stand-alone wind and solar energy system Internarial Journal of Electrical Power and Energy System, Vol.56, pp.361-373, 2014.

17. Bouthaina Madaci , Rachid Chenni , Erol Kurt, Kamel Eddine Hemsas. Design and control of a stand-alone hybrid power system. International Journal of Hydrogen Energy, vol. 41, pp. 12485-12496, 2016.

18. T.Bogaraj , J.Kanakaraj. A Novel Energy Management Scheme using ANFIS for Independent Microgrid. International Journal of Renewable Energy Research, Vol.6, No.3, 2016.

19. Ghada Boukettaya, Lotfi Krichen. A dynamic power management strategy of a grid connected hybrid generation system using wind, photovoltaic and Flywheel Energy Storage System in residential application Energy; 71pp.148-159, 2014.

IMPROVED MODAL TRUNCATION APPROXIMANT: A HYBRID APPROACH

Awadhesh KUMAR*. Dinesh CHANDRA**

* Electrical Engineering Department, Motilal Nehru National Institute of Technology, Allahabad India
(Tel: 0551-6050028; e-mail: awadhesg26@ gmail.com).
** Electrical Engineering Department, Motilal Nehru National Institute of Technology, Allahabad India
(e-mail:dinesh@mnnit.ac.in)

Abstract: *A hybrid method using modal truncation and singular perturbation to derive the reduced order model for a stable higher order system is presented. The approach is based on retaining the dominant modes of the system and truncating comparatively the less significant once. As the reduced order model has been derived from retaining the dominant modes of the original high order stable system, the reduced order model preserves the stability. The strong demerit of the modal truncation method is that, the steady state value of the reduced model does not match with the original system. This demerit has been overcome by applying singular perturbation approach of the balanced truncation method. Results obtained show the effectiveness of the proposed technique. Numerical examples are carried out to illustrate the procedure. Further it has been also applied to a system of order 1006 to check its applicability to large scale systems as well.*

Keywords: *Modal truncation, Singular perturbation, Steady state value, Eigen value, Large scale systems*.

1. INTRODUCTION

More and more accurate modelling of physical systems such as multi-machine power systems leads to a system with very high dimension. It is often called higher order system. Control design, simulation and analytical understanding of these high order systems become difficult and cumbersome. So the need arises to have the lower dimension representation of the system to better cope with the aforesaid problems.

Researchers have been trying for better approximation of the high order system nearly more than four decades which has now evolved as a promising pasture of research in system and control theory, known as "Model order reduction (MOR)". The target of the MOR is to have a model of considerably lower order for a system with very high order while keeping the key features of the original systems intact; such as stability and passivity etc. Moreover the algorithm or the method adopted should be reliable and computationally efficient. A number of methods for MOR are available in literature both in frequency domain as well as in time-domain [1-7].

One of the popular methods is modal truncation [1-4]. Different methods belonging to this category were also proposed [5,6]. Infect it is a mapping based on a sub-matrix of the full-order system's modal matrix. The elements at the columns of this matrix are its eigenvectors, which can be ordered according to their dominancy. The eigenvector with eigen-values closest to the jw-axis were considered dominant. Another novel approach to select dominant poles is suggested in [7] where the dominant pole is decided by considering the ratio of residue to the real value of pole. E. J. Davison suggested that a system with greater dimension can be represented by a model with lower dimension by considering the effects of the r most dominant eigen-values. The eigen values which were close to jw axis were retained and the eigen values farthest from jw axis were neglected.

It has been observed that the aforesaid methods were able to produce the transient response of the high order system quite well. But, as pointed out in [3] and rectified in [4], there is an error in the steady state value of the system response. An improvement in the method was proposed in [8]. In view of the basic model of Davison gave the deviation in steady state with original system, Chidambara, in his correspondence with Davison had suggested an alternative approach for model order reduction [3]. S. A. Marshall had also proposed an alternate way to compute the reduced order model [5]. The methods discussed above give a reduced order model which is an approximation of the original system. However, it was not clear that to what extent a given system can be reduced while representing a close approximation to the original high order system. It was observed that the proximity of the approximate model can be determined in terms of the principal eigen-value

neglected, the size of the original plant, and the reduced plant. This criterion is judged by comparing the time responses of various low order systems. An approach for selecting the order of the model for Davison technique was proposed by Mahapatra [8].

In this present work the reduced order model has been obtained through modal truncation technique. The steady state mismatch has been avoided by utilizing singular perturbation technique. The author has proposed to utilize the singular perturbation method [9] of balance truncation to hybridize with modal truncation method. In singular perturbation the states are grouped into two modes slow and fast modes. The fast mode is made equal to zero thus getting the slow modes of the system along with the contribution of the fast modes also. This is also known as residualization. With this the steady state of the reduced system matches with the higher order system. The advantage of the proposed method is its applicability to large scale systems which has been validated through an example of a system of order 1006 [10].

Statement of the problem

Consider the linear time-invariant stable n^{th} order state space model described by following equations

$$\left.\begin{aligned}\dot{x} &= Ax + Bu \\ y &= Cx + Du\end{aligned}\right\} \quad (1)$$

with the transfer function matrix

$$G(s) = C(sI - A)^{-1} B + D \quad (2)$$

where $x \in R^n$, $y \in R^m$, $u \in R^p$

the aim of the model order reduction is to obtain the low order representation described as

$$\left.\begin{aligned}\dot{x}_r &= A_r x_r + B_r u \\ y_r &= C_r x_r + D_r u\end{aligned}\right\} \quad (3)$$

with transfer function matrix

$$G_r(s) = C_r(sI - A_r)^{-1} B_r + D_r \quad (4)$$

where $x_r \in R^r$, $y_r \in R^m$ such that $y_r(t)$ is a close approximation to $y(t)$ for all input $u(t)$. Moreover the key features of the original system should be preserved in the reduced model such as stability.

2. PROPOSED MODEL REDUCTION ALGORITHM

The proposed algorithm is the result of hybridization of modal truncation [1, 11-13] and singular perturbation [9] approach. It consists of two sections namely modal truncation and singular perturbation.

2.1 Modal truncation

- State space realization of the high order system (HOS) as in (1) is obtained.
- All the Eigen values $\sigma(A)$ of the HOS are evaluated.
- Hankel singular values (HSV) of the HOS is computed and checked for comparatively significant HSV. The number of dominant HSV will be the order of reduction r.
- Modal matrix P is calculated and partitioned as below

$$P = \begin{bmatrix} P_{11} & P_{12} \\ P_{21} & P_{22} \end{bmatrix} \quad (5)$$

where P_{11} is a matrix of order $r \times r$, P_{22} is a matrix of order $(n-r)\times(n-r)$, P_{12} is a matrix of order $r \times (n-r)$ and P_{21} is a matrix of order $(n-r)\times r$.

- Modal inverse matrix Q which is inverse of matrix P is obtained and partitioned as below

$$Q = \begin{bmatrix} Q_{11} & Q_{12} \\ Q_{21} & Q_{22} \end{bmatrix} \quad (6)$$

where Q_{11} is a matrix of order $r \times r$, Q_{22} is a matrix of order $(n-r)\times(n-r)$, Q_{12} is a matrix of order $r \times (n-r)$ and Q_{21} is a matrix of order $(n-r)\times r$.

- Partition the matrices A, B, C and D as given below

$$\left.\begin{aligned} A &= \begin{bmatrix} A_{11} & A_{12} \\ A_{21} & A_{22} \end{bmatrix} \\ B &= \begin{bmatrix} B_1 \\ B_2 \end{bmatrix} \\ C &= \begin{bmatrix} C_1 & C_2 \end{bmatrix} \end{aligned}\right\} \quad (7)$$

Where A_{11} is a matrix of order $r \times r$, A_{22} is a matrix of order $(n-r)\times(n-r)$, A_{12} is a matrix of order $r \times (n-r)$ and A_{21} is a matrix of order $(n-r)\times r$

- Now after the completion of section (i) the reduced order model can be given as

$$\left.\begin{aligned} \hat{A}_{11} &= A_{11} + A_{12} P_{21} P_{11}^{-1} \\ \hat{B}_1 &= B_1 \\ \hat{C}_1 &= C_1 \\ \hat{D}_1 &= D \end{aligned}\right\} \quad (8)$$

Due to mismatch in DC gain of the reduced order model thus obtained with the original system, further singular perturbation is applied. This overcomes the DC gain mismatch problem. Singular perturbation steps are carried out in continuation to modal truncation steps. It has been explained in next sect

2.2 Singular Perturbation

Partitioned forms as above can be used to construct singular perturbation approximation [9]. The matrices of the final reduced system can be given as

$$\left.\begin{aligned} A_r &= \hat{A}_{11} - A_{12}A_{22}^{-1}A_{21} \\ B_r &= \hat{B}_1 - A_{12}A_{22}^{-1}B_2 \\ C_r &= \hat{C}_1 - C_2A_{22}^{-1}A_{21} \\ D_r &= \hat{D} - C_2A_{22}^{-1}B_2 \end{aligned}\right\} \quad (9)$$

The proposed algorithm is the result of hybridization of conventional modal truncation technique with singular perturbation approximation method so as to utilize the merits of the two methods. The technique has been applied to higher order systems which are discussed in the preceding section.

3. NUMERICAL EXPERIMENTS

3.1 Example-1

This example is taken from [9]. It is a continuous, linear, time-invariant and stable system of order four. The state-space matrices are described as follows

$$\left.\begin{aligned} A &= \begin{bmatrix} -0.43781 & 1.1685 & 0.41426 & 0.05098 \\ -1.1685 & -3.1353 & -2.8352 & -0.32885 \\ 0.41426 & 2.8352 & -12.4753 & -3.2492 \\ -0.05098 & -0.32885 & 3.2492 & -2.9516 \end{bmatrix} \\ B &= \begin{bmatrix} -0.11814 \\ -0.1307 \\ 0.05634 \\ -0.006875 \end{bmatrix} \\ C &= \begin{bmatrix} -0.11814 & 0.1307 & 0.05634 & -0.006875 \end{bmatrix} \\ D &= \begin{bmatrix} 0 \end{bmatrix} \end{aligned}\right\} \quad (10)$$

The step response and bode diagram of the HOS is shown in Fig. 1 and Fig. 2 respectively.

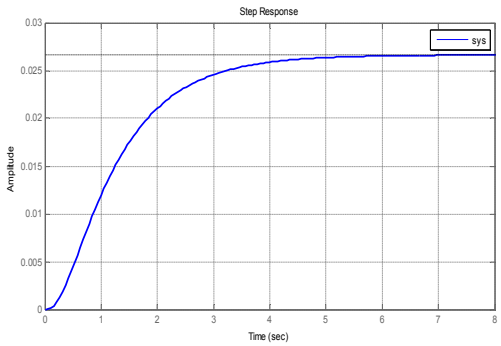

Fig. 1. Step response of the HOS

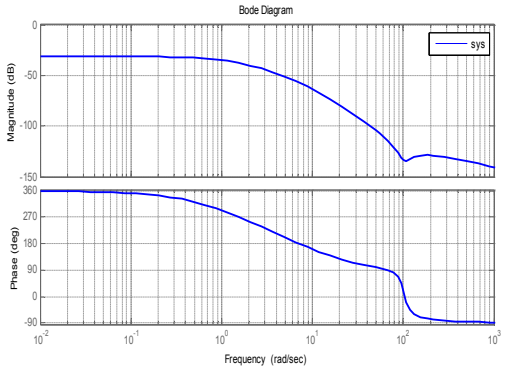

Fig. 2. Bode magnitude and phase plot of the HOS

The various steps to derive the reduced order model has been presented as follows.

The eigen-values of the HOS are given as $\sigma(A)$.

$$\sigma(A) = \{-1, -3, -5, -10\}$$

As all the poles lie in the left half of s-plane so the HOS is stable.

Henkel singular value of the HOS has been calculated and also plotted in Fig. 3, which gives the indication of the order of reduction. Comparatively the number of nonzero dominant singular values is taken as order of the reduction. Here, from Fig. 3, the first two singular values are significant and the last two singular values have become insignificant.

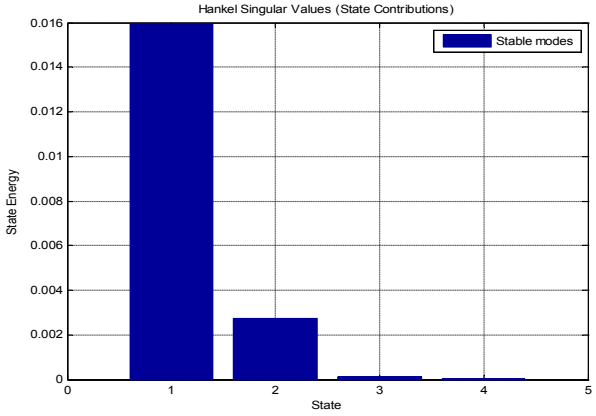

Fig. 3. Hankel singular values plot of the HOS

From the above plot order of the system to which it should be reduced is decided as 2.

The algorithm for modal truncation has been applied to the high order system (10).

The modal matrix P obtained is as:

$$P = \begin{bmatrix} -1.0314 & 0 & 0 & 0 \\ 0 & -2.8885 & 0 & 0 \\ 0 & 0 & -5.1070 & 0 \\ 0 & 0 & 0 & -9.9731 \end{bmatrix} \quad (11)$$

Partitioned matrices P_{11} ,P_{12}, P_{21} and P_{22} are given as

$$P_{11}=\begin{bmatrix} -1.0314 & 0 \\ 0 & -2.8885 \end{bmatrix};\quad P_{12}=\begin{bmatrix} 0 & 0 \\ 0 & 0 \end{bmatrix}$$
$$P_{21}=\begin{bmatrix} 0 & 0 \\ 0 & 0 \end{bmatrix};\quad P_{22}=\begin{bmatrix} -5.1070 & 0 \\ 0 & -9.9731 \end{bmatrix} \qquad (12)$$

The inverse modal matrix obtained is as follows

$$Q=\begin{bmatrix} -0.9696 & 0 & 0 & 0 \\ 0 & -0.3462 & 0 & 0 \\ 0 & 0 & -0.1958 & 0 \\ 0 & 0 & 0 & -0.1003 \end{bmatrix} \qquad (13)$$

Partitioned matrices Q_{11} ,Q_{12}, Q_{21} and Q_{22} are given as

$$Q_{11}=\begin{bmatrix} -0.9696 & 0 \\ 0 & -0.3462 \end{bmatrix};\quad Q_{12}=\begin{bmatrix} 0 & 0 \\ 0 & 0 \end{bmatrix}$$
$$Q_{21}=\begin{bmatrix} 0 & 0 \\ 0 & 0 \end{bmatrix};\quad Q_{22}=\begin{bmatrix} -0.1958 & 0 \\ 0 & -0.1003 \end{bmatrix} \qquad (14)$$

Now the partitioning the matrices A, B, C and D results into A_{11}, A_{12}, A_{21}, A_{22}, B_1, B_2, C_1 and C_2 shown as below.

$$A_{11}=\begin{bmatrix} -0.4378 & 1.1685 \\ -1.1685 & -3.1353 \end{bmatrix};\quad A_{12}=\begin{bmatrix} 0.4143 & 0.0510 \\ -2.8352 & -0.3288 \end{bmatrix}$$
$$A_{21}=\begin{bmatrix} 0.4143 & 2.8352 \\ -0.5098 & -0.3288 \end{bmatrix};\quad A_{22}=\begin{bmatrix} -12.4753 & -3.2492 \\ 3.2492 & -2.9516 \end{bmatrix} \qquad (15)$$
$$B_1=\begin{bmatrix} -0.1181 \\ -0.1307 \end{bmatrix};\quad B_2=\begin{bmatrix} 0.0563 \\ -0.0069 \end{bmatrix}$$
$$C_1=\begin{bmatrix} -0.1181 & 0.1307 \end{bmatrix};\quad C_2=\begin{bmatrix} 0.0563 & -0.0069 \end{bmatrix}$$

Now applying the modal truncation only as given by (8) the reduced system matrices obtained are given as $sysr=\{A_r,B_r,C_r,D_r\}$

$$\left.\begin{aligned} A_r&=\begin{bmatrix} -0.4378 & 1.1685 \\ -1.1685 & -3.1353 \end{bmatrix} \\ B_r&=\begin{bmatrix} -0.1181 \\ -0.1307 \end{bmatrix} \\ C_r&=\begin{bmatrix} -0.1181 & 0.1307 \end{bmatrix} \\ D_r&=\begin{bmatrix} 0 \end{bmatrix} \end{aligned}\right\} \qquad (16)$$

The step response of the reduced system with high order system is compared in the Fig. 4, which is seen to be close approximant of the HOS. From the Fig. 4, it is observed that the steady state value of the reduced system differs from the original high order system.

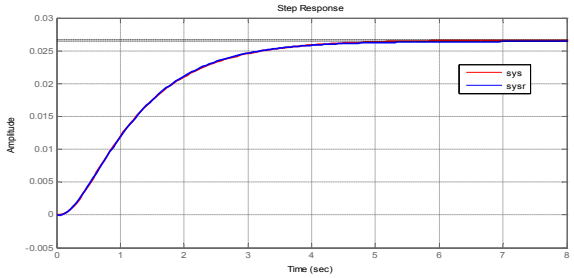

Fig. 4. Step response of reduced system with HOS using modal truncation only

Further the proposed algorithm ie singular perturbation (9) hybridized with modal truncation (8) has been applied to the high order system (10). The reduced system matrices obtained are given as $sysr1=\{A_{r1},B_{r1},C_{r1},D_{r1}\}$

$$\left.\begin{aligned} A_{r1}&=\begin{bmatrix} -0.4249 & 1.2565 \\ -1.2565 & -3.7355 \end{bmatrix} \\ B_{r1}&=\begin{bmatrix} -0.1164 \\ -0.1427 \end{bmatrix} \\ C_{r1}&=\begin{bmatrix} -0.1166 & 0.1412 \end{bmatrix} \\ D_{r1}&=\begin{bmatrix} 2.1019\times10^{-4} \end{bmatrix} \end{aligned}\right\} \qquad (17)$$

The comparison of reduced order system with the original HOS is shown in Fig. 5. From the Fig. 5, it is clear that the response of reduced order system is a better approximation by proposed technique than the modal truncation method applied alone.

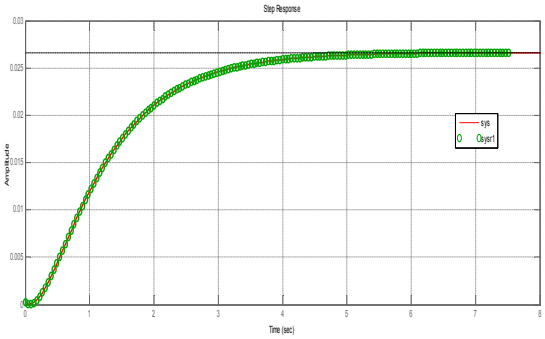

Fig.5. Step response of reduced system with HOS

The comparative responses have been plotted in Fig.6. It clearly shows that with the application of modal truncation alone there is steady state mismatch while with the singular perturbation applied as well the offset has been overcome. Thus it reveals that by the proposed technique the reduced system obtained to be a far superior approximation of HOS than the modal truncation method applied alone.

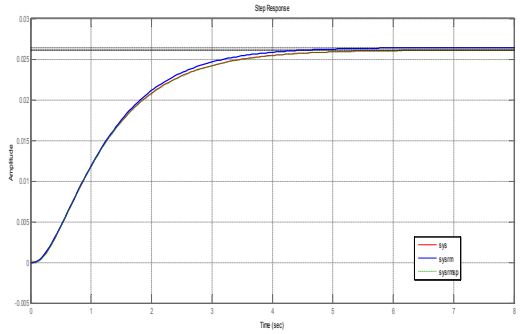

Fig.6. Comparision of response of reduced system with HOS by proposed algorithm and modal method

Integral Square Error (ISE) has been calculated to show the effectiveness of the approach. It is defined as

$$ISE = \int e^2(t)\,dt \qquad (18)$$
$$where\ e(t) = y(t) - y_r(t)$$

$y(t)$ is the step response of high order system and $y_r(t)$ is the step response of reduced order system.

The ISE has been obtained for the above two cases. The table shows the values obtained.

Table.1. Integral Square Error

S.No.	Method used	ISE
1	Modal Truncation	$1.27\text{x}10^{-6}$
2	Proposed Approach	$6.21\text{x}10^{-8}$

ISE value by the proposed approach is much less as compared to modal truncation method. So it confirms the effectiveness of the proposed approach.

3.1 Example-2

This example is taken from [10]. It is a dynamical system of order 1006. The state-space matrices are given by

$$sys = \{A, B, C, D\}$$

$$\left.\begin{aligned} A &= \begin{bmatrix} A_1 & 0 & 0 & 0 \\ 0 & A_2 & 0 & 0 \\ 0 & 0 & A_3 & 0 \\ 0 & 0 & 0 & A_4 \end{bmatrix} \\ A_1 &= \begin{bmatrix} -1 & 100 \\ -100 & -1 \end{bmatrix}; A_2 = \begin{bmatrix} -1 & 200 \\ -200 & -1 \end{bmatrix}; A_3 = \begin{bmatrix} -1 & 400 \\ -400 & -1 \end{bmatrix}; \\ A_4 &= -diag(1,2,...,1000) \\ B^T = C &= \left[\underbrace{10,10,...,10}_{6}\underbrace{1,1,...,1}_{1000}\right]; D = [0] \end{aligned}\right\} \qquad (19)$$

The step response and bode diagram of the original high order system is shown in Fig.7. and Fig.8. respectively.

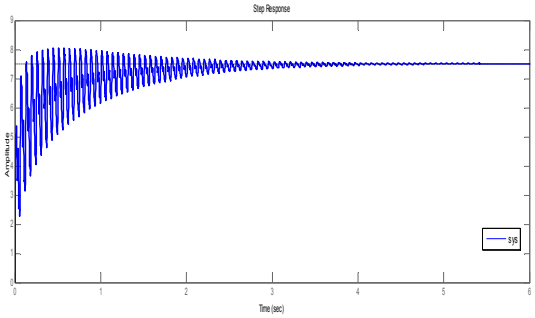

Fig.7. Step response of the high order system (19)

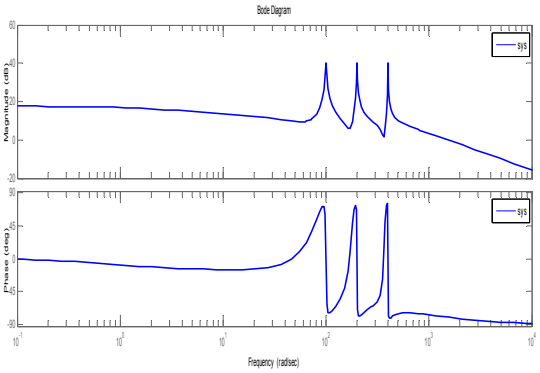

Fig.8. Bode magnitude and phase plot of the HOS (19)

The eigen-values of the high order system are given as $\sigma(A)$ and corresponding pole zero plot is given in Fig.9.

$$\sigma(A) = \{-1, -2, ..., -1000, -1 \pm 100j, -1 \pm 200j, -1 \pm 400j\}$$

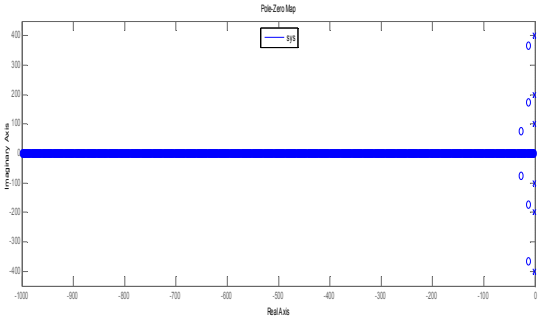

Fig.9. Pole-zero plot of the high order system (19)

Henkel singular value of the high order system has been calculated and also plotted in Fig.10, which is indication of the order of reduction. Comparatively the number of nonzero dominant singular values is taken as order of the system to be reduced. Here the first eight singular values are significant and after that ninth singular values onwards have decayed sharply [14], becoming insignificant. So the order of reduction is decided as eight.

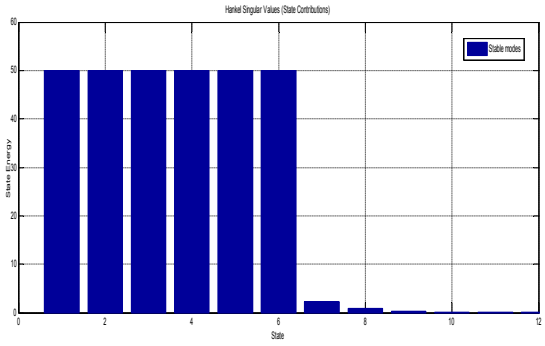

Fig.10. Henkel singular value plot of the HOS (19)

From the plot of Fig.11., order of the system to which it should be reduced is decided as 8.

The Modal truncation method alone has been applied to the high order system (19). The reduced system matrices obtained are given as $sysr = \{A_r, B_r, C_r, D_r\}$

$$A_r = \begin{bmatrix} -1 & 100 & 0 & 0 & 0 & 0 & 0 & 0 \\ -100 & -1 & 0 & 0 & 0 & 0 & 0 & 0 \\ 0 & 0 & -1 & 200 & 0 & 0 & 0 & 0 \\ 0 & 0 & -200 & -1 & 0 & 0 & 0 & 0 \\ 0 & 0 & 0 & 0 & -1 & 400 & 0 & 0 \\ 0 & 0 & 0 & 0 & -400 & -1 & 0 & 0 \\ 0 & 0 & 0 & 0 & 0 & 0 & -1 & 0 \\ 0 & 0 & 0 & 0 & 0 & 0 & 0 & -2 \end{bmatrix}$$

$$B_r = [10 \quad 10 \quad 10 \quad 10 \quad 10 \quad 10 \quad 1 \quad 1]^T$$

$$C_r = [10 \quad 10 \quad 10 \quad 10 \quad 10 \quad 10 \quad 1 \quad 1]$$

$$D_r = [5.9855] \qquad (20)$$

The step response of the reduced system (20) with high order system (19) is compared in the Fig.11, which is seen to be approximant of the system with dc gain mismatch.

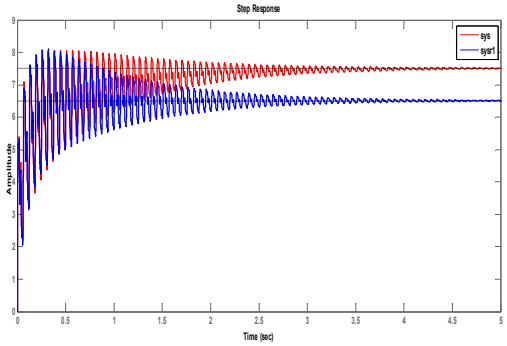

Fig.11. Step response of reduced system with high order system using Modal truncation only

Frequency response of the reduced system with the higher order system is also presented in Fig.12, which reveals the reduced system to be close approximation of the high order system. Fig.12 shows deviation at very high frequency which is equivalent to high initial transient behaviour as shown in Fig.12.

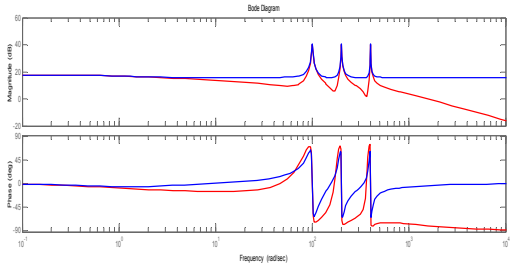

Fig.12. Frequency response of reduced system with high order system using modal truncation only

Further, proposed approach has been applied to the system. The reduced system matrices obtained are given as $sysr1 = \{A_{r1}, B_{r1}, C_{r1}, D_{r1}\}$

$$A_{r1} = \begin{bmatrix} -6.112 & 1.276 & -80.26 & 0.3737 & -69.88 & -180.3 & 9.427 & 9.229 \\ 1.276 & -0.2662 & 361.8 & -0.07799 & 44.53 & 81.91 & -1.968 & -1.927 \\ 80.26 & -361.8 & -0.0003607 & 12.95 & -0.0004454 & -0.00143 & 0.0791 & 0.07371 \\ 0.3737 & -0.07799 & -12.95 & -0.02285 & 154.6 & 50.48 & -0.5769 & -0.5648 \\ 69.88 & -44.53 & -0.0004454 & -154.6 & -0.00055 & -0.001766 & 0.09769 & 0.09104 \\ 180.3 & -81.91 & -0.00143 & -50.48 & -0.001766 & -0.005669 & 0.3137 & 0.2924 \\ 9.427 & -1.968 & -0.0791 & -0.5769 & -0.09769 & -0.3137 & -90.56 & -120.5 \\ 9.229 & -1.927 & -0.07371 & -0.5648 & -0.09104 & -0.2924 & -120.5 & -189.3 \end{bmatrix}$$

$$B_{r1} = \begin{bmatrix} 24.73 \\ -5.159 \\ -0.1899 \\ -1.511 \\ -0.2344 \\ -0.7526 \\ -19.91 \\ -19.03 \end{bmatrix}$$

$$C_{r1} = [24.73 \; -5.159 \; 0.1899 \; -1.511 \; 0.2344 \; 0.7526 \; -19.91 \; -19.03]$$

$$D_{r1} = [5.9855] \qquad (21)$$

The step response of the reduced system (21) with high order system (19) is compared in the Fig.13, which is seen to have close approximant with steady state matching from the original high order system.

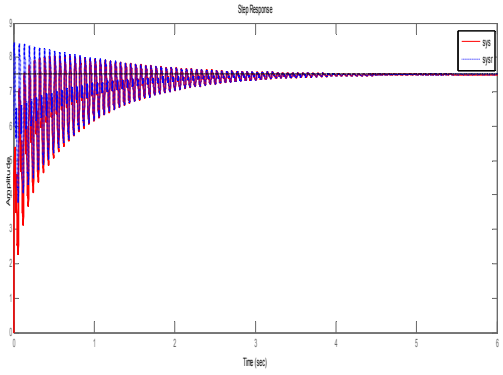

Fig.13. Step response of reduced system with high order system by proposed technique

Frequency response of the reduced system with the higher order system is also shown in Fig.14, which reveals the reduced system to be close approximation of the high order system.

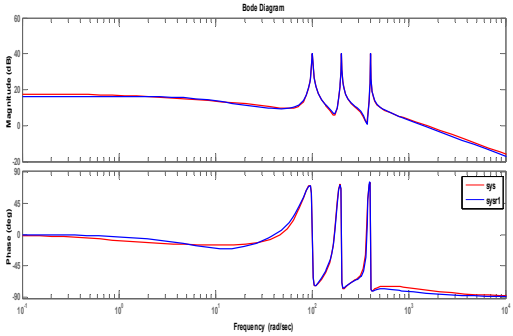

Fig.14. Frequency response of reduced system with high order system by proposed technique

Further another step response of the reduced system with the high order system for one second has also been shown in Fig.15 to clearly view the transient behaviour comparison. From Fig.15, the response show considerable deviation from the high order response but it lasts for 0.03 seconds only. This short high dynamic behaviour, if ignored the rest of the response is quite close.

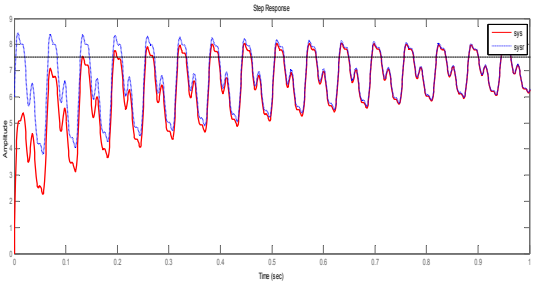

Fig.15. Step response of reduced system with high order system for short duration (one second)

Integral Square Error (ISE) has been calculated to show the effectiveness of the approach. The ISE obtained ignoring the short transient is 0.1966, which ensures the effectiveness of the method.

4. CONCLUSION

A hybrid method utilizing modal truncation and singular perturbation approximation approach has been applied successfully to determine the reduced replica of a high order system. One of the important demerits of the modal truncation method is dc-gain mismatch i.e., steady state value of the reduced order system do not agree with high order system. This demerit has been removed in the proposed approach. Further the method has been tested on high order system of order 1006. The results obtained confirm the validity of the approach. Applicability to large scale systems makes the method more advantageous. The high frequency transients show approximation error though it is of very short duration which is open for further investigation.

REFERENCES

1. DavisonE. J.: *A method for simplifying linear dynamic systems,* In: IEEE Transactions on Automatic Control AC-11: 93-101. 1966
2. Chidambara M. R. and Davison E. J.: *A method for simplifying linear dynamic systems*. In: IEEE Transactions on Automatic Control (Correspondence) AC-12: 119-121. 1967
3. Chidambara M. R. and Davison E. J.: *Further remarks on simplifying linear dynamic systems* IEEE Transactions on Automatic Control (Correspondence) AC-12: 213-214. 1967.
4. Chidambara M. R. and Davison E. J.: *Further remarks on 'A method for simplifying linear dynamic systems.* In: IEEE Transactions on Automatic Control (Correspondence) AC-12: 799-800,1967a.
5. Marshall, S. A.: *An approximate method for reducing the order of a linear system*. In: International journal of Control: 642-643, 1966.
6. Mitra D. : *The reduction of complexity of linear time-invariant systems*. In: Proceedings of 4th IFAC technical series 67, (warsaw): 19-33 1969.
7. Kumar A. and Chandra D.: *Improved Padé-Pole Clustering Approximant*. In: International Conference on Computer Science and Electronics Engineering, Dubai, UAE,17-18 November, 2013.
8. Mahapatra G. B.: *A Note on Selecting a Low-Order System Davison's Model Simplifcation Technique.* IEEE Transactions on Automatic Control AC-22(4): 677-678., 1977.
9. Liu Y. and Anderson B.D.O. : *Singular perturbation approximation of balanced systems*. In: International journal of control 50: 1379-1405, 1989.
10. Chahlaoui Y. and Dooren P. Van. : *A collection of benchmark examples for model reduction of linear time invariant dynamical systems*. SLICOT Working Note, 2002.
11. Antoulas, A.C.: *SIAM Book series, Advances in Design and Control*, DC-06. 2008.
12. Antoulas, A.C.: *A new result on passivity preserving model reduction*. Systems and Control Letters 54(4): pp.361-374.2005.
13. Antoulas, A. C., Sorensen, D.C. & Zhou, Y.: *On the decay rate of Hankel singular values and related issues*. In: Systems and Control Letters, 46(5), pp.323–342. 2002.

14. Soni M.G., Chitra D. R. and Pooja Soni :*Model Order Reduction- A Time Domain Approach* In: Special Issue of International Journal of Computer Applications (0975-8887) on Electronics, Information and Communication Engineering-ICEICE (2): 6-9,2011.

15. AvadhPati, Kumar Awadhesh and Chandra Dinesh *Suboptimal Control Using Model Order Reduction.* In: Chinese Journal of Engineering, Hindawi Publishing Corporation Article ID 797581, 2014(2014),pp.1-5, 2013.

16. Awadhesh Kumar, Bhoomika Maurya and Dinesh Chandra: *Dimension reduction and controller design for a waste water treatment plant* In: IEEE International Conference on Power and Advanced Control Engineering (ICPACE), Pages:413-417, 13-14 August, 2015, IEEE Conference Publications DOI: 10.1109/ICPACE.2015.7274983

17. Deepak Gupta and Awadhesh Kumar: *Approximation of Large Scale Systems by Balanced Truncation And Singular Perturbation Method* In: i-manager's Journal on Instrumentation and Control Engineering, Volume: 4, No. 2, Issue : Feb-Apr 2016, Pages : 1-6, 2016.

APPENDIX

```
% Program for the Modal Truncation and
Singular Perturbation

% Defining FOM real time model from
benchmark examples
A1=[-1 100;-100 -1]
A2=[-1 200;-200 -1]
A3=[-1 400;-400 -1]
A4=diag(-1:-1:-1000)
A=blkdiag(A1,A2,A3,A4)
C1a=[10 10 10 10 10 10]
C2a=ones(1,1000)
C=[C1a C2a]
B=C'
D=[0]

% Eigen analysis and Hankel singular
values
eig(A)
sys=ss(A,B,C,D)
hankelsv(sys)

% Defining Example-1 4th order model
A=[-0.43781 1.1685 0.41426 0.05098;
    -1.1685 -3.1353 -2.8352 -0.32885;
    0.41426 2.8352 -12.4753 -3.2492;
    -0.5098 -0.32885 3.2492 -2.9516]
B=[-0.11814;-0.1307;0.05634;-0.006875]
C=[-0.11814 0.1307 0.05634 -0.006875]
D=[0]

% Algorithm for Modal truncation in
time domain
A=input('A=')
B=input('B=')
C=input('C=')
D=input('D=')
E=eigs(A)
M=modreal(A)
n=size(M)
r=input('r=')
M1=M(1:r,1:r)
M2=M(1:r,r+1:n)
M3=M(r+1:n,1:r)
M4=M(r+1:n,r+1:n)
N=inv(M)
A11=A(1:r,1:r)
A12=A(1:r,r+1:n)
A21=A(r+1:n,1:r)
A22=A(r+1:n,r+1:n)
B1=B(1:r,:)
B2=B(r+1:n,:)
C1=C(:,1:r)
C2=C(:,r+1:n)

% Applying Only Modal Truncation
Ar=A11+A12*M3*inv(M1)
Br=B1
Cr=C1
Dr=D
Dr=D-C*inv(A)*B+Cr*inv(Ar)*Br

% Applying Singular Purturbation to
match steady state
A11n=A11+A12*M3*inv(M1)
Ar=A11n-A12*inv(A22)*A21;
Br=B1-A12*inv(A22)*B2;
Cr=C1-C2*inv(A22)*A21;
Dr=D-C2*inv(A22)*B2;

% Ploting rsponse and comparision
sys=ss(A,B,C,D)
sysr=ss(Ar,Br,Cr,Dr)
fig1=figure
step(sys,'r',sysr,'bo')
fig2=figure
bode(sys,'r',sysr,'bo')

% ISE CALCULATION..
t=0:0.1:6;
[y,t]=step(sys,t)
[y1,t]=step(sysr,t)
e=y-y1
j=e.^2
ISE=sum(j)
% END of program%
```

DUAL STATOR INDUCTION MOTOR DRIVE

*** Sivaprasad.R, #Dr.V.Jamuna**

* Assistant Professor at Sri Sairam Engineering College & *Research Scholar at* Jerusalem College of Engineering, prasad2303@gmail.com, sivaprasad.eee@sairam.edu.in
# *Professor*, Jerusalem College of Engineering, jamuna_22@yahoo.com

Abstract: *The Induction Motor is commonly used for almost all industrial applications. The losses that occur in an industrial motor can be minimized by making changes in its construction, by using a suitable control strategy and by making changes in the methodologies by which the power is being fed. The induction motor proposed in this paper consists of two stator windings. These two stator windings of the DSIM are fed by two different modified inverters. The working of three phase induction motor load fed by modified inverters has been analyzed. A prototype model of induction machine is also developed. The performance analysis of three phase Induction motor fed by different types of modified inverters and a Dual Stator Induction Motor- DSIM fed by two different modified inverters was done using MATLAB Simulink and the results are presented. The THD with respect to output voltage and output current are significantly reduced. The fundamental values of Voltage and Current are also improved drastically.*

Key words: *Induction motor, DSIM, Modified Inverters.*

1. Introduction

Induction Motors consume a major portion of electrical energy produced. These Induction motors are widely used because of their rugged nature, reliability and less cost. The energy saving of three-phase induction motor is significant as it consumes great quantity of electrical power [1, 2]. Improvement in the Energy Saving of the Induction motor results in huge profit for the end user, the industrial units and the society. The working of Induction motor fed by traditional inverters and ZSI is compared [3, 4, 5].The traditional inverters like VSI and CSI are found to offer more THD and lesser value of fundamental values of voltage and current. Energy saving can be achieved by making changes in the supply voltage, by usage of proper control strategy [6, 7, 8]. Energy saving is obtained by varying the supply voltage of the induction motor, by using voltage regulation control. The value of energy efficiency is controlled and optimized.

A new model of three-phase induction machine with two sets of stator windings is introduced [9]. Two different types of inverters feed the windings of a Dual Stator Induction motor. The power consumed by the motor is shared by a VSI and CSI. The effective energy saving is achieved by combined improvement of induction motor, inverters and control strategy [10, 11, 12]. Comparison of different types of modified Z- source inverters and CFSI is carried out [13, 14, 15]. The Modified ZSIs namely L-ZSI and Extended Γ-ZSI offer better efficiency to the Induction motor when being fed by them. This paper describes the block diagram of the Dual Stator Three Phase Induction Motor fed by two modified inverters in section II. In section III and IV two modified ZSI's are analyzed and their performance values are presented. The DSIM is fed with two different modified inverters and the results are presented in section V. The design details and construction of the Dual Stator Induction Motor is explained in the section VI and the paper concludes in the section VII.

2. Block Diagram of Proposed System

The block diagram of the DSIM is shown in Fig.1. This diagram shows a Dual Stator Three Phase Induction Motor.

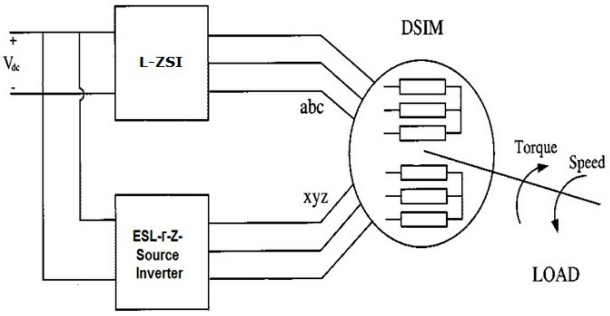

Fig. 1 Block Diagram

The two windings are fed individually by using two different inverters. The two windings are named as

Sivaprasad.R is a Research Scholar at Jerusalem College of Engineering. He is now with the Department of EEE, Sri Sairam Engineering College. (e-mail: prasad2303@gmail.com).
Dr.V.Jamuna is a Professor with the Electrical & Electronics Engineering Department, Jerusalem College of Engineering.

active winding and reactive winding. One Stator winding is fed by using a L-ZSI and the other winding is fed by using an ESL-Γ-ZSI.

3. L-ZSI Fed Induction Motor

The L-ZSI circuit is shown in Fig 2. The L-ZSI inverter requires lesser number of passive components. The problem of high inrush current at starting and resonance are eliminated.This inverter does not include bulky capacitor

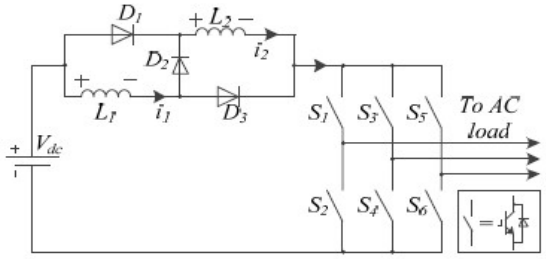

Fig. 2 L-ZSI Circuit Diagram

By using a L-ZSI the number of passive elements are reduced when compared to conventional ZSI. The losses that occur due to capacitors in a conventional ZSI are eliminated as voltage across the capacitor (V_c=0) as no capacitors are employed in a L-ZSI.

The working of L-ZSI in two modes is shown in Fig 3 and Fig 4.

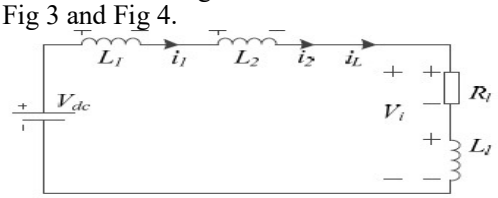

Fig. 3 Non – Shoot through State of L-ZSI

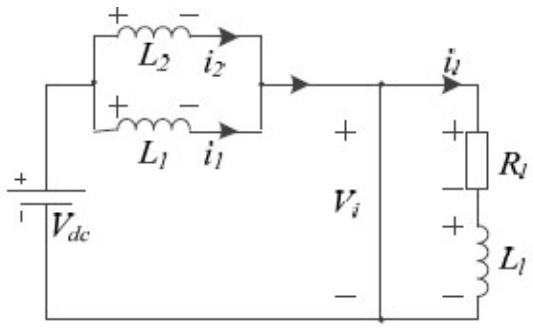

Fig.4 Shoot through State of L-ZSI

Table 1
Comparison between a conventional ZSI and L-ZSI

Parameters	Inverter type ZSI	L-ZSI
Stages	1	1
Passive elements	6	4
I/P current	Discontinuous	Continuous
V_c (or) V_{c1}	$V_{dc}(1-D)/(1-2D)$	0
B-boost factor	$1/1-2D$	$1+(n-1)D/1-D$
V_{c2}	$1-D/1-2D\ V_{dc}$	0

By using this type of inverter the THD at output voltage (V_0) and output current (I_0) is significantly reduced. The Table 1 gives the comparison between a conventional ZSI and L-ZSI.

The circuit diagram for L-ZSI fed three-phase induction motor (Fig 5).

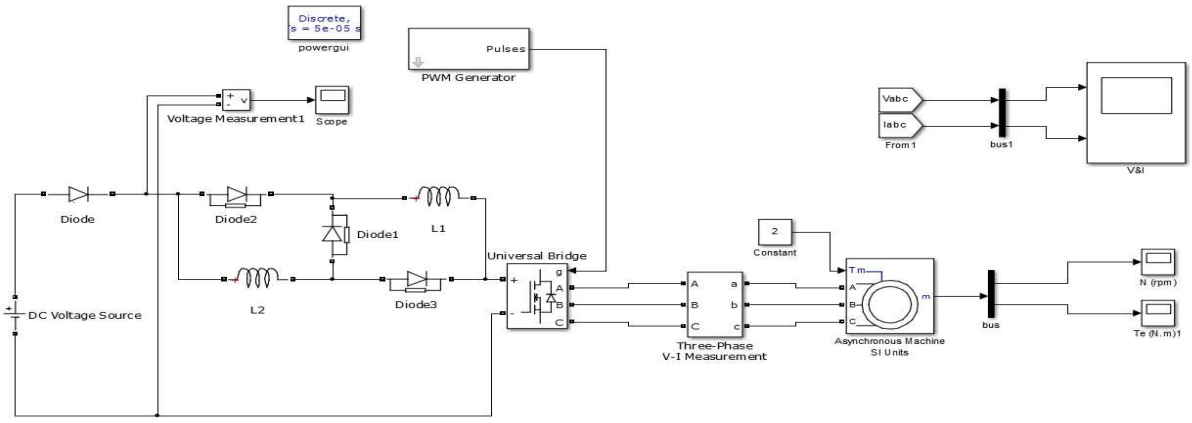

Fig.5 Simulation Circuit of L-ZSI fed Induction Motor Drive

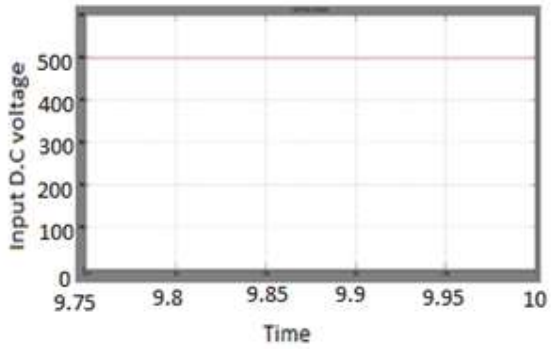

Fig.6 a) Input D.C Voltage to the LZSI vs Time

The Fig.6 a) shows the Input D.C Voltage to the L-ZSI (0 to +500 V in steps of 100 V) along Y Axis vs Time (9.75s to 10s in steps of .05s) along X Axis

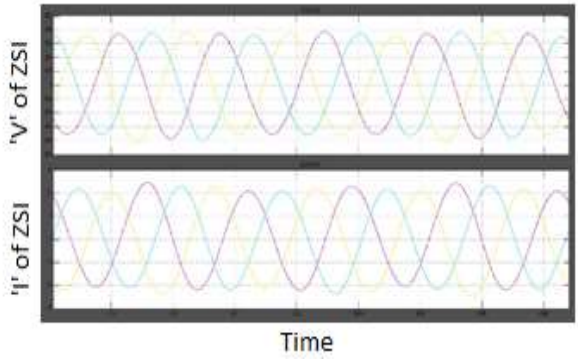

Fig.6 b) Voltage & Current Waveforms of L-ZSI vs Time

Fig.6 b) shows the Voltage (-500 to +500 V in steps of 100 V) & Current Waveforms of L-ZSI(-15 to +15 A in steps of 5 A) along Y- axis vs Time (0.78 s to 0.86 s) along X- axis

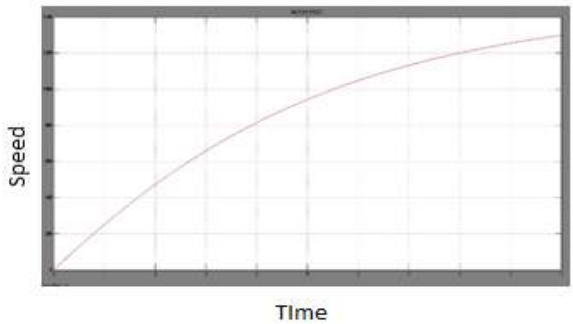

Fig.6c) Speed vs Time
Waveform of L-ZSI fed Induction Motor

Fig.6c) shows the Speed (0 to 1400 r.p.m in steps of 200 r.p.m) along Y-axis vs Time (0 to 10s in steps of 1 s) along X-axis Waveform of L-ZSI fed Induction Motor.The performance of an Induction motor fed by L-ZSI is understood from the waveforms 6a), 6b) and 6c)

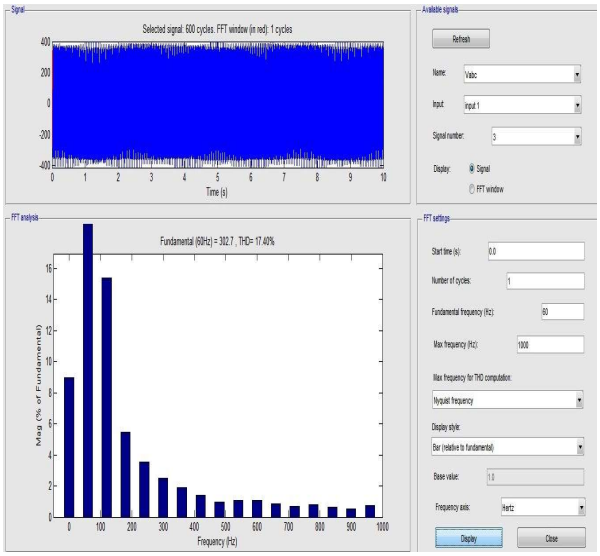

Fig. 7a) THD at Output Voltage (V_0) & the fundamental Value of Voltage (V_{01}).

The magnitude % of fundamentals is taken along Y – Axis and frequency along X-Axis. The fundamental value of voltage is 302.7V and the value of THD is 17.40 %

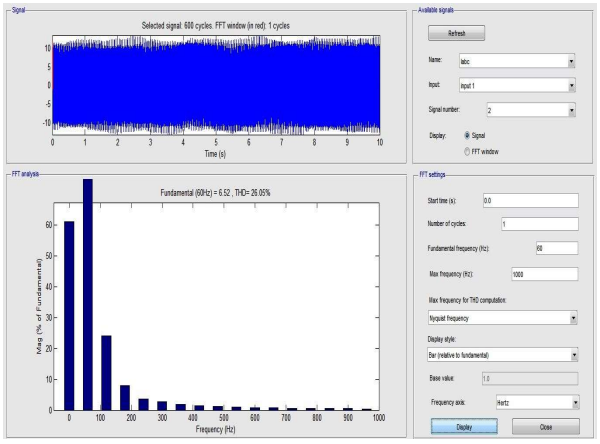

Fig. 7b) The THD at Output Current (I_0) and fundamental Value of Current (I_{01})

The magnitude % of fundamentals is taken along Y – Axis and frequency along X-Axis. The fundamental value of current is 6.52 A and the value of THD is 26.05 %. The difference between the figures 7a) and

7b) is that the former shows the FFT analysis and THD calculation for fundamental voltage whereas the latter shows the FFT analysis and THD calculation for fundamental current.

The THD at Output Voltage (V_0) and Output Current (I_0) and the Fundamental Values of Voltage (V_{01}) and Current (I_{01}) obtained by using this inverter are presented in Table 2.

Table 2

Values obtained by Simulation of L-ZSI

Parameter	ZSI	L-ZSI
THD at output voltage	36.13%	17.4%
THD at output current	51.11%	26.05%
V_{o1}	178.8 V	302.7 V
I_{o1}	5.185 A	6.52 A

4. E S L- Γ-ZSI Inverter Fed Induction Motor

The ESL- Γ -ZSI inverter circuit is shown in Fig. 8. The working of this inverter is presented in Fig 9 and Fig 10.

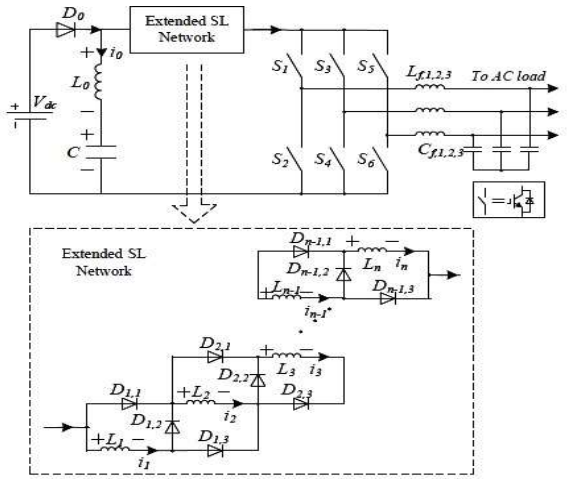

FIG. 8 ESL- Γ -ZSI Circuit

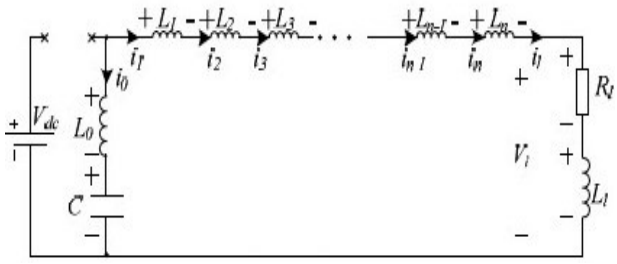

Fig.9 Non – Shoot through State of ESL- Γ –ZSI

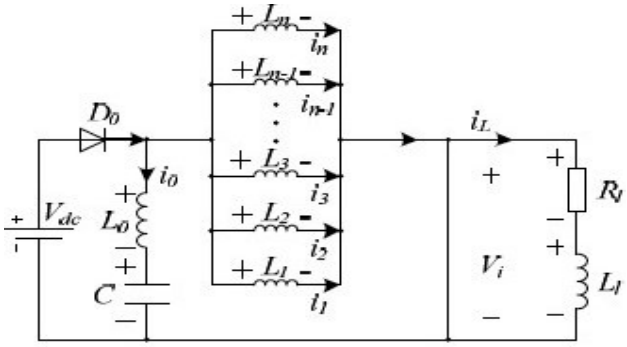

Fig.10 Shoot through State of ESL- Γ –ZSI

The simulation circuit (Fig 11), waveforms (Fig 12), FFT Analysis and THD calculation (Fig 13) are also presented.

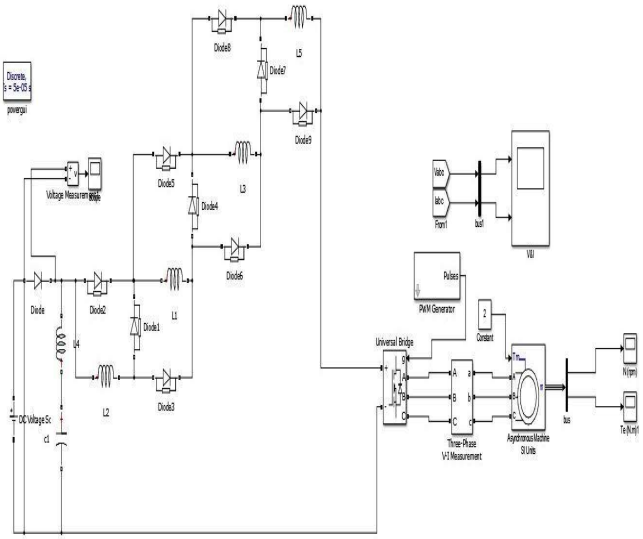

Fig.11 Simulation Circuit of ESL- Γ –ZSI fed Induction Motor Drive

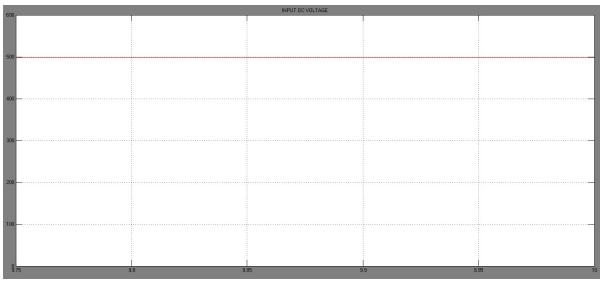

Fig.12 a) Input D.C Voltage to the ESL- Γ –ZSI (Y- axis) vs Time (X- axis)

The Fig.12a) shows the Input D.C Voltage to the ESL-Γ –ZSI (0 to +500 V in steps of 100 V) along Y Axis vs Time (9.75s to 10s in steps of .05s) along X Axis

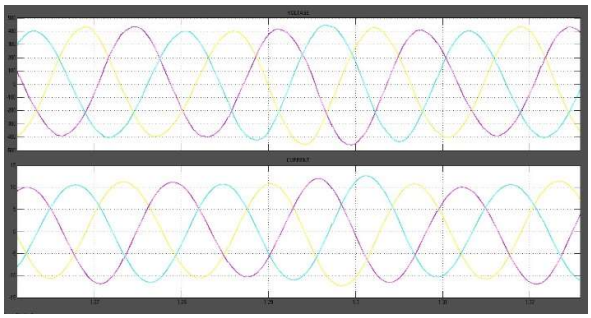

Fig.12 b) Voltage & Current Waveforms of the ESL- Γ –ZSI vs Time

Fig.12b) shows the Voltage (-500 to +500 V in steps of 100 V) & Current Waveforms (-15 to +15 A in steps of 5 A) of ESL- Γ –ZSI along Y- axis vs Time (1.26 s to 1.32 s) along X- axis

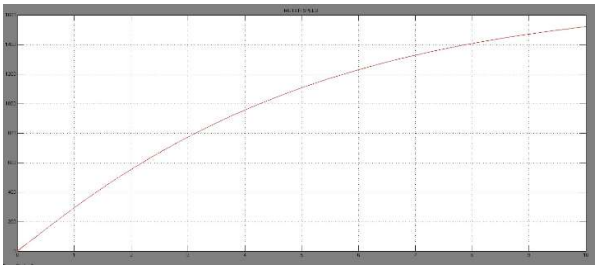

Fig.12c. Speed (X axis) vs Time (Y axis) Waveform of ESL- Γ –ZSI fed Induction Motor Drive

Fig.12c) shows the Speed (0 to 1600 r.p.m in steps of 200 r.p.m) along Y-axis vs Time (0 to 10s in steps of 1 s) along X-axis Waveform of ESL- Γ –ZSI fed Induction Motor.

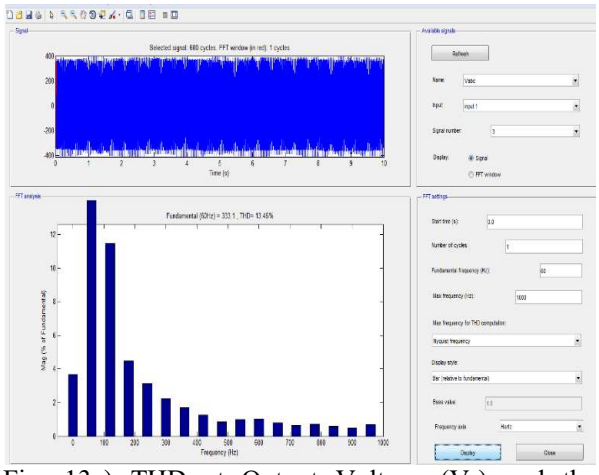

Fig. 13a) THD at Output Voltage (V_0) and the Fundamental Value of Voltage (V_{01}) for Γ-ZSI

The magnitude % of fundamentals is taken along Y – Axis and frequency along X-Axis. The fundamental value of voltage is 333.1 V and the value of THD is 13.45 %

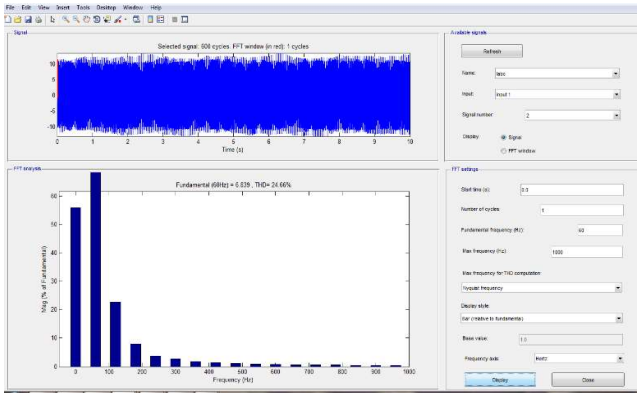

Fig. 13b) THD at Output Current (I_0) and the Fundamental Value of Current (I_{01}) for Γ-ZSI

The magnitude % of fundamentals is taken along Y – Axis and frequency along X-Axis. The fundamental value of current is 6.839 A and the value of THD is 25.66 %.The difference between the figures 13a) and 13b) is that the former shows the FFT analysis and THD calculation for fundamental voltage whereas the latter shows the FFT analysis and THD calculation for fundamental current. The THD at Output Voltage (V_0), THD at Output Current (I_0) and the Fundamental Values of Voltage (V_{01}) and Current (I_{01}) obtained by using this inverter are presented in Table 3.

Table 3

THD and Fundamental Values obtained by Simulation of ESL- Γ –ZSI

Parameter	Γ –ZSI
THD at output voltage	13.45 %
THD at output current	25.66%
V_{ol}	333.1 V
I_{ol}	6.839 A

The THD is reduced significantly and the Fundamental Values were found to be high.

5. DSIM fed by L-ZSI & ESL-Γ-ZSI

The Dual Stator Induction Motor fed by L-ZSI & ESL-Γ-ZSI Simulation circuit is given in Fig 14. The FFT analysis and THD Calculation results are given in Fig 15.

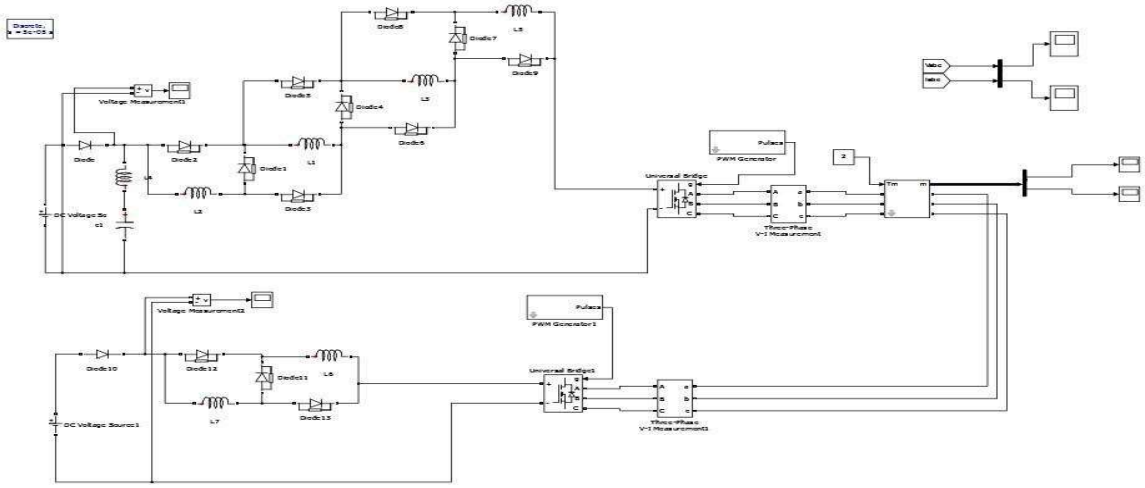

Fig 14.The Dual Stator Induction Motor fed by L-ZSI & ESL-Γ-ZSI Simulation circuit

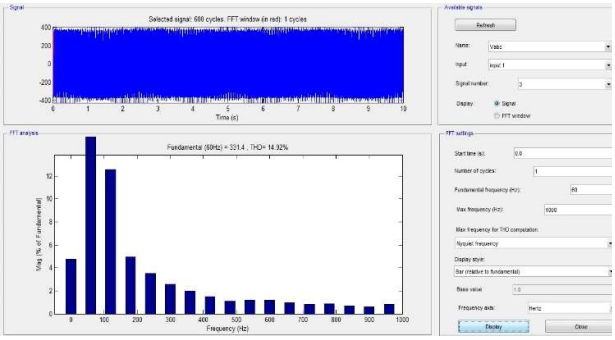

15 a) THD at Output Voltage (V_0) and the Fundamental Value of Voltage (V_{01}) for a Modified DSIM System fed by L-ZSI & ESL-Γ-ZSI

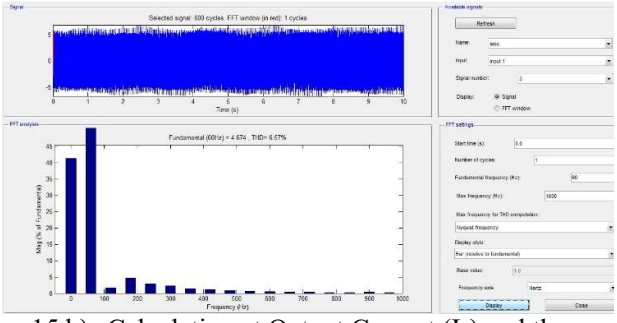

15 b) Calculation at Output Current (I_0) and the Fundamental Value of Current (I_{01}) for a Modified DSIM System fed by L-ZSI & ESL-Γ-ZSI

.

Table 4

THD for a DSIM fed by L-ZSI & ESL-Γ-ZSI

Parameters	SSIM with conventional ZSI	Proposed DSIM	Percentage Decrease in THD
THD at Ouput current	50.72 %	6.57 %	87.04
THD at Output Voltage	36.13%	14.92%	58.70

From Table 4, a major reduction of THD is observed in an Induction motor fed by L-ZSI & ESL-Γ-ZSI.

Table 5

Fundamental Values for a Modified DSIM System fed by L-ZSI & ESL-Γ-ZSI

Parameters	SSIM with conventional ZSI	Proposed DSIM	Percentage increase in fundamental value
Fundamental voltage	178.8 V	333.4 V	86.465
Fundamental current	3.3 A	4.674 A	35.363

From Table 5, significant improvement is found in the fundamental Values of Output Voltage and Output Current. Two different inverters namely, L-ZSI & ESL-Γ-ZSI are employed for obtaining improvement of fundamental values and for achieving considerable reduction of THD

6. Hardware Description

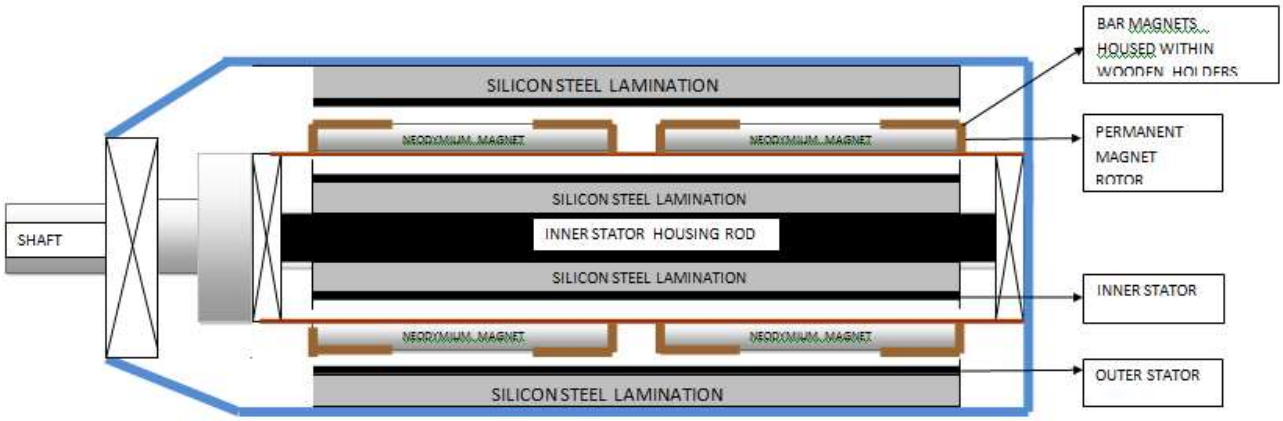

Fig.18 Constructional details of Dual Stator Machine

The proposed Dual Stator Induction Machine has two stators. The rotor is made hollow. One stator winding is placed inside the hollow rotor. Another stator winding is placed outside the hollow rotor. Fig.19, Fig. 20 and Fig. 21 show the exploded view, Inner and Outer Stators respectively.

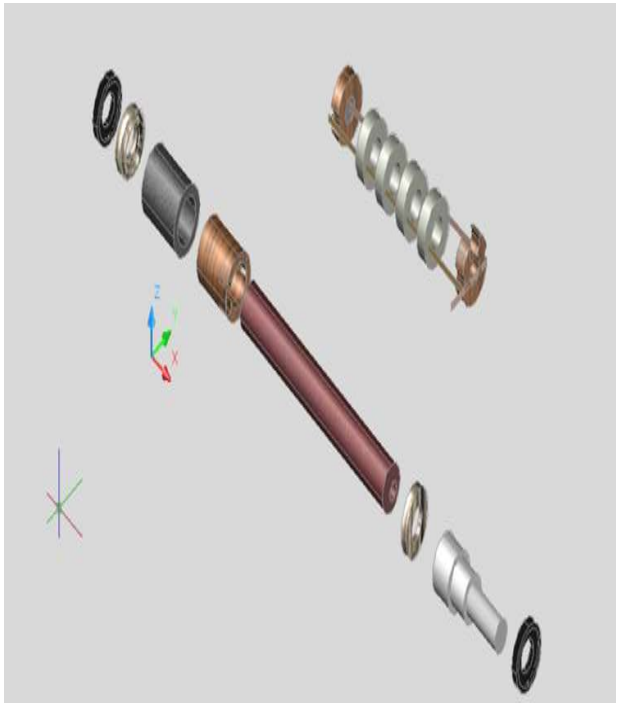

Fig.19 Exploded View of Dual Stator Machine

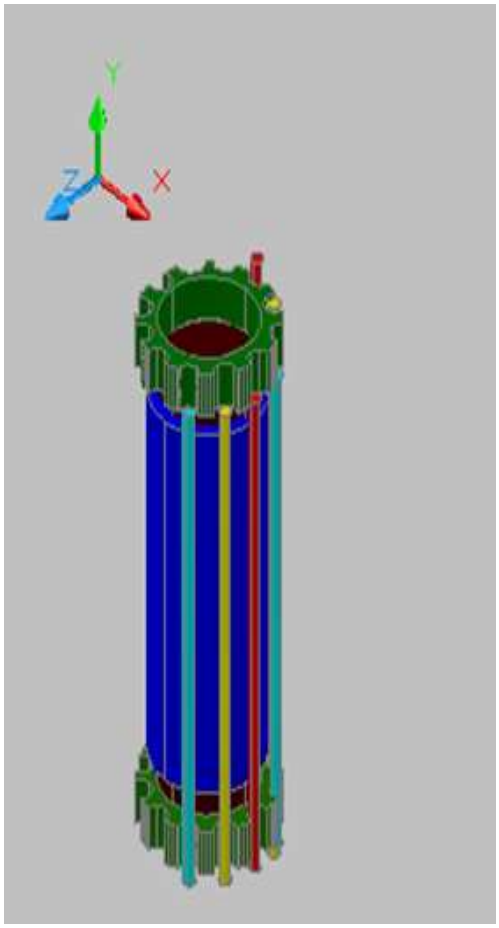

Fig.20 Inner Stator of Dual Stator Machine

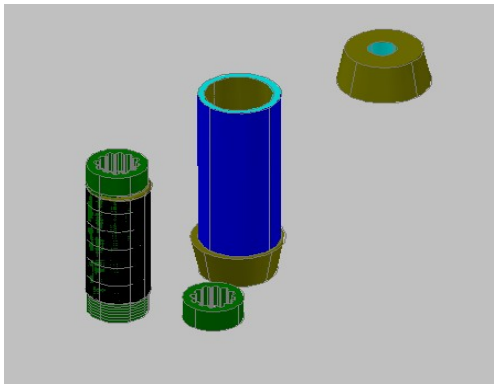

Fig.21 Outer Stator of Dual Stator Machine

The fabricated parts of the Dual Stator Machine are shown in Fig.22, Fig.23 and Fig.24.

Fig.22 Fabricated Hollow Rotor of Dual Stator Machine

Fig.23 Fabricated Inner Stator of Dual Stator Machine

Fig.24.Fabricated Outer Stator of Dual Stator Machine

Shorting of end wires has been done to ensure proper star connection of the machine. Number of turns of the machine has been decided depending upon the required output voltage. i.e. 15 volts.

Since the flux per pole obtained from the permanent magnet =0.505mWb, (1)

Frequency f =50Hz, (2)

Winding factor K_w = 0.955 (3)

E.M.F per phase, $E = 4.44 \times f \times \text{flux} \times Tph \times K_w$ (4)

Hence, $Tph = E/(4.44 \times f \times \phi \times K_w) = 140$turns. (5)

Each coil was wound on a former, making one coil side shorter than the other. The shorter coils were placed first, then the longer coils were placed. Mush

winding was selected due to the following characteristics:

- The coils have a constant span and it should be odd.
- There is only one coil side per slot and therefore the number of coils was equal to number of slots.
- There is only one coil group per phase per pole pair and therefore maximum number of parallel paths is equal to pole pairs.

A layer of varnish has been coated over the coils in order to prevent short circuiting of coils due to lamination failure. A layer of compound material has been coated for lamination purpose. The coils have been taken out through a hole drilled at the rear end through sleeve. Proper winding of the conductors have been checked using continuity test and by providing magnetic field through an external source. An output of 3V for turns through the 12th slot has been observed. Fig.25 shows the winding diagram for the inner stator.

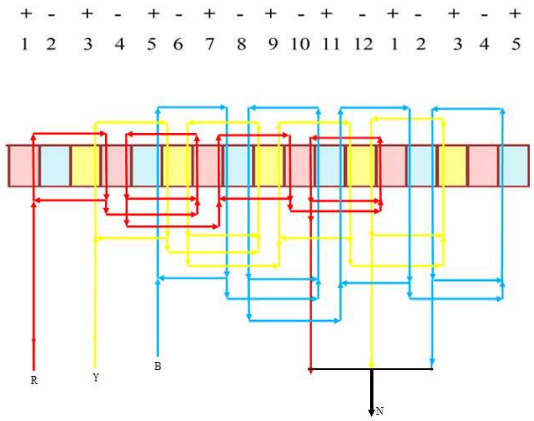

Fig.25 Winding Diagram for Inner Stator

The Outer stator has been fabricated with an air gap of 2 mm from the rotor. A hollow iron rod of thickness 3 mm has been used as an outer core. This provides protection for the entire machine. Silicon steel sheets with both axial and radial laminations have been provided similar to inner stator. Wooden support for windings has been provided in order to position the coils. Choice of wood was made from available insulators. Plastic, mount boards, wood and other materials might also be used to provide support for the windings. Inner stator and outer stator were expected to produce equal output voltage. This necessitated the alignment of winding pattern of inner and outer stator. The first slot support of the outer stator and the center of south pole was aligned. This made the outer stator and the magnetic poles to be aligned to each other. The same winding pattern as in inner stator is followed for the outer stator. The number of turns of the outer stator was determined depending upon the inner stator's number of turns. Variation in number of turns were made since, both the stators were expected to produce equal output voltage.

Induced e.m.f. in inner stator,

$$E1 = 4.44 \times f \times \phi \times \text{phase1} \times K_w \quad (6)$$

Induced e.m.f. in outer stator,

$$E2 = 4.44 \times f \times \phi \times t\ \text{phase2} \times K_w \quad (7)$$

In order to produce equal voltages in both the stators, the necessary condition is:

$$E1 = E2 \quad (8)$$

$$\text{i.e.} 4.44 \times f \times \phi_1 \times T\text{phase}_1 \times K_w = 4.44 \times f \times \phi_2 \times T\text{phase}_2 \times K_w \quad (9)$$

Since ϕ and T phase are the only variables in this equation,

Bavg x area under the influence of the magnetic = Bavg x area under the influence of the magnetic field x Number of turns in inner stator field x Number of turns in outer stator. Since the variation in area of inner or outer stator would have caused changes in the air gap length, the number of turns were the only variable to be changed.

Number of turns in outer stator, N_2 is obtained as follows,

$$A_2/A_1 = N_2/N_1 \quad (10)$$

$$\text{Thus, } N_2 = N_1 \times A_2/A_1 \sim = 140 \text{ turns.} \quad (11)$$

This is obtained by assuming that the area for both the inner stator and the outer stator are equal.

In order to improve the output voltage for same number of turns of outer stator, copper wire with larger thickness have been used. AWG 22 with

greater thickness than inner stator conductors have been used.

In order to get parallel operation between the inner and outer stator, the frequency, voltages, phase sequence, phase and line voltages must be equal. Here the frequency and voltages for both the inner and outer stator will be same, but the phase sequence will not be same. To get equal phase sequence, the output from anyone stator is rectified and then inverted as according to the other stator output phase sequence. So that both stator can be operated in parallel to get better performance.

7.Conclusion

The working of two different modified inverters is analyzed and the results are presented. The ESL- Γ - ZSI is found to be having least THD value. A prototype model of Dual Stator Induction Machine was designed and the constructional details are given. The simulation of a three phase induction motor and DSIM fed by using two separate inverters was carried out with the help of MATLAB Simulation. There is a considerable improvement in the fundamental values of the system.

References

1. Cao-Minh Ta, Membervand Yoichi Hori: *Convergence Improvement of Efficiency-Optimization Control of Induction Motor Drives.* In: IEEE transactions on industry applications, November/December 2001.
2. Olga Muravleva, Oleg Muravlev: *Induction Motor Improvement for Energy Saving Technologies*. In: Proceedings of the 7th Korea-Russia International Symposium, KORUS 2003
3. F. Z. Peng:, *Z-source inverter.*In: IEEE Trans. Ind. Appl., vol. 39, No. 2,pp. 504-510, Apr.2003.
4. Viswanathan, K. ; Oruganti, R. ; Srinivasan, D : *Dual-mode control of tri-state boost converter for improved performance*. In: IEEE Transactions on Power Electronics, vol.20, No.4, pp. 790-797, July 2005.
5. M. Shen, A. Joseph, J. Wang, et al: *Comparison of traditional Inverters and Z-source inverter for fuel cell vehicles*. In: IEEE Trans. Power Electron., vol. 22,No. 4, pp. 1453-1463, Jul. 2007.
6. C. D. Pitis, M. W. Zeller:*Power Savings Obtained from SupplyVoltage Variation on Squirrel Cage Induction Motors.*In:Proceedings of the Electrical Power Conference EPEC, 2008.
7. Peihua Hao, Ming Cheng, Ruiwu Cao, Yubin Wang, Zheng Wang: *Research on Induction Motor Energy Saving Strategy Using Voltage Regulation Control*. In: Proceedings of the International Conference on Electrical Machines and Systems, December 2010.
8. Hussein Sarhan: *Energy Efficient Control of Three-Phase Induction Motor Drive.* In: Journal of Energy and Power Engg, Vol.3, May 2011.
9. Kamalesh Hatua, Ranganathan V.T: *A Novel VSI- and CSI-Fed Dual Stator Induction Motor Drive Topology for Medium-Voltage Drive Applications*. In: IEEE Transactions on Industrial Electronics, Vol.58, No.8, Aug.2011.
10. Mishra.S, Adda. R , Joshi.A: *Switched-boost inverter based on Inverse Watkins-Johnson topology*.In: Proceedings of the Energy Conversion Congress and Exposition, IEEE, Sept. 2011.
11. Kamalesh Hatua, Ranganathan V.T: *A Novel VSI and CSI Fed Active – Reactive Induction Motor Drive with Sinusoidal Voltages and Currents.* In: IEEE Transactions on Power Electronics, Vol.26, No.12, December 2011.
12. Ravindranath. A, Mishra S.K, Joshi.A: *Analysis and PWM Control of Switched Boost Inverter*. In: IEEE Transactions on Industrial Electronics, Vol.60, No.12, Dec.2013.
13. Lei Pan, Hexu Sun, Beibei Wang, Yan Dong and Rui Gao: *ESL-Γ- Z – Source Inverter*. In: Journal of Elect. Eng. Techol.Vol. 9,No. 2: 589-599, 2014.
14. Lei Pan: *L-Z- Source Inverter*. In: IEEE Transactions on Power Electronics, Vol.PP,Issue .99, Feb.2014.
15. Soumya Shubhra Nag, Santanu Mishra: *Current Fed Switched Inverter*. In: IEEE Transactions on Industrial Electronics,Vol.61, No.9, September 2014.

R. Sivaprasad is a research scholar of Anna University.He is currently working as Asst. Prof in the Department of EEE, Sri Sairam Engineering College. His areas of interest are Control Systems, Energy Saving, Electrical Machines and Drives.

Dr. V. Jamuna is currently working as Professor in the Electrical and Electronics Engineering Department, Jerusalem College of Engineering, Chennai, India. She has secured the 5th university rank in her M.E. degree. She has published many technical papers in international journals. Her research interests include Induction Motor Drives and Neural Network controller for the drives.

Jamming aware unrestricted data transmission in multi-hop wireless networks

R.Uma Mageswari[1], Dr.S.Baulkani[2]

[1] *Associate Professor, Department of Computer Science and Engineering, Vardhaman College of Engineering (Autonomous), Shamshabad, Hyderabad, Telangana, India.*

[2] *Professor, Department of Electronics and Communication Engineering, Government College of Engineering, Tirunelveli, Tamilnadu, India.*

Email: umaphd71@gmail.com

Abstract- The basic entity of the wireless communication is the electromagnetic waves. Electromagnetic waves carry data that can be used by digital appliances in the wired and wireless network. In Multi-Hop Wireless Network (MHWN) data transmission is performed by the cooperation of neighbor nodes. The functionality of this network is severely affected by jammer, an intended node that blocks the ongoing communication as the media is open in nature. The jammer localization is required to predict the occurrence of jammer and its location in the network. Most of the existing jammer localization techniques only suits for predicting static jammer. The proposed jammer localization is capable of localizing both the static jammer as well as portable jammer. The jammer localization is followed by diverting the data that passes through the jammed area. The proposed Reliable Lookup Algorithm (RLA) enhances the data transmission in the MHWN by the obtained next region information thereby the ongoing data communication is retained. The simulation result proves this proposed work.

Key Words: Portable Jammer, Multi-Hop Wireless Network, Jammer localization, Data transmission.

1. Introduction

Wireless communication's rapid growth is widely involved in the different fields as it utilizes available electromagnetic spectrum for communication. The evolution of wireless communication from electromagnetism was discussed [24] Vinay Kumar Nassa 2011. The ease of use, cheapest price, ease to carry, ubiquitous nature, and adequate consumption has made it admired further. The realistic solution for achieving communication between universal networks is considered as Multi-Hop Wireless Network (MHWN) rather than fixed infrastructure based wireless network, where its services cannot be expanded. In MHWN's the participated device known as nodes which have the capability to communicate with each other without the support of any other external devices in the multi-hop fashion. Due to the open nature of the electromagnetic medium, leads the intruders to easily entered and degrade the functionality of the network [6] Gesic et al. 2016. Especially any form of attack in the wireless network is detected by the degradation in the received SNR i.e. signal-to-noise ratio [1] Adamy 2014. Also jamming attack is categorized under Denail of Service (DoS) attack, since it restricts the communication by denying the channel for legitimate users and is outlined as "any event that removes or decreases the ability of a network to fulfill its intended idea" [27] Wood et al. 2002. Though jamming attack is considered as physical layer attack, this attack can also be made through different layers in the existing protocols stack, thereby its cruel intention of degrading network performance is achieved through available resource usage restriction [17] Pelechrinis et al. 2016.

The current jammer localization algorithm can be categorized as two parts based on the data's used in position identification. First method depends on the range-based and the other is range-free. The Least square method [10] Liu et al. 2010, the Crowd Location method [21] Sun et al. 2011, etc., locates the jammer in the first method. As per [10] Liu et al. 2010, the jammer can be easily localize by using least square problem, that utilizes the variation caused to the range of hearing for the network. In the existing paper [9] Liu et al. 2009 uses VFIL Virtual Force Iterative Localization technique to identify the jammer position by measuring the distance between the nodes in the network and the jammer. The identification of the jammer depends largely on the jammed region's physical properties. Eventhough there are many existing jammer localization techniques are available based on the above two methods, but none of

them consider the jammer under mobility i.e. portable jammer. The proposed work consider portable jammer is equipped with motor that support the jammer to roam around the concerned area of Multi Hop Wireless Network.The Portable jammer can strongly differ its point in order to control the jamming signals in physical distribution that will result in a change in network setup. This renders the method of jammer positioning more complicated and difficult. This portability generates discrimination in the above said two methods. In the former method the distance computation is critical, in later the shape of the jammer varies.

In common this portable jammer affects the ongoing communication of the valid users and therefore it is the need to implement certain techniques to come out of its effect. This is only possible when the nodes in the network predict the presence of the jammer followed by portable path. Thereby present limitation in the existing network is overthrown. The steps provided below are included in this paper for the portable jammer detection efficiently. Identifying the right node and to observe the concerned node is the initial step. The second step is to estimate the jammer signal strength. The gather of the data from the concerned concert is the third step and the last step is to supervise the transfer of the concerned node i.e. handover function and fix the location of the jammer.

2. Associated work

This session gives details about the various existing attacks found in MHWN, follow by elaborately explains the main idea behind localization of the jammer and the way by which the target devices are tracked in the Wireless sensor Network.

2.1. Categories of Denial-of-Service attacks (DoS)

DoS attacks are used to prevent network resources from being accessed. This is usually accomplished by flooding the victim system or network with excessive traffic, rendering it incapable of responding to real user inquiries. As per [8] Islam et al. 2020 showcases the various DoS attacks occurs in WSN which is been categorized based on the existing different layers of networks. In the physical layer the attacks were listed as jamming and node tampering attack whereas as in data link layer the attacks were categorized as collision, interrogation and denial of sleep as well as in the network layer the specified attacks were spoofing, black hole attack and hello flood attack. In the transport layer attack were of synchronize flood attack, desynchronized attack and content attack and the last layer known to be application layer gets the attack called as overwhelming sensor node and path-based DoS.

The work done by [7] Hussaini et al. 2019 states there may be some untrusty nodes within the network which creates attack or compromising the network security. They designed the algorithm to detect and localize the untrusty nodes within the WSN and the way to isolate these nodes out of the network during the routing process. In [29] Xu et al. 2005 explained the initial layer jamming and it determines various forms of jammers based on its activity by reserving the channel for the concern duration as reactive jammer, constant jammer, proactive jammer, and random jammer. Apart from the above mention jammers there are many kinds of jammers are available now a day. In [30] Xu et al. 2008 provides mechanism to identify the jammer followed by retreating the interference effect by adopting spectral evasion techniques like channel surfing and spatial retreats thereby communication is achieved in presence of jammer.

2.2. Way to track end nodes inside WSN

Due to the modern IoT boards embedded with lot of location tracking modules analogy added up with the sensors it becomes quite practical to track the location of the end nodes. However, based on the survey from previous articles it's been identified that the following steps are adopted to track the device in WSN which is as per the figure 1.

Figure. 1. Steps for device tracking

In the first module of the diagram reflects the recognition of the end device where the detected is done by certain methods like Passive Infra-red (PIR) in case of the acoustic sensor [23] Vasuhi et al. 2016. The next module which is the reporting Process done after the target node has been successfully identified. The target device is identified using triangulation technology through this measurement details are reported. The last module is the region prediction as per the literature this phase has been using Particel filter, Kalman filter, Hidden Markov model. One can identify the next point of the device

movement based on the previous two steps in the WSN. Thus, the target device is traced by repeating these steps in the WSN.

2.3. Localization of the Jammer

According to literature there are numerous works focuses on jammer identification as well as localization. These algorithms are classified as range free and range based localization method. The range free method, functions by analyzing the geographical property of the jammed area. The DCL Double Circle Localization (DCL) algorithm was explained by [4] Cheng et al. 2012, existing mechanism worked on the basis of bounding circle i.e. minimum bounding circle (MBC) and maximum inscribed circle (MIC). Convex hull, is used to calculate the MBC and MIC. The improved PSO algorithm (particle swarm optimization) [16] Pang.et al. 2017, proposed the technique for manipulating the minimum occupying coverage jammed area. This paper [26] Wei et. al. 2017, keenly provides the existing techniques for jammer localization as well as it stated the MHWN performance under jammer done by the analysis of the various researchers. The existing [9] Liu et al. 2009 VFIL algorithm worked to identify the jammer based on the range of nodes changes, here F pull and F push mechanisms are used iteratively to find the jammer position more effectively. This method creates a measured jammed region in circular form. The center of this constructed circle will be fixed as the jammer location and which is predicted to be the actual jammed region.

Only a fewer jammer localization method are fixing up in the recent years, devoid to dedicated devices [17] Pelechrinis et al 2009. The current paper explained that PDR degradation due to the jammer presence in the network when a node comes nearer to the location of jammer, there will be decrease in PDR value. Hence the gradient-descent for PDR estimation-based jammer localization technique must be enabled; it worked based on the network topology's distinct axis in order to identify the jamming. The existing paper [13] Liu et al. 2012 developed the mechanisms to localize the jammer by exploiting neighbor changes. Initially they determined the jamming effect analysis as free-space model by examining the way through which communication range changes with the location of jammer and the power of transmission. Then the estimation of the jammer location was done by solving it as a least-squares (LSQ) problem. It provided the hypothesis, that when the jammer attacked the node, it moves from its hearing range. Then [14] Liu et al. 2012 devised an estimation scheme for jammer localization by introducing ambient noise floor technique as well as for improving localization accuracy an evaluation feedback metrics was formulated to quantify the error in estimation. This existing paper also suggest genetic algorithm to reduce the localization error. In this paper [22] Sun et al. 2011Centroid Localization (CL) technique was proposed, the calculated average for the jammed nodes co-ordinate is used to fix the jammer's location. This above mentioned situation was assumed there by the received signal strength varies by means of jammed nodes which were present in the various locations. Weighted Centroid Localization WCL [2] Blumenthal et al. 2007 suggested that it improves the localization accuracy when compared with CL by assuming further weight metrics to the jammer location, thereby only the exact nearby jammed nodes near to the jammer was used to compute the location of the jammer rather than considering than whole jammed nodes in the network. In [4] Cheng et al. 2012 Double Circle Localization (DCL) algorithm the Convex hull is used to calculate the MBC and MIC. In this existing work [28] Xiong et al. 2012 proposed the robust fault-tolerant algorithm, which discovers the location of the jammer in wireless sensor network. The existing paper [11] Liu et al. 2011 suggested the leverage network topology mechanism and the multiple jammers were identified. Each node modifies its location table based on signal strength and PDR to identify network topology change and this identification localized the jammer. Cheng suggested the M-cluster algorithm which was based on the grouping of jammed nodes with a clustering algorithm, and each jammed node group is used to estimate one jammer location. And the bifurcation points on the skeleton base on skeletonization was used to localize jammers as per X-ray algorithm. According to the paper work was organized as mapping the jammed region, followed by identifying the bifurcation point in the jammed area and finally locate the jammer.

. In summary, the current WSN device has the mechanisms for object tracking. By using this node can spot and track the target device. The target is assisted with the sensing equipments and transmission is reliable in the network. However in the situation of portable jammer tracking, the legal packets transmission may be embarrassed due to jammer. Thereby unpredictability occurs in the data reporting step as well as it causes huge impacts on the process of target identification and tracking.

3. Problem formulation

This section illustrates the issues associated with the portable jammer localization in the network as well as the necessity and the way to localize jammer and the hurdles inculcated in the jammer localization.

3.1 Network model

It was suggested in the anticipated system that it must have some static MHWN nodes that know their network spots. It is designed in such a manner that, the portable jammer node is connected via the entity i.e. motor which has the capability to pass through the entire MHWN's defined network area. The area where the nodes can able to sense each other, in which the node can effectively obtain the messages from other nodes and is represented as the node's hearing range. Thus, in this area the signal strength will be better for performing flawless communication. The other nodes that are not available in that concern region are connected by neighbours node. The jammer introduced into this network causes attack and hence reduces the Signal Noise Ratio and this node is represented as the node that has been jammed node, here called as dormant node. The author [14] Lie et al. 2012 adopts this classification of MHWN methodology. Based on the severity of the jammer attack, the MHWN is categorized as three parts.

- **Normal node**. If the node in the network can able to communicate with its neighbour nodes without any interruption and it is signal strength is found to be not degraded then the concern node is marked as Normal Node.
- **Dormant node**. If the node does not receive any message from any of its neighbours node then it is marked as Dormant node.
- **Border node**. The rest of the nodes in the MHWN are represented as Border node.

3.2. Jammer Representation

In order to affect the performance of the MHWN an intruder who purposefully blend with the network is identified here as the portable jammer. This jammer's main task is to makes the medium busy by engaging the concern channel frequency, thereby disturbing the transmission between the nodes which are under its range of transmission. Due to this the receiver signal was affected.

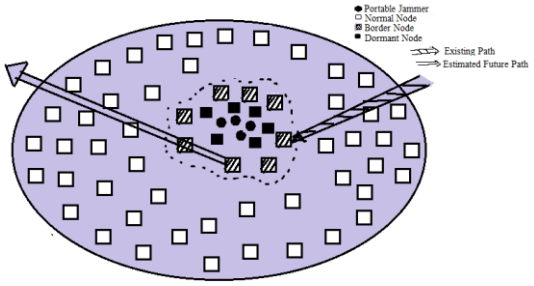

Figure. 2. Model of portable jammer path tracing in MHWN

In figure 2 portrait the structure of the MHWN, where multiple nodes are scattered and are pictures as flat nodes. These nodes have the capability to communicate with each other as these nodes are fixed with omni directional antennas and these communications are highly affected because of the open nature of the electromagnetic media. Until there is no circumstance of signal degradation all the participants' node can communicate with each other and the nodes are treated to be normal nodes. Also, these nodes have the capability to known about its position in the network by the support of GPS devices [3] Bulusu et al. 2000 accommodate with it. If in the network there are 'N' nodes, its coordinates are represented in two-dimension as {($a1$, $b1$), (a2, $b2$), …, (aN, bN)}. Generally, the nodes retain the routing table which holds its neighbor node information and will be updated frequently in a particular interval of time. The dark circular node represents the portable jammer in its motion. Due to its effect in this figure certain nodes are marked as border nodes which have partial communication capability in particular direction due to jammer presence and the rest of the nodes are marked as dormant nodes as they can't participate in the communication because it is fully under the influence of the jammer.

3.3. Signal Strength Measurement and Transmission Model

The wireless transmission follows numerous prototype for channeling, some of them are shadow path loss prototype, free space prototype etc. In the proposed work shadow path model is used to find out sustaining strength for certain distance, and it is also accepted for tracing the signal transmission path [26] Wei et al. 2018.

The Shadow path prototype is provided by applying Equation 1

$$SU_s = CH_s / d_n \quad (1)$$

Where the channeling strength is represented as CH_s and the node's sustaining strength is represented as SU_s. In the Equation (1), the connection between CHs and SUs is represented and d denotes the distance between the jammer node and sustain node and n is fading factor.

The relaying of signal and prototype for computation holds mainly on the Received Signal Strength (RSS), which won't need any additional hardware since RSS indicator (RSSI) itself is an indicator for system of regulated communication. The logarithm design format for Equation (1) is represented in the Equation 2.

$$RSSI(d) = 10 \log SUs\ 10 \log CHs - 10n \log d + X\sigma \quad (2)$$

Where, $X\sigma$ is the shadow vanishing parameter and this parameter is represented by standard deviation. The distributed random variable also models the shadow prototype.

4. Proposed system

The Proposed work consider the network as in the figure 2 that holds channeling requirement as specified in the Equation 1 and the jamming prototype used in this work is the shadow path prototype. Also the proposed system uses RSSI for tracing the location of the jammer by following it and compute its path in the concern tracing period 't'. This tracing period is marked into several time slots 't' and during this time slots the analysis of this prototype is done. Thereby the jammer spot is estimated in the MHWN and a moving derived. The proposed work consider that the portable jammer is fixed with an omni directional antenna, thus the effect is recognized by the all the nodes surround it and the speed of the jammer is considered to be moderate, so that it won't damage the performance of the network as well as support for the smooth functioning of the network. The proposed path detection mechanism for portable jammer contains 4 steps, depending on these considerations i.e. i) selection of observing node ii) computation for jammer localization iii) next observing node selection iv) On / Off handover mechanism. Followed-by these steps the next region known to be A*A without jammer effect is identified for the data transmission even though degradation occurs by the portable jammer.

4.1 Node State Categorizations

The state of the node within the MHWN must be detected after the successful identification of the jammer. Based on that the node's state devised into i)Normal Node (NN), ii)Border Node (BN) and iii)Dormant Node (DN). The following algorithm is used to detect the node's state in the concerned timeslot based on the Signal to Noise Ratio (SNR). The threshold value (P) is set based on the signal strength. If the node does not lose any of its neighbour node then it is Normal node during the specific trace period by the observing node. In case the observing node identifies the jammer then that particular node with SNR below the threshold and can't participate in the communication is represented as the dormant node also if the node in the jammer region is represented as Border node if it does not lose any of its neighbor. The count of Border nodes in this algorithm is represented as 'K'.

Algorithm1:

Identification of Node's State:

```
If   N not found a jammer
Then
N=NN
Else
If  N= K &&  ON(SNR) > P
Then
N=NN
Else if
N≠K && ON(SNR )< P
Then
N=DN
Else
N=BN
End
End
End
```

For each period of time, a significant initial work i.e. the detection of dormant nodes due to the effect of jammer, traced the jammer's attack and the localization of the jammer is done. There are many detection methods exists for detection of basic jammers. Based on jamming attack at physical layer, many localization methods are available, which uses the signal strength computation like PDR etc. [25] Wei et al. 2017.

4.2 Observing Node Selection and Handoff process

To identify the portable jammer the proposed system, elects the exact observing node. This observing node identify the region or spot of the portable jammer at each of its tracing timeslot accurately by predicting the affected region with dormant nodes. It is necessary to dynamically regulate the observing nodes, as each observing nodes has only a limited observing area. An observing region denotes the region wherever it gets the jammer signal and discovers the jammer region. The

observer node is chosen in such a way as a node among the border nodes. The survival of more than one border nodes in this region is the critical issue, since all these nodes are ready to act as observing node by sending willing to act packet, that increases unwanted overhead. To overcome this Algorithm 2 is proposed.

In this work the value of 'K' plays the major role where 'K' is the count of the border nodes in the particular time slot 't'. During this time period the observing node sends the hello packet to its neighbour node, in case of all the border nodes 'K' receive this hello packet, the nodes in this region are normal and hence they are active to participating in communication, in cased the value of 'K' decreased, it assures one or more than one nodes are affected. But before sending a hello signal to the border node if no other signal from the outside of the border is received by the observing node, then the current observing node cannot act as observing node further. In this situation new observing node should be nominated. The overhead of the observing node will be reduced by these procedures. Figure. 3 represents the observing node's activity.

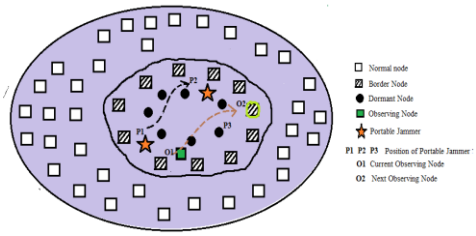

Figure. 3. Observing Node Activity Representation

Whenever the jammer begins to plot a route out of the current observing node's observing region, the tracing task will be reallocated wisely by choosing the next observing node near to the jammer's new location. Accordingly, the process of reallocating the duty of current observing node to the next newly elected observing node is known to be Handoff process. In the above figure 3 the O1 is acting as current observing node, it can able to monitor the jammer within its observing range. The portable jammer is shown in this figure which can able to move from the position P1 to P2. The current observing node has the capability to observe the jammer only up to P2 after that it won't get the signal from jammer, hence the present observing node O1 can't act as the observing node further. Based on the jammer movement the next observing node has to be chosen, here the next position of the jammer is predicted to be P3 therefore the observing node should be chosen to be boundary node near to P3 location. Process of choosing the next observing node from the current i.e. O1 to O2, while doing this all the data collected during its period will be given to the next observing node O2.

Algorithm 2: Selection of Observing node and Handover function:

Observing Node Selection

If BN wants to act as ON
Set t_wait (between 0 to time before sending WILL_ON packet)
End
Sleep(t_wait)
If this BN doesn't receive any other WILL_ON or ON_ENG within t_wait
Mark this node as ON
Else one or more WILL_ON
Select the ON with least time stamp
Mark this node as ON
Else ON_ENG received
Do Nothing
End

Observing Node declaration

If BN doesn't received WILL_ON or ON_ENG within t_wait
Compose WILL_ON packet with its {Node id, Time Stamp}
Broadcast this WILL_ON to its neighbours
Wait for a period > t_wait
Compose ON_ENG packet with {INI_BRO packet's id, Timestamp}
Broadcast the ON_ENG packet to its neighbor
Mark this node as ON
Else
Mark this node as BN
End

Observing Node Handoff

If the ON's RJSS is lower than threshold 'a'
Calculate the moving direction and moving path based on its tracking record
Calculate target position's coordinates
Initiate Handoff process by making the concern node to initiate WILL_ON
If succeeds then
Send ON_ENG to its neighbour nodes
Handover the records from precious ON to the present ON

Previous ON becomes border node
End
End

In this algorithm 2 WILL_ON represents the packet willing to act as observing node, ON_ENG represents the packet which specify observing node engagement. These packets are passed into the MHWN nodes just like the transmission of hello packets in the network.

4.3 Reliable Lookup Algorithm (RLA) for Packet Redirection

Due to the prominent signal noise introduces in the channel because of the open nature of the medium the jammer localization become complicated RSS variation by this factor. Thereby efficiency of jammer localization will be reduced to some extent. To overcome this RLA algorithm is proposed. The threshold (β) value is set in this RLA which is the essential metric based on the level of signal strength which is 50% of the original RSS. The 'β' value is fixed based on node hearing range as well as historical evidence on signal loss or path loss exponent information. The progression in tracking the jammer attack is achieved by this threshold value. The observing node (a_o,b_o) estimated their channeling power (P) to calculate the position of each jammer node with its axis (a_j, b_j). If the concerned node relieves a higher level signal than the threshold value, then the erroneous node is discarded. The Figure 4 explains the request for destination and acknowledgement / replay packet format.

Node_ID	Time Slot	(a,b)	A*A(next region detail)

Figure. 4. Packet Format for Des_Req

In the Figure. 4 The Des_Req packet, the field (a,b) is coordinate spot of the destination. This packet format is adopted by [26] Wie et al. 2018 and the extra field A*A is added to obtain next region or next hop based on the concerned signal. The algorithm 1 is used to predict the node's state and is noted in the table for every time slot. The node id list provides the information regarding node's coordinates. Whenever the process of handoff is essential, these available nodes's table list provides the signal strength details in order to make observing node handover process successful.

This proposed mechanism is intended to redirect the data packets with the measured channeling strength obtained from the additional filed in the DES-REQ packet in the particular time slot thereby it act as the layer in the network. In this proposed mechanism, the packets are retransferred from the dormant region to the obtains next region or next hop A*A via observing node without dormant nodes by invoking border nodes which holds the node list containing the signal strength information and uses the information of the future path of this portable jammer by the observing node.

The redirection of the packet using A*A additional field is explained in this following algorithm.

Algorithm 3: RLA Algorithm

Input: Available Maximum number of try H_{max}
If Received Jammer Signal Strength RJSS < β
Evaluate the jammer node direction and trace the path
Calculate the destination axis spot
If current ON's present in the specified region
Evaluate the Destination node
If the flag of A*A =1 then
Build a Des_Req packet to next A*A region
Transmit the Des_Ack packet to the nearest neighbour
Sleep upto the Time period t_wait
Receive Des_Res packet and target node list
Else
Call Algorithm 2 for Handover of ON
If Handover succeeds
Perform the usual task of ON
End
//Packet diversion procedure
Declare HON'=0
If (HON'< H_{max})
Build HO_REQ packet from the list
If (HO_ACK) packet is received
HON'=HON'+1
Else return
End
End
End

In this algorithm HON' represents Handover Node which performs handover of data from dormant area and HO_REQ represents packet for Handover Request and HO_ACK represents packet for Handover Acknowledge. The detail of the handover are carried by the additional A*A field.

5. Simulation and result analysis

This section discusses about the simulation setup and the results obtained for the proposed work by using NS-3 simulator

5.1. Simulator NS-3

The network was setup as per the details provide in Table 1. MHWN's performance is evaluated under the proposed portable jammer using NS-3 simulator. The nodes are spread over the entire area of the grid. The portable jammer considered here can travel the entire network and is fixed with an omni directional antenna that covers all the directions. The travelling path is divided into T = 50 separate timeslots.

Log-Distance propagation loss model is an extension of the Friis free space model. It is used to predict the propagation loss for a wide range of environment which is referred from [20]. The log-normal shadowing introduces some kind of randomness into the received signal power.

Table 1. Simulation Parameters (Setup of MHWN)

Notation	Meaning	Parameter
RP	Routing Protocol	DSR
TS	Topology Size Grid (N×N)	where N is from 10 to 20
GD	Grid Distance	1200 m
NN	Number of Nodes	*900*
SN_*ID*	Source Node ID	*#N6*
DN-ID	Destination Node	ID #9
FT	Flow Type	HTTP
PR	Packet Rate	20 pkt/sec
D	Duration	20 sec
NP	Number of packets	200
PS	Packet Size	1088 bytes
MAC	Physical address	IEEE 802.11b
WIM	Wireless Interface Mode	Ad hoc
PLM	Propagation Loss Model	Log-distance Path Loss Model
PDM	Propagation Delay Model	Constant Speed Model
S	Simulator Version	ns-3.11-RC2
L	Deployment range of wireless network	1600 m
P_T	Transmitting power of MHWN node	46.67 dBm
P_J	Transmitting power of the portable jammer	46.67 dBm
P_N	Power of Noise	−60dBm
G	Gain of transmitter and receiver	1
N	Path loss exponent	3
M	Mean of shadow shading	0
Σ	Standard deviation of shadow shading	1

5.2. Experimental results

As per the Table 1 the simulation setup, using this the simulation was done for portable jammer localization and tracing its path followed by packet diversion in the dormant region for achieving better packet delivery rate. Figure 5 shows the arrangement of various nodes in the simulation environment present in the network, as well as the portable jammer moving path.

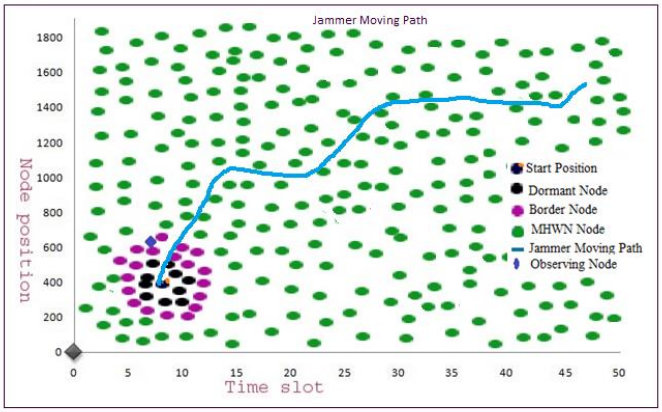

Figure. 5. Arrangement for Simulation

5.3 Measurement Estimate.

The localization of the jammer and the accuracy in path tracing is the primary measure requirement for validating the result. It represents the exactness of the jammer's original location and estimated location in each timeslot.

This was classified as three parts i) based on the position ii) based on the area iii) based on the distance. The proposed system uses the metrics based on position. In order to minimize error AMAE (Adapted Mean Absolute Error) must be computed. According to proposed system at i^{th} time slot, the simulation the Portable Jammer is marked as PJ i.e. (a_j,b_j) and Observing Node ON i.e. (a_o,b_o). The portable jammer position is represented as PJ^1_i.....PJ^n_i , respectively. If it is M observing nodes present in the every time slot 'i' then it is represented as

$$AMAE_i = 1 / M \sum_{j=1}^{M} (||ON_i^j||) \quad (4)$$

The figure 6 shows that the traced jammer position can be robust with the original jammer location of the jammer in each timeslot. The figure 6 shows the result of the traced path for portable jammer obtained by average of every observing node traced value. In this graph the X axis represent the time slot where as the Y axis specifies the node position.

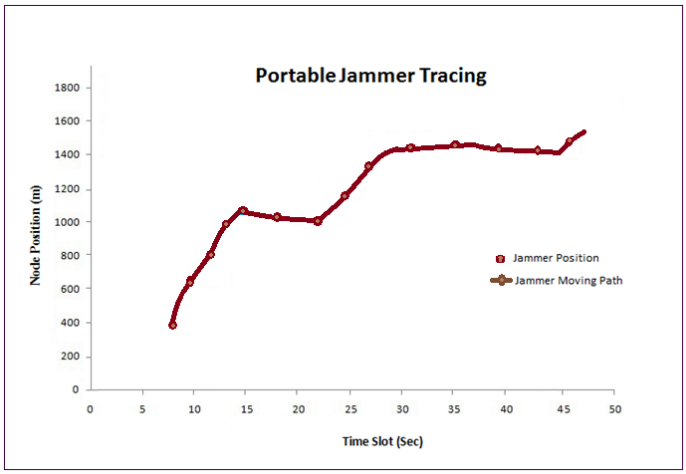

Figure. 6. Proposed Tracing Scheme

5.3 Packet Transmission under Portable Jammer

Figure 7 shows the simulation result for the packet transmission under portable jammer using RLA as well as with usual technique without RLA adoption. The graph is obtained by varying the number of nodes present in the MHWN considered in x axis and number of packets transmitted in y axis where the total packets consider for transmission are 20 packets/Sec.

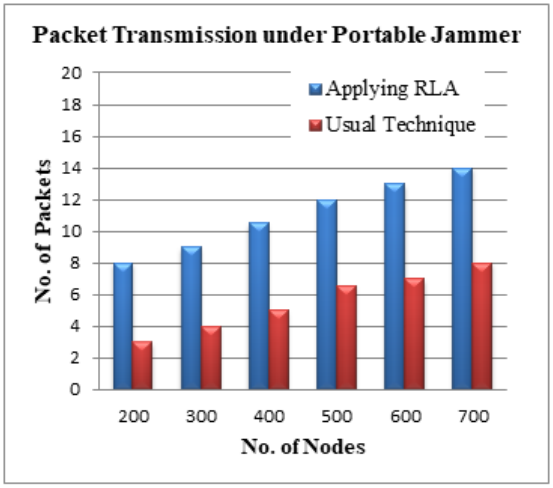

Figure. 7. Packet Transmission under Portable Jammer

6. CONCLUSION AND FUTURE WORK

The proposed work localizes the portable jammer as well as trace its path efficiently which the existing static jammer localizations mostly fails. The proposed RLA divert the data from the jammed region after localizing jammer, thereby the data packets reach its destination node. The proposed system selects the observing node first, and then identifies the location of the jammer followed by tracing its path is done. In case the

present observing node can't sense the jammer then handoff process will be achieved in order to elect the next observing node, this is achieved by signal strength degradation. The simulation results show the tracing path of jammer as per these steps. This result showcases that the proposed algorithms have done it by efficiently traced portable jammer meanwhile it also predicts the next hop neighbour or next region information without signal degradation as A*A. Thereby proposed RLA algorithm redirects the data packet transmission. Simulation results compares and shows the packet delivery rate is achieved in the case of adopting RLA algorithm as well as with the usual transmission case. In future the work will focus on considering portable jammer with varying speed as well as diverting the data by considering the energy level of the nodes and path length there by further packet transmission can be improved.

REFERENCES

[1] Adamy, David. *EW 102: a second course in electronic warfare*. Artech house, 2004.

[2] Blumenthal, Grossmann, Golatowski and Timmermann. "Weighted centroid localization in zigbee-based sensor networks." *Proceedings of the IEEE International Symposium on Intelligent Signal Processing, WISP 2007* (2007): 1–6.

[3] Bulusu, Heidemann, and Estrin. "Gps-less low cost outdoor localization for very small devices." *IEEE Personal Communications Magazine* 7.5 (2000): 28–34.

[4] Cheng, Tianzhen, Ping Li, and Sencun Zhu. "An algorithm for jammer localization in wireless sensor networks." *Advanced Information Networking and Applications (AINA), 2012 IEEE 26th International Conference on*. IEEE, 2012.

[5] Cheng, Tianzhen, et al. "M-cluster and X-ray: Two methods for multi-jammer localization in wireless sensor networks." *Integrated Computer-Aided Engineering* 21.1 (2014): 19-34.

[6] Gezici, Sinan, et al. "Jamming of wireless localization systems." *IEEE Transactions on Communications* 64.6 (2016): 2660-2676.

[7] Hussaini, M.M. and Rajalakshmi, A., 2019. "Design and development of a new algorithm for detecting and localization of multiple attacks in wireless sensor network." *Journal of Electrical Engineering*, 19.3 (2019).

[8] Islam, M.NU., Fahmin, et al. "Denial-of-Service Attacks on Wireless Sensor Network and Defense Techniques." *Wireless Personal Communications* 116.3 (2020): 1993-2021.

[9] Liu, Hongbo, et al. "Localizing jammers in wireless networks." *Pervasive Computing and Communications, 2009. PerCom 2009. IEEE International Conference on*. IEEE, 2009.

[10] Liu, Zhenhua, et al. "Wireless jamming localization by exploiting nodes' hearing ranges." *International Conference on Distributed Computing in Sensor Systems*. Springer, Berlin, Heidelberg, 2010.

[11] Liu, Hongbo, et al. "Determining the position of a jammer using a virtual-force iterative approach." *Wireless Networks*17.2 (2011): 531-547.

[12] Liu, Sisi, Loukas Lazos, and Marwan Krunz. "Thwarting control-channel jamming attacks from inside jammers." *IEEE Transactions on mobile computing* 11.9 (2012): 1545-1558.

[13] Liu, Zhenhua, et al. "Exploiting jamming-caused neighbor changes for jammer localization." *IEEE Transactions on Parallel and Distributed Systems* 23.3 (2012): 547-555.

[14] Liu, Zhenhua, et al. "Error minimizing jammer localization through smart estimation of ambient noise." *Mobile Adhoc and Sensor Systems (MASS), 2012 IEEE 9th International Conference on*. IEEE, 2012.

[15] Liu, Zhenhua, et al. "An Error-Minimizing Framework for Localizing Jammers in Wireless Networks." *IEEE Trans. Parallel Distrib. Syst.* 25.2 (2014): 508-517.

[16] Pang, Liang, et al. "A novel range-free jammer localization solution in wireless network by using PSO algorithm." *International Conference of Pioneering Computer Scientists, Engineers and Educators*. Springer, Singapore, 2017.

[17] Pelechrinis, Konstantinos, et al. "Lightweight jammer localization in wireless networks: System design and implementation." *Global Telecommunications Conference, 2009. GLOBECOM 2009. IEEE*. IEEE, 2009.

[18] Proano, Alejandro, and Loukas Lazos. "Packet-hiding methods for preventing selective jamming attacks." *IEEE Transactions on dependable and secure computing* 9.1 (2012): 101-114.

[19] Rau, Adoor Vikramaditya, et al. "A novel method for jammer localization in large scale sensor networks." *Wireless And Optical Communications Networks (WOCN), 2010 Seventh International Conference On*. IEEE, 2010.

[20]www.gaussianwaves.com/2013/09/log-distance-path-loss-or-log-normal-shadowing-model/

[21] Sun, Yanqiang, et al. "CrowdLoc: wireless jammer localization with crowdsourcing measurements." *Proceedings of the 2nd international workshop on Ubiquitous crowdsouring*. ACM, 2011.

[22] Sun, Yanqiang, et al. "Catch the Jammer in Wireless Sensor Network." *PIMRC*. 2011.

[23] Vasuhi, S., and Vijay Vaidehi. "Target tracking using interactive multiple model for wireless sensor network." *Information Fusion* 27 (2016): 41-53.

[24] Vinay Kumar Nassa . "Wireless communications: past, present and future." *Dronacharya Research Journal* 3.2 (2011): 50-54.

[25] Wei, Xianglin, et al. "Jammer localization in multi-hop wireless network: a comprehensive survey." IEEE Communications Surveys & Tutorials 19.2 (2017): 765-799.

[26] Wei, Xianglin, et al. "Collaborative mobile jammer tracking in multi-hop wireless network." *Future Generation Computer Systems* 78 (2018): 1027-1039.

[27] Wood, Anthony D., and John A. Stankovic. "Denial of service in sensor networks." *computer* 35.10 (2002): 54-62.

[28] Xiong, Kaiqi, and David Thuente. "Locating jamming attackers in malicious wireless sensor networks." *Performance Computing and Communications Conference (IPCCC), 2012 IEEE 31st International*. IEEE, 2012.

[29] Xu, Wenyuan, et al. "The feasibility of launching and detecting jamming attacks in wireless networks." *Proceedings of the 6th ACM international symposium on Mobile ad hoc networking and computing*. ACM, 2005.

[30] Xu, Wenyuan, et al. "Jamming sensor networks: attack and defense strategies." *IEEE network* 20.3 (2006): 41-47.

Three-Level DTC-SVM with DC-Link Voltages Balancing Strategy of Double Star Induction Machine

Elakhdar Benyoussef[1] and Said Barkat[2]

[1]Faculty of Science Applied, Department of Electrical Engineering, University of Kasdi Merbah, Ouargla 30000, BP. 511, Algeria.
[2]Electrical Engineering Laboratory, Faculty of Technology, University of M'sila, M'sila 28000, BP. 166, Algeria.

Corresponding author: lakhdarbenyoussef@yahoo.com

Abstract: **This paper deals with direct torque control based on space vector modulation strategy of a double star induction machine supplied by two three-level diode-clamped inverters. This type of inverters has several advantages over the standard two-level inverter, such as lower voltage stress on power switches and less harmonic distortion in voltage and current waveforms. However, a very important issue in using a diode clamped inverter is the ability to guarantee the stability of the DC-link capacitors voltages. This drawback can be solved in satisfactory way by using multilevel space vector modulation technique equipped by a balancing strategy. Simulations results are given to show the effectiveness of the proposed control approach**.

Key words: **Double Star Induction Machine; Three-Level Inverter; Direct Torque Control; Space Vector Modulation; DC-voltages balancing strategy.**

1. Introduction

For many years, electrical drives are founded on the traditional three-phase machines. However, when enhancing power capabilities of the drive is considered, multiphase machine drives are potentially recommended. In fact, multiphase drives are useful for large systems such as naval electric propulsions systems, locomotive traction and electrical vehicles applications [1, 2].

A multiphase drive has more than three phases in the stator and the same number of inverter legs is in the inverter side. The main advantages of multiphase drives over conventional three-phase drives include increasing the inverter output power, reducing the amplitude of torque ripple and lowering the DC-link current harmonics [3].

One way to perform multiphase machines is to use double star technology. Indeed, in double star machine two sets of three-phase windings spatially phase shifted by 30 electrical degrees are implemented in the same stator. Two common examples of such structures are the double star synchronous machine and double star induction machine (DSIM) [4].

Normally two two-level inverters are indispensable for double star electrical drives. However, for high power applications multilevel inverters are often required. Many multilevel topologies have been developed [5], among them, the diode-clamped topologies (DCI), which can reach high output voltage, and high power levels with higher reliability due to its modular topology [6]. However, the unbalance of the input DC voltages constitutes the major limitation facing the use of this kind of power converter. Several methods are proposed to suppress the unbalance of DC-link capacitors voltages. Some of these methods are based on adding a zero sequence or a DC-offset to the output voltage [7]. Addition of auxiliary power electronics circuitry is another solution used to redistribute charges between capacitors [8]. SVM based DC capacitors voltages balancing method, which exploits the switching vectors redundancy to mitigate DC capacitors voltages drift, is one of the prominent solutions proposed in the literature to face this type of issues [9].

The multilevel direct torque control (DTC) of the multiphase machine has become an attracting topic in research and academic community over the past decade. This control is characterized by its good dynamic performances and robustness, because it requires no current regulators, no coordinate transformation and depends only on stator resistance [10]. This drives control utilizing hysteresis comparators suffers from high torque ripple and variable switching frequency. One common solution to those problems is to use the space vector modulation [11].

In this paper, a multilevel DTC-SVM with balancing strategy based on the switching states redundancy is proposed in order not only to improve the DSIM based drive performance but also to balance the DC-link capacitors voltages.

The remainder of this paper is structured as follows: in Section 2, the DTC-SVM with voltage balancing strategy scheme is presented. The model of the DSIM is presented in section 3; a suitable transformation matrix is used to develop a simple dynamic model. The proposed three-level DCI is presented in section 4. Section 5 is reserved to DC capacitor voltages balancing strategy. The DTC-SVM strategy is presented in section 6. The advantages of the proposed control system are shown by simulation results in section 7.

2. Structure of the Proposed Multilevel DTC-SVM Equipped by a Voltage Balancing Strategy

The general structure of the double star induction machine fed by two three-level inverters and controlled by direct

torque control based on space vector modulation with balancing strategy is represented in Fig. 1.

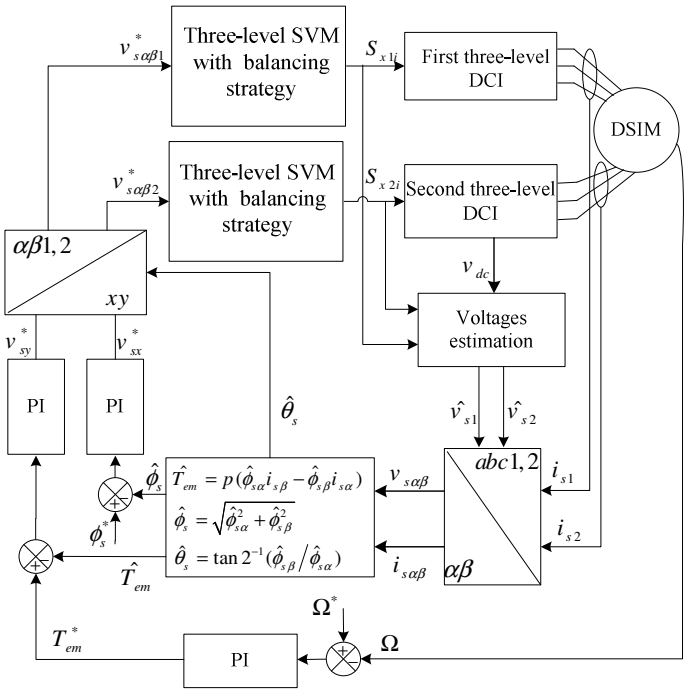

Fig. 1. DTC-SVM with balancing strategy of DSIM (with *i=1, 2, 3, 4*).

3. Double Star Induction Machine Modeling

The stator voltage equations can be expressed as:

$$\begin{bmatrix} v_{sa1} \\ v_{sb1} \\ v_{sc1} \\ v_{sa2} \\ v_{sb2} \\ v_{sc2} \end{bmatrix} = \begin{bmatrix} R_s & 0 & 0 & 0 & 0 & 0 \\ 0 & R_s & 0 & 0 & 0 & 0 \\ 0 & 0 & R_s & 0 & 0 & 0 \\ 0 & 0 & 0 & R_s & 0 & 0 \\ 0 & 0 & 0 & 0 & R_s & 0 \\ 0 & 0 & 0 & 0 & 0 & R_s \end{bmatrix} \begin{bmatrix} i_{sa1} \\ i_{sb1} \\ i_{sc1} \\ i_{sa2} \\ i_{sb2} \\ i_{sc2} \end{bmatrix} + \frac{d}{dt} \begin{bmatrix} \phi_{sa1} \\ \phi_{sb1} \\ \phi_{sc1} \\ \phi_{sa2} \\ \phi_{sb2} \\ \phi_{sc2} \end{bmatrix} \quad (1)$$

The rotor voltage equations can be expressed as:

$$\begin{bmatrix} 0 \\ 0 \\ 0 \end{bmatrix} = \begin{bmatrix} R_r & 0 & 0 \\ 0 & R_r & 0 \\ 0 & 0 & R_r \end{bmatrix} \begin{bmatrix} i_{ra} \\ i_{rb} \\ i_{rc} \end{bmatrix} + \frac{d}{dt} \begin{bmatrix} \phi_{ra} \\ \phi_{rb} \\ \phi_{rc} \end{bmatrix} \quad (2)$$

with

v_{sa1}, v_{sb1}, v_{sc1} : Stator voltages of the first winding;
v_{sa2}, v_{sb2}, v_{sc2} : Stator voltages of the second winding;
i_{sa1}, i_{sb1}, i_{sc1} : Stator currents of the first winding;
i_{sa2}, i_{sb2}, i_{sc2} : Stator currents of the second winding;
i_{ra}, i_{rb}, i_{rc} : Rotor currents;
ϕ_{sa1}, ϕ_{sb1}, ϕ_{sc1} : Stator flux of the first winding;
ϕ_{sa2}, ϕ_{sb2}, ϕ_{sc2} : Stator flux of the second winding;
ϕ_{ra}, ϕ_{rb}, ϕ_{rc} : Rotor flux;

The DSIM stator voltage equation (1) can decomposed into three subsystems (α,β), (z_1,z_2) and (z_3,z_4), using the following transformation:

$$\begin{bmatrix} X_{s\alpha} & X_{s\beta} & X_{z1} & X_{z2} & X_{z3} & X_{z4} \end{bmatrix}^T = [A][X_s] \quad (3)$$

with

$$[X_s] = [X_{s1} \quad X_{s2}]^T = [X_{sa1} \quad X_{sb1} \quad X_{sc1} \quad X_{sa2} \quad X_{sb2} \quad X_{sc2}]^T$$

where X_s can refer to stator currents vector, stator flux vector, or stator voltages vector.

The matrix A is given by:

$$[A] = \frac{1}{\sqrt{3}} \begin{bmatrix} \cos(0) & \cos\left(\frac{2\pi}{3}\right) & \cos\left(\frac{4\pi}{3}\right) & \cos(\gamma) & \cos\left(\frac{2\pi}{3}+\gamma\right) & \cos\left(\frac{4\pi}{3}+\gamma\right) \\ \sin(0) & \sin\left(\frac{2\pi}{3}\right) & \sin\left(\frac{4\pi}{3}\right) & \sin(\gamma) & \sin\left(\frac{2\pi}{3}+\gamma\right) & \sin\left(\frac{4\pi}{3}+\gamma\right) \\ \cos(0) & \cos\left(\frac{4\pi}{3}\right) & \cos\left(\frac{2\pi}{3}\right) & \cos(\pi-\gamma) & \cos\left(\frac{\pi}{3}-\gamma\right) & \cos\left(\frac{5\pi}{3}-\gamma\right) \\ \sin(0) & \sin\left(\frac{4\pi}{3}\right) & \sin\left(\frac{2\pi}{3}\right) & \sin(\pi-\gamma) & \sin\left(\frac{\pi}{3}-\gamma\right) & \sin\left(\frac{5\pi}{3}-\gamma\right) \\ 1 & 1 & 1 & 0 & 0 & 0 \\ 0 & 0 & 0 & 1 & 1 & 1 \end{bmatrix} \quad (4)$$

The voltage stator and rotor equations in stationary reference frame can be expressed as:

$$\begin{cases} v_{s\alpha} = R_s i_{s\alpha} + \dfrac{d\phi_{s\alpha}}{dt} \\ v_{s\beta} = R_s i_{s\beta} + \dfrac{d\phi_{s\beta}}{dt} \end{cases} \quad (5)$$

with

$v_{s\alpha}$, $v_{s\beta}$: The α-β components of stator voltage;
$i_{s\alpha}$, $i_{s\beta}$: The α-β components of stator current;
$\phi_{s\alpha}$, $\phi_{s\beta}$: The α-β components of stator flux;

The stator voltage equations in the stator flux reference frame are given by:

$$\begin{cases} v_{sx} = R_s i_{sx} + \dfrac{d\phi_{sx}}{dt} - p\Omega\phi_{sy} \\ v_{sy} = R_s i_{sy} + \dfrac{d\phi_{sy}}{dt} + p\Omega\phi_{sx} \end{cases} \quad (6)$$

with

v_{sx}, v_{sy}: The *x*-*y* components of stator voltage;
i_{sx}, i_{sy} : The *x*-*y* components of stator current;
ϕ_{sx}, ϕ_{sy}: The *x*-*y* components of stator flux;

The electromagnetic torque generated by the DSIM is:

$$T_{em} = p\left(\phi_{sx} i_{sy} - \phi_{sy} i_{sx}\right) \quad (7)$$

4. Three-Level DCI Modelling

The structure of a three-level diode-clamped inverter is shown in Fig. 2. Each leg is composed of two upper and lower switches with anti-parallel diodes. Two series DC-link capacitors split the DC-bus voltage in half, and six clamping

diodes confine the voltage across the switches within the voltage of the capacitors, each leg of the inverter can have three possible switching states; *2*, *1* or *0* [7].

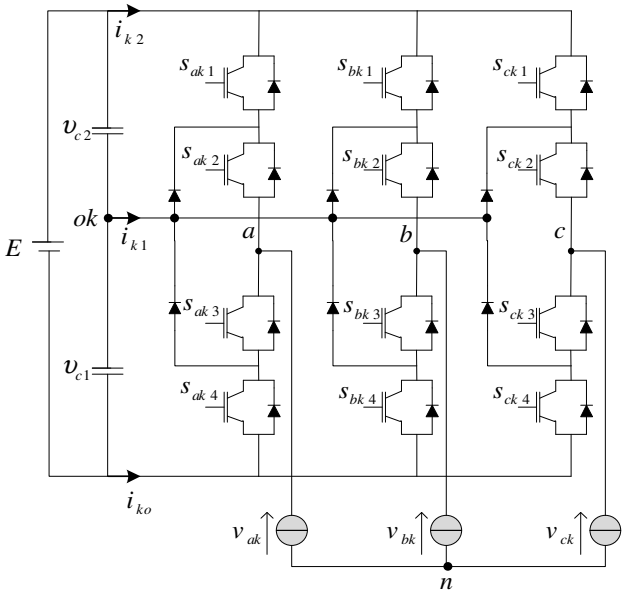

Fig. 2. Three-level DCI (*k*=1 for the first inverter and *k*=2 for the second inverter).

Functions of connection are given by:

$$\begin{cases} F_{xk2} = s_{xk1}.s_{xk2}, \quad x = a,b,c \\ F_{xk1} = s_{xk3}.s_{xk2} \end{cases} \tag{8}$$

The phase voltages v_{ak}, v_{bk}, v_{ck} can be written as:

$$\begin{bmatrix} v_{ak} \\ v_{bk} \\ v_{ck} \end{bmatrix} = \begin{bmatrix} 2F_{ak2}-F_{bk2}-F_{ck2} & 2F_{ak1}-F_{bk1}-F_{ck1} \\ 2F_{bk2}-F_{ak2}-F_{ck2} & 2F_{bk1}-F_{ak1}-F_{ck1} \\ 2F_{ck2}-F_{ak2}-F_{bk2} & 2F_{ck1}-F_{ak1}-F_{bk1} \end{bmatrix} \begin{bmatrix} v_{c1}+v_{c2} \\ v_{c1} \end{bmatrix} \tag{9}$$

The space vector diagram of a three-level inverter is showed in Fig. 3. The 27 switching states of three levels inverter corresponds to 19 different space vectors. These vectors have different effects on neutral point voltage variations [7].

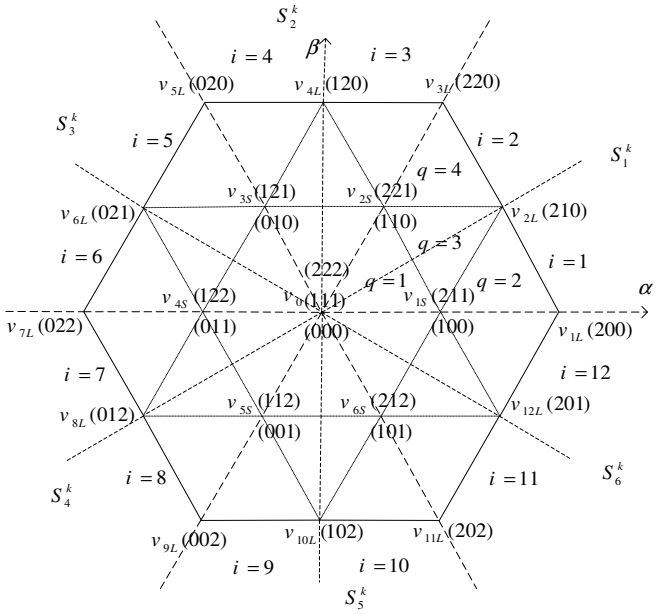

Fig. 3. Space vector diagram showing switching states for the three-level DCI.

In order to simplify three-level SVM algorithm, the reference voltage vector is only synthesized by the three basic voltage vectors within the minimum equilateral triangular area in which the reference voltage vector is located.

- Determination of the sector numbers

The reference vector magnitude and its angle are determined from:

$$\begin{cases} u_{refk} = \sqrt{u_{ref\,\alpha k}^2 + u_{ref\,\beta k}^2} \\ \vartheta_k = \tan 2^{-1}\left(\dfrac{u_{ref\,\beta k}}{u_{ref\,\alpha k}}\right) \end{cases} \tag{10}$$

The sector numbers *1-6* is given by:

$$S_n^k = ceil\left(\frac{\vartheta_k}{\pi/3}\right) \in \{1,\ 2,\ 3,\ 4,\ 5,\ 6\} \tag{11}$$

where ceil is the C-function that adjusts any real number to the nearest, but higher, integer [e.g. ceil (3.1) =4], (*n=1,…, 6*).

- Identification of the triangles

The reference vector is projected on the two axes making 60° between them. In each sector S_n^k, its components $u_{refk1}^{S_n^k}$ and $u_{refk2}^{S_n^k}$ are given by:

$$\begin{aligned} u_{refk1}^{S_n^k} &= 2M_k\left(\cos(\vartheta_k - (S_n^k - 1)\frac{\pi}{3}) - \frac{1}{\sqrt{3}}\sin(\vartheta_k - (S_n^k - 1)\frac{\pi}{3})\right) \\ u_{refk2}^{S_n^k} &= 2M_k\left(\frac{2}{\sqrt{3}}\sin(\vartheta_k - (S_n^k - 1)\frac{\pi}{3})\right) \end{aligned} \tag{12}$$

The modulation factor M_k is given by:

$$M_k = \frac{u_{refk}}{v_{dc}\sqrt{2/3}} \tag{13}$$

In order to determine the number of the triangle in a sector S_n^k, the two following numbers are to be defined:

$$\begin{aligned} l_{k1}^{S_n^k} &= \text{int}(u_{refk1}^{S_n^k}) \\ l_{k2}^{S_n^k} &= \text{int}(u_{refk2}^{S_n^k}) \end{aligned} \tag{14}$$

where *int* is a function which gives the whole part of a given real number.

Fig. 4 presents the projection of u_{refk} in the first sector.

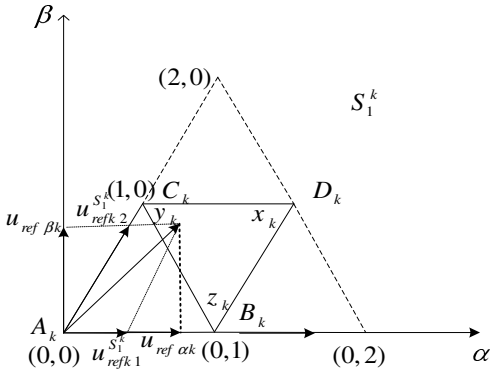

Fig. 4. First sector corresponding to the space voltage vectors of a three-level inverter.

In a reference frame formed by the two vectors $u_{refk\,1}^{S_n^k}$ and $u_{refk\,2}^{S_n^k}$ the coordinates of the tops A_k, B_k, C_k and D_k are given by:

$$\begin{aligned}
&\left(u_{A_{k1}}^{\Delta_q^{S_n^k}},\ u_{A_{k2}}^{\Delta_q^{S_n^k}}\right)=\left(l_{k1}^{S_n^k},\ l_{k2}^{S_n^k}\right)\\
&\left(u_{B_{k1}}^{\Delta_q^{S_n^k}},\ u_{B_{k2}}^{\Delta_q^{S_n^k}}\right)=\left(l_{k1}^{S_n^k}+1,\ l_{k2}^{S_n^k}\right)\\
&\left(u_{C_{k1}}^{\Delta_q^{S_n^k}},\ u_{C_{k2}}^{\Delta_q^{S_n^k}}\right)=\left(l_{k1}^{S_n^k},\ l_{k2}^{S_n^k}+1\right)\\
&\left(u_{D_{k1}}^{\Delta_q^{S_n^k}},\ u_{D_{k2}}^{\Delta_q^{S_n^k}}\right)=\left(l_{k1}^{S_n^k}+1,\ l_{k2}^{S_n^k}+1\right)
\end{aligned} \tag{15}$$

The following criteria (16) and (17) determine if the reference vector is located in the triangle formed by the tops A_k, B_k and C_k or in that formed by the tops B_k, C_k and D_k.

u_{refk} is in the triangle $A_kB_kC_k$ if:

$$u_{refk\,1}^{S_n^k}+u_{refk\,2}^{S_n^k}<l_{k1}^{S_n^k}+l_{k2}^{S_n^k}+1 \tag{16}$$

u_{refk} is in the triangle $B_kC_kD_k$ if:

$$u_{refk\,1}^{S_n^k}+u_{refk\,2}^{S_n^k}\geq l_{k1}^{S_n^k}+l_{k2}^{S_n^k}+1 \tag{17}$$

- *Calculation of application times*

If tops x_k, y_k, z_k corresponding has A_k, B_k, C_k, respectively, the application times are calculated by:

$$\begin{aligned}
t_{y_k}^{\Delta_q^{S_n^k}}&=\left(u_{refk\,1}^{S_n^k}-l_{k1}^{S_n^k}\right)T_s\\
t_{z_k}^{\Delta_q^{S_n^k}}&=\left(u_{refk\,2}^{S_n^k}-l_{k2}^{S_n^k}\right)T_s\\
t_{x_k}^{\Delta_q^{S_n^k}}&=T_s-\left(t_{yk}^{\Delta_q^{S_n^k}}-t_{zk}^{\Delta_q^{S_n^k}}\right)
\end{aligned} \tag{18}$$

where $t_{x_k}^{\Delta_q^{S_n^k}}, t_{y_k}^{\Delta_q^{S_n^k}}, t_{z_k}^{\Delta_q^{S_n^k}}$ are the application times of the vectors $u_{x_k}^{\Delta_q^{S_n^k}}, u_{y_k}^{\Delta_q^{S_n^k}}, u_{z_k}^{\Delta_q^{S_n^k}}$, respectively;

x_k, y_k and z_k are the tops of A_k, B_k, C_k respectively, $q=1,\ldots,4$.

5. Voltage Balancing Approach

The total energy of the two condensers is given by:

$$W=\frac{1}{2}\sum_{y=1}^{2}C_y\,\upsilon_{cy}^2 \tag{19}$$

Based on appropriate selection of redundant vectors [4], W can be minimized (ideally reduced to zero) if the capacitor voltages are maintained at voltage reference values of $E/2$. Assuming that all capacitors are identical, $C_1=C_2=C$, the mathematical condition to minimize W is:

$$\frac{dW}{dt}=C\sum_{y=1}^{2}\Delta\upsilon_{cy}\,\frac{d\,\upsilon_{cy}}{dt}=\sum_{y=1}^{2}\Delta\upsilon_{cy}\,i_{cy} \tag{20}$$

where $\Delta\upsilon_{cy}$ is the voltage deviation of capacitor C_y, $\Delta\upsilon_{cy}=\upsilon_{cy}-(E/2)$ and i_{cy} is the current through capacitor C_y. The capacitor currents i_{cy} in (20) are affected by the DC-side intermediate branch currents $i_{k\,2}$ and i_{k1}. These currents can be calculated if the switching states used in the switching pattern are known. Thus, it is advantageous to express (20) in terms of $i_{k\,2}$ and i_{k1}. The DC-capacitor current is expressed as:

$$i_{c\,2}=i_{c1}+\sum_{k=1}^{2}i_{k\,1} \tag{21}$$

Considering a constant DC-link voltage

$$\sum_{y=1}^{2}\Delta\upsilon_{cy}=0 \tag{22}$$

From (22) it is possible to deduced the following equation

$$\sum_{y=1}^{2}i_{cy}=0 \tag{23}$$

Solving (21) and (23), yields

$$i_{cy}=\frac{1}{2}\sum_{m=1}^{2}m\left(\sum_{k=1}^{2}i_{km}\right)-\sum_{m=y}^{2}\left(\sum_{k=1}^{2}i_{km}\right) \tag{24}$$

where $m=1, 2$.

By substituting i_{cy} into (20), the following condition to achieve voltage balancing is deduced:

$$\sum_{y=1}^{2}\Delta\upsilon_{cy}\left(\frac{1}{2}\sum_{m=1}^{2}m\left(\sum_{k=1}^{2}i_{km}\right)-\sum_{m=y}^{2}\left(\sum_{k=1}^{2}i_{km}\right)\right)\leq 0 \tag{25}$$

By substituting $\Delta\upsilon_{c\,2}$, calculated from (23), in (25) it yields

$$\Delta \upsilon_{c1}\left(\sum_{k=1}^{2} i_{k1}\right) \geq 0 \tag{26}$$

Applying the averaging operator, over one sampling period, to (26) results in:

$$\frac{1}{T}\int_{KT}^{(K+1)T} \Delta \upsilon_{c1}\left(\sum_{k=1}^{2} i_{k1}\right) dt \geq 0 \tag{27}$$

Assuming that the capacitor voltages can be assumed as constant values over one sampling period and consequently (27) is simplified to:

$$\Delta \upsilon_{c1}(K)\left(\frac{1}{T}\int_{KT}^{(K+1)T}\left(\sum_{k=1}^{2} i_{k1}\right)\right) dt \geq 0 \tag{28}$$

From (28), the final form of the cost function is given by:

$$W_k = \Delta \upsilon_{c1}(K)\left(\sum_{k=1}^{2} \bar{i}_{k1}(K)\right) dt \tag{29}$$

where $\Delta \upsilon_{c1}(K)$ is the voltage drift of C_1 at sampling period K, and $\bar{i}_{k1}(K)$ is the averaged value of the first DC-side intermediate branch current. Current $\bar{i}_{k1}(K)$ should be computed for different combinations of adjacent redundant switching states over a sampling period and the best combination which maximizes (29) is selected. If the reference vector is in the triangle $\Delta_q^{S_n^k}$ ($i=1,\ldots,6$, $q=1,..,4$), and $t_{x_k}^{\Delta_q^{S_n^k}}, t_{y_k}^{\Delta_q^{S_n^k}}, t_{z_k}^{\Delta_q^{S_n^k}}$ are the vectors application times presented in figure 2, the current $\bar{i}_{k1}^{S_n^k}$ is expressed by:

$$\bar{i}_{k1}^{S_n^k} = \frac{1}{T}\left[i_{1x_k}^{S_n^k} \quad i_{1y_k}^{S_n^k} \quad i_{1z_k}^{S_n^k} \right]\left[t_{x_k}^{\Delta_q^{S_n^k}} \quad t_{y_k}^{\Delta_q^{S_n^k}} \quad t_{z_k}^{\Delta_q^{S_n^k}} \right]^T \tag{30}$$

where $i_{1x_k}^{S_n^k}, i_{1y_k}^{S_n^k}$ and $i_{1z_k}^{S_n^k}$ are the charging currents to the states of commutation x_k, y_k and z_k in the triangle $\Delta_q^{S_n^k}$ minimizing the cost function W.

6. Direct Torque Control Based on Space Vector Modulation

The main idea behind the DTC-SVM control strategy is to force the torque and stator flux to follow their references by applying in one switching period several voltage vectors. This control algorithm uses prefixed time intervals within a cycle period and in this way a higher number of voltage space vectors can be synthesized with respect to those used in basic DTC technique [11].

The stator voltage can be estimated using equation (31) as follows:

$$\begin{bmatrix} \hat{v}_{s\alpha} \\ \hat{v}_{s\beta} \end{bmatrix} = [A]\begin{bmatrix} \hat{v}_{s1} \\ \hat{v}_{s2} \end{bmatrix} \tag{31}$$

with $\hat{v}_{s1} = [\hat{v}_{sa1} \quad \hat{v}_{sb1} \quad \hat{v}_{sc1}]$, $\hat{v}_{s2} = [\hat{v}_{sa2} \quad \hat{v}_{sb2} \quad \hat{v}_{sc2}]$

The presented control strategy is based on simplified stator voltage equations described in stator flux oriented x-y coordinates. The rotation transformation (32) transforms command variables in stator flux reference frame x-y to the stationary reference α-β :

$$\begin{bmatrix} v_{s\alpha 1}^* \\ v_{s\beta 1}^* \end{bmatrix} = [P(\theta_s)]\begin{bmatrix} v_{sx}^* \\ v_{sy}^* \end{bmatrix}, \quad \begin{bmatrix} v_{s\alpha 2}^* \\ v_{s\beta 2}^* \end{bmatrix} = [P(\theta_s - \gamma)]\begin{bmatrix} v_{sx}^* \\ v_{sy}^* \end{bmatrix} \tag{32}$$

with

$$[P(\theta_s)] = \begin{bmatrix} \cos(\theta_s) & -\sin(\theta_s) \\ \sin(\theta_s) & \cos(\theta_s) \end{bmatrix}$$

Since the stator flux is along the x-axis, it results in $\phi_{sy} = 0$ and $\phi_{sx} = \phi_s$. The presented control strategy is based on simplified stator voltage equations described in stator flux oriented x-y coordinates:

The stator voltage equations in x-y frame are:

$$\begin{cases} v_{sx} = R_s i_{sx} + \dfrac{d\phi_s}{dt} \\ v_{sy} = R_s i_{sy} + \omega_s \phi_s \end{cases} \tag{15}$$

The torque expression is simplified to:

$$\hat{T}_{em} = p\left|\hat{\phi}_s\right| i_{sy} \tag{16}$$

7. Simulation results

To verify the validity of the proposed controller, the system was simulated using the DSIM parameters given in Appendix. The DC side of the inverter is supplied by a constant source *600V*. The simulation results are obtained using the following DC-link capacitors values $C_1 = C_2 =$ *1*mF.

The obtained results are presented in Figs. 5 and 6 for the DTC-SVM without balancing strategy and that with balancing strategy, respectively. The DSIM is accelerated from standstill to reference speed *100* rad/s. The drive is simulated with load torque (T_L=*10*N.m), afterwards a step variation in the rated load (T_L = -*10*N.m) as well as a speed inversion from 100rad/s to -100rad/s are introduced at *0.8*s.

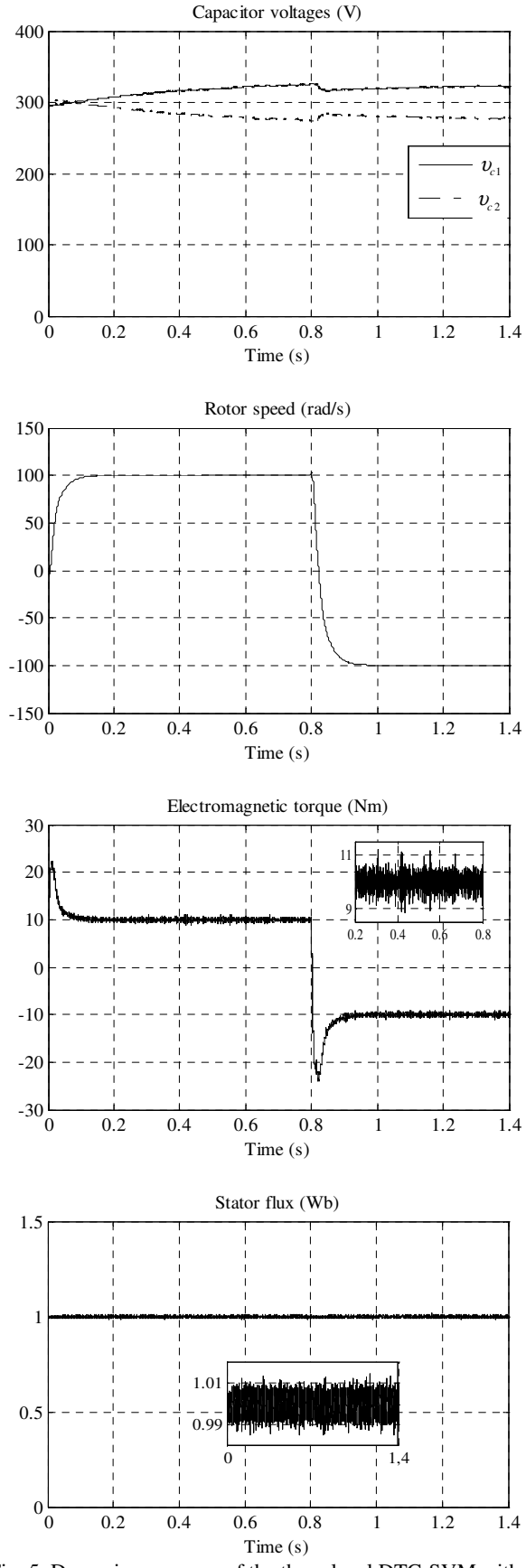

Fig. 5. Dynamic responses of the three-level DTC-SVM without balancing strategy for DSIM.

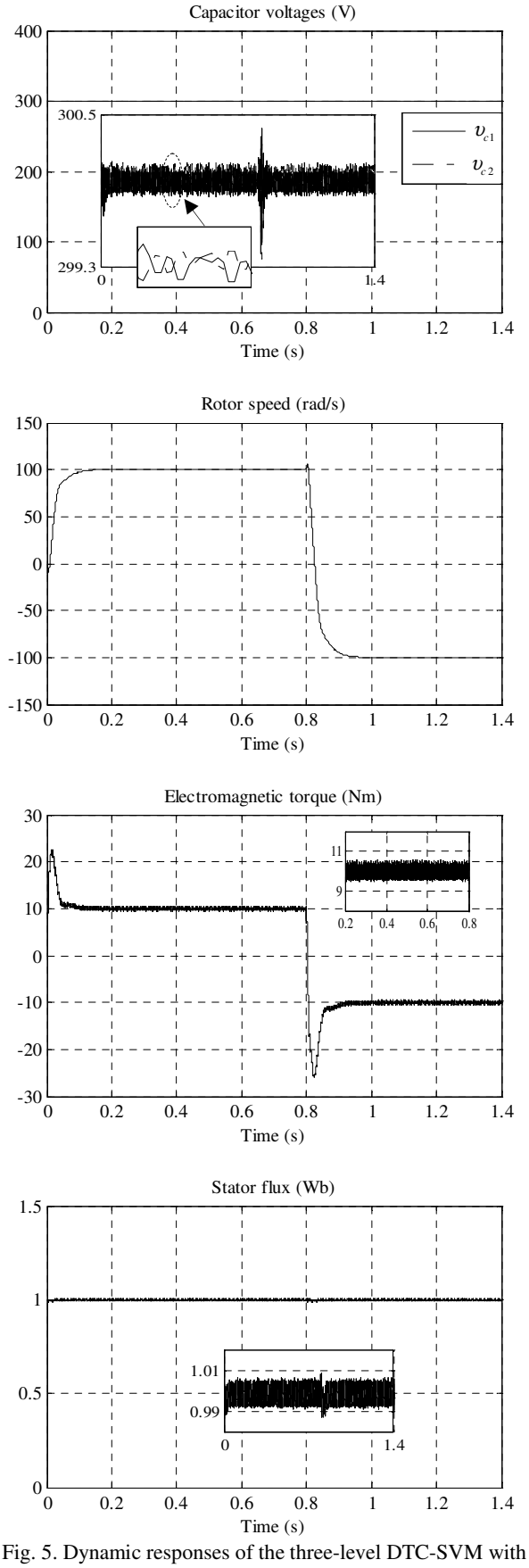

Fig. 5. Dynamic responses of the three-level DTC-SVM with balancing strategy for DSIM.

Note that the both proposed controls schemes present an excellent performance in terms of starting, rejection of disturbance and speed tracking. Also, the decoupling between the stator flux and electromagnetic torque is maintained in both configurations, confirming the good dynamic performances of the developed multiphase drive systems.

Referring to Fig. 5, it appears that the capacitor voltages given by v_{c1} and v_{c2} are deviating from their reference voltage value ($v_{dc}/2$). This result shows the problem of the unbalance capacitor voltages and its consequence on electromagnetic torque and stator flux harmonics rate. In order to improve the performance of the previous system, a three-level DTC-SVM based on balancing mechanism is proposed.

As expected in Fig. 6, the proposed solution is very efficient to solve the above-mentioned instability problem. As result, each capacitor voltage merged with its reference voltage value. Consequently, the torque and flux ripples decreases considerably using the proposed balancing strategy.

8. Conclusion

In this paper, an effective three-level DTC-SVM of DSIM is presented. The idea behind this control method is to gather the merits of the well-known DTC and those of the SVM equipped by a balancing strategy in the aim to improve the performance of the overall multiphase drive.

From the obtained simulation results, it is pointed out that the robustness of the controlled DSIM drive against speed and load torque variations is guaranteed. On the other hand, to take full benefit of multilevel DCI inverter, the proposed control method is endowed by a suitable balancing strategy able to ensure the stability of DC-link capacitor voltages. The simulation results confirm that the proposed direct torque control based on space vector modulation scheme with balancing strategy achieves a fast electromagnetic torque response with low torque ripples, in comparison to that control scheme without balancing strategy. Moreover, it performs well under various condition variations such as sudden change in the speed reference, speed reversion operation, and step change of the load torque.

Declaration of conflicting interest

This work was supported by the Directorate-General for Scientific Research and Technological Development (DG-RSDT) of Algeria under PRFU project number A01L07UN300120200001.

9. Appendix

The parameters of DSIM are given in Table 1.

Table 1. DSIM parameters.

1kW, 2 Poles, 220 V, 50 Hz		
Quantity	Symbol	Value
Stator resistance	R_s	4.67 Ω
Rotor resistance	R_r	8 Ω
Stator inductance	L_s	0.374 H
Rotor inductance	L_r	0.374 H
Mutual inductance	M	0.365 H
Inertia moment	J	0.003 kgm^2

11. References

1. Levi E., "Multiphase Electric Machines for Variable-Speed Applications," IEEE Transactions on Industrial Electronics, Vol. 55, No. 5, 2008, pp. 1893-1909.
2. Riveros, B. Bogado, J. Prieto, F. Barrero, S. Toral, and M. Jones, "Multiphase Machines in Propulsion Drives of Electric Vehicles," International Power Electronics and Motion Control Conference, Ohrid, Macedonia, September 2010, pp. 201-206.
3. Abuishmais I., Arshad W., and Kanerva S., "Analysis of VSI-DTC Fed 6-phase Synchronous Machines," IEEE International Power Electronics and Motion Control Conference, December 2009, pp. 867-873.
4. Oudjebour Z., Berkouk E., and Mahmoudi M., "Stabilization by New Control Technique of the Input DC Voltages of five-level Diode-Clamped Inverters Application to Double Star Induction Machine," International Symposium on Environment-Friendly Energies and Applications, Newcastle upon Tyne, UK, 25-27 June 2012, pp. 541-544.
5. Singh B., Mittal N., Verma D., Singh D., Singh S., Dixit R., Singh M., and Baranwal A., "Multi-Level Inverter: a Literature Survey on Topologies and Control Strategies," International Journal of Reviews in Computing, Vol. 10, 2012, pp. 1-16.
6. Saeedifard M., Iravani R., and Pou J., "Control and DC-Capacitor Voltage Balancing of a Space Vector-Modulated Five-Level STATCOM," Institution of Engineering and Technology, IEEE Transaction on Energy Conversion, Vol. 2, No. 3, 2009. pp. 203-215.
7. Pan Z., Peng F., Corzine K., Stefanovic V., Leuthen j., and GataricS., "Voltage Balancing Control of Diode-Clamped Multilevel Rectifier/Inverter Systems," IEEE Transactions on Industry Applications, Vol. 41, No. 6, 2005, pp. 1698-1706.
8. Chibani R., Berkouk E., and Boucherit M., "Five-Level NPC VSI: Different Ways to Balance Input DC Link Voltages," Elektrika, Vol. 11, No. 1, 2009, pp. 19-33.
9. Saeedifard M., Iravani R., and Pou J., "Analysis and Control of DC-Capacitor-Voltage-Drift Phenomenon of a Passive Front-End Five-Level Converter," IEEE Transactions on Industrial Electronics, Vol. 54, No. 6, 2007, pp. 3255-3266.
10. Wenhao C., and jiangxia C., "Speed Identification Method in Direct Torque Control of Asynchronous Machine Based on Neuron Network Theory," IEEE, International Conference on Computer Application and System Modeling, Taiyuan, China, October 2010, pp. 133-136.
11. Hassankhan E., and Khaburi D., "DTC-SVM Scheme for Induction Motors Fed with a Three-level Inverter," World Academy of Science, Engineering and Technology, Vol. 44, 2008, pp. 168-172.

DESIGN AND IMPLEMENTATION OF FLYBACK CONVERTER WITH SYNCHRONOUS RECTIFICATION FOR SATELLITE ELECTRIC POWER SYSTEMS

RAVICHANDRAN CHINNAPPAN
Design, Centum Electronics Ltd, Bangalore, India, ravichandranc@centumelectronics.com

BHOOPENDRA KUMAR SINGH
Design, Centum Electronics Ltd, Bangalore, India, bksingh@centumelectronics.com

VINOD CHIPPALKATTI
Design, Centum Electronics Ltd, Bangalore, India, vinod@centumelectronics.com

Abstract: *The DC-DC switching mode converter for an electric power system (EPS) to provide a regulated voltage is one of the important components of a satellite mission and subsystem. The flyback converter is one of the most attractive isolated converters in SMPS applications because of its simple configuration, less component count and cost effectiveness. This present work describes the recent EPS structure and implementation of flyback converter based on self-synchronous rectification with suitable choices of interface driver with secondary side, as it features a low cost and high efficiency. The steady-state analysis and operating principle of the synchronous rectifier flyback converter is presented. The characteristics of a 50W (5V, 10A) output prototype converter are implemented and verified experimentally with a 20 V to 45 V maximum power point tracking (MPPT) based photo voltaic (PV) dc-dc converter output. This presented design illustrates an example for a future space-grade isolated intermediary bus converter of commercial communication satellites. The various design factors for space applications are considered while designing and are implemented successfully.*

Key words: *EPS, PV, MPPT, SMPS, Flyback, Synchronous Rectifier, PWM controller, Space, Driver*

1. Introduction

In most of the low wattage isolated SMPS applications, the single-stage Flyback converter is extensively used because of its simple structure and low cost [1],[2]. This converter is a very attractive solution due to the absence of output filter inductor and transformer reset circuit and employing only one power switch and output rectifier diode. However, the design with low magnetizing inductance can minimize the transformer size but increases the primary peak current which intern increases the switch turn off loss and conduction loss [2]. The high conduction losses of the output rectifier diode result in low power conversion efficiency.

Hence to minimize both switching losses on the primary switch and conduction losses on the secondary rectifier diode, certain techniques of improvement such as using synchronous rectifier on secondary side is widely used [3],[4]. The present works employ design and implementation of synchronous rectifier flyback converter to achieve high conversion efficiency for space applications. The increased use of ultra-low drain source resistance, R_{ds}(on) MOSFETs based synchronous rectification has an attractive solution than passive Schottky rectification [5],[6],[7]. It is proved that for less than 40A, synchronous rectifiers have less conduction loss than Schottky diodes.

The topologies of synchronous rectifier flyback converter can be classified based on control method as primary isolated gate drive control and self-driven control based synchronous rectifier.

The self-driven control-based topology is a widely used feature as it requires simple gate driving logic, absence of complex control circuits, cost-effective solution and can be easily realized by additional winding or through self-synchronous driver circuit [8]. However, the control timing is not accurate in the self-driven synchronous rectifier driver circuit. Hence the improvement of the system efficiency is limited, and it is mainly used in low frequency applications. In this mode of operation, when the primary switch is turned on, the gate to source voltage across the secondary synchronous switch is negative and hence it is turned off. Similarly, when the primary switch is turned off, the gate to source voltage across the secondary synchronous switch is positive and hence it is turned on.

External gate control drive synchronous rectifier is a very common topology with improved control accuracy and increased circuit complexity. The efficiency of the converter is sensitive to the dead time and is greatly affected due to conduction of body diode. Hence the dead time is maintained shortly to minimize the turn on time of body diode but increases the control complexity and cost.

The main objective of the presented paper is to design and implement an efficient method of synchronous rectifier flyback converter by using an analogue integrated circuit. The designed converter is used for satellite EPS power distribution converter [15],[16],[17]. The goal of the design is to demonstrate that an optimized distributed EPS can be realized such that the efficiencies of the distributed power dc-dc converter design are not significantly different than the inherently non-optimized converters [18].

The proposed structure of the EPS system is presented in section 2. Brief description and analysis of the MPPT dc-dc converter system is given in section 3. Section 4 describes the proposed dc-dc flyback converter, and their steady analysis. Section 5 illustrates the design criteria of the flyback converter. Section 6 presents the simulation details and experimental hardware prototype results of the synchronous rectifier flyback converter. Finally, the conclusion is presented in section 7.

This presented work has focused into following important contributions,

1) A new variation of a PV-MPPT dc-dc flyback converter integration system for satellite EPS.
2) The application of MPPT dc-dc converter with improved dynamic response controller.
3) The dynamic interaction among the MPPT controller, dc-dc flyback converter and loads.
4) Mitigation of low frequency bus voltage oscillations reflecting to the PV bus.

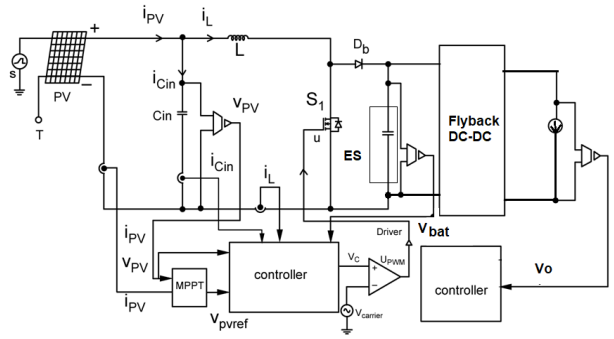

Figure 1. EPS architecture

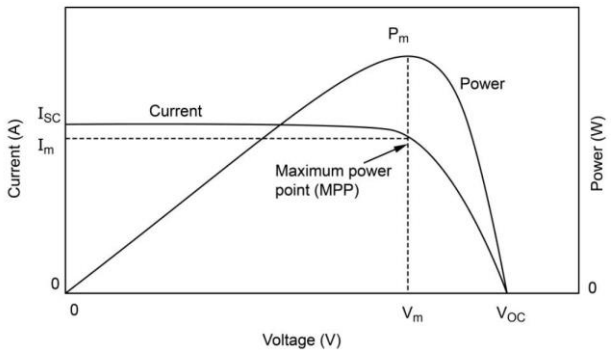

Figure 2. MPP Operation of PV Array

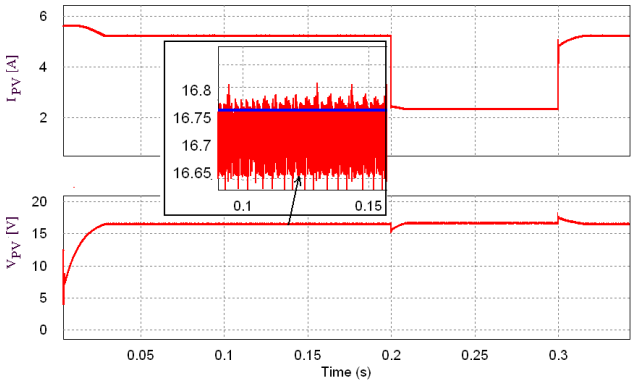

Figure 3. Tracked PV current and PV voltage

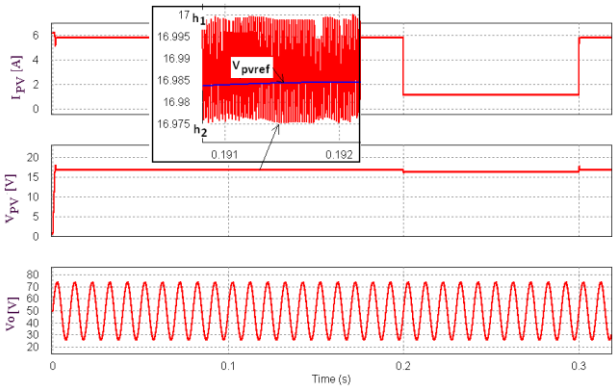

Figure 4. Tracked PV current and PV voltage

2. DESCRIPTION OF THE PROPOSED STRUCTURE OF EPS SYSTEM

The proposed structure of the satellite EPS system shown in Figure 1 are the PV source used to convert the solar energy to electrical energy, MPPT converter for power regulation and control, energy storage (ES) system typically rechargeable batteries and power distribution system. The power distribution system of a typical dc-dc converter is considered as a part of the EPS in modern satellite systems. High efficiency MPPT converters based on fixed frequency nonlinear controllers are used for regulation and control [14],[17].

The MPPT architecture consists of a dc-dc regulator usually buck, boost or buck boost converter between the PV array and the loads. The MPPT converter regulates the voltage (V_{pv}) and current (I_{pv}) extracted from the array such that it maintains its Maximum Power Point called as (MPP). Advantages of this MPPT based architecture is that the PV array can be decoupled from the load, permitting simpler array designs.

To utilize the energy provided by the PV panel maximally, its operating point must be kept at the maximum called MPP as represented in Figure 2. From Figure 2 the point near the knee of the I-V curve is called the MPP in which the voltage and current at

the MPP are designated as V_m and I_m. Figure 3 shows the illustration of MPPT architecture with tracking performance of PV current and PV voltage with different environmental conditions. Similarly Figure 4 shows the tracked PV voltage and converter output voltage (typical 24V to 70V bus system) under different environmental conditions. The bus voltage is unregulated during the eclipse portion of the orbit. The battery state of charge regulates the bus voltage for this time period.

This bus voltage is further regulated down to the different voltage levels and is distributed to the various loads of the satellite and power required by modern electronic components.

3. DESCRIPTION OF MPPT DC-DC CONVERTER

The dc-dc converters are widely employed to "match" the load impedance to the panel equivalent impedance to maximize the power drawn from the PV panel. Power circuit diagrams of the MPPT boost converter shown in Figure 1, includes PV module voltage V_{PV}, input capacitor C_{in}, inductor L, power switch S_1, output capacitor C_o, diode D_o and load impedance.

During the on condition of power switch S_1 shown in Figure 5 (a), the input PV voltage source V_{PV} supplies energy to the inductor L and the diode D_o is reverse biased. Also, the increase in supply current flows through the inductor L, capacitor C_o and releases energy to output load terminals.

During the off condition of power switch S_1 shown in Figure. 5 (b) the diode D_o is forward biased due to the energy stored in the inductor L. The input PV voltage source V_{PV}, and the inductor L supply energy to load terminal through the capacitor C_o and the diode D_o.

3.1 Gain of the Boost Converter

The voltage on capacitor C_o can be derived from energy balance on inductor L during on and off periods of switch S_1 and can be written as:

$$\frac{1}{T}\int_0^{t_{on}} V_{PV}\ dt = \frac{1}{T}\int_0^{t_{off}} (V_O - V_{PV})\ dt$$

$$\frac{1}{T}\int_0^{dT} V_{PV}\ dt = \frac{1}{T}\int_0^{(1-d)T} (V_O - V_{PV})\ dt$$

$$V_O = \frac{1}{(1-d)} V_{PV} \qquad (1)$$

where d is duty cycle of boost converter.

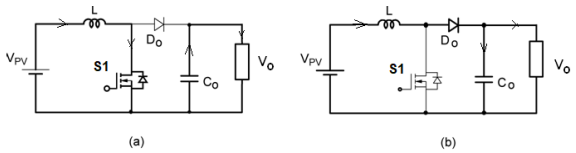

Figure 5. Steady-state Operating Modes of Boost converter (a) S_1 ON (b) S_1 OFF

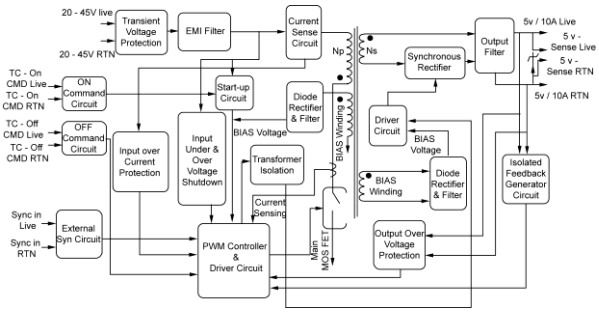

Figure 6. Functional block of a flyback converter with synchronous rectification

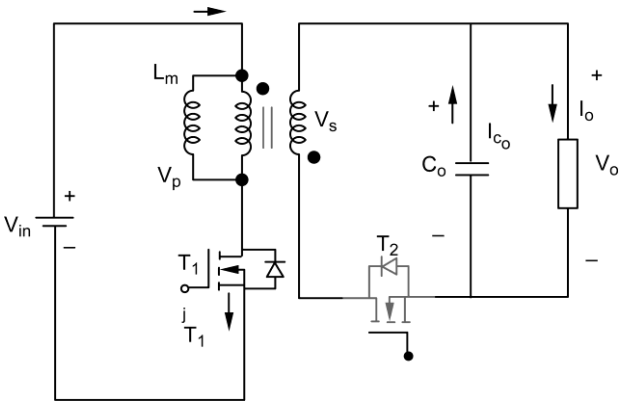

Figure 7(a). Mode 1 operation (T1 is on and T2 is off).

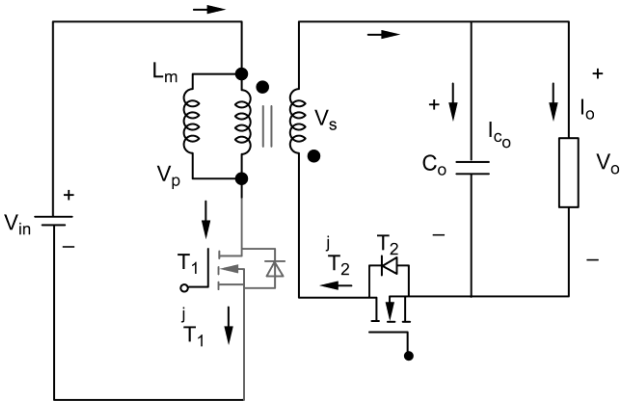

Figure 7(b). Mode 2 operation (T_1 is off and T_2 is on)

4. DESCRIPTION OF PROPOSED FLYBACK DC-DC CONVERTER

The flyback dc-dc converter is usually employed between bus voltage and various loads as less weight,

low cost, tight regulations, high reliability, and high efficiency. The functional block representation of synchronous rectifier flyback converter is shown in Figure 6. The proposed structure consists of a synchronous rectifier flyback converter as shown in Figure 7.

The magnetic isolated feedback generator circuit (using UC2901) senses the output voltage and provides isolated feedback to the PWM controller (UC2825) to complete the control loop. The power circuit schematic for a synchronous rectifier flyback converter with low-side configuration at the output is shown in Figure 7. When the primary MOSFET T_1 is turned off, the secondary current will flow through the body diode of the synchronous MOSFET T_2 which is analogous to the current flowing through the conventional output diode rectification.

4.1 STEADY STATE OPERATIN OF FLYBACK CONVERTER

From power circuit diagram of the dc-dc flyback converter shown in Figures 7, include input voltage V_{in}, main switch T_1, synchronous rectifier switch T_2, isolation transformer, magnetizing inductance L_m, output capacitor C_O and load impedance r_o. Two operating modes are analyzed under steady-state operation.

During mode 1 operation of the converter, main switch T_1 is turned on and synchronous switch T_2 is turned off as shown in Figure 7. (a). The input voltage source V_{in} supplies energy to the magnetizing inductance L_m of transformer. The energy stored in capacitor C_O releases energy to output load terminals.

During mode 2 operation of converter main switch T_1 is turned off and auxiliary switch T_2 is turned on as shown in Figure 7. (b). During on condition of power switch T_2, the secondary current will flow through the body diode of the synchronous MOSFET T_2, which is analogous to the current flowing through the conventional output diode rectification. The magnetizing inductance L_m supply energy to load terminal through the capacitor C_O and the body diode of T_2.

4.1.1 Input and Output Voltage Relation

The output voltage on capacitor C_O can be derived from energy balance on magnetizing inductor L_m during on(t_{on}) and off periods(t_{off}) of main switch T_1 and can be written as:

$$\frac{1}{T}\int_0^{t_{on}} v_L dt = \frac{1}{T}\int_0^{t_{off}} n\, v_s\, dt$$

$$\frac{1}{T}\int_0^{dT} V_{in}\, dt = \frac{1}{T}\int_0^{(1-d)T} n\, V_O\, dt\,; \quad v_s = n\, V_O$$

$$V_{in}\, dT = n\, V_O (1-d)T$$

$$V_O = \frac{V_{in}}{n}\frac{d}{(1-d)} \tag{2}$$

Where, d is duty cycle of flyback converter and 'n' is the primary to secondary turns ratio of flyback transformer.

5. DESIGN CONSIDERATIONS

5.1 Switching Frequency

The choices of switching frequency selection have a crucial parameter between efficiency and bandwidth. The selection of higher switching frequencies will have more bandwidth, but a lower efficiency at lower switching frequencies [8],[9],[10]. The sufficient values of timing resistor (R_T) and timing capacitor (C_T) in PWM controller chip (UC2825) determines the desired switching frequency of the converter.

5.2 Transformer Design

The two major parameters in the design of flyback transformer are turns ratio and magnetizing inductance [5]. The equation (2) describes the relation between the turns ratio as a function of maximum duty cycle (d_{max}) with minimum input voltage.

$$V_O = \frac{V_{in\_\min}}{n}\frac{d_{\max}}{(1-d_{\max})};$$

Where; $n = \frac{N_p}{N_s}$ (3)

5.3 Primary peak current (I_{pp})

$$I_{pp} = \frac{I_o}{n}\frac{1}{(1-d_{\max})} + \frac{\Delta I_L}{2}; \tag{4}$$

where $\Delta I_L = \frac{I_{pp}}{2}$ in CCM operation.

5.4 Peak to Peak ripple current (ΔI_L)

Peak to peak ripple current of magnetizing inductance is.

$$\Delta I_L = \frac{V_{in\_\min}\, d_{\max}}{L_m f_s} \quad (5)$$

5.5 Minimum number of primary turns

$$N_P = \frac{L_m\, I_{pp}}{B_m A_e} \quad (6)$$

5.6 Number of secondary turns

$$n = \frac{N_p}{N_s};\ N_s = \frac{N_p}{n} \quad (7)$$

5.7 Primary RMS current

$$I_{prms} = I_{pp}\sqrt{\frac{D_{\max}}{3}} \quad (8)$$

5.8 Secondary RMS current

$$I_{srms} = I_{sp}\sqrt{\frac{1-D_{\max}}{3}} \quad (9)$$

5.9 Synchronous Rectifier MOSFET Selection

The voltage stress of primary MOSFET can be calculated as

$$V_{ds1} = V_{in\_\max} + V_F \quad (10)$$

The voltage stress of SR-MOSFET can be calculated as

$$V_{ds2} = \frac{V_{in\_\max}}{n} + V_o \quad (11)$$

The current stress is equal to the secondary peak current. The power loss in the SR-MOSFET can be calculated as below:

5.10 Output Capacitor

The following equation describes the calculation of desired value of output capacitor with the desired output voltage ripple.

$$C_o = \frac{(I_{spk} - I_o)^2 (1 - D_{\max})}{2\Delta V_o I_{spk} f_s} \quad (12)$$

The ESR of the capacitor considering the output voltage ripple and can be calculated as,

$$\Delta V_o = ESR\ (I_{spk} - I_o) \quad (13)$$

The operation of flyback converter in CCM has lesser peak current than operating in DCM. Hence the ESR is the main criteria for output capacitor selection. In this design, the output voltage ripple must be less than 200mV with approximately 10A of secondary side ripple current. A capacitor with an ESR less than 15m-Ohm is required.

5.11 Current Sensing and Slope Compensation

The ripple current of the converter is sensed by the current transformer (CT) and makes to shut down the converter if sensed current is too high. The threshold voltage level of the current sensing (CS) pin is 1 V.

5.12 Feedback Loop Compensation

The Feedback loop compensation of converter is used to prevent oscillation. The design of loop compensation in CCM Flyback is complicated compared to DCM, due to the existence of right half plane zero in the power design stage [11]. A PID-type-3 compensation is required for achieving stability and sufficient faster response. A detailed discussion and analysis about feedback loop compensation can be well presented on [12]. The PID controller loop is constructed using UC2825 PWM controller. The controller gains are tuned in order to mainatin stability and regulation at all conditions of perturbations in output load and input voltage [13],[14].

Table 1. System Specifications and Components

Parameter/Components	**Values**
Input voltage	20 V to 45 V
Output voltage	5 V
Output current	10A
Output power	50W
Switching frequency of magnetic isolation	500 KHz
Switching frequency of PWM controller	150 KHz
Band width	2 KHz
Maximum duty cycle	0.45
Transformer ratio (n)	1.3
Magnetizing inductance (L_m)	15µH
Primary peak ripple current (I_{pp})	10A
MOSFETs T_1 and T_2	IPB107N20N3 G, IPI075N15N3 G
Output capacitor C_o	940µF
PWM controller	UC2825
Main switch driver	UCC27512
Synchronous MOSFET driver	UCC27511

6. SIMULATION & EXPERIMENTAL RESULTS

The features of the synchronous rectifier flyback converter for EPS architecture are verified with the various simulation studies performed. The parameter considered for simulation studies are

represented in Table.1. The implemented simulation schematic is represented in Fig. 8. In simulation studies, the flyback transformer is considering as a magnetic inductor L_m, and leakage inductor L_k.

The simulation studies are performed with various values of input voltage and load current. Figure.9 represents the simulated switching voltage waveform of primary MOSFET and secondary synchronous MOSFET and its gating signal at 20V input with a load current of 5A. The simulation results are presented in Figures 10 and 11 represents the switch voltage of primary MOSFET, primary peak current and gating signal with input voltage of 20V at load current of 5A and 10A respectively. Similarly, the Figures 12 and 13 represent the simulated switching voltage waveform of primary MOSFET and secondary synchronous MOSFET and its gating signal at 45V input with a load current of 5A and 10A respectively. The simulation results are presented in Figures 14 and 15 represents the switching voltage of primary MOSFET, primary peak current and gating signal with input voltage of 45V at load current of 5A and 10A respectively. Simulation result of output voltage (Vo) with step change in load current of 5A to 10A is shown in Figure.16.

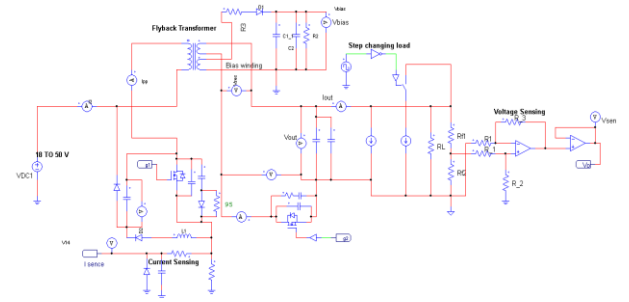

(a)

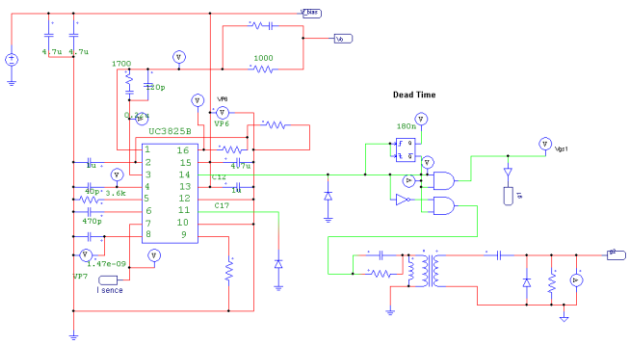

(b)

Figure 8. Simulation scheme of proposed 50W synchronous rectifier flyback converter (a) power circuit (b) PWM controller circuit.

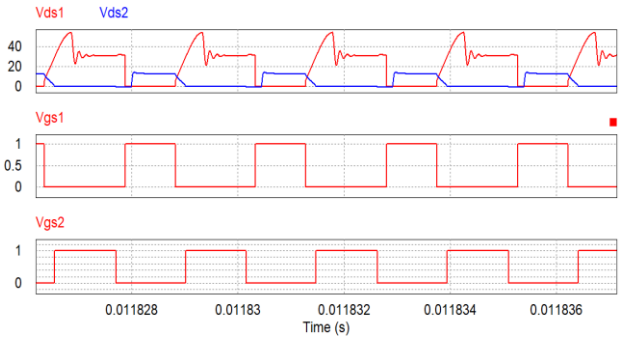

Figure 9. Simulation results of switch voltages (Vds1 and V_{ds2}) and per unit gating signals (V_{gs1} and V_{gs2}) at V_{in}:20V and I_{load}:5A).

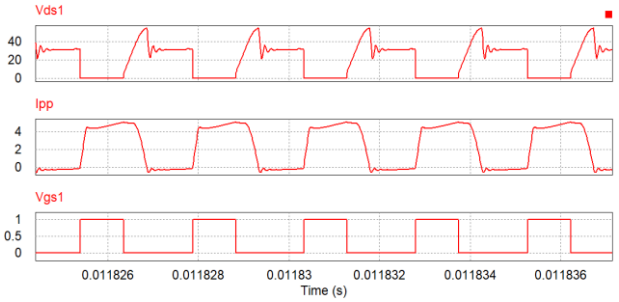

Figure 10. Simulation results of main switch voltage (V_{ds1}), primary peak current (I_{pp}) and per unit gating signals (V_{gs1}) at V_{in}:20V and I_{load}:5A).

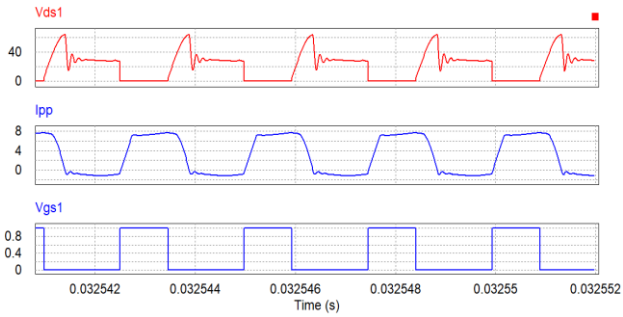

Figure 11. Simulation results of main switch voltage (V_{ds1}), primary peak current (I_{pp}) and per unit gating signals (V_{gs1}) at V_{in}:20V and I_{load}:10A).

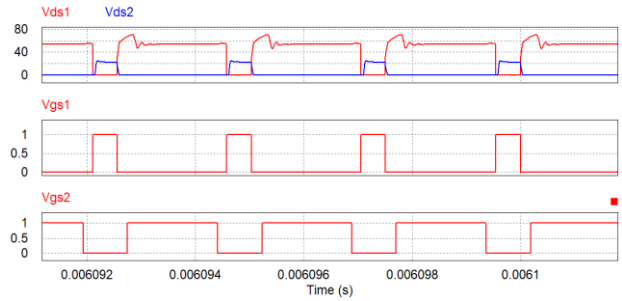

Figure 12. Simulation results of switch voltages (V_{ds1} and V_{ds2}) and per unit gating signals (Vgs1 and V_{gs2}) at V_{in}:45V and I_{load}:5A).

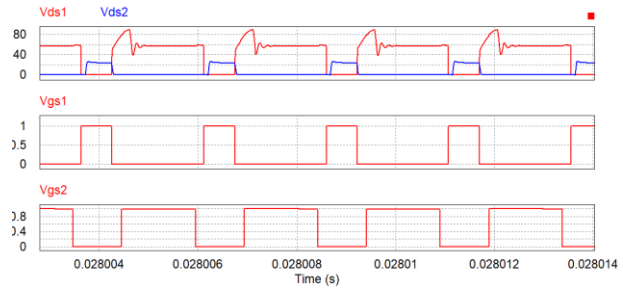

Figure 13. Simulation results of switch voltages (V_{ds1} and V_{ds2}) and per unit gating signals (V_{gs1} and V_{gs2}) at V_{in}:45V and I_{load}:10A).

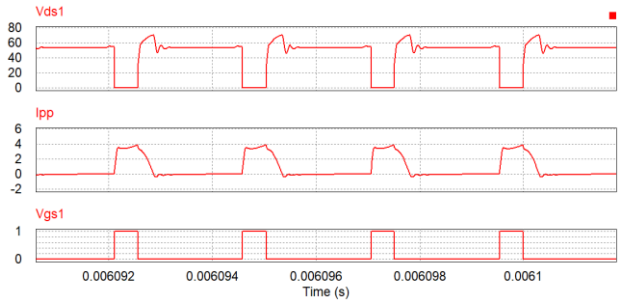

Figure 14. Simulation results of main switch voltage (V_{ds1}), primary peak current (I_{pp}) and per unit gating signals (V_{gs1}) at V_{in}:45V and I_{load}:5A).

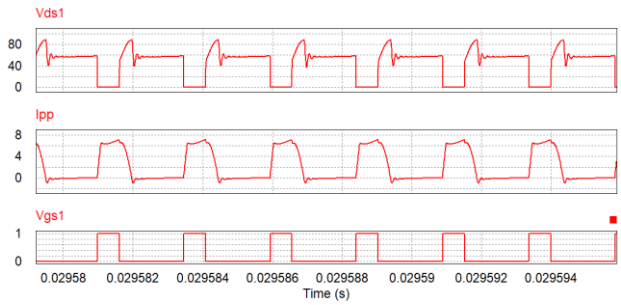

Figure 15. Simulation results of main switch voltage (V_{ds1}), primary peak current (I_{pp}) and per unit gating signals (V_{gs1}) at V_{in}:45V and I_{load}:10A).

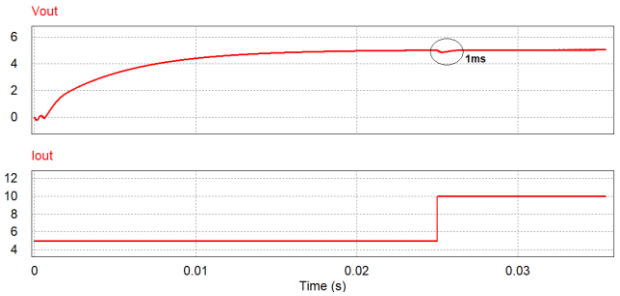

Figure 16. Simulation results of output voltage (Vo) with step change in load current of 5A to 10A.

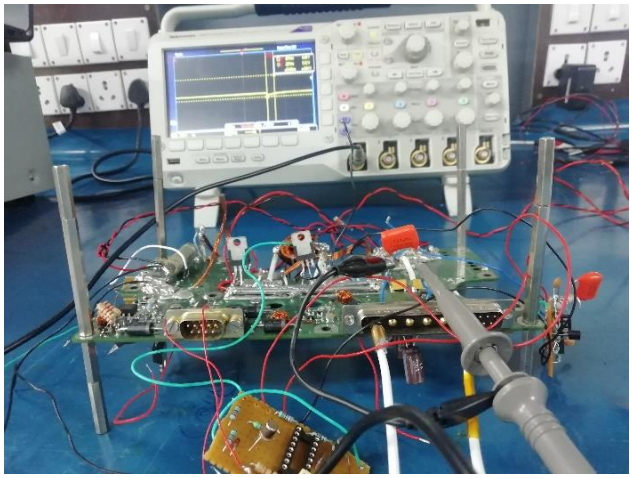

Figure.17 Experimental hardware prototype (BBM) test bench.

The designed flyback converter shown in simulation circuit of Figure.8 has been implemented in experimental hardware prototype. Figure. 17 shows the test bench setup of designed 50W prototype of the flyback converter. The specifications and key parameters of the designed prototype are shown in Table 1. Choices of a selection of a Flyback converter PWM controller and driver circuit mainly depends on precise requirements and certain design consideration such as cost, size, and various design form factor, respectively. Also, the requirements such as undervoltage, overvoltage, over current protection features, and standby power are easily be met by selecting the sufficient controller. UCC27511 is a compact driver IC which is configured to drive secondary synchronous power MOSFETs in this design. The presented driver IC has a feature to control single or cascaded MOSFETs to match the behavior of Schottky rectifiers.

Figure 18 represents the switching voltage and gating signal of the main switch with minimum input voltage (20V) at full load condition. Similarly Figure 19 represents the switching voltage and gating signal of synchronous MOSFET with minimum input voltage (20V) at full load condition.

Figure 20 represents the switching voltage of both main MOSFET and synchronous MOSFET with minimum input voltage (20V) at full load condition.

Figure 21 shows the gating signal of both main MOSFET and synchronous MOSFET with minimum input voltage (20V) at full load condition.

Similarly, Figures 22 to 25 represents the switching voltage and gating signal of main and synchronous MOSFET with maximum input voltage (45V) at full load condition.

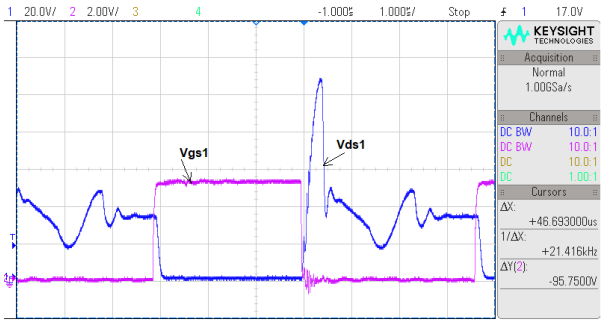

Figure18. Main switch voltage V_{ds1} and gating signal V_{gs1} at V_{in}:20V and I_{load}:10A).

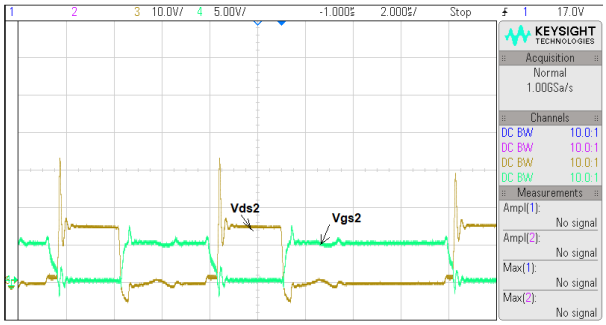

Figure 19. Synchronous switch voltage V_{ds2} and gating signal V_{gs2} V_{in}:20V and I_{load}:10A).

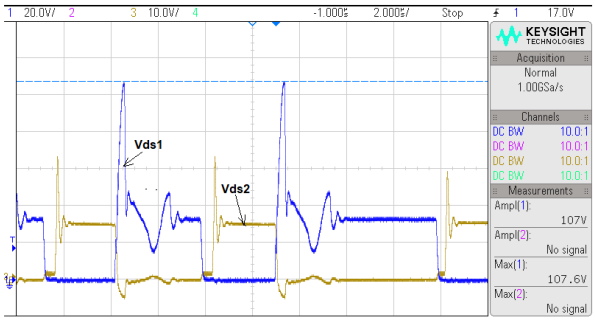

Figure 20. Switching voltage of main switch V_{ds1} and synchronous switch V_{ds2} (V_{in}:20V and I_{load}:10A).

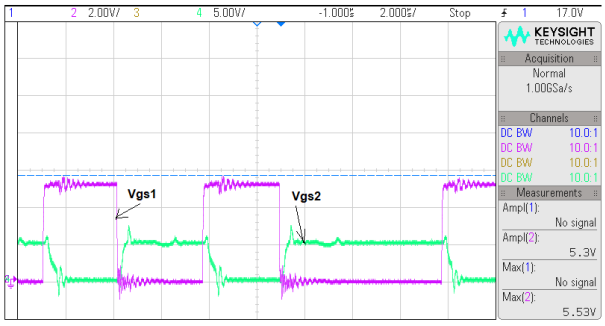

Figure.21 Gating signal of main switch V_{gs1} and synchronous switch V_{gs2} V_{in}:20V and I_{load}:10A).

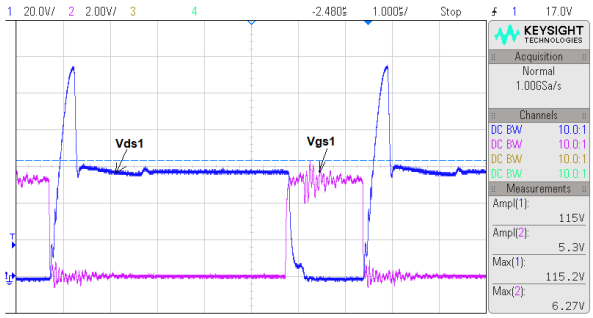

Figure 22. Main switch voltage V_{ds1} and gating signal V_{gs1} V_{in}:45V and I_{load}:10A).

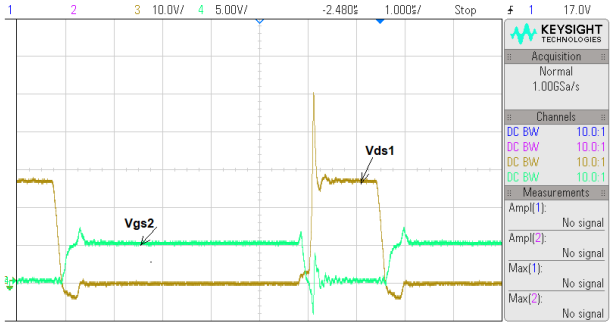

Figure 23. Synchronous switch voltage V_{ds2} and gating signal V_{gs2} (V_{in}:45V and I_{load}:10A).

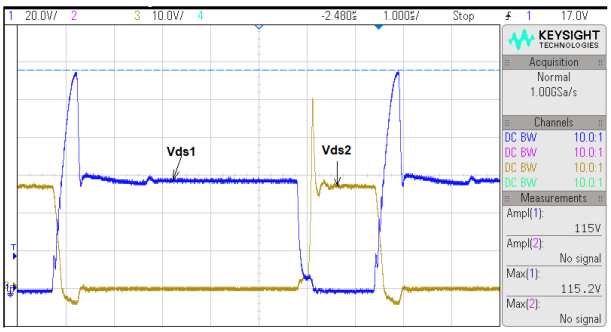

Figure 24. Switching voltage of main switch V_{ds1} and synchronous switch V_{ds2} (V_{in}:45V and I_{load}:10A).

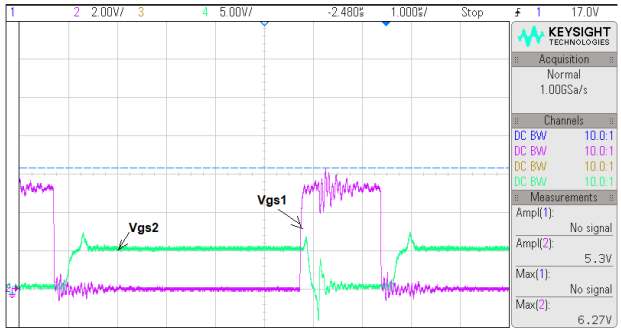

Figure25. Gating signal of main switch V_{gs1} and synchronous switch V_{gs2} (V_{in}:45V and I_{load}:10A).

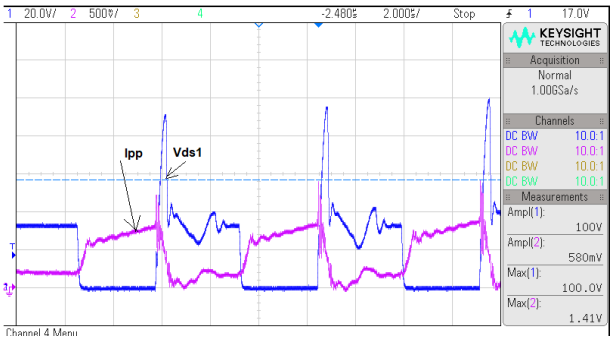

Figure 26. Measured main switch voltage (V_{ds1} and Primary peak current I_{pp} at (V_{in}:20V and I_{load}:10A).

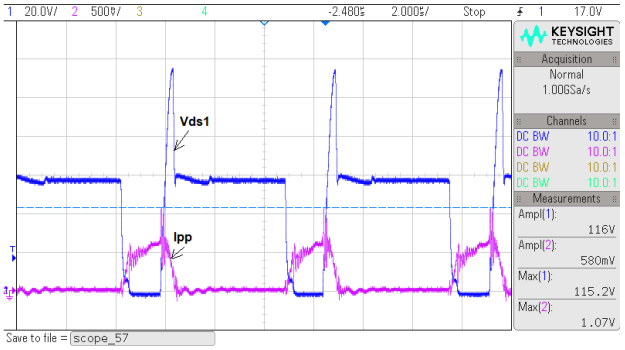

Figure 27. Measured main switch voltage and peak current (V_{ds1} and Primary peak current I_{pp} at (V_{in}:20V and I_{load}:10A).

Table 2. Line and Load Regulation

Input Voltage (Vin)	Input current at full load (Iin)	Output voltage at full load (Vo)	Line Regulation (%)	Load Regulation (%)
20.475	3.280	5.031	-0.020	-0.179
27.94	2.255	5.030		0.000
36.29	1.773	5.029		-0.358
45.158	1.432	5.040		-0.179

Table 3. Measured Efficiency at Full Load (10A)

Input Voltage (V_{in})	Input current at full load (I_{in})	Output voltage) at full load (V_o)	Input power (P_{in})	Output power (Po)	Efficiency (%)
20.475	3.280	5.031	67.16	50.290	74.898
27.94	2.255	5.030	63.93	50.290	79.810
36.29	1.773	5.029	64.34	50.290	78.160
45.158	1.432	5.030	65.66	50.290	77.768

Figure 26 and 27 shows the measured primary peak current (I_{pp}) and main switch voltage (V_{ds1}) with minimum and maximum input voltage at full load conditions respectively. Figure 28 and 29 shows the measured ripple waveform with minimum and maximum input voltage of 20V and 45V at full load condition, respectively. Table 2, 3 and 4 illustrates the line and load regulation, measured efficiency, and measured peak to peak ripple voltage with the variation of input voltage and load condition respectively. It is noted that the obtained experimental results had similar performance obtained in simulation results with various value of input voltage and load conditions.

Table 4. Peak-Peak Ripple Voltage

Input Voltage (V_{in})	Measured ripple voltage (peak-peak) at full load (mV)
20	103
28	72
36	67
45	64

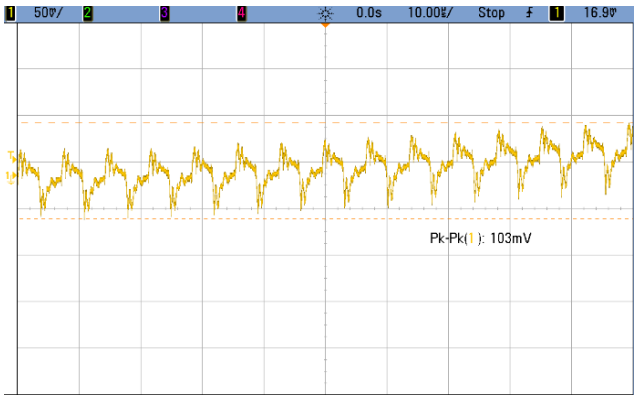

Figure.28 Measured ripple voltage at Vin: 20V and full load

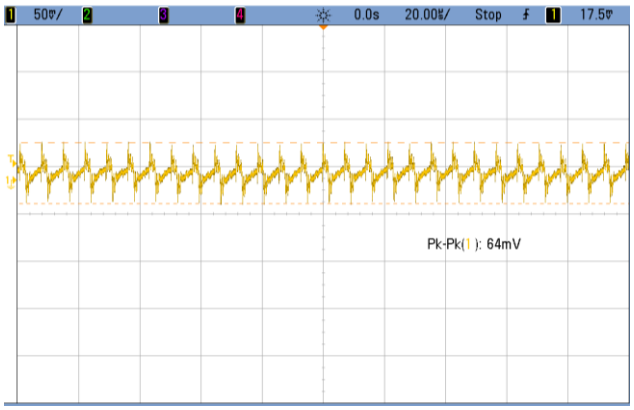

Figure.29 Measured ripple voltage at V_{in}: 45V and full load.

7. CONCLUSIONS

A fixed-frequency PWM-based current mode synchronous rectifier flyback converter for satellite EPS mission is presented from a circuit design perspective. Subsequently, the designed nonlinear controller based MPPT dc-dc converter has been used to input the interfacing flyback dc-dc converter. The synchronous rectifier-based flyback converter is a cost-effective solution for low output power application in EPS. The steady-state operation and the converter design methodology is described in detail. A practical approach to the design of the self-synchronous secondary driver circuit is also proposed in this paper. An analog form of the PWM controller is presented. The tuned controller used for voltage regulation is type-3 PID compensator to satisfy the sufficient magnitude and phase margin. The experimental results show that the response of the converter agrees with the theoretical and simulation design. The developed converter in a prototype model can be extended for space grade electric power systems in future. The efficiency of the converter can be improved further by tuning the snubber network and feedforward control technique. The goal of the design is to implement an optimized EPS can be realized such that the efficiencies of the distributed flyback dc-dc converter design are not significantly varied.

REFERENCES

1. Mohammed, A.A., Nafie., S.M, ‘‘Flyback converter design for low power application’’ *International Conference on Computing, Control, Networking, Electronics and Embedded Systems Engineering,2015(ICCNEEE)*. DOI: 10.1109/ICCNEEE.2015.7381410.
2. Zhang, F., Yan, Y., “Novel Forward–Flyback Hybrid Bidirectional DC–DC Converter” *IEEE Transactions on Industrial Electronics*, 56(5), 1578 –1584,2019. DOI:10.1109/TIE.2008.2009561.
3. Chen, S.J., Chang, H.C., “Analysis and Implementation of Low-side Active Clamp Forward Converters with Synchronous Rectification” *The 33rd Annual Conference of the IEEE Industrial Electronics Society* (IECON), 1506-1511,2007. DOI:10.1109/IECON.2007.4460226.
4. Lin, B.-R., Huang C.E., Wang, D, “Analysis and implementation of a zero-voltage switching forward converter with a synchronous rectifier” IEE Proc.-*Electr. Power Appl*., 152(5), 1805-1092,2005. DOI:10.1049/ip-epa:20050190.
5. Zhang, J., Liu, J., Bing, L., “A High Efficiency Synchronous Rectifier Flyback for High Density AC/DC Adapter” *Texas instruments application report*, 2011.
6. Zhung, M. T., Jovanovic, M. M., LCC, F.C., “Design Consideration and Performance Evaluations of Synchronous Rectification in Flyback Converters," *IEEE Trans. Power Electronics*, 3 (1), 538-546, 1998. DOI: 10.1109/63.668117.
7. Xuefei Xie, X., Joe Chui Pong Liu, J.C., *et.al*., *“*A Novel High Frequency Current-Driven Synchronous Rectifier Applicable to Most Switching Topologies. IEEE Transactions on power Electronics,16(5), 635 –648, 2001. DOI:10.1109/63.949496.
8. Zhou,J., Ming Xu, M., Sun, J., Lee, F.C., “Study of The Applicability of Self-Driven Synchronous Rectification to Resonant Topologies” *IEEE Transaction on Power Electronics*, 20(4), 806-814,2005. DOI: 10.1109/PESC.1992.254783 S1-S8.
9. Jia, H., Abdel-Rahman, O., *et.al*, “MHz-Frequency Operation of Flyback Converter with Monolithic Self-Synchronized Rectifier (SSR)” *IEEE, Intelec 2010*. DOI:10.1109/INTLEC.2010.5525665.
10. Dong, H., Xie, X., Zhang, L, “A New CCM/DCM Hybrid-Mode Synchronous Rectification Flyback Converter” *IEEE Transactions on power Electronics* ,67(5),4457 – 4461, 2020. DOI:10.1109/TIE.2019.2920474
11. Dong, H., Xie, X., Zhang, L., “A New Primary PWM Control Strategy for CCM Synchronous Rectification Flyback Converter”, *EEE Transactions on power Electronics*,35(5), 4457 – 4461,2020. DOI: 10.1109/TPEL.2019.2944492.
12. Demystifying Type II and Type III Compensators Using Op-Amp and OTA for DC/DC Converters. (2014). Texas instruments application notes.
13. Adel Alganidi, A., Amit Kumar, A, “PI Controller Tuning & Stability study of the Flyback Converter with an Energy Regenerative Snubber” *IEEE Canadian Conference of Electrical and Computer Engineering,(CCECE)*,2019. DOI: 10.1109/CCECE.2019.8861586.
14. Ravichandran, C., Premalatha L, Rengaraj, R, “ Fixed frequency integral sliding-mode current-controlled MPPT boost converter for two-stage PV generation system” *IET Circuits Devices Syst,13(6),* 793-805,2019. *https://doi.org/10.1049/iet-cds.2018.5221*
15. Halder, T., “Spacecraft electrical power systems (EPS) using the Flyback converters” IEEE International Conference on Non-Conventional

Energy (ICONCE 2014), 2014. DOI:10.1109/ICONCE.2014.6808681.

16. Usman Khan, M., Ali, A., Haider Ali, H., Khattak, M.S., Iftikhar Ahmad, I., "Designing efficient Electric Power Supply System for Micro-Satellite" *IEEE_International Conference on Computing, Electronic and Electrical Engineering (ICE Cube)*,2014. DOI: 10.1109/ICECUBE.2016.7495225
17. Demirel, S., Erol Sanli, E., Gokten, M., Yagli, A.F., Gulgonul, S., "Properties and performance comparison of Electrical Power sub-system on TUSAT Communication Satellite" *IEEE First AESS European Conference on Satellite Telecommunications (ESTEL)* ,2013. DOI: 10.1109/ESTEL.2012.6400162
18. Sulistya, A.H *et al*., "Design and Implementation of Effective Electrical Power System for Surya Satellite-1" *IOP Conf. Ser.: Earth Environ. Sci.* 149 012059, 2018. DOI :10.1088/1755-1315/149/1/012059
19. Mojallizadeh, M.R., Karimi, B., "Nonlinear Control of a Satellite Electrical Power System Based on the Sliding Mode Control" *Hindawi Publishing Corporation ISRN Aerospace Engineering*, 2013, 1-8, 2013. DOI://dx.doi.org/10.1155/2013/253564.

Modeling and Performance Analysis of Simplified Three-Diode Photovoltaic Module

S Bhanu Prakash[1] Gagan Singh[2] and Sonika Singh[3]
Research Scholar[1], Professor[2], Associate Professor[3], Department of EECE, DIT UNIVERSITY, Dehradun, Uttarakhand, India. +91-7895316811, sb.prakash@dituniversity.edu.in[1], gagan.singh@dituniversity.edu.in[2], sonika.singh@dituniversity.edu.in[3]

Abstract- Developing the mathematical model of photovoltaic (PV) cell, to simulate the module and predict their actual performance at varying temperature and irradiance condition, is very significant for evaluation of photovoltaic cell, as well as for dynamic analysis of dc-dc converters and design of maximum power point algorithms. This work proposes the analysis and modeling of photovoltaic module using the three-diode five parameter model formed based on manufacturer's datasheet. The constraints of electrical equivalent circuit of photovoltaic cell are analyzed by solving the non-linear current-voltage equation based on manufacturer datasheet provided at standard operating conditions with reduced computation period by using an effective iteration procedure. The photovoltaic current-voltage formulation is analyzed at three main points specifically at open circuit, short circuit and maximum power point condition. This model is identified to have better performance and precise compared to two-diode model mainly at lesser irradiance and higher temperature levels. To verify the accuracy and conformity of the proposed model the method is applied on two different multi or poly-crystalline photovoltaic module and obtained results were compared by manufacturer performance data. By using the standard mathematical equations of photovoltaic cell this model is developed and simulated in MATLAB/Simulink software.

Keywords: Three-diode Photovoltaic model, Two-diode Photovoltaic model, Multi-crystalline solar cell, Iteration procedure, Shunt resistance

1. Introduction

Modelling of photovoltaic (PV) cell needs to predict the performable behavior of actual photovoltaic cell at various ecological conditions and to produce its power-voltage and current-voltage curves. The most common modelling method is to employ equivalent (electrical) circuit that includes both non-linear and linear mechanisms. In general, the manufacturer's datasheet only tabulate about some constraints like open circuit voltage (V_o), short circuit current (I_{SC}), peak or maximum power (P_{mpp}), current at P_{mpp} (I_{mpp}) and voltage at P_{mpp} (V_{mpp}) at standard operating conditions and unfortunately these data is far away from what is critical for modelling because photovoltaic cell is used to operate at various irradiance and temperature points. The non-linear behavior of current-voltage characteristics needs the adjustment of parameters by using manufacturer data. Several researchers have been proposed some model based on single-diode R_S model, R_P model, double-diode and three-diode photovoltaic model [3], [4] and [7]. The modest system is one-diode photovoltaic model it comprises only three parameters in ideal case like current at short circuit, voltage at open circuit and ideality factor of diode. The improved form of the ideal model is addition of series resistance R_s to the electrical equivalent circuit [10]. Although this model suffers from irregularities with the variation in the temperature values as it not considered the voltage temperature coefficient. The advanced form of model is the R_P model by addition of parallel resistor to the equivalent circuit [11]. This R_P model has improved performance in comparison to one diode R_S model.

In past many researchers have presented single diode model by making an assumption that absence of recombination loss in depletion layer. In actual it is not possible to reasonably develop a model by means of single diode. In practice for precise model by consideration of this recombination loss results in more actual model identified as a two-diode model [16]. The improved version of both one diode and two-diode model is by insertion of third diode in parallel with the two diodes which taken into consideration of recombination of the defect regions results in more accurate model identified as a three-diode model [2]. Though these enhanced models possess improved accuracy but with the insertion of additional diodes which results in more computational parameters and leads to more computational complexity. The main objective is now to evaluate the model constraints while keeping a realistic computational energy.

The significant knowledge of this paper is to develop a comprehensive model of three-diode photovoltaic module is by simplifying the current equation and thereby reducing the constraints to five. Multi or polycrystalline silicon material is progressively useful for the production of photovoltaic

cell owing to its low cost. In order to realize the performance of multi-crystalline solar cell, it is significant to study their electrical properties [12]. The output performance of this simplified three-diode model is confirmed by two different multi or polycrystalline solar cells from manufacturer performance data and precision of this model is compared with two diode model. This simplified model can be useful for researchers those who works on the accurate modelling of photovoltaic module for design of maximum power point tracking algorithms and power converters for energy storage devices.

2. Electrical Equivalent Circuit and Modeling of Photovoltaic Cell

2.1 Equivalent Circuit model of One-diode and Two-diode Photovoltaic Cell

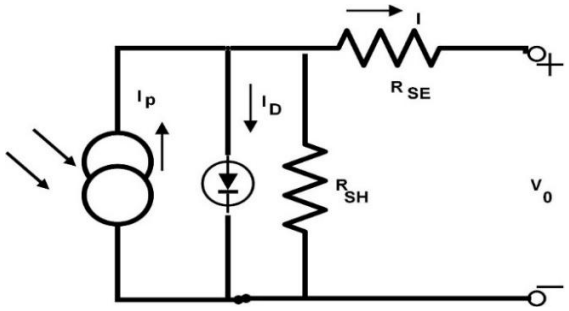

Figure 1: One-Diode R_{SH} Photovoltaic Cell equivalent circuit model [7]

.

The one-diode R_{SH} model considers one diode connected in parallel to the constant current source with series resistance R_{SE} and shunt resistance R_{SH} is shown in Figure 1 [7]. In case of modeling of one-diode model the number of constraints will become five. The constraints are photo or incident current I_P, diode saturation current I_{DS}, ideality factor of diode C, series resistance R_{SE} and shunt resistance R_{SH}. The one-diode R_{SH} model is identified as most popular and easy to implement. In spite of its advantages the model precision will become worse at lesser irradiance [8].

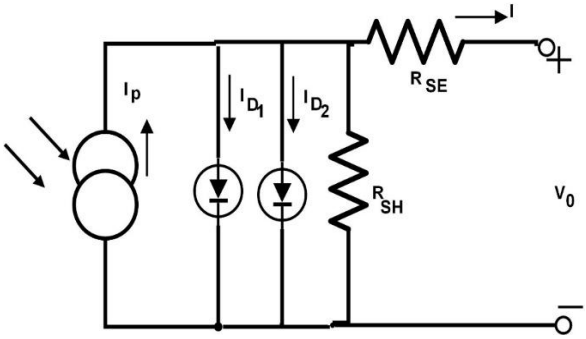

Figure 2: Two-diode Photovoltaic Cell equivalent circuit model [4]

The Two-diode model considers two diodes connected in parallel to the constant current source as shown in Figure 2 [4] obviously now two more new constraints are essential to be considered is the reverse saturation diode current I_{DS2} and ideality factor C_2. The current I_{DS2} compensates the consequence of recombination loss in the depletion area [15]. The number of constraints will become seven in case of two-diode model. The constraints are photo or incident current I_P, diode saturation current I_{DS1} and I_{DS2}, ideality factor of diode C_1 and C_2, series resistance R_{SE} and shunt resistance R_{SH}. Two-diode model is identified as more accurate model and better performance especially at lower irradiance.

2.2 Modeling of Three-diode photovoltaic (PV) cell

The Three-diode model considers three diodes connected in parallel to the constant current source as shown in Figure 3 [2] obviously now two more new constraints are essential to be considered while modeling is the reverse saturation diode current I_{DS3} and ideality factor C_3. The current I_{DS3} compensates the consequence of recombination in the defects area [2]. The number of constraints will become nine in case of three-diode model. The constraints are photo or incident current I_P, diode saturation current I_{DS1}, I_{DS2} and I_{DS3}, ideality factor of diode C_1, $C_2$and C_3, series resistance R_{SE} and shunt resistance R_{SH}. Three-diode model is identified to be more accurate model and better performance especially at lower irradiance and higher temperature points.

By applying KVL to Fig.3 we get the expression for output or module current I:

$$I = I_p - I_{D1} - I_{D2} - I_{D3} - \frac{V_0 + IR_{SE}}{R_{SH}} \qquad (1)$$

I_P is the Photo or incident current, I_{D1}, I_{D2} and I_{D3} is the diode currents, I_{SH} is Current through shunt resistor = $\frac{V_0 + IR_{SE}}{R_{SH}}$, R_{SE} and R_{SH} are series and shunt resistances, V_0 is Applied voltage across diode and I is output current of module [1].

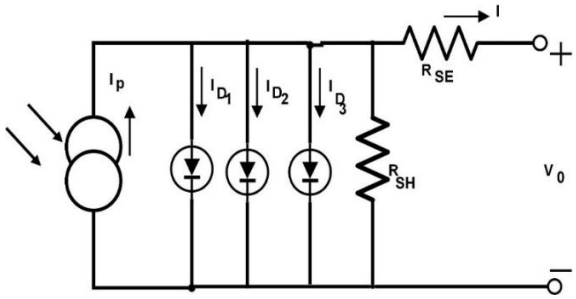

Figure 3: Three-Diode photovoltaic Cell equivalent circuit model

Currents through diodes 1 and 2 is given by

$$I_{D1} = I_{Ds1}[(e^{\frac{V_o + IR_{SE}}{C_1 V_T N_{SE}}}) - 1]$$

$$I_{D2} = I_{Ds2}[(e^{\frac{V_o + IR_{SE}}{C_2 V_T N_{SE}}}) - 1] \text{ and } I_{D3} = I_{Ds3}[(e^{\frac{V_o + IR_{SE}}{C_3 V_T N_{SE}}}) - 1]$$

$$I = I_p - I_{Ds1}[(e^{\frac{V_o + IR_{SE}}{C_1 V_T N_{SE}}}) - 1] - I_{Ds2}[(e^{\frac{V_o + IR_{SE}}{C_2 V_T N_{SE}}}) - 1] - I_{Ds3}[(e^{\frac{V_o + IR_{SE}}{C_3 V_T N_{SE}}}) - 1] - \frac{V_0 + IR_{SE}}{R_{SH}} \quad (2)$$

I_{Ds1}, I_{Ds2} and I_{Ds3} are reverse saturation diode current, C_1, C_2 and C_3 is Diode Ideality factor of 1,2 and greater than 2, N_{SE} is number of series connected PV cell's, V_T is called as Thermal Voltage = $\frac{K\,T_{Ac}}{q}$, V_T is approximately 25.856 mV at 300 Kelvin, q is ($1.602\ X\ 10^{-19}$) C is electron charge, K – ($1.38\ X\ 10^{-23}$) $Joule/_{Kelvin}$ is a Boltzmann constant, T_{Ac} is Cell's absolute temperature in Kelvin. Photo current [9] is given by

$$I_p = (I_{SC} + K_{SC}\Delta T_{Ac})\frac{G_{ir}}{G_{SC}} \quad (3)$$

G_{ir} – Irradiance in $W/_{m^2}$, G_{SC} – Irradiance at Standard Test Condition (STC) = 1000 $W/_{m^2}$, $\Delta T_{Ac} = T_{Ac} - T_{Ac,ref}$ (Kelvin), $T_{Ac,ref}$ – $(25 + 273 = 298\ Kelvin)$, I_{SC} is Cell's short circuit current of Cell at STC (25^0), K_{SC} is temperature coefficient of current (A/K).

Simplified diode saturation current equation in terms of temperature coefficient (K_V) can be written as

$$I_{DS} = I_{DS1} = I_{DS2} = I_{DS3} = \frac{I_{SC} + K_{SC}\Delta T_{Ac}}{(e^{\frac{V_0 + K_V \Delta T_{Ac}}{V_T[\frac{C_1 + C_2 + C_3}{P}]}} - 1)} \quad (4)$$

where

K_V – temperature coefficient of voltage (V/K)

In development of three-diode model it required to estimate nine constraints which makes analysis very complicated and not so simple for simulation of PV module. For ease analysis and to make the model simple the nine constraints are reduced to five as described in [1] the same assumption can be applied for modeling of three-diode model. To make it simple in analysis the following assumptions are considered: the $I_{DS} = I_{DS1} = I_{DS2} = I_{DS3}$ and $(C_1 + C_2 + C_3)/_p) = 1$. In the equations (3) and (5) by substituting the temperature and irradiance inputs the photo current and diode saturation currents are estimated based on data provided by constructor. By setting the values of ideality factors $C_1 = 1$, $C_2 = 2.2$, C_3 is chosen greater than 2 yields in the best suitable outcomes in current-voltage curve of PV cell module [2]. These changes make three-diode model to easy system and attractive for PV system simulator and only five constraints to be evaluated.

Therefore

$$I_{DS} = I_{DS1} = I_{DS2} = I_{DS3} = \frac{I_{SC} + K_{SC}\Delta T_{Ac}}{(e^{\frac{V_0 + K_V \Delta T_{Ac}}{V_T}} - 1)} \quad (5)$$

2.2 Determination of R_{SE} and R_{SH} Constraints

Several analytical and numerical approaches [3], [5], [6], [9], [13] and [14] have been proposed in the literature to evaluate the constraints of one-diode and two-diode model. In this work the constraints R_{SE} *and* R_{SH} is evaluated by same approach as described in [9]. The key information is the value of R_{SE} *and* R_{SH} are selected such that calculated power $P_{mpp,C}$ must be equal to experimental power $P_{mpp,STC}$ provided by constructor data sheet. Figure 4 illustrates the flow chart of iteration process to adjust the current-voltage curve. This iteration process initiates from $R_{SE} = 0$ which must vary in path until to match the calculated maximum power to $P_{mpp,STC}$ must be equal to experimental power $P_{mpp,STC}$ and simultaneously R_{SH} is then calculated. By adjusting the values of R_{SE} *and* R_{SH} based on the fact that at only one pair (R_{SE} , R_{SH}) which guarantees that $P_{mpp,C} = P_{mpp,STC} = V_{mpp}.I_{mpp}$ at maximum power point of current-voltage curve.

In general manufacturer gives data of current at short circuit (I_{SC}), voltage at open circuit (V_o) and peak or maximum power (P_{mpp}). Now evaluate the current equation shown below at three conditions: current (I_{SC}) at short circuit, voltage (V_o) at open circuit and peak or maximum power (P_{mpp}) point condition.

$$I = I_p - I_{D1} - I_{D2} - I_{D3} - \frac{V_0 + IR_{SE}}{R_{SH}}$$

At short circuit condition

$I = I_{SC,STC}$; $V_0 = 0$

$$I_{SC,STC} = I_{p,STC} - I_{D1,STC} - I_{D2,STC} - I_{D3,STC} - \frac{I_{SC,STC}R_{SE}}{R_{SH}} \quad (6)$$

Where, $I_{D1,STC} = I_{Ds1,STC}[(e^{\frac{I_{SC,STC}R_{SE}}{C_1 V_T N_{SE}}}) - 1]$ $I_{D2,STC} = I_{Ds2,STC}[(e^{\frac{I_{SC,STC}R_{SE}}{C_2 V_T N_{SE}}}) - 1]$ and $I_{D3,STC} = I_{Ds3,STC}[(e^{\frac{I_{SC,STC}R_{SE}}{C_3 V_T N_{SE}}}) - 1]$

At open circuit condition

$$I = 0;\ V_0 = V_{o,STC}$$

$$0 = I_{p,STC} - I_{D1,STC} - I_{D2,STC} - I_{D3,STC} - \frac{V_{o,STC}}{R_{SH}} \quad (7)$$

From equation (7)

$$I_{p,STC} = I_{D1,STC} + I_{D2,STC} + I_{D3,STC} + \frac{V_{o,STC}}{R_{SH}} \quad (8)$$

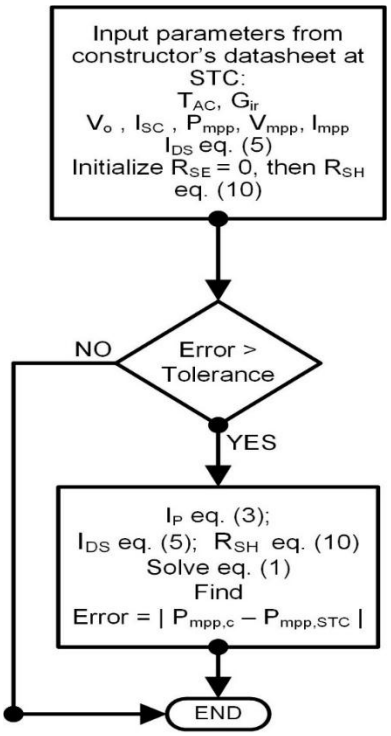

Figure 4: Flow Chart for Iteration process

Where $I_{D1,STC} = I_{Ds1,STC}[(e^{\frac{V_{o,STC}}{C_1 V_T N_{SE}}}) - 1]$, $I_{D2,STC} = I_{Ds2,STC}[(e^{\frac{V_{o,STC}}{C_2 V_T N_{SE}}}) - 1]$ and

$$I_{D3,STC} = I_{Ds3,STC}[(e^{\frac{V_{o,STC}}{C_3 V_T N_{SE}}}) - 1]$$

At maximum power condition

$$I_{mpp,STC} = I_{p,STC} - I_{D1,STC} - I_{D2,STC} - I_{D3,STC} - \frac{V_{mpp,STC} + I_{mpp,STC}R_{SE}}{R_{SH}} \quad (9)$$

From equation (9)

$$\frac{V_{mpp,STC} + I_{mpp,STC}R_{SE}}{R_{SH}} = I_{p,STC} - I_{D1,STC} - I_{D2,STC} - I_{D3,STC} - I_{mpp,STC}$$

$$R_{SH} = \frac{V_{mpp,STC} + I_{mpp,STC}R_{SE}}{I_{p,STC} - I_{D1,STC} - I_{D2,STC} - I_{D3,STC} - I_{mpp,STC}} \quad 10)$$

Where P_{mpp} is the peak or maximum power, $V_{mpp,STC}$ is voltage at P_{mpp} and $I_{mpp,STC}$ is current at P_{mpp}, diode saturation currents at maximum power condition is given by relation as shown below:

$$I_{D1,STC} = I_{Ds1,STC}[(e^{\frac{V_{mpp,STC} + I_{mpp,STC}R_{SE}}{C_1 V_T N_{SE}}}) - 1],$$

$$I_{D2,STC} = I_{Ds2,STC}[(e^{\frac{V_{mpp,STC} + I_{mpp,STC}R_{SE}}{C_2 V_T N_{SE}}}) - 1] \text{ and}$$

$$I_{D3,STC} = I_{Ds3,STC}[(e^{\frac{V_{mpp,STC} + I_{mpp,STC}R_{SE}}{C_3 V_T N_{SE}}}) - 1]$$

By using iteration process the value of R_{SE} *and* R_{SH} can be estimated with help of equation (10).

4. Simulation of Proposed Three-diode Model

Based on the equations (2), (3), (4) and (5) it is simple to frame an overall simulation model by MATLAB/Simulink software. The overall three-diode model and sub-system group model are represented in Figure 5 and Figure 6. The detailed simulation models of diode saturation currents are represented in Fig.7 of proposed three diode model. Simulation model of Photo current and module output currents of proposed three diode model are simulated and represented in Figure 8 and Figure 9

5. Results and Discussion

The modelling system proposed in this work is confirmed by estimated constraints of certain PV cell modules. The proposed model is validated by two different multi or polycrystalline PV modules; KC200GT [17] and MSX-64 [18]. The product specifications of two different PV modules are shown in Table 1. Table 2 illustrates the measured values of proposed three-diode model and Table 3 illustrates the measured values of two-diode model. Table 4 and Table 5 summarizes the study of relative error of P_{mpp}, V_{mpp}, I_{mpp}, V_o and I_{SC} of both poly-crystalline solar cell. From Table 4 and Table 5 we can observe that the estimated values somewhat diverge from manufacture data sheet value at STC. However, for poly-crystalline (KC200GT) is exactly fits the current-voltage curve based on manufacturer product data for proposed three-diode model.

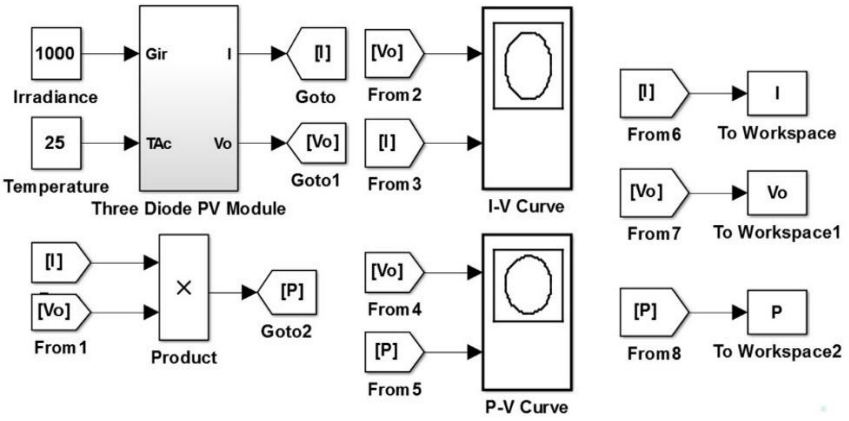

Figure 5: Overall Photovoltaic Model of proposed three diode model

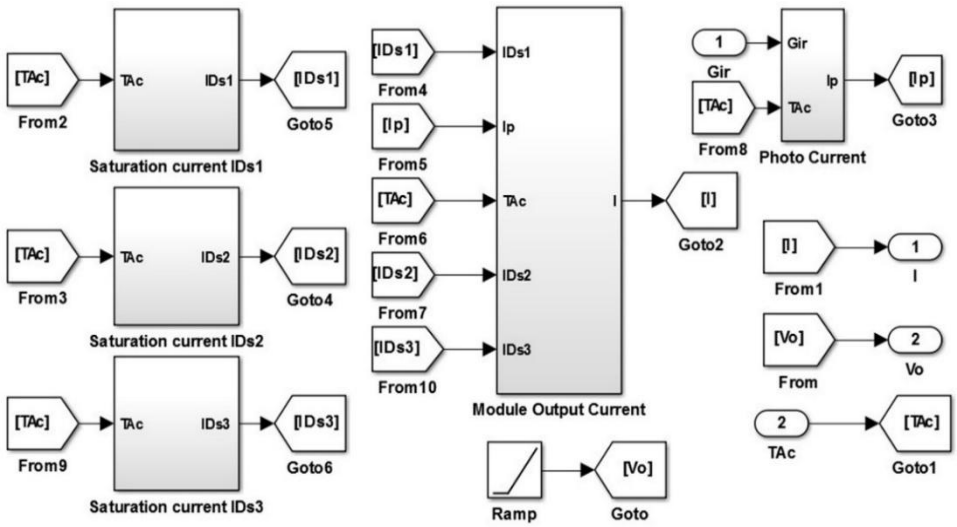

Figure 6: Complete Sub-system Model of proposed three diode photovoltaic cell

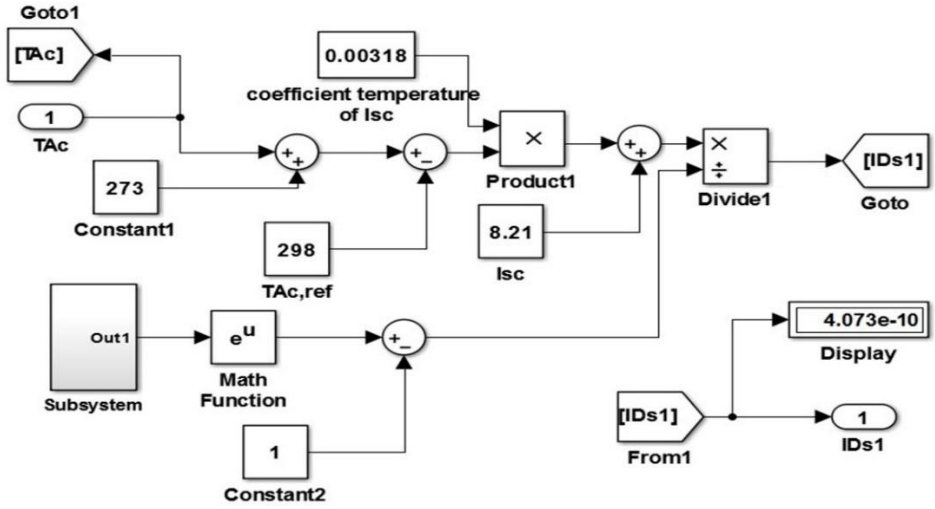

Figure 7: Saturation Current I_{DS} of proposed three diode photovoltaic cell

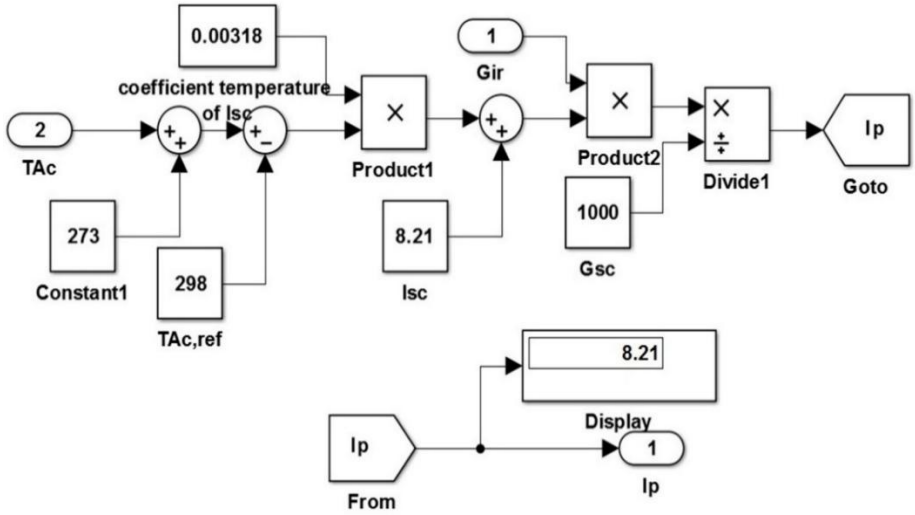

Figure 8: Light Current I_p of proposed three diode photovoltaic cell

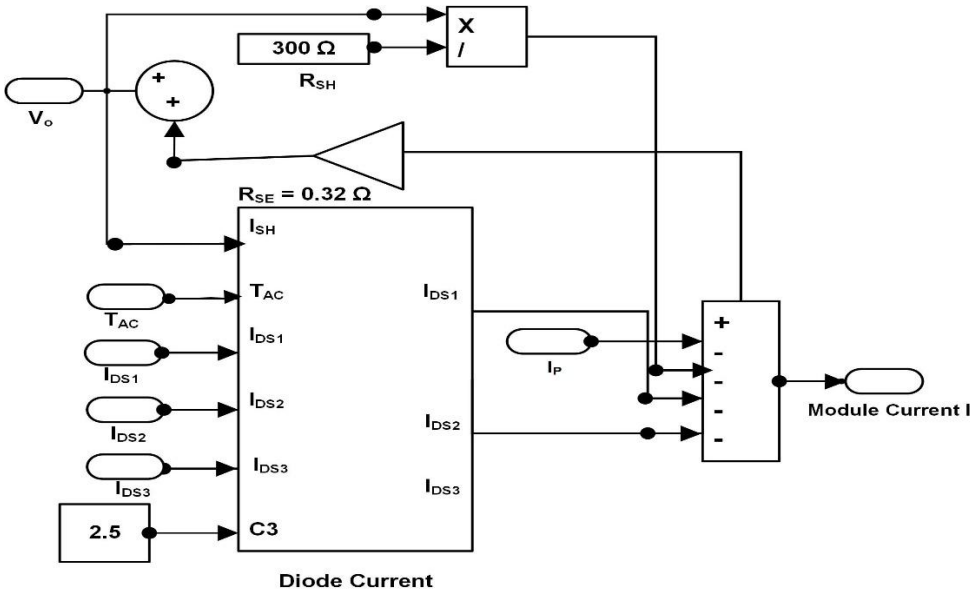

Figure 9: Module Output Current of proposed three diode photovoltaic cell

Table 1: Module Specifications from constructor data sheet

Constraints	**Poly-crystalline Kyocera KC200GT Solar Panel [17]**	**Poly-crystalline Solarex MSX-64 [18]**
Maximum Power (P_{mpp})	200 W	64 W
Voltage at P_{mpp} (V_{mpp})	26.3 V	17.5 V
Current at P_{mpp} (I_{mpp})	7.61 A	3.66 A
Voltage at open circuit (V_o)	32.9 V	21.3 V
Current at short circuit (I_{SC})	8.21 A	4 A
Series Connected cell (N_{SE})	54	36
Voltage Temperature coefficient (K_v)	-123 mV/^{0}C	-80 mV/^{0}C
Voltage Temperature coefficient (K_{SC})	0.318 A/^{0}C	0.65 ^{0}C

Table 2: Estimated Values of Proposed Three-diode model

Constraints	Poly-crystalline Kyocera KC200GT	Poly-crystalline Solarex MSX-64
Maximum Power (P_{mpp})	200.11 W	64.67 W
Voltage at P_{mpp} (V_{mpp})	26.32 V	17.466 V
Current at P_{mpp} (I_{mpp})	7.603 A	3.682 A
Voltage at open circuit (V_o)	32.9 V	21.3 V
Current at short circuit (I_{SC})	8.21 A	4 A
Light Current (I_p)	8.21 A	4.01 A
Saturation Currents ($I_{DS1} = I_{DS2} = I_{DS3}$)	4.073 x 10^{-10} A	3.937 x 10^{-10} A
Diode Ideality Factor (C)	$C_2 = 2.2$, C_3=2.5	$C_2 = 1.3$
Series Resistance (R_{SE})	0.32 Ω	0.3 Ω
Shunt Resistance (R_{SH})	300 Ω	160.4 Ω

Table 3: Estimated Values of Two-diode model

Constraints	Poly-crystalline Kyocera KC200GT	Poly-crystalline Solarex MSX-64
Maximum Power (P_{mpp})	198.14 W	62.9 W
Voltage at P_{mpp} (V_{mpp})	26.32 V	17.46 V
Current at P_{mpp} (I_{mpp})	7.528 A	3.605 A
Voltage at open circuit (V_o)	32.9 V	21.3 V
Current at short circuit (I_{SC})	8.21 A	4 A
Light Current (I_p)	8.21 A	4.01 A
Saturation Currents ($I_{DS1} = I_{DS2}$)	4.073 x 10^{-8} A	3.937 x 10^{-8} A
Diode Ideality Factor (C)	$C_2 = 2.2$, C_3=2.4	$C_2 = 1.2$
Series Resistance (R_{SE})	0.36 Ω	0.35 Ω
Shunt Resistance (R_{SH})	282.33 Ω	167.25 Ω

Table 4: Comparison of estimated values at maximum power (P_{mpp}) of Three-diode model and Two-diode model for poly-crystalline (KC200GT) solar cell

Constraints	Manufacturer Data at STC	Three-diode model	Two-diode Model	% Relative Error of Three-diode model	% Relative Error of Two-diode model
Maximum Power (P_{mpp})	200 W	200.11 W	198.14 W	- 0.055	0.93
Voltage at P_{mpp} (V_{mpp})	26.32 V	26.32 V	26.32 V	0.00	0.00
Current at P_{mpp} (I_{mpp})	7.61 A	7.603 A	7.528 A	0.091	1.077
Voltage at open circuit (V_o)	32.9 V	32.9 V	32.9 V	0.00	0.00
Current at short circuit (I_{SC})	8.21 A	8.21 A	8.21 A	0.00	0.00

Table 5: Comparison of estimated values at maximum power (P_{mpp}) of Three-diode model and Two-diode model for polycrystalline solar cell (MSX-64)

Constraints	Manufacturer Data at STC	Three-diode model	Two-diode Model	% Relative Error of Three-diode model	% Relative Error of Two-diode model
Maximum Power (P_{mpp})	64 W	64.67 W	62.9 W	- 1.04	1.71
Voltage at P_{mpp} (V_{mpp})	17.5 V	17.466 V	17.466 V	0.194	0.194
Current at P_{mpp} (I_{mpp})	3.66 A	3.682 A	3.605 A	- 0.601	1.5
Voltage at open circuit (V_o)	21.3 V	21.3 V	21.3 V	0.00	0.00
Current at short circuit (I_{SC})	4 A	4 A	4 A	0.00	0.00

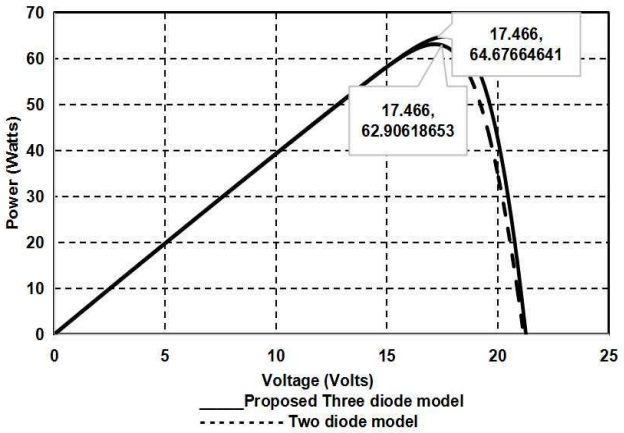

Figure 10: Power (W) Vs Voltage (V) Curve of Proposed Three-diode model and Two-diode model for MSX-64 at STC (25^0 C and 1000 KW/m^2)

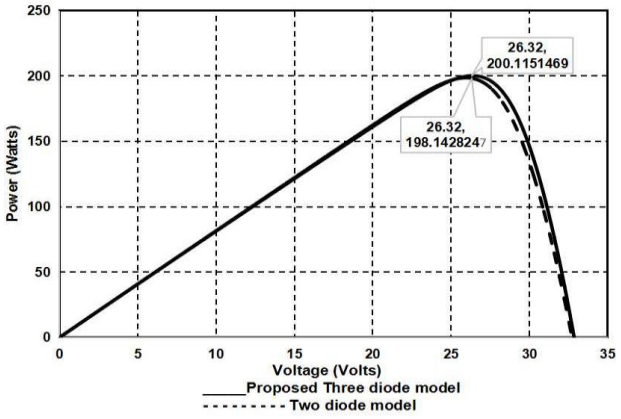

Figure 11: Power (W) Vs Voltage (V) Curve of Proposed Three-diode and Two-diode model for KC200GT at STC (25^0 C and 1000 KW/m^2)

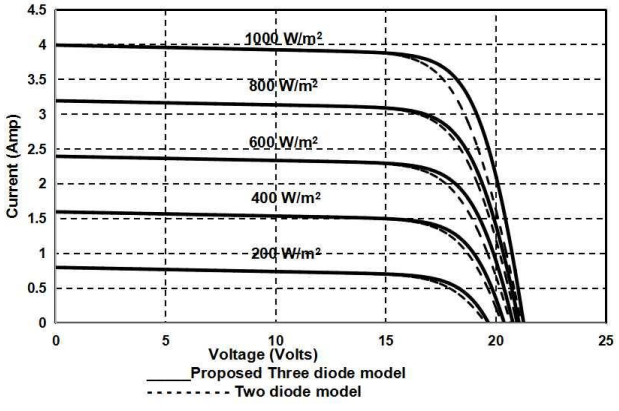

Figure 12: Comparison of Current (A) Vs Voltage (V) Curve of both Proposed Three-diode and Two-diode model for KG200GT with different irradiance at STC (25^0 C)

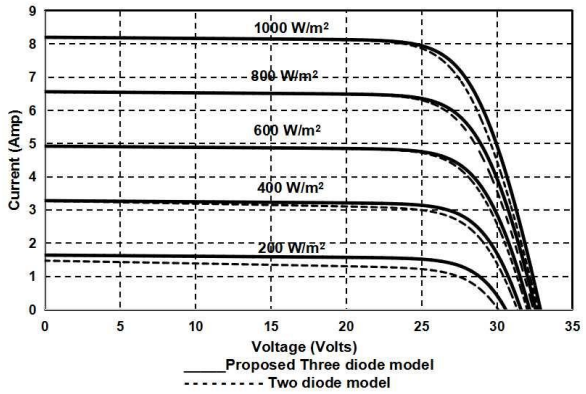

Figure 13: Comparison of Current (A) Vs Voltage (V) Curve of both Proposed Three-diode and Two-diode model for KC200GT with different temperatures at STC (1000 KW/m^2)

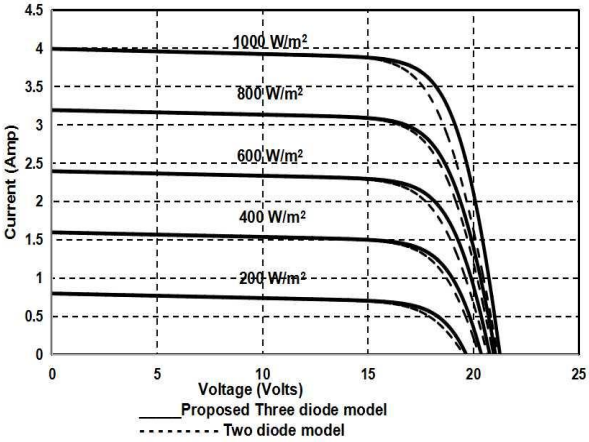

Figure 14: Comparison of Current (A) Vs Voltage (V) Curve of both Proposed Three-diode and Two-diode model for MSX-64 with different irradiance at STC (25^0 C)

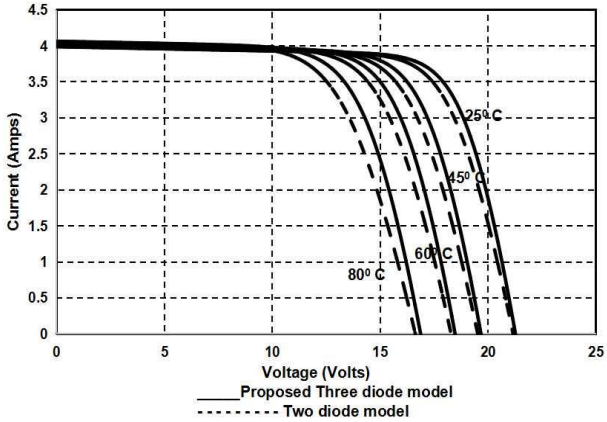

Figure 15: Comparison of Current (A) Vs Voltage (V) Curve of both Proposed Three-diode and Two-diode model for MSX-64 with different temperatures at STC (1000 KW/m^2)

The proposed three-diode model truly requires only five constraints because saturation current $I_{DS1} = I_{DS2} = I_{DS3} = I_{DS}$ whereas $C_1 = 1, C_2 = 2.2,$ C_3 is chosen greater than 2 [2] and the value of p is recommended to be value larger than 2.2 [1].

Figure10 and Figure 11 signifies the power versus voltage curve of two diode and proposed three-diode model for multi or poly-crystalline solar cell at STC. Comparison of Current versus voltage curves of both two diode and proposed three-diode model for KC200GT solar cell at various temperature and irradiance points are illustrated in Figure 12 and Figure 13. Comparison of Current versus voltage curves of both two diode and proposed three-diode model for poly-crystalline MSX-64 at various temperature and irradiance points are illustrated in Figure 14 and Figure 15. From the obtained outcomes we can witness that both models exhibit the same performance at STC. However, proposed three diode model shows the better performance compared to two diode model precisely at lesser irradiance and higher temperature points especially for open circuit voltage.

6. Conclusion

Developing the mathematical model of photovoltaic (PV) cell, to simulate the module and predict their actual performance at varying temperature and irradiance condition, is very significant for evaluation of photovoltaic cell, as well as for dynamic analysis of dc-dc converters and design of maximum power point algorithms. In this work the general method on modeling of photovoltaic cell module using three diode model is presented. The photovoltaic (PV) cell current-voltage equation formulation is analyzed at three main points specifically at open circuit voltage (V_o) short circuit current (I_{SC}) and maximum power point (P_{mpp}) condition. Distinct to the earlier model presented by some researchers this simplified three diode model needs the calculation of five constraints only. This paper has developed the detailed equations for modelling of three-diode PV module and necessary algorithm for evaluating constraints by effective iteration procedure. The accuracy of the developed model is validated by using experimental data provided by manufacturer's datasheet for two different multi or polycrystalline photovoltaic (PV) modules. The proposed three-diode model have better performance regardless to variations in temperature and irradiance. In specific, this model shows the improved performance and accurateness at lower irradiance and higher temperature situations in comparison with two-diode model especially at the point of open circuit voltage condition.

References

1 Vun J. Chin, Zainal Salam, Kashif Ishaque, "Cell modelling and model parameters estimation techniques for photovoltaic simulator application: A review", Applied Energy, vol. 154, pp. 500 – 519, 2015.

2 Vandana Khanna, B.K. Das, Dinesh Bisht, Vandana, P.K. Singh, "A three-diode model for industrial solar cells and estimation of solar cell parameters using PSO algorithm", Renewable Energy vol. 78, pp. 105 – 113. 2015.

3 Mohammad Hejri, Hossein Mokhtari, Mohammad Reza Azizian, Mehrdad Ghandhari, Lennart Soder, "On the parameter extraction of five parameter double-diode model of photovoltaic cell and modules", IEEE journal of photovoltaic cells, Vol. 4, pp. 915-923, May 2014.

4 N. Mohamed Abd A. Shannan, Nor Z. Yahaya, B. Singh, "Single-Diode and Two-Diode model of PV modules: A comparison", IEEE International Conference on Gontrol system, Computing and Emerging 2013, pp. 210 - 214.

5 Priyanka Singh, Nuggehalli M Ravindra, "Analysis of series and shunt resistance in silicon solar cells using single and double exponential models", Emerging Materials Research, vol. 1, pp. 33-38, 2011.

6 M.R. AlRashidi, M.F. AlHajri, K.M. El-Naggar, A.K. Al-Othman, "A new estimation approach for determining the I–V characteristics of solar cells", Solar Energy 85, pp. 1543-1550, 2011.

7 Lo Brano V, Orioli A, Ciulla G, Di Gangi A, "An improved five-parameter model for photovoltaic modules", Solar Energy Materials & Solar cell, pp. 1358 – 1370, 2010.

8 Salam Z, Ishaque K, Taheri H, "An improved two-diode photovoltaic (PV) model for PV system" International conference on power electronics, drives and energy systems (PEDES) Power India, pp. 1–5. 2010.

9 Villalva MG, Gazoli JR, Filho ER, "Comprehensive approach to modeling and simulation of photovoltaic arrays". IEEE Transaction in Power Electronics", pp. 1198–1208, 2009.

10 R. Chenni, M. Makhlouf, T. Kerbache, A. Bouzid, "A Detailed modeling method for photovoltaic cells", Energy vol. 32, pp. 1724–1730. 2007

11 D. Sera, R. Teodorescu, P. Rodriguez, "PV panel model based on datasheet values", Proceedings of the IEEE International Symposium on Industrial Electronics (ISIE), pp. 2392–2396, 2007.

12 Kensuke Nishioka, Nobuhiro Sakitani, Yukiharu Uraoka, Takashi Fuyuki, "Analysis of multicrystalline silicon solar cells by modified 3-diode equivalent circuit model taking leakage current through periphery into consideration", Solar Energy Materials & Solar Cells 91, pp. 1222–1227, 2007.

13 M. C. Alonso-Gracia, J. M. Ruiz, and F. Chenlo, "Experimental study of mismatch and shading effects in I-V characteristics of a PV module", Solar Energy Materials & Solar Cells, vol. 90, pp. 329–340, Feb. 2006.

14 Weidong Xiao, William G. Dunford, Antoine Capel, "A Novel Modeling Method for Photovoltaic Cells", IEEE Power Electronics Specialists Conference, pp. 1950-1956, 2004.

15 Keith Mcintosh, Pietro P. Altermatt, G. Heiser, "Depletion-region recombination in silicon solar cells: when does m_DR = 2?", in Proceeding of the 16th European photovoltaic solar energy conference, vol. 16, pp. 251- 254, 2000.

16 Chih-Tang S, Noyce RN, Shockley W, "Carrier generation and recombination in p–n junctions and p–n junction characteristics", Proceedings of IRE, Vol. 45, pp. 1228–1243, 1957.

17 KC200GT High efficiency polycrystalline module Kyocera Solar cell [Online]. Available: http://www.solarhub.com/product-catalog/pv-modules/352-KC200GT-Kyocera-Solar

18 MSX-64 polycrystalline module Solarex Solar cell datasheet [Online]. Available: https://www.solarelectricsupply.cSom/media/custom/upload/Solarex-MSX64.pdf

Oscillations Damping Enhancement using Load Frequency Control and Improved Power System Stabilizer Considering Wind Power Integration

Nesrine MEKKI[1*], Lotfi KRICHEN[1a]
[1]Department of Electrical Engineering, ENIS, Tunisia
∗Corresponding author, Doctor-Engineer, E-mail: mekki_nesrine@hotmail.fr
[a]Professor, E-mail: lotfi.krichen@enis.tn

Abstract. *The undamped oscillations problem in an interconnected power system has been a matter of concern in several power systems for a long time. In fact, the oscillatory response of power plants under normal and fault conditions is one of the most dominant grid connection requirements to be met by robust control systems. This paper presents a new control scheme coordinating the Load Frequency Control (LFC) process with an Improved Power System Stabilizer (IPSS) loop whose main purpose is the power swings damping enhancement whenever subjected to sudden changes in load levels as well as disturbances. Accordingly, a performant tuned PI controller for LFC and an IPSS tuning method, are thoroughly discussed. Additionally, the impact of integrated wind farms of Doubly-Fed Induction Generator (DFIG) on the studied power system stability is investigated under different operating conditions. The simulation results of a modified 9-Bus IEEE test system are carried out proving the proposal's applicability.*

Keywords: *Load Frequency Control, Optimal Tuning, Improved Power System Stabilizer, PI Controller, Doubly-Fed Induction Generator*

1. INTRODUCTION

Recently, with the rapid increase in energy demand, operation and control of interconnected power systems become one of the challenging issues to ensure sustainable and reliable supply. Practically, unpredictable load deviations even with slight amount may affect the nominal system behavior regarding especially its frequency value and the scheduled power exchanges [1]. Thus, modern energy management systems implicate several multi-level control schemes for each area such as importantly theAutomatic Generation Control (AGC), commonly referred to load-frequency control (LFC), which constitutes almost additional secondary control aiming to eliminate the system deviations [2]. This control has been implemented adding an Area Control Error (ACE), which acts on the Turbine Governor's (TG) load reference settings [3]. It is a function of the real power interchange variations that the AGC mechanism desires to make zero [4] [5]. Literately, for a multi area system, various generation control strategies have been proposed since the 1970s [2] [6]. In fact, in [7], an overview about the AGC issue has been reported, it includes an overview of its schemes, power system models, control techniques, load characteristics, and its coordination with the renewable resources.

Likewise, a review of LFC's control design has been revealed different approaches generally related to Proportional–Integral–Derivative (PID), full state feedback, adaptive and variable structure, intelligent, and networked control schemes. Pandey et al. suggested a thorough survey of LFC issue for distribution and conventional power systems [8]. Rerkpreedapong et al. proposed two robust decentralized control designs [9] using linear matrix inequalities technique and Proportional-Integral (PI) basically tuned by the genetic algorithm. Similarly, Yu et al. presented a linear matrix inequalities based robust controller taking into consideration the communication delays [10]. The fuzzy controller is investigated in [11]. In [12], the sliding mode controller is recommended. Particularly, among all these proposals, PI controllers are frequently adopted in industrial applications in order to reduce the steady-state error to zero [13]. Previous studies have presented a combined LFC-AVR control design for power system stability improvements. In fact, the main concern was to judge only the mutual effects between LFC and AVR loops by coordinating a redesigned PSS [14]. In [15], the artificial bee colony approach has been applied. Other investigations using the metaheuristic bat inspired algorithm have been proposed in order to improve the LFC and AVR control strategies [16].

As a matter of fact, monitoring modern interconnected power systems effectively may necessitate the involvement of auxiliary powerful regulators such as the Power System Stabilizer (PSS) that aims basically to resolve oscillatory stability troubles as well as they are technically ameliorated. Over the last few decades, the great growth in electrical links were hosted new kinds of oscillation between the different areas constituting the power system. In fact, in case of large

immersion, inter-area modes possibly will be as low as 0.2 Hz. Besides, inter-machines oscillations in certain power plant could attain frequencies as high as 4.0 Hz with small machine inertia and high exciter gains [17]. Hence, damping all these oscillating modes efficiently is the major task that a PSS must assign. Literately, PSSs that are out of service or poorly tuned are the major stimulators of several blackouts such as the western U.S. in 1996. Additionally, even these difficulties have been fixed, great disturbances tend to induce 0.2Hz low-frequency oscillations in the network [18]. In point of fact, in Brazil for example, the north-south interconnection has witnessed an increase to a new low-frequency inter-area mode needing a retuning of the existing PSSs [18]. Meanwhile, by retuning and coordinating PSSs efficiently, utilities are able enough to enhance extremely the damping of dominant inter-area modes. The most of the existing PSSs are power acceleration analog devices, but far ahead, modern manufacturers offer a digital PSS, denoted as PSS2B, which can be tuned simply as a speed-based PSS [19]. Later, a novel PSS design was suggested in [20] and incorporated in the revised IEEE standards as PSS4B. As well, it builds on a simple multiband transfer function while offering robust PSS tuning over a wide range of frequency. A thorough evaluation of these two types of PSSs was extensively explained in [18]. Likewise, recent researches focused on comparing different types of PSS taking into account its ability in judging local-mode and inter-area damping performances especially while facing the possible adverse factors.

The growing amount in electricity consumption stimulates the need to investigate the renewable energy resources. Chiefly, wind energy has witnessed a great revolution in several countries which try to carry out detailed analysis of its impact on their grid stability [21]. In fact, these studies deal mainly with different challenging aspects such as the fluctuating nature of wind power, its location, the generator technologies and its control strategy. The literature review has been presented various wind turbine generator technologies and has been focused basically on analyzing its influence and applicability in the power system under both disturbances and normal conditions. Generally, three types of wind turbine are widely used in industry namely, squirrel cage induction generator, direct drive synchronous generator, and especially Doubly Fed Induction Generator (DFIG) which becomes increasingly popular among the wind power conversion systems. Several comparative studies have been revealed the differences between these concepts regarding the generating system and the rotor aerodynamic efficiency especially during high wind speeds [22].

The contribution of this paper is to investigate a new combination between an optimal LFC design and an Improved Power System Stabilizer (IPSS) in order to damp effectively power system oscillations and enhance the dynamic performances. The performed LFC design is basically equipped with a PI controller whose parameters are optimally tuned using a nonsmooth H_∞ optimization technique. Later, in order to reinforce the operational grid capabilities while damping its fluctuations, a modified Multi Band-Power System Stabilizer (MB-PSS) is added and favorably tuned in the control process using the symmetrical approach which helps to meet the increasing load demand requirements. The whole system then will be subjected to a disturbance to validate the role of the coordinated AGC-IPSS design in restoring the system balance. The rest of paper carries out the performance validation of the suggested controllers in a modified IEEE 9-bus test system including DFIG wind turbines under different operating conditions.

2. Proposed Control Strategy

The research under investigation concerning power system control suggested a coordinated AGC-IPSS design as a challenging issue helping in monitoring the upcoming advances while keeping reasonably uniform system frequency.

2.1. PI-Based LFC Design

The change in frequency occurs whenever the load changes randomly. The error signal is amplified, mixed and transmuted into real power command signal which is dispatched then to the TG rising the torque value. The governor operates to restore the balance between the input and output by changing the turbine output while respecting the specified tolerance [23].

Evidently, an auxiliary control action of a PI controller is chosen to be included in the present work as depicted in Fig. 1 in order to ensure a robust AGC loop design that keeps the power plant frequency under its nominal value. Fig. 2 displays the models of hydraulic turbine and governor associated with the synchronous machine block. Initially, the power system operates without wind power integration which will be the main purpose of the next section. All the system parameters are given in the Appendix.

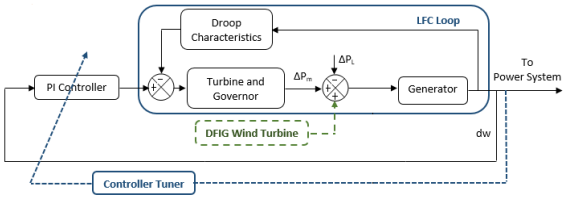

Fig. 1. Block diagram of AGC design in a single area power plant with DFIG

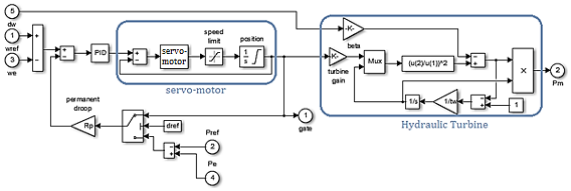

Fig. 2. Block diagram of hydraulic turbine and governor

dw Speed deviation (Hz)

ΔP_m Change in mechanical power (pu)

ΔP_L Load disturbance (pu)

Compared to multiple candidate control techniques such as PID, intelligent control (hybrid neuro fuzzy and fuzzy logic controllers..), variable structure, full state feedback (linear quadratic regulator) and other advanced strategies, PI controllers still widely used in industries thanks to their simplicity. Yet, in order to assure high dynamic system performances, tuning a PI regulator parameters becomes critical especially to meet the system non-linearity and its high complexity requirements [24]. Almost, as the dynamics of the investigated power system are typically nonlinear, special attentions are considered for designing the PI controller as follows [25][26]:

Each area contributes to the frequency control and regulates its own load variations. Transient behavior should be reached optimally.

In steady state, frequency and tie-line power exchanges are, respectively, returned to their nominal values (ACE = 0).

The controller would be robust to meet the system parameters variation.

As manual procedures are time-consuming, searching for new PI tuning software may help to meet the aims of tuning automatically the controller parameters while keeping a reasonable tradeoff between performance and robustness and offering simultaneously the desirable maximum overshoot, the phase and gain margins and the bandwidth of the closed-loop system. Therefore, the controller parameters are optimally selected through a PID tuner which provides a fast applicable single-loop tuning method with transfer function based-settings. PI parameters can be easily tuned while reaching a robust design with the desired response time. First, the software computes a linearized plant model perceived by the controller, identifies its input and output automatically, and uses the actual operating point for the linearization.

The tuning approach deals mainly with the non-smooth H_∞ minimization technique. It solves the following constrained problem:

$$\text{Minimize} \quad \max_i f_i(x) \tag{1}$$

- $f_i(x)$ and $g_j(x)$ are the normalized values of soft and hard tuning requirements [24].

Subject to (2)

$$\max_j g_j(x) < 1, \text{ for } \quad x_{min} < x < x_{max}$$

- x is the vector of PI parameters to tune.
- xmin and xmax are the minimum and maximum values of the free parameters of the controller.

In point of view of the tuning goals [27], the software approaches the optimization problem by resolving a sequence of unconstrained subproblems given by:

$$\min_x \max(\alpha f(x), g(x)) \tag{3}$$

The multiplier '**α**' is adjusted so that the solution converges to the solution of the original constrained optimization problem. Afterward, the tuning process will give new values of PI parameters that best solve the minimization problem. The block performances are verified finally in the test system.

Additionally, in order to identify the optimal tuning method, a comparison study of using different optimization techniques may be significantly important. Thus, three criterions such as the Integral of the Square of the Error (ISE), Integral of the Absolute value of Error (IAE) and Integral of Time-weighted Absolute Error (ITAE) are calculated for each algorithm to evaluate the controller response. Meanwhile, the main objective here is to obtain the minimum values of these performance indices which are defined as follows:

$$ISE = \int_0^\infty ACE^2 dt$$

$$IAE = \int_0^\infty |ACE| dt$$

$$ITAE = \int_0^\infty |ACE| t \, dt$$

Literately, the ITAE minimization is mostly referred as a good tuning criterion to get PI parameters and useful index which penalizes long-duration transients. The system response could have then a settling time much more quickly using the ITAE than using the ISE which penalizes in general large errors more than smaller ones. Likewise, to eliminate small errors, IAE index is accordingly taken into account as it affords slower

response than ISE with less sustained fluctuations [28]. Hence, a great attention will be given importantly to the IAE and ITAE indices which help later to compare different tuning methods.

2.2. Investigated IPSS Design

Referring to several comparative studies, The IPSS model on which investigations in this paper are carried out is mainly based on the MB-PSS model (IEEE PSS4B) which presents competitive features in comparison with other controllers. Actually, it keeps greatly most of the PSS2B properties in local and torsional modes using an electrical power transducer that tracks high-frequency dynamics as well as affording an improved lower-frequency inter-area modes. Fig. 3 depicts the additional control loop of the performed IPSS which is installed in the excitation system whose block diagram is presented in Fig. 4.

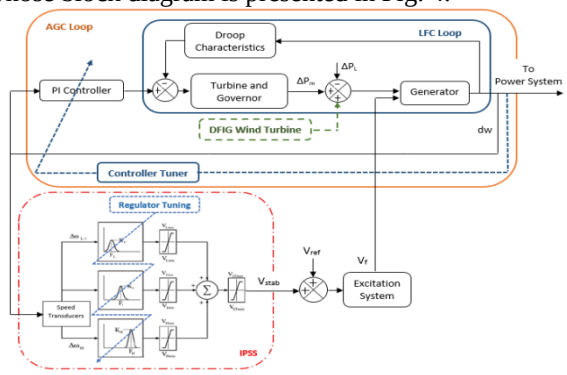

Fig. 3. Block diagram of the coordinated LFC-IPSS design in a single area power plant

V_{ref} Reference voltage (pu)
V_f Field voltage (pu)
F_L Center frequency of low frequency band
K_L Peak gain of the low frequency band
F_I Center frequency of the intermediate frequency band
K_I Peak gain of the intermediate frequency band
F_H Center frequency of the high frequency band
K_H Peak gain of the high frequency band
V_{Smax} Limits imposed on the output of the stabilizer.
V_{stab} Stabilization voltage (pu)

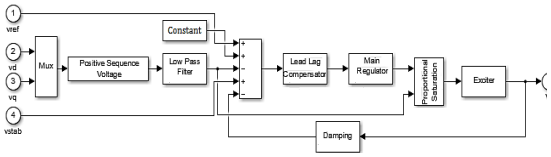

Fig. 4. Block diagram of the excitation system associated to the generator

The MB-PSS block diagram constituting the IPSS block comprises principally three functions, namely the transducers, the lead-lag compensation and the limiters. In fact, two speed deviation transducers are implemented in the structure to feed three bands defining the lead-lag compensation. In addition to that, four adaptable limiters are offered for each band and the whole PSS output.

In fact, the low band concerns very slow oscillating phenomena like common modes possibly created on isolated systems with frequency range typically under 0.2 Hz. The intermediate band deals with inter-area modes often found in the range of 0.2 to 1.0 Hz while the high band concerns local modes, either plant or inter-machines, with a frequency range of 0.8 to 4.0 Hz. Besides, the speed deviation transducers are linked with the machine terminal currents and voltages. The first one measures accurately in the 0 to 2.0 Hz range, while the second one is intended for the high band with a range of frequency of 0.8 to 5.0 Hz. Importantly, the lead-lag compensation circuit is globally identified with six parameters which are the three filter central frequencies $\mathbf{F_L}$,$\mathbf{F_I}$, $\mathbf{F_H}$ and the gains $\mathbf{K_L}$, $\mathbf{K_I}$, $\mathbf{K_H}$. They are primarily required for efficient IPSS tuning. Time constants and branch gains for the low band case satisfy the following equations [29]:

$$T_{Li}=\frac{1}{2\pi F_L\sqrt{R}} \quad \text{for} \quad i=2,7 \tag{7}$$

$$T_{L1}=\frac{T_{L2}}{R} \tag{8}$$

$$T_{L8}=T_{L7}.\ R \tag{9}$$

$$K_{Li}=\frac{R^2+R}{R^2-2R+1} \quad \text{for} \quad i=1,2 \tag{10}$$

Table 1 proposes four candidate settings for the PSS4B [29]. They were elected from recent researches closely reflecting the greatest practices in the tuning process.

The strategy of the current study deals mainly with the symmetrical approach which is based on varying the center frequency and gain of each band so as to accomplish a nearly flat phase response at the frequency of interest which is globally between 0.1 Hz and 5Hz.

Table 1. Proposed Settings for PSS4B

Settings	1	2	3	4	5
R=1.2, $V_{smax} = -V_{smin} = 0.1$					
$V_{Imax} = -V_{Imin} = V_{Hmax} = -V_{Hmin} = 0.6$					
V_{Lmin}	-0.04	-0.04	-0.04	-0.02	-0.02
V_{Lmax}	+0.08	+0.08	+0.08	+0.02	+0.02
K_L	20.5	13.7	13.7	6	6
F_L	0.116	0.116	0.116	0.08	0.19
K_I	41	27.3	31	27	30
F_I	0.506	0.506	0.506	0.8	1.1
K_H	85	75	68	159	150
F_H	12.1	12.1	12.1	12.1	12

Setting 1 is the base core from which further sets are derived. Even it reaches relatively a uniform phase advance, this kind of PSS can support high gain whenever needed. The second setting helps in decreasing low-, intermediate-, and high-frequency gains. Setting 3, approximately same as setting 2, adds a washout in the high-frequency band in order to reduce the sensitivity to fast mechanical power ramps. Besides, setting 4 is the simple tuning one. It is based on three symmetrical bands related mainly to six parameters and designated to mimic setting 2 over a wide range of frequency.

Accordingly, based on the selected set, the IPSS parameters are tuned and mentioned as 'Setting 5' which diminishes fruitfully the regulator complexity without losing out so much on performance. In fact, this setting reveals the greatest oscillations damping as depicted in Fig. 5 which presents the frequency response of 'Gen 2' for different MB-PSS settings. As well, comparison between simulations shows the difference in frequency between all the settings as displayed in Fig. 6.

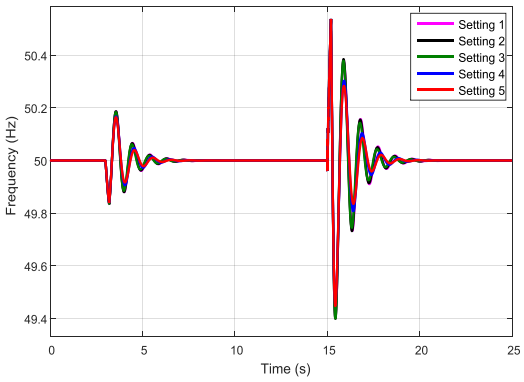

Fig. 5. Frequency response of 'Gen 2' for different settings under fault conditions

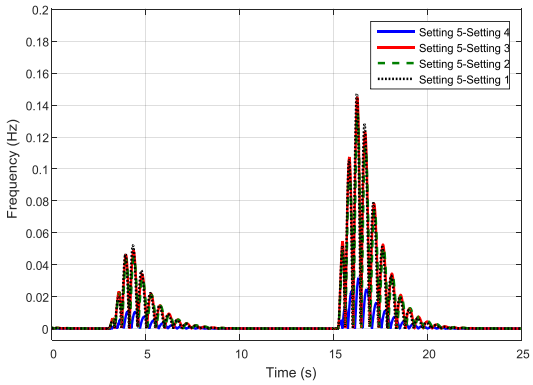

Fig. 6. Difference in frequency between the proposed settings

3. DFIG Wind Turbines Integration

The simulation study of the investigated test system including DFIG wind turbines as shown in Fig. 1 aims essentially to highlight the impact of renewable energy whenever integrated on the power system under normal conditions as well as under disturbance. Meanwhile, treating the dynamic performances of this kind of turbines becomes a challenging issue that may affect the system stability. Reciprocally, this technology is able enough to support the grid with the appropriate reactive power and stable frequency and voltage, as well as helping in damping the power oscillations [30-32].

The impact of wind power generation on the dynamic behavior of network is a key factor in considering a robust LFC design which may improve the system frequency response whenever exposed to slow changes of load and renewable resource especially in case of a disturbance event as it attracts more reactive power which may lead to withering voltage drop.

Commonly, conventional power plants are rather effective at adjusting the power output to meet the load balance. Still, due to wind power intermittency, it is more difficult for wind turbines to track the load demand variation. Therefore, simulation purposes address mainly the robustness of the optimized LFC loop in coordination with the performed IPSS while restraining the frequency deviation efficiently and showing faster response and stability.

4. Simulation and Results

The IEEE 9-bus system illustrated in Fig. 7 is adopted in this study. This test case represents a simple approximation of the western system coordinating council to an equivalent system with 9 buses, 3 generators, 3 two-winding power transformers, 6 lines and 3 loads. The line

complex powers are around hundreds of MVA each and the voltage levels are 13.8 kV, 16.5 kV, 18 kV, and 230 kV. 'Gen 1' designs the swing generator. The standard test system witnessed a modification regarding the generators 'Gen 2' and 'Gen 3' which are replaced by new power plants involving similarly the LFC and IPSS equipments as well as integrating DFIG wind turbines in an advanced step. The proposed control scheme is incorporated into the HTG and excitation system blocks as shown in Fig. 8.

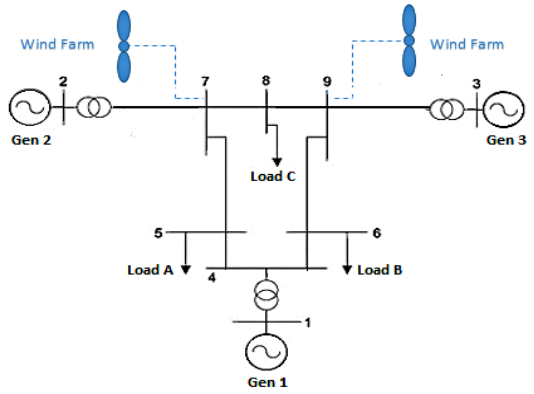

Fig. 7. 9-Bus IEEE test system

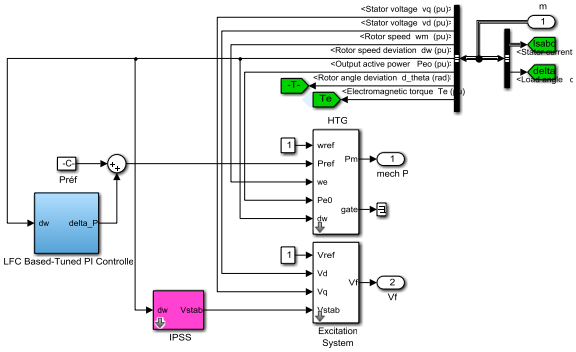

Fig. 8. Simulink model of the Hydraulic Turbin e and Governor (HTG) and Excitation System blocks associated to Generator 'Gen 2'

4.1. LFC Based-Tuned PI Controller Impact

The major interest is to evaluate first the designed LFC performances in an interconnected power system basically related to the loading conditions.

According to Fig. 9 which depict the frequency response delivered by 'Gen 2', it's clear that after its integration, the swings constituting the signal decrease in number and amplitude to get finally a frequency recovered close to the nominal frequency which is around 50 Hz. Particularly, the sudden increase in load demand at 3 s causes thorough frequency perturbations which are attenuated gradually. Meanwhile, AGC application may help significantly in maintaining the frequency at the scheduled values.

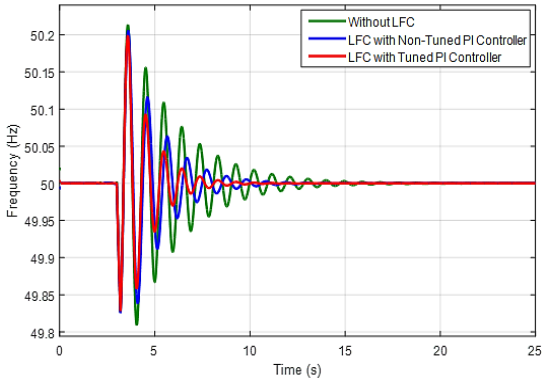

Fig. 9. Frequency Response of Generator 'Gen 2'

In fact, choosing randomly the controller parameters may not ensure the best performances regarding the frequency's stability. Yet, the application of the tuning process reveals better frequency response nearly close to the nominal system frequency. Actually, during overloading condition, the frequency deviations persist for a long period, thus, with the optimized LFC loop, the governor system will be able to absorb effectively the frequency fluctuations. Simulation results prove definitely that LFC based-tuned PI controller application can damp efficiently the frequency oscillations in reaction to the changing demand. Beforehand, In order to justify the efficiency of the proposed method, several approaches are implemented and applied for optimal tuning of PI parameters. In fact, based on the comparative analysis shown in Table 2, the non-smooth optimization technique is chosen to be adopted in this study as it demonstrates its excellence in giving better results by affording the least values of IAE and ITAE indices and meeting the desired requirements.

Table 2. Comparison of Performance Indices fo r PI controller

Tuning Approach / Performance Indices	Genetic Algorithm	Simplex Search	Sequential Quadratic Programming	Active Set	Nonsmooth H_∞
ISE	$7.26\ 10^{-5}$	$7.22\ 10^{-5}$	$7.32\ 10^{-5}$	$7.29\ 10^{-5}$	$7.29\ 10^{-5}$
IAE	0.015	0.016	0.016	0.015	0.015
ITAE	0.24	0.24	0.24	0.24	0.23

Eventually, as the system voltage and frequency responses are strongly sensitive even to slight changes in load, results will take into account the effect of the designed LFC connection particularly on the load buses. Therefore, analysis will basically

focus on the nearest variable load located at bus 8. Its voltage magnitude profile is shown in Fig. 10.

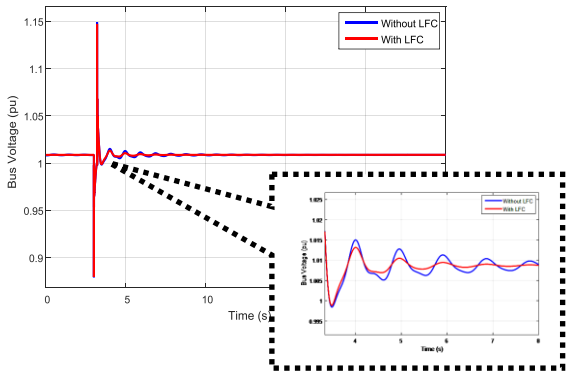

Fig. 10. Voltage Profile of Bus 8

Evidently, it is clearly shown that the load variation would cause remarkable perturbations which are later damped out significantly after integrating the performed LFC process into the system.

4.2. Involvement of IPSS Control

In addition to the performed LFC equipment, the designed IPSS is now installed for each generator. Its parameters are tuned and defined in 'setting 5' as mentioned previously in Table 1. The IPSS frequency response is definitely plotted in Fig. 11.

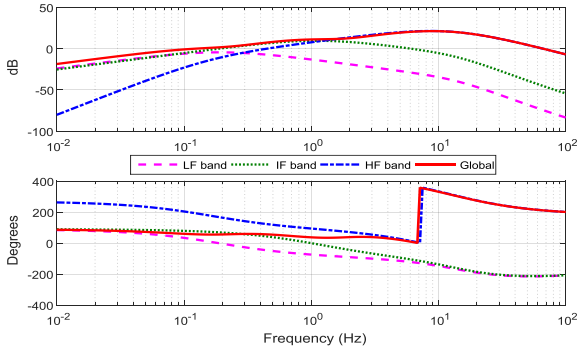

Fig. 11. IPSS Frequency Response

Evidently, the IPSS gains seem to be more aggressive and consequently more effective especially in the critical inter-area frequency range from 0.1 to 1 Hz. Furthermore, its frequency response confirms definitely that the IPSS phase is nearly flat around 80 degrees in the frequency range of interest. In fact, to guarantee robust damping, this PSS ought to imply, at all frequencies of interest, a moderate phase advance in order to compensate the lag created between the field excitation and the electrical torque.

For reasons of simplicity, this study chooses as example of concern the generator number 2 'Gen 2'. IPSS will definitely control the excitation system in order to reduce the power swings rapidly as shown in Fig. 12 which depicts the frequency response of 'Gen 2' in reaction to the load variation.

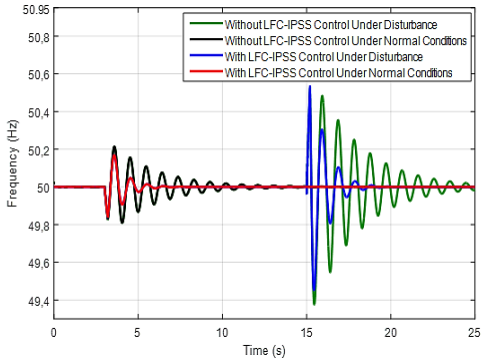

Fig. 12. Frequency Response of Generator

Likewise, grid security may involve also the analysis of each contingency of any disturbance occurring in the power system. Thus, a three-phase fault is investigated in this work. In fact, several studies gave great concern to this type of disturbance as the most severe one for transient stability problems. First, the fault occurs temporary on the load bus (bus 8) at time t = 15 s, and it is cleared at time t = 15.2 s.

The frequency oscillations are remarkably reduced and kept limited after the application of the designed control system coordinating the optimized LFC with the IPSS. It reveals great damping of swings compared to the case where the performed controllers are not installed.

Actually, the performed IPSS provides an additional signal aiming essentially to dampen the generator torque oscillations. This control signal affords positive damping effect, while keeping the voltage level under its limit of stability. Fig. 13 reveals the voltage magnitude profile at bus 8 where the variable load is set.

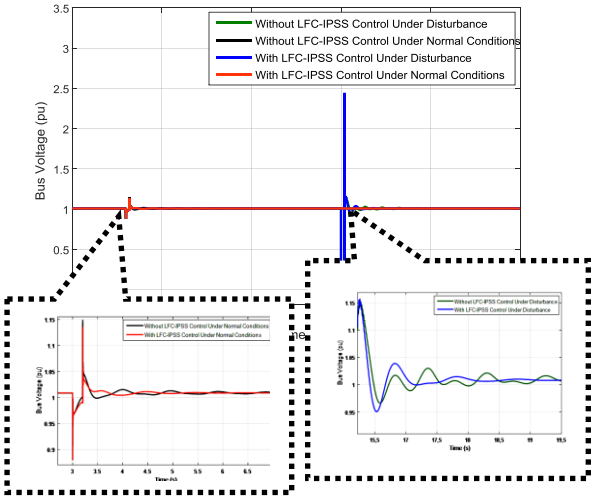

Fig. 13. Voltage Profile of Bus 8

Likewise, Fig. 13. (a) displays clearly a detailed zoom of the voltage oscillations of that bus at the moment of load demand rise at 5 under normal conditions. In fact, adding the IPSS to the current system delivers fast response with less number of swings and decreased amplitudes. Subsequently, Fig. 13. (b) shows great result only after installing the coordinated LFC-IPSS loops in the power system when subjected to a fault. It helps absolutely in keeping the voltage of the disturbed bus almost stable around the nominal value.

Furthermore, one other important variable that should be considered in the control process as to generator stability is basically related to its load angle. In fact, it demonstrates how close the machine is to the static stability limit. It increases proportionally with the active load: as well as the angle is amply large, the generator is close enough to the stability limit while keeping its synchronism.

Fig. 14 shows the load angle evolution of 'Gen 2'. It's remarkable that the load angle is retained between 20° to 30°. Consequently, it provides a great margin of stability whenever the power demand rises. The generator will be then able to outfit the load by increasing its load angle up to 90° maximally.

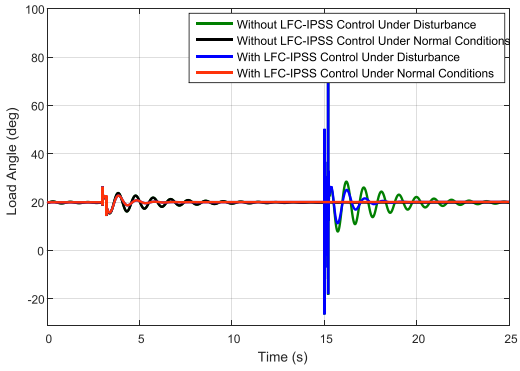

Fig. 14. Load Angle of Generator 'Gen 2'

Equally, the control process involves several operating parameters such as the electromagnetic torque and the rotor angle deviation especially to evaluate the dynamic system stability. The simulation results shown in Fig. 15 and Fig. 16 confirm the crucial role that the IPSS plays in damping the undesirable fluctuations in number and amplitude in order to enhance the system response to any sudden load variation. All the previous simulations prove that ensuring power system stability may require certainly powerful control tools including LFC and IPSS equipments.

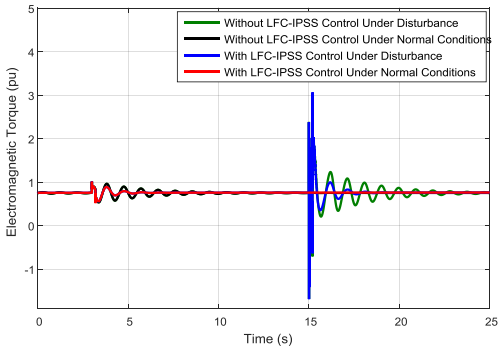

Fig. 15. Electromagnetic Torque of Generator 'Gen 2'

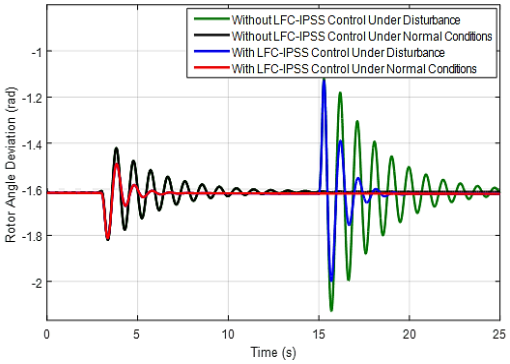

Fig. 16. Rotor Angle Deviation of Generator ' Gen 2'

4.3. Evaluation of Wind Power Penetration

To analyze the impact of wind power generation on the dynamic behavior of the power system, different wind power penetration levels at 10 to 30 % are examined. In fact, two wind farms are installed in bus 9 and bus 7 just near to the designed power plants (Gen 3 and Gen 2, respectively). Each wind farm is connected locally to a 25 kV distribution system and consisted of DFIG wind turbines, rated 9 MW each. The system response is investigated first under normal conditions. Subsequently, in order to test the efficiency of the proposed controller in solving the system stability problem in presence of DFIG wind turbines, a three phase fault is created at theload bus (bus 8) at t=15 s and cleared at t =15.2 s. The frequency responses of generator 'Gen 2' for 10% and 20% of wind power penetration are presented in Fig. 17 and Fig. 18,

respectively.

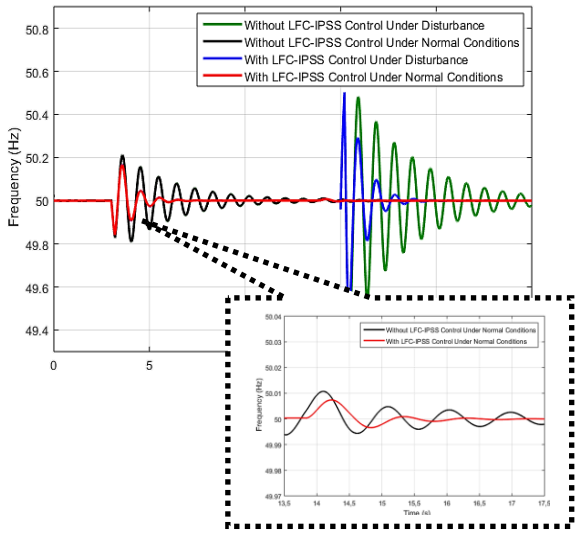

Fig. 17. Frequency Response of Generator 'Gen 2' with 10% wind penetration scenario

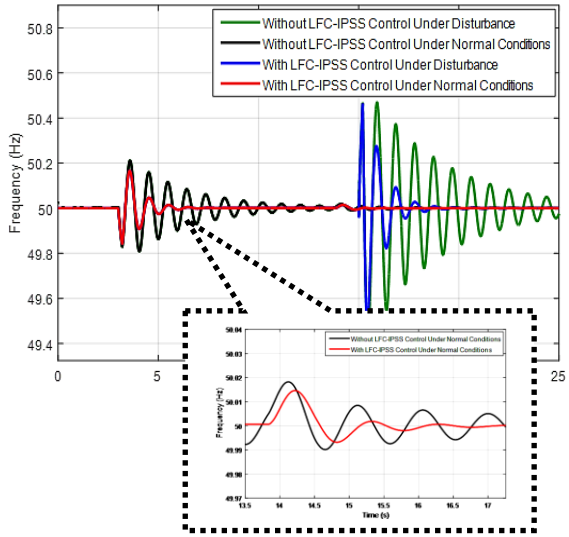

Fig. 18. Frequency Response of Generator 'Gen 2' with 20% wind penetration scenario

Obviously, the results are relatively similar. It is noticeable that on implementing coordinated LFC-IPSS process, when compared with the initial situation, the frequency of the machine under test achieves great response in terms of power oscillations especially when the wind farms generate the maximum of their power at 14 s as shown in detail in the zoomed in plot of the frequency responses of generator 'Gen 2'. The generator frequency oscillations demonstrate enhanced response too before, during and after the fault only in case where both of the performed LFC and IPSS regulators are involved in the grid's control system. Yet, when wind penetration increases beyond 30%, the frequency stability is significantly degraded as shown in Fig. 19. The generator unit equipped with the proposed control scheme is unable to maintain ideally desirable frequency deviations. Thus, in order to keep stable operation of generators, the simulation study will be conducted mainly for 20% wind penetration into the test system. The installed DFIG wind turbines export in total 72 MW.

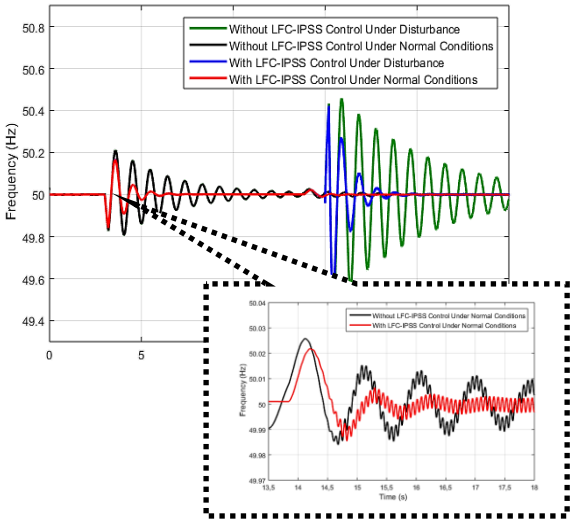

Fig. 19. Frequency Response of Generator 'Gen 2' with 30% wind penetration scenario

Practically, the generator torque evolution is one of the most challenging issues that should be controlled for system stability improvement purposes. In fact, it is clearly shown that injecting an intermittent power with rate of 72 MW to the power system is able enough to disturb the system waveforms. The more electrical power is generated, the more small fluctuations occur. Fig. 20 and Fig. 21 depict the electromagnetic torque and the load angle of generator 'Gen 2', respectively, before and after adding the proposed control scheme to the test system. It demonstrates considerable effect of these regulators in regaining approximately the nominal value reached in the initial case as well as maintaining the equilibrium of the system and damping the power oscillations. Additionally, applying a disturbance to the system may definitely result in change in frequency, load angle, machine's torque or voltage.., forcing the system to trip. Thus, only the wind turbine will operate until the fault is cleared. Therefore, the proposed controllers try to increase damping the maximum of the generated swings and regulate the waveforms at their set points.

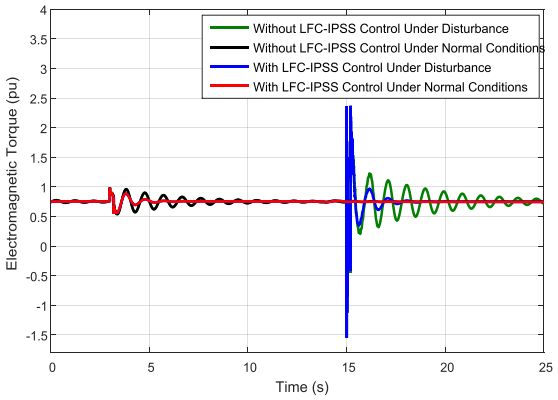

Fig. 20. Electromagnetic Torque of Generator ' Gen 2'

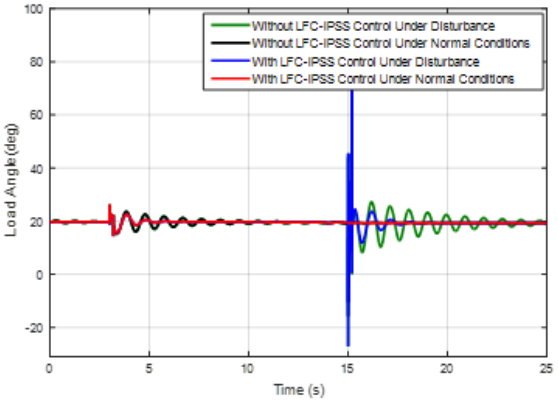

Fig. 21. Load Angle of Generator 'Gen 2'

The investigated wind farm is able enough to support the power system voltage during fault condition. In fact, DFIG wind turbines generate increasingly sufficient reactive power during the disturbance and decreases to its value after the fault clearance. Hence, in addition to DFIG support, coordinated LFC-IPSS process is also considered as shown in Fig. 22 which represents the voltage profile of the load bus under different operating conditions. Fig. 22. (a) proves that wind power incorporation may cause important voltage dip whenever involved with irrational rates. As well, Fig. 22. (b) which is a zoomed in plot of the bus voltage at the moment of fault reveals an improved oscillatory evolution roughly stable around the nominal value.

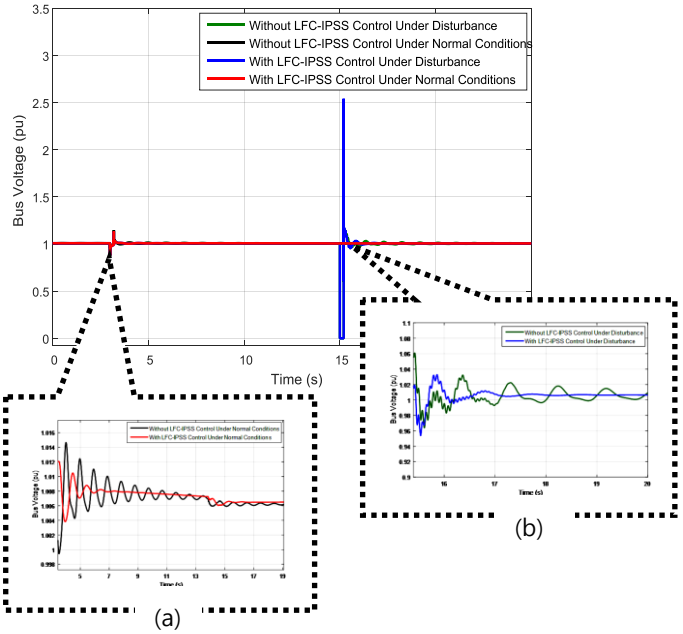

Fig. 22. Voltage Profile of Bus 8

5. Conclusion

The main contribution of this paper deals with designing and implementing a LFC based tuned-PI controller in coordination with an IPSS regulator under different operating conditions. This control scheme design is applied to the investigated model of the studied power system which shows effective response while enhancing its stability. In fact, robustness is critical in these control loops design since the loading conditions are unpredictably changing. An attempt is made first to PI controller which helps practically whenever tuned optimally in enhancing the dynamic performance of LFC in such interconnected power system. Actually, the use of H_∞ methodology for the tuning goal helps considerably in synthesizing PI controller in the frequency-domain. Typically, the controller design requirements such as speed of response, control bandwidth, disturbance rejection, and robust stability can be reached. However, in terms of speed of execution, it takes a significant amount of computer time. The comparison of different techniques proves that the H_∞ methodology provides the minimum values of the performance indices (ISE, IAE, and ITAE). Additionally, a great attention is given to system stability which is improved while integrating the designed IPSS loop. The tuning process is also investigated in the present work. In fact, the proposed IPSS settings show superior performances to the other settings in providing efficient damping of power system oscillations. Furthermore, the current study shows appreciable enhancements in the system response

in presence of the suggested control structure after being affected by DFIG wind turbines installation. The simulation results prove that optimized LFC and IPSS regulator is very effective and guarantees good dynamic performance under normal and fault conditions.

Nomenclature

LFC	Load Frequency Control
IPSS	Improved Power System Stabilizer
DFIG	Doubly Fed Induction Generator
ACE	Area Control Error
AGC	Automatic Generation Control
TG	Turbine Governor
PI	Proportional-Integral
PID	Proportional-Integral-Derivative
PSS	Power System Stabilizer
MB-PSS	Multi Band-Power System Stabilizer
ISE	Integral of the Square of the Error
IAE	Integral of the Absolute value of Error
ITAE	Integral of Time-weighted Absolute Error

Appendix

System parameters [33]

Table 3. Synchronous generator parameters

Parameters	Value
Nominal power	192 MVA
line-to-line voltage	13.8 KV
Nominal frequency	50 Hz
d-axis synchronous reactance, x_d	1.305 pu
d-axis transient reactance, X_d'	0.296 pu
d-axis sub-transient reactance, X_d''	0.252 pu
q-axis synchronous reactance, Xq	0.474 pu
q-axis sub-transient reactance, X_q''	0.243 pu
Leakage reactance, X_l	0.18 pu
d-axis transient short circuit time constant, T_d'	1.01 s
d-axis sub-transient short circuit time constant, T_d''	0.053 s
q-axis sub-transient open circuit time constant, T_{qo}''	0.1 s
Stator resistance, R_s	0.00285 pu
Inertia coefficient, H	3.7 pu

Table 4. Hydraulic turbine and governor parameters

Parameters	Value
Servo gain, K_a	3.3
Servo time constant, T_a	0.07 s
Permanent droop, R_p	0.05
Water starting time, T_w	2.67 s
Filter time constant, T_d	0.01
Proportional gain, K_p	1.163
Integral gain, K_i	0.105
Derivative gain, K_d	0

Table 5. Excitation system parameters

Parameters	Value
Low-pass filter time constant, T_r	0.02 s
voltage regulator gain, K_a	300
voltage regulator time constant, T_a	0.001
Exciter gain, K_e	s
Exciter time constant, T_e	1
Damping filter gain, K_f	0
Damping filter time constant, T_f	0.001
Transient gain reduction lag time constant, T_b	0.1 s
Transient gain reduction lead time constant, T_c	0
	0

Table 6. DFIG parameters

Parameters	Value
Nominal power	9 MW
Rated voltage	575 V
Pair of poles	3
Rated frequency	50 Hz
Stator resistance, Rs	0.00706 pu
Rotor resistance, R_r'	0.005 pu
Stator leakage inductance, L_{ls}	0.171 pu
Rotor leakage inductance, L_{lr}'	0.156 pu
Mutual inductance, Lm	2.9 pu
Inertia constant, H	5.04 s
Friction factor, F	0.01 pu

References

[1] K. Máslo, M. Kolcun, "Load–frequency control management in island operation", Electric Power Systems Research, vol. 114, pp 10-20, September 2014.

[2] J. Biswas, P. Bera, "Design of Rule-Based Load Frequency Controller for Multi-machine System", Industry Interactive Innovations in Science, Engineering and Technology, pp 47-57, , July 2017

[3] H. Shayeghi, H.A. Shayanfar, and A. Jalili, "Load frequency control strategies: a state-of-the art survey for the researcher", Energy Conversion and Management, vol. 50, no. 2, pp 344–353, February 2009.

[4] D. Apostolopoulou, P.W. Sauer, and A.D. Dominguez-Garcia, "Automatic Generation Control and its Implementation in Real Time", 47th Hawaii International Conference on System Science, January 2014.

[5] M. Scherer, E. Iggland, A. Ritter, and G. Andersson, "Improved frequency bias factor sizing for non-interactive control", International Council on Large Electric Systems, pp C2-113, August 2012.

[6] H. Bevrani, T. Hiyama, "Intelligent Automatic Generation Control", pp 11-35, March 2017.

[7] H. Bevrani, "Robust Power System Frequency Control", pp 8-30, Springer, April 2014.

[8] X. Liu, X. Kong, K.Y. Lee, "Distributed model predictive control for load frequency control with dynamic fuzzy valve position modelling for hydro–thermal power system", IET Control Theory Applications., vol. 10, no. 14, pp. 1653-1664, September 2016.

[9] I. Nasiruddin, T.S. Bhatti and N. Hakimuddin, "Automatic Generation Control in an Interconnected Power System Incorporating Diverse Source Power Plants Using Bacteria Foraging Optimization Technique",

Electric Power Components and Systems, vol. 43, no 2, pp 189-199, December 2014.
[10] K. Tang, G.K.Venayagamoorthy, "Adaptive inter-area oscillation damping controller for multi-machine power systems", Electric Power Systems Research, vol. 134, pp 105-113, May 2016.
[11] S.K. Jain, A. Bhargava and R.K. Pal, "Three area power system load frequency control using fuzzy logic controller", International Conference on Computer, Communication and Control, pp 1-6, September 2015.
[12] K. Vrdoljak, N. Peric, and I. Petrovic, "Sliding mode based load frequency control in power systems", Electric Power Systems Research, vol.80, no. 5, pp. 514–527, May 2010.
[13] S.S. Dhillon, J.S. Lather, S. Marwaha, "Multi Area Load Frequency Control Using Particle Swarm Optimization and Fuzzy Rules", Procedia Computer Science, vol. 57, pp 460 – 472, August 2015.
[14] E. Rakhshani, J. Sadeh, "Application of Power System Stabilizer in a combined model of LFC and AVR loops to enhance system stability", International Conference on Power System Technology, October 2010.
[15] O. Abedinia, H. Shayanfar, B. Wyns, A. Ghasemi, "Design of Robust PSS to improve stability of composed LFC and AVR using ABC in deregulated environment", Proceedings of the international conference on artificial intelligence, July 2011.
[16] NY. Kouba, M. Menaa, M. Hasni, M. Boudour, "A novel robust automatic generation control in interconnected multi-area power system based on bat inspired algorithm", International Conference on Control, Engineering & Information Technology, May 2015.
[17] I. Kamwa, R. Grondin, and G. Trudel, "IEEE PSS2B Versus PSS4B: The Limits of Performance of Modern Power System Stabilizers", IEEE Transactions on Power Systems, vol. 20, no. 2, pp 903 – 915, May 2005.
[18] G. Chen, Y. Sun, L. Cheng, J. Lina, W. Zhao, Ch. Lin, "A novel PSS-online re-tuning method", Electric Power Systems Research, vol. 91, pp 87-94, October 2012.
[19] Z. A. Obaid, L.M. Cipcigan, and M.T. Muhssin, "Power system oscillations and control: Classifications and PSSs' design methods: A review", Renewable and Sustainable Energy Reviews, vol. 79, pp 839-849, November 2017.
[20] S. M. Said, M.M. Aly and M. Abdel-Akher, "Capacity and Location Effects of Wind Turbine Energy Systems on Power Systems Stability", International Journal on Power Engineering and Energy, vol. 4, no. 1, January 2013.
[21] M. Zamanifar, B. Fani, M.E.H. Golshan, H.R. Karshenas, "Dynamic modeling and optimal control of DFIG wind energy systems using DFT and NSGA-II", Electric Power Systems Research, vol. 108, pp 50-58, March 2014.
[22] O. Barambones, J.A. Cortajarena, P. Alkorta and J.M. Gonzalez de Durana, "A real-time sliding mode control for a wind energy system based on a Doubly Fed Induction Generator", Energies, vol. 7, no. 10, pp 6412-6433, October 2014.
[23] L. L. Grigsby, "Power System Stability and Control", 3d Edition, Part 2, 8-1, April 2012.
[24] M.I. Alomoush, "Load frequency control and automatic generation control using fractional-order controllers", Electrical Engineering, vol. 91, no. 10, pp 357–368, March 2010.
[25] Ch. Huang, K. Zhang, X. Dai and Q. Zang, "Robust Load Frequency Controller Design Based on a New Strict Model", Electric Power Components and Systems, vol. 41, no. 11, pp 1075-1099, July 2013.
[26] P.S.R. Murty, "Power system analysis", 2nd Edition, Chapter 13, June 2017.
[27] P.Apkarian, P. Gahinet, and C. Buhr, "Multi-model, multi-objective tuning of fixed-structure controllers", European Control Conference, pp 856–861, July 2014.
[28] M.H. Marzaki, M. Tajjudin, M.H.F. Rahiman, R. Adnan, "Performance of FOPI with Error filter Based on Controllers Performance Criterion (ISE, IAE and ITAE)", 10th Asian Control Conference, June 2015.
[29] J.M. Ramirez, R.E. Correa, and D.C. Hernández, "A strategy to simultaneously tune power system stabilizers", International Journal of Electrical Power & Energy Systems, vol. 43, no. 1, pp 818-829, December 2012.
[30] W. Yi, X. Lie, "Coordinated control of DFIG and FSIG-based wind farms under unbalanced grid conditions", IEEE Transactions on Power Delivery, vol. 25, no. 1, pp 367–377, January 2010.
[31] J. Yao, H. Li, Z. Chen, X. Xia, X. Chen, Q. Li, Y. Liao, "Enhanced Control of a DFIG Based Wind-Power Generation System With Series Grid-Side Converter Under Unbalanced Grid Voltage Conditions", IEEE Transactions on Power Electronics, vol. 28, no. 7, pp 3167 – 3181, September 2012.
[32] M.J. Zandzadeh, A. Vahedi, "Modeling and improvement of direct power control of DFIG under unbalanced grid voltage condition", International Journal of Electrical Power & Energy Systems, vol. 59, pp 58-65, July 2014.
[33] A. Delavari, I. Kamwa, P. Brunelle, "Simscape power systems benchmarks for education and research in power grid dynamics and control", IEEE Canadian Conference on Electrical & Computer Engineering, May 2018.

ENHANCEMENT OF DYNAMIC VOLTAGE RESPONSE IN UPF MODE OF DFIG WIND TURBINE DURING GRID DISTURBANCES USING STATCOM AND SAPF

Mohamed A. Ali[1], Hazem Hassan Ali[2]

[1]Faculty of Engineering Shoubra, Benha University, Cairo, Egypt
[2]College of Industry and Energy Technology, New Cairo Technological University, Cairo, Egypt,
hazemhassan481@yahoo.com

Abstract - *Protection of Doubly Fed Induction Generator (DFIG) wind turbine from failure operation due to grid disturbances is necessary via accomplishing reactive power compensation. Static Synchronous Shunt Compensator (STATCOM) based on AC voltage magnitude regulator and Shunt Active Power Filter (SAPF) based on load calculations at Point of Common Coupling (PCC) are used to enhance the dynamic response of DFIG regulated voltage during grid disturbances. An assessment performance study between these devices is introduced in this paper. STATCOM and SAPF are proposed under the presence of the weak grid and the power converter of DFIG is operated in Unity Power Factor (UPF) mode. Also, the maximum energy production of DFIG using Genetic Algorithm (GA) optimization feeding the load and the grid is still working over the entire operation. Simulation results reveal that STATCOM enhanced the dynamic voltage response of DFIG compared to SAPF under grid disturbances and wind speed variation.*

Keywords: *DFIG wind turbine; MPPT; STATCOM; Shunt active power filter; PI controller; Power quality; Voltage terminal regulation.*

1. Introduction

Most of Doubly Fed Induction Generator (DFIG) large size wind turbines based Wind Energy Conversion System (WECS) are in isolated places due to its noise pollution. Those areas have weak electric power grids with low fault current ratios, low reactance/resistance ratio of the transmission line and under voltage conditions. Conventional reactive power compensation devices especially in weak grid interconnected with DFIG wind turbines like AC filters cannot adjust reactive power balance continuously [1]. This paper presents Static Synchronous Shunt Compensator (STATCOM) and Shunt Active Power Filter (SAPF) based different reactive power control strategies to realise continuous adjustment. DFIG wind turbine is designed to do its function and track the maximum power between cut-in speed and rated wind speed under grid disturbances and different wind speed. The peak power is obtained by speed regulator in Rotor Side Converter (RSC) of DFIG which regulates the rotor speed at optimum value using Genetic Algorithm (GA) optimization via optimum Tip Speed Ratio (TSR) technique that achieves the peak power coefficient [2]-[3].

There are problems produced from grid disturbances happened in weak grid interconnected with DFIG wind turbines such as loss of speed, influence on the performance of generator, and peak current due to voltage sag occurrence and damage of insulation of generator due to voltage swell occurrence. Where the grid disturbances used here in this study are sudden inductive load, sudden capacitive load, and three phase fault.

The right observing of voltage stability response versus real-time in a power system under grid disturbances and wind speed variation is needed for protecting generator and working efficiently at any condition. The bus voltage at Point of Common Coupling (PCC) is local quantity so it is very costly to control the bus voltage at the remote node by the use of conventional power stations. It is because the reactive power flow in the system is related to changes in voltage which increases the power losses in the electric grid. Hence, it is important to install voltage control devices in the transmission or distribution network even if the wind turbine has voltage controlling capability because the wind turbines are located at a far distance location from the load center [4].

To overcome this problem, one of Flexible AC Transmission Systems (FACTS) devices based power electronic converters such as STATCOM is used and one of active power filter devices like SAPF is also used. The two devices each separately are used to regulate the terminal voltage of DFIG at its nominal level. Where, STATCOM based AC voltage magnitude regulator and SAPF based load calculations are tested by connecting each of them separately in parallel with the sudden load at PCC. The sudden load is connected to PCC through three phase circuit breaker. The sudden load in the first case is inductive load causes a disturbance leads to voltage sag and in the second case is a capacitive load causes a

disturbance leads to voltage swell. Also, STATCOM and SAPF each separately are tested under three phase fault as a grid disturbance happened through using ground resistance. The cases under study represent the grid power quality disturbances. The selection of these study cases is according to the power quality indices mentioned in different international standards and specifications such as IEC 62271-100 for high voltage switchgear limits, IEC 60255 for medium voltage limits, and IEC 364 for low voltage installation [5-6]. MATLAB /Simulink environment is used to implement the cases under study. The results of the simulations for previous mentioned cases are examined, with and without compensation, to indicate the advantages and differences between performance of STATCOM and SAPF design for power quality improvement and voltage regulation of DFIG wind turbine.

This study is arranged as follows. Section 2 summarizes the related work. The wind turbine description is elaborated in Section 3 to find out the aerodynamic system and the operating regions of wind turbine. In Section 4, it describes the TSR optimum technique using GA optimization. In Section 5, it indicates the way of solving power coefficient equation in terms of pitch angle and TSR using GA. The fourth order state-space model of the DFIG wind turbine is described in Section 6. A design of the RSC control circuit based speed regulator and Grid Side Converter (GSC) based DC-link voltage regulator are explained in Section 7 to illustrate how DFIG tracks the maximum power point and keeps the DC-link voltage at a constant required level for RSC. Operating DFIG wind turbine before occurrence of grid disturbances is demonstrated in Section 8. Appearance of grid disturbances effect before using STATCOM and SAPF is explained in Section 9. In section 10, it illustrates the design of STATCOM. In section 11, it explains the control scheme of SAPF. In section 12, the PI controller method used for all regulators in this study is demonstrated with values. Moreover, the digital simulation results are discussed in Section 13 under wind speed variation followed by a conclusion in Section 14.

2. Related work

Significant research on the dynamic voltage response of DFIG wind turbine has been reported in the literature with Stability Improvement of DFIG-Based Wind Farm Integrated Power System Using ANFIS Controlled STATCOM [7] included how to achieve system stability using STATCOM based on intelligence technique but the performance between STATCOM and SAPF based on voltage control has not been illustrated. Static Reactive Power Compensator Design, Based on Three-Phase Voltage Converter [8] mainly introduced only how to design STATCOM based on three phase voltage converter in regulating of terminal voltage using conventional controllers for renewable energy and its role in achieving fast response compared to SVC, but the effect of voltage sag and swell were not studied. A Simulation Model for Providing Analysis of Wind Farms Frequency and Voltage Regulation Services in an Electrical Power System [9] only considered accomplishing of the voltage regulation via power converter of the wind turbine under load condition, but the comparative analysis study between STATCOM and SAPF under effect of voltage sag and swell are not studied .While some researchers have concentrated on the Power Quality Issues and Mitigation for Electric Grids with Wind Power Penetration [10], it was only concluded that the voltage fluctuations due to wind intermittency based on Saudi daily load profile can be mitigated via reactive power compensation of the interface inverter without any illustration to control schemes of these devices. MPPT operation can be accomplished using traditional methods without using current control based on intelligence techniques for MPPT performance. The paper Maximum power production operation of doubly fed induction generator wind turbine using adaptive neural network and conventional controllers [11] focused only how to track the maximum power point using conventional and intelligence techniques, but the voltage regulation effect under this operation is not considered. The paper Two-Level Grid-Side Converter-Based STATCOM and Shunt Active Power Filter of Variable-Speed DFIG Wind Turbine-Based WECS Using SVM for Terminal Voltage [12] proposed only a voltage regulation of DFIG wind turbine via modification of GSC control circuit to operate as SAPF and STATCOM separately, but the fault occurrence is not studied. In LVRT and Stability Enhancement of Grid-Tied Wind Farm Using DFIG-Based Wind Turbine [13] focused only on accomplishing terminal voltage regulation via control scheme of RSC using conventional regulators by supplying the required amount of reactive power to achieve system stability, but the voltage swell case in not studied.

The main contributions of this study contain on (1) illustration of the performance of STATCOM based AC voltage magnitude regulator and SAPF based load calculations and to illustrate the difference between each performance under different grid disturbances, (2) during the operation of voltage regulation, the power coefficient equation in terms of TSR at zero pitch angle for wind speed less than rated speed is optimized using GA under conditions of the MPPT control region, and (3) a detailed mathematical model for STATCOM to indicate its performance in voltage regulation.

3. Operating region and aerodynamics of the wind turbine

A. Operating region of the wind turbine

The wind turbine works at different dynamics from the cut-in wind speed (4 m/s) to the cut-out wind speed (24 m/s) as illustrated in Figure 1. Three operating wind speed point can be observed in this figure [14]. The important used notations are described in Table 1.

Table 1
Notations

Notation	Description
$P_{m,rated}$	Rated mechanical power (W)
$T_{m,rated}$	Rated mechanical torque (N-m)
V_w	Wind Speed (m/s)
V_{dc}^*	Reference DC-link voltage (V)
C_p	Power coefficient
$C_{p,max}$	Maximum power coefficient
λ	Tip Speed Ratio (TSR)
λ_{opt}	Optimum TSR
β	Pitch angle
ω_t	Rotational turbine speed (rad/s)
$\omega_{t,opt}$	Optimum rotational turbine speed (rad/s)
ω_e	Synchronous angular velocity (rad/s)
ω_r	Rotor electrical angular speed (rad/s)
ω_m	Mechanical angular speed of generator (rad/s)
$\omega_{m,rated}$	Rated value of ω_m (rad/s)
ω_0	Bandwidth frequency (rad/s)
$\omega_{0\omega r}$	Bandwidth frequency of speed regulator (rad/s)
ω_{0Qs}	Bandwidth frequency of var regulator (rad/s)
ω_{0dc}	Bandwidth frequency of DC-link voltage regulator (rad/s)
f_{sw}	Switching frequency (Hz)
ω_{sw}	Switching frequency (rad/s)
ω_{outer}	Bandwidth frequency of outer loop
$v_{s,abc}$	Three phase stator voltages (V)
$i_{s,abc}$	Three phase stator currents (A)
$i_{r,abc}$	Three phase rotor currents (A)
$i_{G,abc}$	Three phase grid currents (A)
$i_{GSC,abc}$	Three phase GSC currents (A)
$i_{DFIG,abc}$	Three phase wind turbine currents (A)
$i_{l,abc}$	Three phase load currents (A)
$i_{f,abc}$	Three phase fault currents (A)
i_{filter}	Three phase filter currents (A)
$v_{stat,d}$	Voltage source converter output voltage in d-axis
$i_{stat,d}$	Converter output current in d-axis
$v_{PCC,d}$	PCC bus voltage in d-axis
$M_{stat,d}$	Modulation index of STATCOM in d-axis
$v_{stat,q}$	Voltage source converter output voltage in q-axis
$i_{stat,q}$	Converter output current in q-axis
$v_{PCC,q}$	PCC bus voltage in q-axis
$M_{stat,q}$	Modulation index of STATCOM in q-axis
C_{dc}	Capacitance of DC-link voltage of STATCOM
v_{PCC}	PCC bus voltage
α_{dc}	Output of DC-link voltage regulator
C_m	Filter capacitor
i_{Gd}	Grid current in d-axis
i_{Gq}	Grid current in q-axis
α_{PCC}	Output of PCC terminal voltage regulator
$i_{stat,d}^*$	Reference converter output current in d-axis
$i_{stat,q}^*$	Reference converter output current in q-axis
$\hat{i}_{Ld}$	Low frequency component of the load current in d-axis
$\hat{i}_{Lq}$	Low frequency component of the load current in q-axis
$\tilde{i}_{Ld}$	High frequency component of the load current in d-axis
$\tilde{i}_{Lq}$	High frequency component of the load current in q-axis
i_0	Load current in zero-axis component
i_{aref}	Compensation reference current in a-axis
i_{bref}	Compensation reference current in b-axis
i_{cref}	Compensation reference current in c-axis

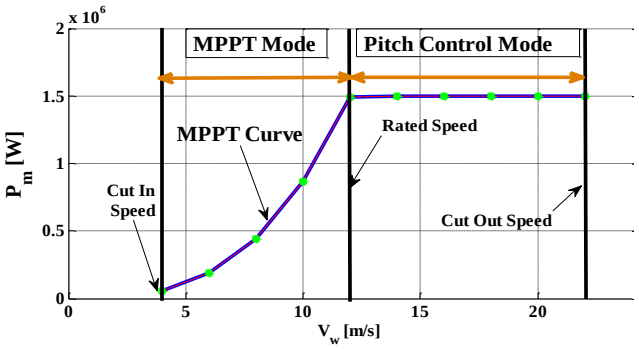

Fig. 1 Power speed curve of variable speed wind turbine.

B. Aerodynamic of the wind turbine

The energy conversion of the wind turbine can be represented by the nonlinear equations as follows [14]:

$$P_m = 0.5\rho A {V_w}^3 C_p \quad (1)$$

Where ρ is the air density (kg/m^3), $A = \pi R^2$ is area covered by turbine blades (m^2), and R is rotor radius (m). The power captured by the wind turbine depends on C_p for a given wind speed. The relationship of $C_p$with λ and β represents output characteristics of the wind turbine as in equation (2):

$$C_p(\lambda,\beta) = 0.5176\left(\frac{116}{\lambda_i} - 0.4\beta - 5\right)e^{-\frac{21}{\lambda_i}} + 0.0068\lambda \quad (2)$$

Where λ is a variable expressing the linear speed of blade tip to speed of wind. λ and $\frac{1}{\lambda_i}$ can be expressed as in equations (3) and (4), respectively.

$$\lambda = \frac{\omega_t R}{V_w} \quad (3)$$

$$\frac{1}{\lambda_i} = \frac{1}{\lambda + 0.08\beta} - \frac{0.035}{\beta^3 + 1} \quad (4)$$

By using equation (2), the typical C_p versus λ curve at various pitch angles β is shown in Figure 2. As mentioned before, there is an optimum value of λ that gives maximum power coefficient $C_{p,max}$. The maximum value of C_p theoretically is nearly 0.59 [14].

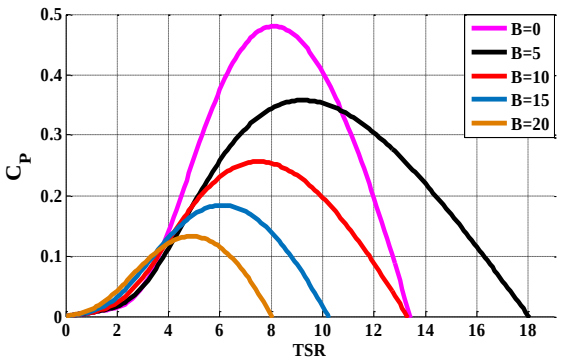

Fig. 2 Power coefficient $C_p(\lambda, \beta)$ versus λ for different values of pitch angle β.

So, in the mode of Maximum Power Point Tracking (MPPT) which is between cut-in wind speed and rated wind speed, If λ is being constant at its optimal value corresponding to $C_{p,max}$, this ensures that the wind turbine is operated at its maximum operating point. Figure 3 shows turbine mechanical power as a function of turbine speed by substituting equations (2), (3) and (4) in equation (1) at various wind speed and TSR λ. The required power for wind speed is a maximum value at $\omega_{t,opt}$. This is the speed which corresponds to λ_{opt} and $C_{p,max}$. To obtain the maximum power, the turbine must work at λ_{opt}. This is available by controlling the rotational speed of the turbine in order to rotate at the optimum speed of rotation. The points of maximum power curve are obtained as illustrated in Figure 3.

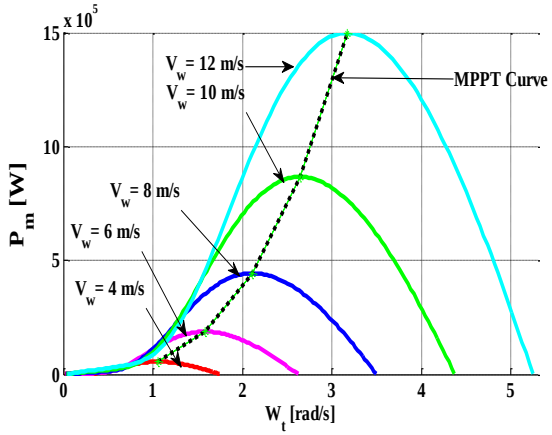

Fig. 3 Output mechanical power of 1.5 MW DFIG turbine and MPP versus turbine speed at various wind speed.

4. MPPT based optimal TSR technique

For MPPT the optimal TSR λ_{opt} is measured at maximum power coefficient $C_{p,max}$ and zero pitch angle β by using equation (2). Equation (2) is optimized for various λ using optimization method called Genetic Algorithm (GA) in present work. The next section will describe the GA method.

5. Genetic algorithm optimization

The GA based on natural selection is a powerful optimization technique [15], [16], [17], [18]. Optimizing functions called fitness functions is the main aim of GA. The GA controller is used in the region between the cut-in speed and the rated wind speed to find the maximum power at various wind speed. To get and track the maximum power point, it must get the optimal value of λ at maximum power coefficient and this is done by GA to solve equation (2) at various values of λ. Where the pitch angle β is zero in this region. The object function used in this work is one variable equation, then it is necessary to define constraints and the other required parameters of GA as the following:

$$0 \leq \lambda \leq 13$$

Where $\lambda_{min} = 0$ and $\lambda_{max} = 13$. The parameters for GA are given in Table 2.

Table 2
Parameters of GA

GA property	Value
Chromosome Length	16
Population Size	200
No. of iterations (Generations)	150

The object function is given as in equation (5):

$$C_p(\lambda) = 0.5176\left(\frac{116}{\lambda_i} - 5\right)e^{-\frac{21}{\lambda_i}} + 0.0068\lambda \qquad (5)$$

Where $\frac{1}{\lambda_i} = \frac{1}{\lambda} - 0.035$ at $\beta = 0$. Then, the above equation is entered in the GA under mentioned conditions and the result value obtained after number of generations (Iterations) of power coefficient using GA is $C_{p,max} = 0.48$ as depicted in Figure 4. The TSR λ corresponding to $C_{p,max}$ is $\lambda_{opt} = 8.1$ is illustrated in Figure 5.

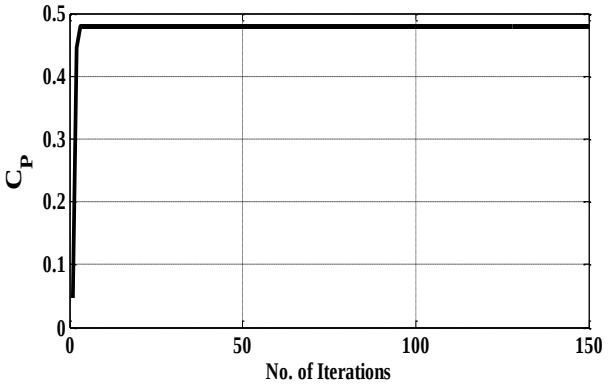

Fig. 4 Maximum power coefficient $C_{p,max}$ versus number of iterations.

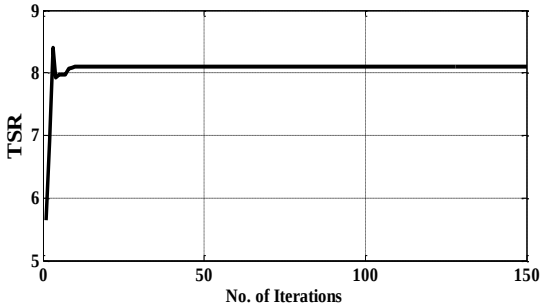

Fig. 5 Optimal value of TSR λ versus number of iterations.

So, it is important to get ω_t which is corresponding to λ_{opt} at different wind speed at specified ω_t corresponding to the maximum power that can be obtained using equation (1) as illustrated in Figure 3. The wind turbine parameters used in this work are shown in Table 3.

Table 3
Parameters of wind turbine

Parameter	Symbol	Value and Units
Air density	ρ	1.225 Kg/m^3
Number of blades	N_{blades}	3
Rated wind speed	$V_{\text{Rated−wind}}$	12 m/sec
Cut-in/out wind speed	$V_{cut-in}/V_{cut-out}$	4/24 m/sec
Rated Power	P_{rated}	1.5 MW
Blade length	R	30.6567m
Gearbox ratio	R_{GB}	57.7996
Max $\mathbf{C_p}$ (MPPT)	C_{pmax}	0.48
Optimal λ (MPPT)	λ_{opt}	8.1

6. Model of DFIG based WECS

The structure of 1.5 MW DFIG is illustrated in Figure 6. The dynamics of 1.5 MW DFIG are represented by state space model (fourth order) using the d-q synchronous reference frame as described in equations (6)-(9) [5]. Where v_{sq}, v_{sd}, $v_{rq}$and v_{rd} are the q and d-axis stator and rotor voltages, respectively. i_{sq} , i_{sd} , i_{rq} and i_{rd} are the q and d-axis stator and rotor currents, respectively. λ_{sq} , λ_{sd} , λ_{rq} and λ_{rd} are the q and d-axis stator and rotor fluxes, respectively.

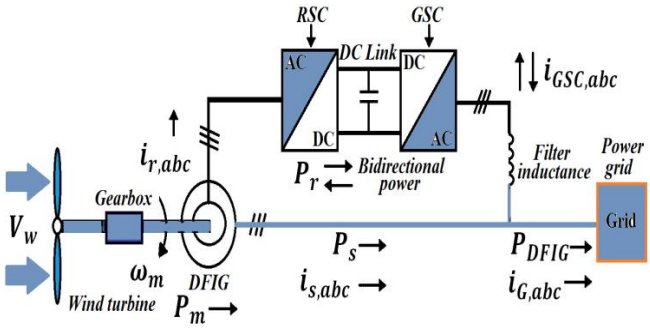

Fig. 6 DFIG wind turbine based WECS.

$$v_{sq} = R_s i_{sq} + \omega_e \lambda_{sd} + \frac{d}{dt}\lambda_{sq} \quad (6)$$

$$v_{sd} = R_s i_{sd} - \omega_e \lambda_{sq} + \frac{d}{dt}\lambda_{sd} \quad (7)$$

$$v_{rq} = R_r i_{rq} + (\omega_e - \omega_r)\lambda_{rd} + \frac{d}{dt}\lambda_{rq} \quad (8)$$

$$v_{rd} = R_r i_{rd} - (\omega_e - \omega_r)\lambda_{rq} + \frac{d}{dt}\lambda_{rd} \quad (9)$$

Where R_s and R_r are the stator and rotor resistances, respectively. The flux linkage equations are described as in equations (10)-(13):

$$\lambda_{sq} = L_s i_{sq} + L_m i_{rq} \quad (10)$$

$$\lambda_{sd} = L_s i_{sd} + L_m i_{rd} \quad (11)$$

$$\lambda_{rq} = L_r i_{rq} + L_m i_{sq} \quad (12)$$

$$\lambda_{rd} = L_r i_{rd} + L_m i_{sd} \quad (13)$$

Where L_s , L_r and L_m are the stator, rotor and mutual inductances, respectively, with $L_s = L_{ls} + L_m$ and $L_r = L_{lr} + L_m$; L_{ls} and L_{lr} are the stator and rotor self-inductance, respectively. All the equations mentioned above represent induction motor equations. When the induction motor works as a generator, the current direction will be opposite. The active and reactive power outputs from stator and rotor side are described as in equations (14)-(17):

$$P_s = \frac{3}{2}\left(v_{sq} i_{sq} + v_{sd} i_{sd}\right) \quad (14)$$

$$Q_s = \frac{3}{2}\left(v_{sq} i_{sd} - v_{sd} i_{sq}\right) \quad (15)$$

$$P_r = \frac{3}{2}\left(v_{rq} i_{rq} + v_{rd} i_{rd}\right) \quad (16)$$

$$Q_r = \frac{3}{2}\left(v_{rq} i_{rd} - v_{rd} i_{rq}\right) \quad (17)$$

The total active and reactive powers produced by DFIG are described as in equations (18)-(19):

$$P_{total} = P_{DFIG} = P_s + P_r \quad (18)$$

$$Q_{total} = Q_s + Q_r \quad (19)$$

If total P_{total} and/or total Q_{total} is negative, DFIG is giving power to the power grid, else it is taking power from the grid. The electromagnetic torque T_e produced by the machine which can be in terms of currents and flux linkages is given as in equation (20):

$$T_e = \frac{3*P}{2}\left(\lambda_{sd} i_{sq} - \lambda_{sq} i_{sd}\right) \quad (20)$$

Where P is the number of the pole pairs.

7. Control scheme of DFIG based WECS

Control of the 1.5 MW DFIG is done by control of the power converter, which contains control of the RSC and control of the Grid Side Converter (GSC) as the following:

A. Design of RSC controller for proposed genetic MPPT

In DFIG wind turbine system, the stator is directly connected to the power grid; its voltage and frequency are constant under the normal operating conditions. Therefore, Stator Voltage Oriented Control (SVOC) is used for the DFIG [14]. The stator voltage oriented control is done by aligning the d-axis of the synchronous reference frame with the stator voltage v_s. The resultant d- and q-axis stator voltages are: $v_{sq} = 0$ and $v_{sd} = v_s$. This DFIG control circuit is rotor side control scheme where the active power is controlled by the direct current axis loop and the stator reactive power is controlled by the quadrature current axis loop. In the active power control loop the rotor electrical angular speed is compared with the reference rotor electrical angular speed obtained by MPPT. Then, the error is fed to a conventional PI (Speed Regulator) controller to generate the reference direct axis current. Where, the proportional gain $K_{P,\omega r}$ and the integral gain $K_{I,\omega r}$ of the speed regulator are shown in Table 4. Similarly, the stator side reactive power is calculated and is compared with the reference stator reactive power ($Q_{s,ref}$ =0). Then, the error is fed to another PI (Var Regulator) controller to produce the reference quadrature axis current. Where, the proportional gain $K_{P,Qs}$ and the integral gain $K_{I,Qs}$ of the var regulator are illustrated in Table 4. The method used in evaluation of these parameters is illustrated in details in section 10. Then, both of the direct i_{rd}^* and quadrature i_{rq}^* axis reference currents are converted from d-q axis reference frame to a-b-c frame. Then, the three phase reference currents are compared with three phase rotor actual currents. Then, the error is the input to hysteresis current controller. Finally, the output of this controller is the switch control signals to the firing gate of RSC. The hysteresis controller output provides the switching pulses for the rotor side bidirectional converter control as shown in Figure 7. The overall control scheme is implemented using MATLAB /Simulink as shown in Figure 8. The stator voltage vector angle θ_s is measured as shown in Figure 9 and the rotor position angle θ_r is determined by an encoder mounted on the generator shaft. The slip angle θ_{sl} for the reference frame transformation can be obtained as the following ($\theta_{sl} = \theta_s - \theta_r$) as shown in Figure 9.

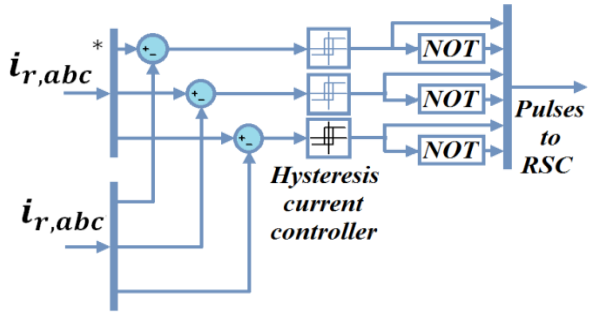

Fig. 7 Hysteresis current controller.

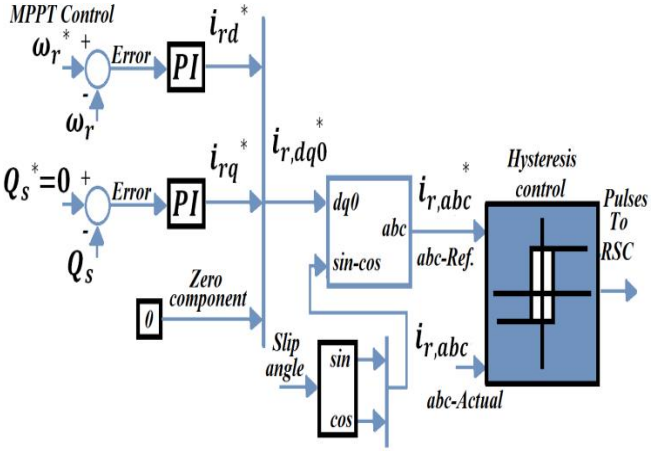

Fig. 8 Block diagram of RSC.

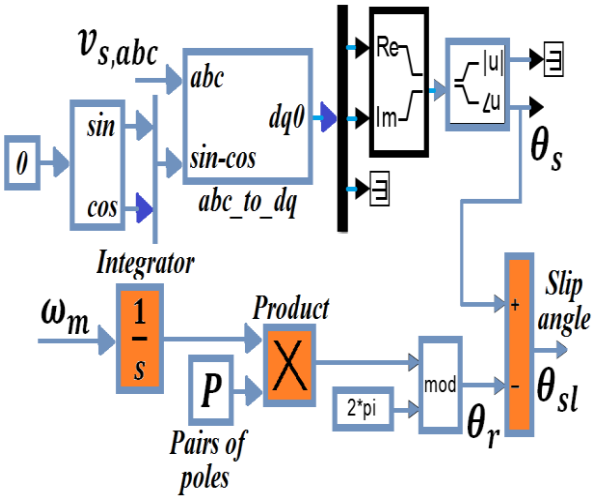

Fig. 9 Block diagram of slip angle calculator.

Table 4
Parameters of the speed and var regulators

Gains of the speed regulator	Values
f_{sw}	$1000\ Hz$
ω_{sw}	$2\pi f_{sw}$
ω_{outer}	$\omega_{sw}/100$
$\omega_{0\omega r}$	$\omega_{outer}/100$
$\mathbf{K_{P,\omega r}}$	$\sqrt{2}\omega_{0\omega r}\frac{J}{P}$
$\mathbf{K_{I,\omega r}}$	$\frac{J}{P}{\omega_{0\omega r}}^2$
ω_{0Qs}	ω_{outer}
$K_{P,Qs}$	$\sqrt{2}\,\omega_{0Qs}\,C_{Qs}$
$K_{I,Qs}$	$C_{Qs}\,{\omega_{0Qs}}^2$

Where C_{Qs} is a constant and its value is $C_{Qs} = \frac{2\,\sigma\,L_s\,L_r}{3\,\omega_e\,L_m} = Const.$ Noting that the switching frequency has the same value in the all parts of this paper. Also, the angular switching frequency is assumed to be 100 times outer loop controller.

B. Design of GSC controller

The objective of the GSC control system is to make the DC-link voltage constant at the required level for RSC, while the main input currents must be sinusoidal and in phase with their counterpart voltages, for which the control system of DFIG achieves unity power factor condition. The proposed control algorithm of GSC adopts the SVO to regulate DC-Link voltage and achieve a unity power factor. This strategy leads to get and control the following active and reactive component fed to grid. This DFIG control scheme allows controlling the DC-link voltage which is controlled by the direct current axis loop and the quadrature current axis which is kept at zero for unity power factor. The actual DC-link voltage is compared with the reference DC-link voltage and the error is fed to a conventional PI (DC Voltage Regulator) controller to generate the reference direct axis current $i_{GSC,d}{}^{*}$. Where, the proportional gain $K_{P,dc}$ and the integral gain $K_{I,dc}$ of the DC voltage regulator are described in Table 5. The strategy applied in estimation of these parameters is shown in details in section 10. Then, both of the direct $i_{GSC,d}{}^{*}$ and quadrature $i_{GSC,q}{}^{*} = 0$ axis reference currents are converted from d-q axis reference frame to a-b-c frame. Then, the three phase reference currents are compared with three phase GSC actual currents. Then, the error is the input to hysteresis current controller. Finally, the output of this controller is the switch control signals to the firing gate of GSC. The hysteresis controller output produces the switching pulses for the grid side bidirectional converter control as shown in Figure 10.

Table 5
Parameters of DC-link voltage regulator

Gains of DC voltage regulator	Values
ω_{0dc}	ω_{outer}
$K_{P,dc}$	$\sqrt{2}\omega_{0dc}\, C$
$K_{I,dc}$	$C\ \omega_{0dc}{}^{2}$

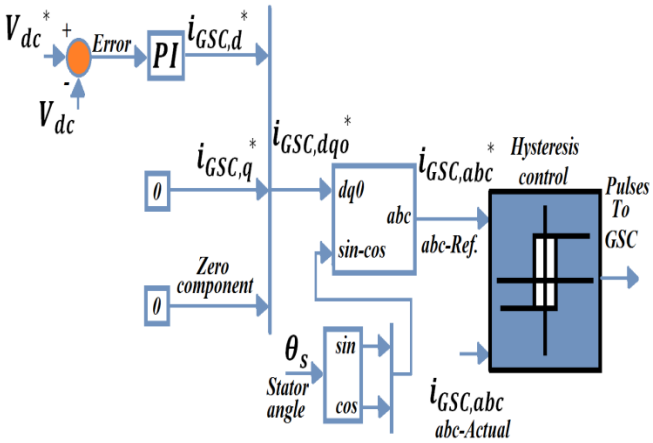

Fig. 10 Block diagram of GSC.

8. Connecting DFIG wind turbine to power grid without incidence of grid disturbances

The 1.5 MW DFIG-based WECS is connected to power grid under normal operating conditions without any grid disturbances. Under varying the wind speed as illustrated in the next sections, the rotor mechanical speed and the output power of DFIG wind turbine will be varied as depicted in Figure 11a and Figure 11b, respectively. Noting that the output power of DFIG with minus signal means that DFIG wind turbine is in generation mode.

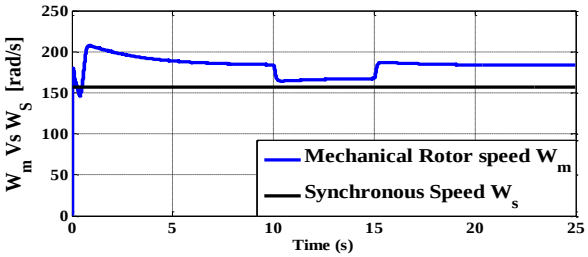

(a)

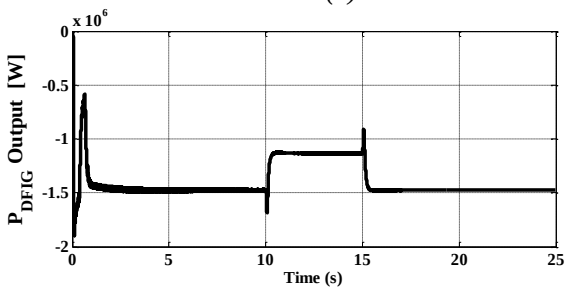

(b)

Fig. 11 The DFIG wind turbine
(a) Mechanical rotor speed versus synchronous speed, (b) Output power.

9. Occurrence of grid disturbances at the PCC with DFIG without connecting STATCOM and SAPF

The 1.5 MW DFIG-based WECS with connecting the sudden load at PCC is shown in Figure 12a. The system is executed for two cases of the sudden load for different wind speed and also for another case under occurrence of three phase fault in transmission line as depicted in Figure 12b. Noting that the three phase fault is through ground resistance R_g and each phase of the three phase fault has a resistance called phase fault breaker R_{on} as illustrated in Figure 12c.

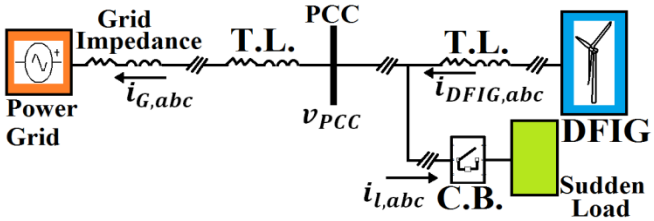

(a)

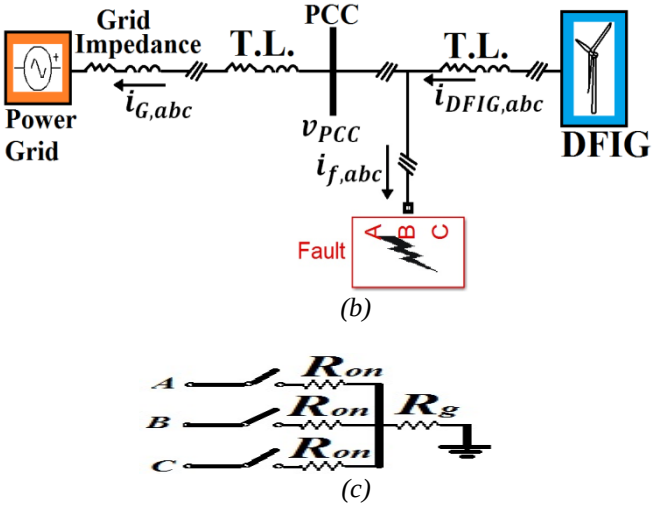

Fig. 12 At PCC in the overall model
(a) For connecting the sudden load, (b) For occurrence of three phase fault, (c) Three phase fault connection circuit

Firstly, in the cases of connecting the sudden inductive load at PCC and happening of three phase fault in transmission line, the effect of voltage sag is appeared as shown in Figure 13 and Figure 14, respectively. Secondly, the case for connecting the sudden capacitive load, the effect of voltage swell is illustrated in Figure 15. In all cases the wind speed is varied as illustrated in Figure 16.

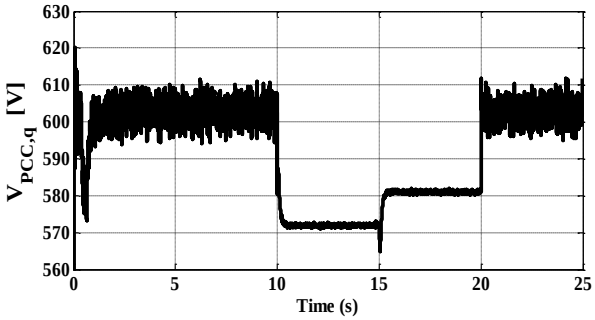

Fig. 13 The PCC voltage sag during connecting sudden inductive load at the DFIG wind turbine without STATCOM and SAPF.

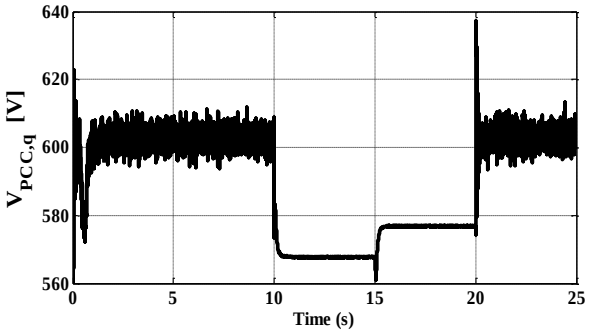

Fig. 14 The PCC voltage $v_{PCC,q}$ sag during occurrence of three phase fault at the DFIG wind turbine without STATCOM and SAPF

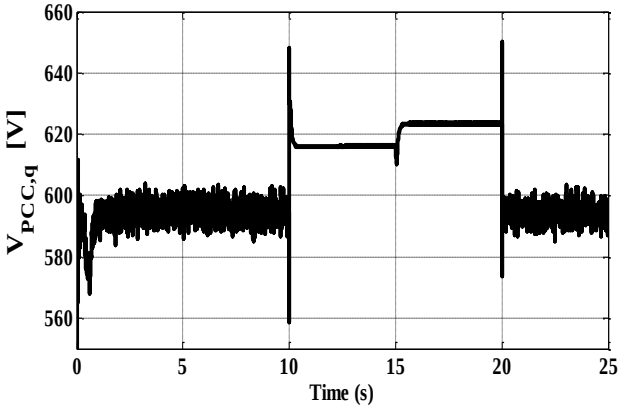

Fig. 15 The PCC voltage swell during connecting of sudden capacitive load at the DFIG wind turbine without STATCOM and SAPF

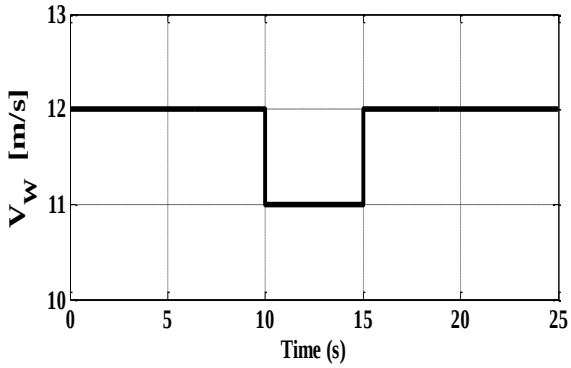

Fig. 16 Wind speed variation.

10. Control design of STATCOM

STATCOM based power electronics is three phase shunt connected device. It is connected near from the load at PCC. The main components of STATCOM with DFIG are connected in power distribution system as illustrated in Figure 17. It consists of DC-link charged capacitor, three phase converter IGBT switches, AC filter is a small filter capacitor C_m is also connected in parallel to the same bus for eliminating harmonics, coupling transformer and a control method [19], [20], [21]. The electronic diagram of STATCOM is the voltage source converter which converts the DC voltage into AC three phase output voltages at fundamental frequency. The controller of the STATCOM is used to operate the converter where the phase angle between the converter voltage and the line voltage is dynamically adjusted so that the STATCOM can generate or absorb the desired reactive power in VAR at PCC. The objective of STATCOM is to regulate the voltage magnitude at the PCC bus within a desired range by exchanging the reactive power with the distribution system. At the same time the converter in STATCOM must maintain the DC-link voltage constant.

STATCOM is modeled as Pulse Width Modulation (PWM) converter; the dynamic equations of STATCOM

in d-q axis reference frame are described as in equations (21) and (22), respectively.

$$\begin{cases} v_{stat,d} = R_{stat} i_{stat,d} + L_{stat} \dfrac{di_{stat,d}}{dt} - \omega_e L_{stat} i_{stat,q} \\ \qquad +v_{PCC,d} \\ v_{stat,d} = \dfrac{M_{stat,d} V_{dc}}{2} \end{cases} \tag{21}$$

$$\begin{cases} v_{stat,q} = R_{stat} i_{stat,q} + L_{stat} \dfrac{di_{stat,q}}{dt} + \omega_e L_{stat} i_{stat,d} \\ \qquad +v_{PCC,q} \\ v_{stat,q} = \dfrac{M_{stat,q} V_{dc}}{2} \end{cases} \tag{22}$$

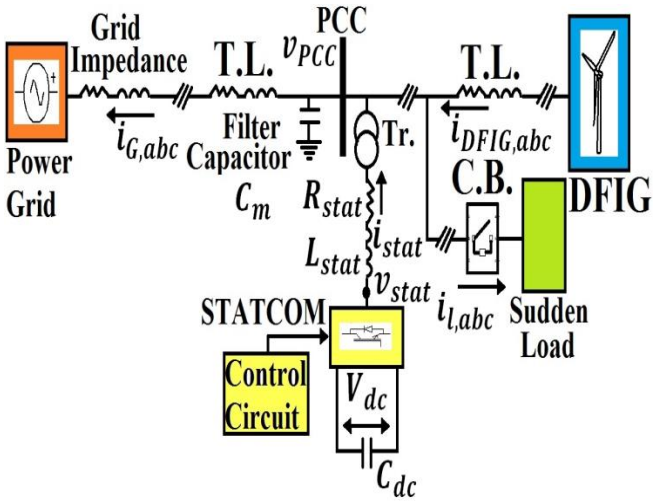

Fig. 17 STATCOM with DFIG in power system.

Where R_{stat} and L_{stat} are line resistance and inductance, respectively. V_{dc} is the DC-link voltage. STATCOM DC voltage dynamics in DC-link is described as in equation (23) [19].

$$C_{dc} \frac{dV_{dc}}{dt} = \frac{-3}{4}\left(M_{stat,q} i_{stat,q} + M_{stat,d} i_{stat,d}\right) \tag{23}$$

The voltage magnitude (v_{PCC}) at the PCC is described as in equation (24).

$${v_{PCC}}^2 = {v_{PCC,d}}^2 + {v_{PCC,q}}^2 \tag{24}$$

By differentiating equation (24) with respect to time as the following:

$$\frac{d{v_{PCC}}^2}{dt} = 2v_{PCC,d} \frac{dv_{PCC,d}}{dt} + 2v_{PCC,q} \frac{dv_{PCC,q}}{dt} \tag{25}$$

Equation (25) describes the square of voltage magnitude dynamics at the PCC and this voltage magnitude will be $v_{PCC} = \left|\sqrt{{v_{PCC}}^2}\right|$. For the DC voltage control, equation (23) can be rewritten as:

$$-\frac{4}{3} C_{dc} \frac{dV_{dc}}{dt} = \left(M_{stat,q} i_{stat,q} + M_{stat,d} i_{stat,d}\right) = \alpha_{dc} = K_{dc}({V_{dc}}^* - V_{dc}) \tag{26}$$

Where K_{dc} is the DC voltage regulator given as $K_{dc} = \left(K_{P,dc} + \frac{K_{I,dc}}{s}\right)$. Then, equation (26) will be:

$$\frac{4}{3} C_{dc} \frac{dV_{dc}}{dt} = \alpha_{dc} = \left(K_{P,dc} + \frac{K_{I,dc}}{s}\right){V_{dc}}^* - \left(K_{P,dc} + \frac{K_{I,dc}}{s}\right) V_{dc} \tag{27}$$

Then, it is required to get the transfer function for DC voltage regulator as described below:

$$\frac{V_{dc}}{{V_{dc}}^*} = \frac{\frac{3}{4C_{dc}}\left(s\, K_{P,dc} + K_{I,dc}\right)}{s^2 + s\,\frac{3}{4C_{dc}} K_{P,dc} + \frac{3}{4C_{dc}} K_{I,dc}} \tag{28}$$

The PI parameters of DC voltage controller are determined by comparing the coefficients in equation (29) with the denominator of the corresponding transfer function in equation (28) as described in Table 6. After comparison in the outer loop of STATCOM design, the PI parameters of DC voltage regulator will be:

$$s^2 + \sqrt{2}\,\omega_0 s + {\omega_0}^2 = 0 \tag{29}$$

Where $s = \frac{d}{dt}$ and ω_0 is the bandwidth frequency.

Table 6
Parameters of STATCOM for DC voltage regulator

Gains	Values
$\boldsymbol{\omega_{0dc}}$	ω_{outer}
$\boldsymbol{K_{P,dc}}$	$\frac{4}{3}\sqrt{2}\,\omega_{0dc}\,C_{dc}$
$\boldsymbol{K_{I,dc}}$	$\frac{4}{3} C_{dc}\,{\omega_{0dc}}^2$

For voltage magnitude control from Figure 18, the dynamic voltage equations at the PCC can be written as:

$$C_m \frac{dv_{PCC,d}}{dt} = i_{stat,d} - i_{Gd} + \omega_e C_m v_{PCC,q} \tag{30}$$

$$C_m \frac{dv_{PCC,q}}{dt} = i_{stat,q} - i_{Gq} - \omega_e C_m v_{PCC,d} \tag{31}$$

Substituting equations (30) and (31) into equation (25) gives:

$$\frac{C_m}{2} \frac{d{v_{PCC}}^2}{dt} = v_{PCC,d}\left(i_{stat,d} - i_{Gd}\right) + v_{PCC,q}\left(i_{stat,q} - i_{Gq}\right) = \alpha_{PCC} = K_{PCC}\left({v_{PCC}}^{2^*} - {v_{PCC}}^2\right) \tag{32}$$

Where K_{PCC} is the PI controller for voltage magnitude control given as $K_{PCC} = \left(K_{P,PCC} + \frac{K_{I,PCC}}{s}\right)$. Substituting for K_{PCC} results in equation (33) and from which the transfer function is found as described in equation (34).

$$\frac{C_m}{2}\frac{d{v_{PCC}}^2}{dt} = \left(K_{P,PCC} + \frac{K_{I,PCC}}{s}\right){v_{PCC}}^{2^*} - \left(K_{P,PCC} + \frac{K_{I,PCC}}{s}\right){v_{PCC}}^2 \quad (33)$$

$$\frac{{V_{PCC}}^2}{{V_{PCC}}^{2^*}} = \frac{\frac{2}{C_m}(s\,K_{P,PCC}+K_{I,PCC})}{s^2+s\,\frac{2}{C_m}K_{P,PCC}+\frac{2}{C_m}K_{I,PCC}} \quad (34)$$

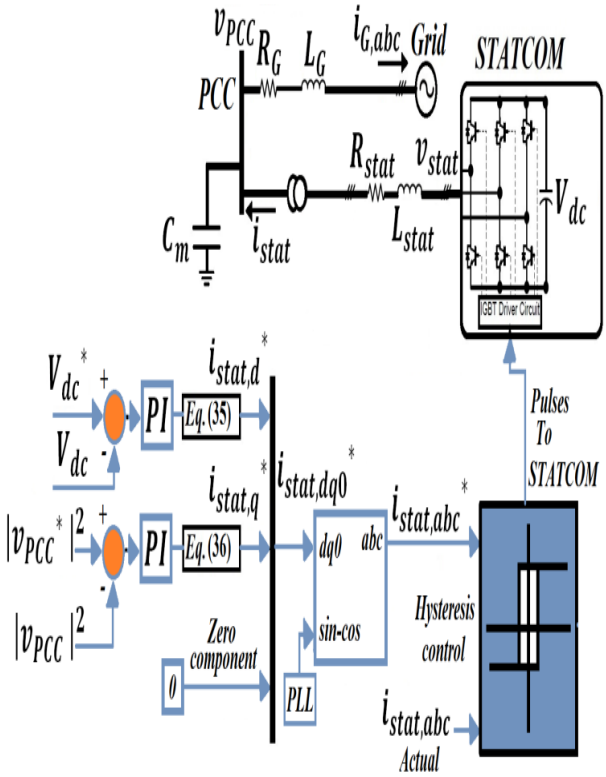

Fig. 18 STATCOM controller.

The PI parameters of voltage magnitude controller are determined by comparing the coefficients in equation (29) with the denominator of the corresponding transfer function in equation (34) as illustrated in Table 7. For the outer loop in STATCOM design $\omega_{0PCC} = \omega_{outer} = 62.8\ rad/s$ after comparison the PI parameters of voltage magnitude regulator will be:

Table 7
Parameters of STATCOM for voltage magnitude regulator

Gains	Values
$\boldsymbol{\omega_{0PCC}}$	ω_{outer}
$\boldsymbol{K_{P,PCC}}$	$\sqrt{2}\,\omega_{0PCC}\,\frac{C_m}{2}$
$\boldsymbol{K_{I,PCC}}$	$\frac{C_m}{2}\,{\omega_{0PCC}}^2$

Where ω_{0PCC} is the bandwidth of the voltage magnitude controller. Finally, the d-q axis current of STATCOM ${i_{stat,d}}^*$ and ${i_{stat,q}}^*$ are obtained by using equations (26) and (32) as illustrated in Figure 18. The currents ${i_{stat,d}}^*$ and ${i_{stat,q}}^*$ are described below:

$${i_{stat,d}}^* = \frac{1}{M_{stat,d}}\left(\alpha_{dc} - M_{stat,q}\,i_{stat,q}\right) \quad (35)$$

$${i_{stat,q}}^* = \frac{1}{v_{PCC,q}}\left(\alpha_{PCC} - v_{PCC,d}\left(i_{stat,d} - i_{Gd}\right)\right) + i_{Gq} \quad (36)$$

Figure 18 shows the control circuit of STATCOM. The proposed control circuit of STATCOM adopts its PLL by using the required angle θ circuit to regulate DC-link voltage and the terminal voltage at PCC. Where the PLL circuit is done by aligning the q-axis of the synchronous reference frame with the voltage v_{PCC}. The parameters of PI controller in PLL circuit are proportional gain $K_{P,pll,stat}$ and integral gain $K_{I,pll,stat}$ that illustrated in Table 8. The resultant d-q axis voltages at PCC are: $v_{PCC,d}$ =0 and $v_{PCC,q} = v_{PCC}$ as illustrated in Figure 19.

Table 8
Parameters of STATCOM for PLL regulator

Gains	Values
$\boldsymbol{\omega_0}$	$\omega_{sw}/15$
$\boldsymbol{K_{P,pll,stat}}$	$\sqrt{2}\,\omega_0/v_s$
$\boldsymbol{K_{I,pll,stat}}$	${\omega_0}^2/v_s$

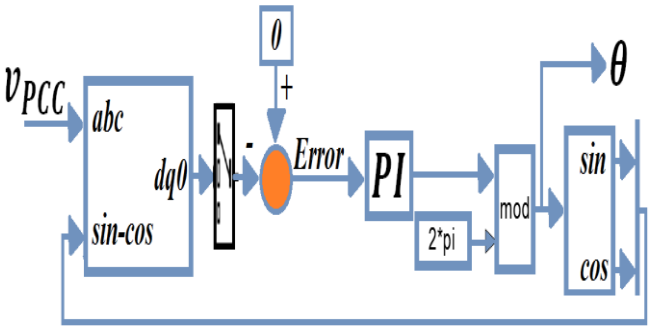

Fig. 19 PLL circuit for STATCOM controller.

This STATCOM allows controlling the DC-link voltage which is controlled by the direct current axis loop ${i_{stat,d}}^*$ and the magnitude of terminal voltage at PCC which is controlled by the quadrature current axis loop ${i_{stat,q}}^*$. The actual DC-link voltage is compared with the reference DC-link voltage and the error is fed to a conventional PI (DC voltage control) controller to generate the reference direct axis current ${i_{stat,d}}^*$. Similarly, The square actual voltage magnitude at PCC is compared with the square reference voltage magnitude and the error is fed to a conventional PI (voltage magnitude control) controller to generate the reference quadrature axis current ${i_{stat,q}}^*$. Then, both of the

direct $i_{stat,d}{}^{*}$and quadrature $i_{stat,q}{}^{*}$axis reference currents are converted from d-q axis reference frame to a-b-c frame. Then, the three phase reference currents are compared with three phase STATCOM actual currents. Then, the error is the input to hysteresis current controller. Finally, the output of this controller is the switch control signals to the firing gates of STATCOM converter.

11. Configuration and control design of SAPF

The present work tries to apply SAPF for voltage terminal regulation of DFIG for different sudden loads such as inductive load (for voltage sag effect) and capacitive load (for voltage swell effect) for power quality improvement where the sudden load is connected to PCC through circuit breaker as shown in Figure 20. Frequency domain compensation based on Fourier analysis, is not common because it requires much real time processing power. There are several methods to define the harmonic currents, phase shift and voltage control, the most classical methods are instantaneous power theory p-q, d-q synchronous detection method and Fryze current control [22], [23], [24], [25], [26]. It is known that the role of SAPF with DFIG connected to three phase balanced power grid and balanced sudden load consuming or supplying reactive power which causes voltage sag or swell is voltage terminal regulation. In this work, the synchronous reference frame d-q axis is used as shown in Figure 21. Practically, the load currents of the sudden load in a-b-c frame (i_{La}, i_{Lb} and i_{Lc}) are obtained by using current sensors. After that, the load currents in a-b-c frame are transformed into d-q-0 axis reference frame (i_{Ld}, i_{Lq} and i_{L0}) according to the same previous PLL circuit design as given in equation (37).

$$\begin{bmatrix} i_{Ld} \\ i_{Lq} \\ i_{L0} \end{bmatrix} = \sqrt{\frac{2}{3}} \begin{bmatrix} \cos(\omega t) & \cos(\omega t - 120^o) & \cos(\omega t + 120^o) \\ -\sin(\omega t) & -\sin(\omega t - 120^o) & -\sin(\omega t + 120^o) \\ \frac{1}{\sqrt{2}} & \frac{1}{\sqrt{2}} & \frac{1}{\sqrt{2}} \end{bmatrix} \begin{bmatrix} i_{La} \\ i_{Lb} \\ i_{Lc} \end{bmatrix} \quad (37)$$

Where ωt is the phase of the positive sequence of the system voltage and it is provided by PLL circuit. Then, a High Pass Filter (HPF) is used in both d and q axis to get the high frequency components of the load current ($i_{Ld}^{\sim}$ and $i_{Lq}^{\sim}$) as follows:

$$i_{Ld}(t) = I_{Ld}(t) + i_{Ld}^{\wedge}(t) + i_{Ld}^{\sim}(t) \quad (38)$$

$$i_{Lq}(t) = I_{Lq}(t) + i_{Lq}^{\wedge}(t) + i_{Lq}^{\sim}(t) \quad (39)$$

Then, the high frequency component will be subtracted from the total current in both d and q axis (i_{Ld} and i_{Lq}). Noting that I_{Ld} and $I_{Lq}$are the DC components of the load current in d-q axis (small values are neglected). Finally, the only remain component is the reference compensation low frequency component of the load current in both d and q axis ($i_{Ld}^{\wedge}$ and $i_{Lq}^{\wedge}$). The compensation reference currents in d-q axis and will be converted into a-b-c frame as given in equation (40).

$$\begin{bmatrix} i_{aref} \\ i_{bref} \\ i_{cref} \end{bmatrix} = \sqrt{\frac{2}{3}} \begin{bmatrix} \cos(\omega t) & -\sin(\omega t) \\ \cos(\omega t - 120^o) & -\sin(\omega t - 120^o) \\ \cos(\omega t + 120^o) & -\sin(\omega t + 120^o) \end{bmatrix} \begin{bmatrix} i_{Ld}^{\wedge} \\ i_{Lq}^{\wedge} \\ i_0 \end{bmatrix} \quad (40)$$

After that, the compensation reference currents will be compared with the compensation actual current of SAPF through hysteresis current controller where the output of this controller is the switch control signals to the inverter of SAPF as shown in Figure 20 and Figure 21. Noting that in Figure 20 a filter inductance is used at the output of the inverter of SAPF to eliminate the distortion produced by switches in the inverter circuit of SAPF. Also, a DC constant voltage source is used in the DC side of the inverter circuit of SAPF.

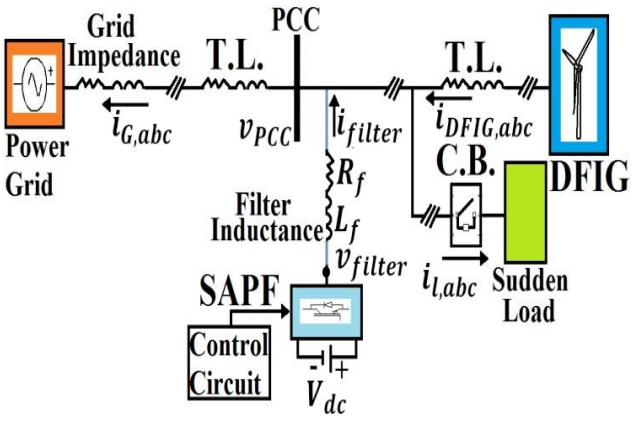

Fig. 20 SAPF with DFIG in power system.

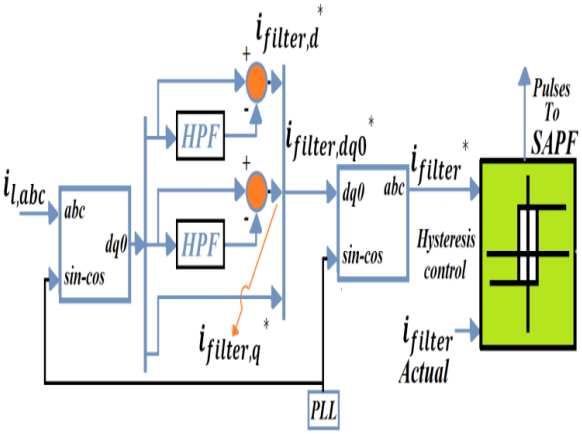

Fig. 21 Block diagram of SAPF controller.

Where $i_{filter,d}{}^{*}$and $i_{filter,q}{}^{*}$are the compensation reference currents in d and q axis, respectively.

12. Design of PI Controller for DFIG and STATCOM

The output signal of a PI controller is obtained by using equation (41):

$$U = K_P * e + K_I \int e * dt \quad (41)$$

Where e, K_P and K_I are the error signal, the proportional gain and integral gain, respectively. Some methods are used to measure the parameters of the system that can save the overall system in the stable zone. Butterworth polynomial method is used here to optimize the closed loop eigenvalue locations [27]. The Butterworth method locates the eigenvalues uniformly in the left half s-plane (stable area) on a circle with radius ω_o, with its center at the origin as illustrated in Figure 22.

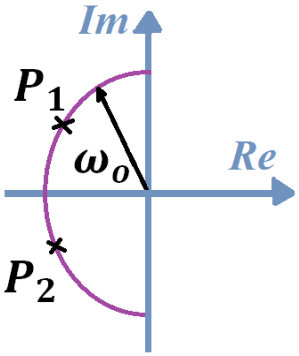

Fig. 22 Location of poles in left half s-plane using Butterworth polynomial.

The Butterworth polynomial for transfer function with second order denominator is described as in equation (29). The PI parameters are measured by comparing the coefficients in equation (29) with the denominators of the corresponding transfer functions and then selecting appropriate ω_o . Where ω_o is the bandwidth of the controller, which depends on the design value. The parameters of each PI controller used in controlling of DFIG and STATCOM are shown in Table 9.

Table 9
Parameters of PI controllers

Converter	Regulator	Symbol	Value
RSC	Speed Regulator	$K_{P,\omega r}$	17.7715
		$K_{I,\omega r}$	7.8957
	Var Regulator	$K_{P,Qs}$	$5.7798*10^{-5}$
		$K_{I,Qs}$	0.0026
GSC	DC Voltage Regulator	$k_{P,dc}$	79.9719
		$k_{I,dc}$	3553.1
	DC Voltage Regulator	$K_{P,dc}$	106.6292
		$K_{I,dc}$	4737.4
STATCOM	AC Voltage Regulator	$K_{P,pcc}$	0.2444
		$K_{I,pcc}$	10.8566
	PLL Circuit	$K_{P,pll,stat}$	1.0466
		$K_{I,pll,stat}$	309.9994

13. Digital simulation results of the overall system

The overall model is simulated two times, the first time was for STATCOM and the second time was for SAPF under the same load and fault conditions as illustrated in Figure 17 and Figure 20, respectively. The main whole model consists of DFIG wind turbine control structure, transmission line and power grid under connecting the balanced sudden load at PCC and occurrence of three phase fault as a grid disturbance. Where the DFIG wind turbine is used to supply the sudden load with the needed power and the remained power is supplied to the power grid. The sudden inductive load and the occurrence of three phase fault are used as a grid disturbance to show and appear the effect of voltage sag. The sudden inductive load is three phase inductive load ($R_{load} = 0.6\,\Omega$ and $L_{load} = 9\,\mu H$) connected to PCC through circuit breaker. The three phase fault is through ground resistance $R_g = 0.001\,\Omega$ and each phase of the three phase fault has a resistance called phase fault breaker $R_{on} = 0.5\,\Omega$. The sudden capacitive load is used as a grid disturbance to indicate the effect of voltage swell. The sudden capacitive load is a three phase capacitive load ($R_{load} = 1\,m\Omega$ and $C_{load} = 5\,mF$) connected to PCC through circuit breaker. The initial status of the circuit breaker at the terminals of the sudden load is normally open and its transition time is from 10 sec to 20 sec of simulation time. The overall model is implemented in MATLAB /Simulink package. The DFIG parameters are shown in Table 10. The simulation for all cases is carried out for the same mentioned varied wind speed and the digital simulation results will be displayed for three cases as the following:

1) Comparison between STATCOM and SAPF connected at PCC under presence of sudden inductive load.
2) Comparison between STATCOM and SAPF connected at PCC under occurrence of three phase fault.
3) Comparison between STATCOM and SAPF connected at PCC under existence of sudden capacitive load.

Table 10
DFIG parameters

Parameter	Value
$P_{m,rated}$	1.5 MW
Rated stator line voltage	690 V (rms)
Rated stator frequency	50 Hz
Rated rotor speed	1750 rpm
P	2
$T_{m,rated}$	8.185 kN-m
R_s	2.65 $m\Omega$
R_r	2.63 $m\Omega$
L_{ls}	0.1687 mH
L_{lr}	0.1337 mH
L_m	5.4749 mH
J	20 $Kg.m^2$
V_{dc}	1600 V
C	900 mF

Noting that, STATCOM is connected in parallel with the grid disturbance at PCC. The STACOM parameters are shown in Table 11.

Table 11
STATCOM parameters

Parameters	Value
Capacitor voltage $\mathbf{V_{dc}}$	1100 V
Line inductance	1 mH
Line resistance	0.1 Ω
DC-link capacitance	0.9 F
Filter capacitor	5.5 mF

Under the same conditions mentioned above the SAPF is used instead of STATCOM. The SAPF is connected in parallel with the grid disturbance at PCC for the same wind speed of DFIG wind turbine. The SAPF parameters are shown in Table 12.

Table 12
SAPF parameters

Parameters	Value
DC side voltage $\mathbf{V_{dc}}$	1100 V
Filter inductance	1 mH
Filter resistance	1 mΩ

A. Comparison between STATCOM and SAPF connected at PCC under presence of sudden inductive load

Firstly, the overall model is simulated in presence of sudden inductive load as a grid disturbance in the period from 10 seconds to 20 seconds without using STATCOM as a result the PCC voltage is sagging which is reduction in voltage through specified time range as illustrated in Figure 13. In this work, the three phase symmetrical voltage is sagging for about 3% from the nominal voltage. Without using STATCOM, when the inductive load is connected at PCC suddenly, it will absorb reactive power. The weak power grid cannot supply the required additional reactive power quickly and the DFIG output power is regulated to its optimum value.

As a result, the PCC voltage drops as illustrated in Figure 13. With using STATCOM at the PCC in this case, STATCOM responds rapidly by giving additional required reactive power. Therefore, the PCC voltage is regulated closely to its nominal voltage according to the reference desired value in AC voltage regulator with small overshoot shown in Figure 23. Also, the STATCOM has the ability to achieve DC voltage regulation of the DC-link as shown in Figure 24. Noting that the transmission line impedances at the side of DFIG and PCC are ($R_{T.L.} = 1\ m\Omega$ and $L_{T.L.} = 0.5\ mH$) and ($R_{T.L.} = 0.0229\ \Omega$ and $L_{T.L.} = 99\ \mu H$), respectively. The power grid impedance is ($R_G = 0.10472\ m\Omega$ and $L_G = 1\ \mu H$).

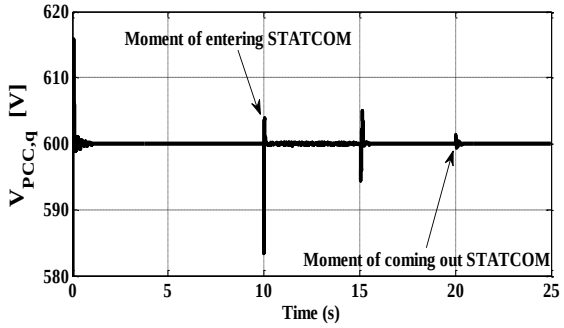

Fig. 23 The PCC voltage sag compensation at the DFIG wind turbine with STATCOM

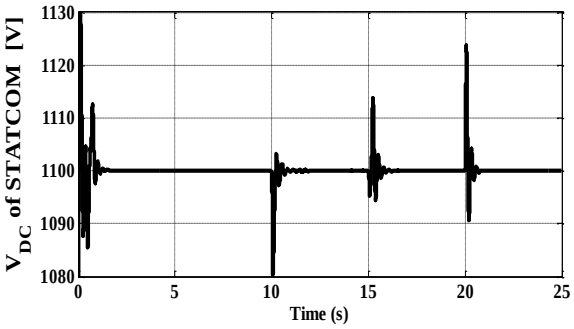

Fig. 24 The DC-link voltage of STATCOM during voltage sag compensation.

Secondly, the whole model is simulated under the same conditions mentioned above but in this case SAPF is used instead of STATCOM. As mentioned before the sudden inductive load is taken as a grid disturbance in the period from 10 seconds to 20 seconds during the same wind variation mentioned before. Before using SAPF, the PCC voltage is sagging for about 3% from the nominal voltage. With using SAPF at the PCC and the same effect of voltage sagging is created; in that case, SAPF will work with this disturbance based on load calculations using d-q axis reference frame as mentioned before. SAPF is controlled by hysteresis current controller to get switch control signals to inverter circuit. At the DC side of the inverter, the DC voltage is considered as a constant voltage (1100 V) and represented in MATLAB/Simulink by constant DC voltage source. SAPF will inject into PCC the required reactive power (supplying) based on inductive sudden load currents by SAPF actual currents.

As a result, the PCC voltage is regulated to be near from its nominal voltage in the period from 15 second to 20 second but in the period between 10 second to 15 second the voltage is raised up compared to the voltage in Figure 13 in the same period and not at its nominal voltage level because a small difference occurred when the wind speed is changed to 11 m/s. Figure 25a illustrates the PCC voltage before and after using SAPF. Figure 25b shows the PCC voltage for both SAPF and STATCOM after connection. It is absolutely clear that the STATCOM is

achieved better results than SAPF due to its AC voltage magnitude regulator. But SAPF depends on load calculations, the overall system of SAPF is affected by any change of the wind speed and it works according to this change of the wind speed according to its load calculations and hasn't the ability to restore the nominal voltage.

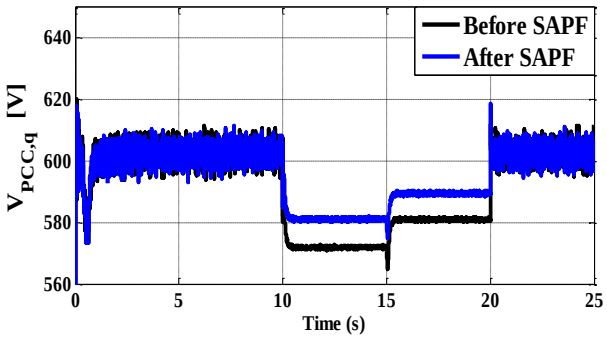

(a)

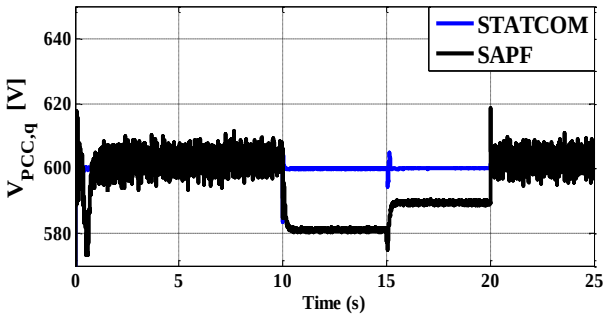

(b)

Fig. 25 The PCC voltage response
(a) Before and after SAPF connection, (b) After connection for both SAPF and STATCOM.

B. Comparison between STATCOM and SAPF connected at PCC under occurrence of three phase fault

The overall model is simulated in presence of three phase fault as a grid disturbance in the period from 10 seconds to 20 seconds during the same variation in wind speed mentioned before as shown in Figure 12a. The three phase fault block represents a three phase circuit breaker where the opening and closing times can be controlled from the simulation program. As a result of this the PCC voltage is sagging which is momentary decreasing in voltage over the time range without using STATCOM as illustrated in Figure 14.

The STATCOM is connected in shunt at PCC where the three phase fault occurred for variation in wind speed of DFIG. The overall model is simulated in presence of three phase fault as a grid disturbance in the period from 10 seconds to 20 seconds without using STATCOM as a result of this, the PCC voltage is sagging as illustrated in Figure 14. In this work, the three phase symmetrical voltage is sagging for about 4% from the nominal voltage. Where the weak power grid cannot supply required additional reactive power with quickly response and the DFIG output power is regulated to its optimum value. When the STATCOM with its capacitor ($C_m = 6.5\ mF$) is connected at the PCC in this case, STATCOM responds rapidly by supplying additional reactive power. As a result, the PCC voltage is regulated closely to its nominal voltage according to the reference desired value in AC voltage magnitude regulator with small overshoot shown in Figure 26.

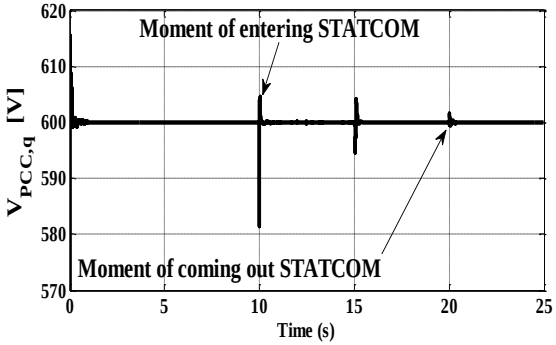

Fig. 26 The PCC voltage $v_{PCC,q}$ sag compensation at the DFIG wind turbine with STATCOM.

Also, the STATCOM has the ability to achieve DC voltage regulation of the DC-link as illustrated in Figure 27. Noting that, the transmission line impedances at the side of DFIG and PCC and power grid impedance are the same as case 1.

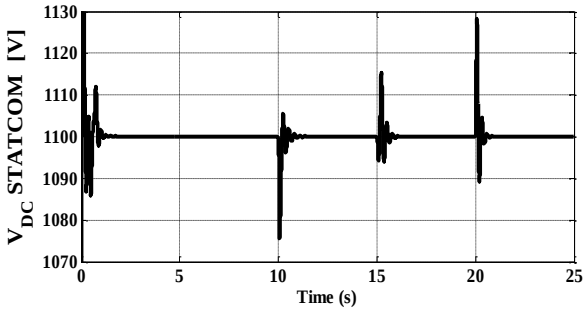

Fig. 27 The DC-link voltage of STATCOM during voltage sag compensation.

The same SAPF in previous case is used instead of STATCOM to inject into PCC the required reactive power (supplying) based on three phase fault currents by SAPF actual currents for the same conditions.

As a result, the PCC voltage is regulated to be closely to its nominal voltage in the period from 15 second to 20 second but in the period between 10 second to 15 second the voltage is raised up compared to the voltage in Figure 14 in the same period and not at its nominal voltage level because a small difference occurred when the wind speed is changed to 11 m/s. Figure 28a illustrates the PCC voltage before and after using SAPF. Figure 28b shows the PCC voltage for both SAPF and STATCOM after

connection. It is obviously clear that the STATCOM is achieved better results than SAPF due to its AC voltage magnitude regulator. But SAPF depends on fault current calculations, the overall system of SAPF is affected by any change of the wind speed and it works according to this change of the wind speed according to its fault current calculations and hasn't the ability to restore the nominal voltage.

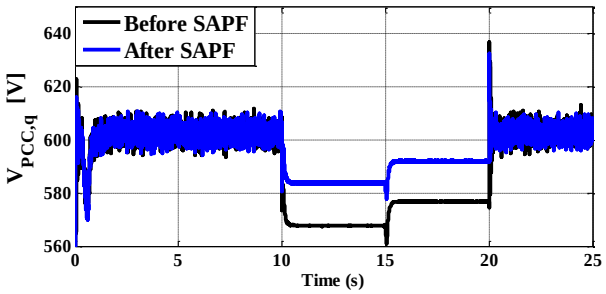

(a)

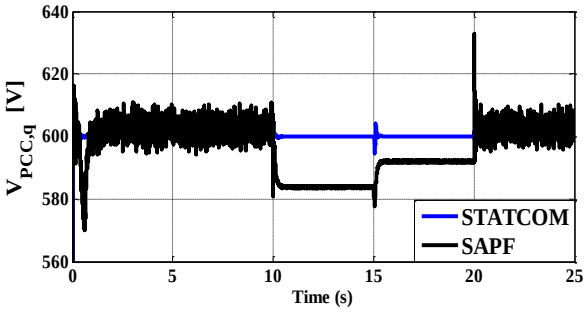

(b)

Fig. 28 The PCC voltage response
(a) Before and after SAPF connection, (b) After connection for both SAPF and STATCOM.

C. Comparison between STATCOM and SAPF connected at PCC under existence of sudden capacitive load

The overall model is simulated in presence of sudden capacitive load as a grid disturbance in the period from 10 seconds to 20 seconds without STATCOM. As a result of this the PCC voltage is swelling which is momentary increasing in voltage over the time range as shown in Figure 15. In this work, the three phase symmetrical voltage is swelling for about 2% from the nominal voltage. Before using the STATCOM, when the sudden capacitive load connected to PCC, it will supply reactive power into it. The weak power grid cannot absorb the required additional reactive power with rapidly response and the DFIG output power is regulated to its optimum value.

As a result, the PCC voltage increases as shown in Figure 15. When the STATCOM is connected at the PCC in this case, STATCOM responds rapidly by absorbing the additional reactive power. As a result, the PCC voltage is regulated nearly to its nominal voltage according to the reference desired value in AC voltage regulator with small overshoot shown in Figure 29. Also, the STATCOM has the ability to achieve DC voltage regulation of the DC-link as shown in Figure 30. Noting that the transmission line impedances at the side of DFIG and PCC are ($R_{T.L.} = 9\ m\Omega$ and $L_{T.L.} = 0.5\ mH$) and ($R_{T.L.} = 0.0179\Omega$ and $L_{T.L.} = 99\ \mu H$), respectively. The power grid impedance is ($R_G = 0.10472\ m\Omega$ and $L_G = 1\ \mu H$).

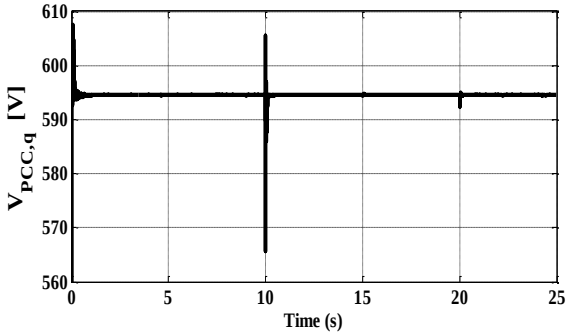

Fig. 29 The PCC voltage swell compensation at the DFIG wind turbine with STATCOM.

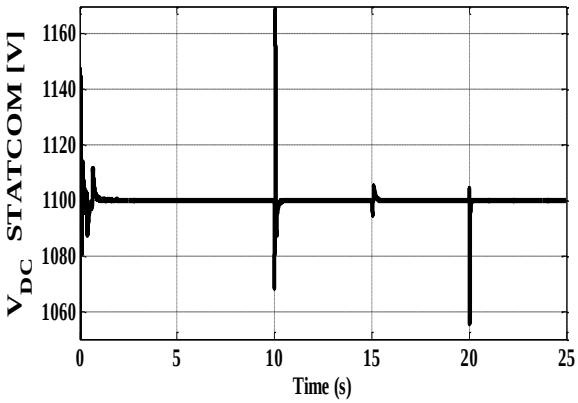

Fig. 30 The DC-link voltage of STATCOM during voltage swell compensation.

The same SAPF in case 1 is used instead of STATCOM in order to inject into PCC the required reactive power (absorbing) based on three phase sudden capacitive load currents by SAPF actual currents for the same conditions.

As a result, the PCC voltage is regulated to be near from its nominal voltage in the period from 15 second to 20 second but in the period between 10 second to 15 second the voltage is decreased compared to the voltage in Figure 15 in the same period and not at its nominal voltage level because a small difference happened when the wind speed is varied to 11 m/s.

Figure 31a illustrates the PCC voltage before and after using SAPF. Figure 31b shows the PCC voltage for both SAPF and STATCOM after connection. It is clearly that the STATCOM is achieved better results than SAPF due to its AC voltage magnitude regulator. But SAPF depends on sudden capacitive load calculations, the overall system of SAPF is affected by any change of the wind speed and it works according to this change of the wind speed

according to its load calculations and hasn't the ability to restore the nominal voltage.

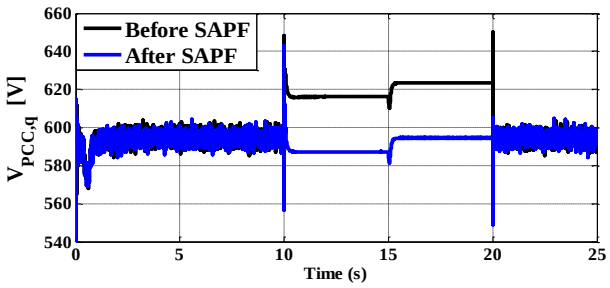

(a)

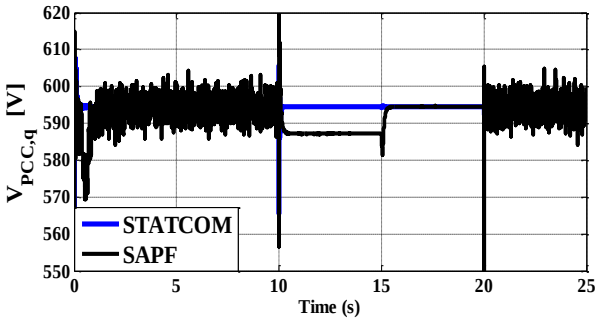

(b)

Fig. 31 The PCC voltage response
(a) Before and after SAPF connection, (b) After connection for both SAPF and STATCOM.

14. Conclusion

This work addressed a comparative analysis of two different control schemes for shunt devices installed in three phase distribution systems has been demonstrated. The performance of these control techniques has been analyzed for voltage swell and sag mitigations using time domain MATLAB/Simulink software. Under grid disturbances, the DFIG accomplished MPPT control technique. The proposed design of STATCOM under variation of wind speed in all cases achieved voltage regulation of DFIG wind turbine. In contrast, the suggested design of SAPF based on reactive power calculations of the load accomplished the voltage regulation of DFIG wind turbine around the nominal voltage. The simulation outcomes show that the proposed controller of STATCOM has the ability to regulate and enhance the PCC voltage response at DFIG wind turbine at its nominal voltage compared to SAPF based on its load calculations. STATCOM achieved better results than SAPF in regulation of the PCC voltage response at DFIG wind turbine due to its controller. Also, the results of both shunt devices give good performance and improve the system stability.

References

[1] Sompracha, C., Jayaweera, D., Tricoli, P. "*Particle swarm optimization technique to improve the energy efficiency of doubly-fed induction generators for wind turbines*", IET Renew. Power Gener., No. 18, pp.4890-4895, 2019.
https://doi.org/10.1049/joe.2018.9348

[2] Touzene, A., Yahyai, S.A., Melgani, F., "*Smart grid resources allocation using smart genetic heuristic*", IJCAT, Vol. 63, No. (1-2), pp.125-134, 2020.
https://doi.org/10.1504/IJCAT.2020.107918

[3] Slama, S., Errachdi, A., Benrejeb, M. "*Online MRAC method using neural networks based on variable learning rate for non-linear systems*", IJCAT, Vol. 60, No. 3, pp.215 – 224, 2019.
https://doi.org/10.1504/IJCAT.2019.100296

[4] Chien, T. H., Huang, Y. C. and Hsu, Y. Y. "*Neural Network-Based Supplementary Frequency Controller for a DFIG Wind Farm*", Energies, Vol. 13, No. 5320, pp.1-15, 2020.
https://doi.org/10.3390/en13205320

[5] Ahyaten, S. and Jalal El Bahaoui, J. "*Modeling of Wind Turbines Based on DFIG Generator*", Proceedings, Vol. 63, No. 16, pp.1-8, 2020.
https://doi.org/10.3390/proceedings2020063016

[6] Gomez, L. A. G., Grilo, A. P., Salles, M. B. C. and Filho, A. J. S. "*Combined Control of DFIG-Based Wind Turbine and Battery Energy Storage System for Frequency Response in Microgrids*", Energies, Vol. 13, No. 894, pp.1-17, 2020.
https://doi.org/10.3390/en13040894

[7] Kumar, V., Pandey, A. S. and Sinha, S. K. "*Stability Improvement of DFIG-Based Wind Farm Integrated Power System Using ANFIS Controlled STATCOM*", Energies, Vol. 13, No. 4707, pp.1-18, 2020.
https://doi.org/10.3390/en13184707

[8] Chauvin, M. A., Kavrakov B. S., Buele, J. and Aldás, J. V. "*Static Reactive Power Compensator Design, Based on Three-Phase Voltage Converter*", Energies, Vol. 14, No. 2198, pp.1-16, 2021.
https://doi.org/10.3390/en14082198

[9] Bialas, H., Pawelek, R. and Wasiak, I. "*A Simulation Model for Providing Analysis of Wind Farms Frequency and Voltage Regulation Services in an Electrical Power System*", Energies, Vol. 14, No. 2250, pp.1-17, 2021.
https://doi.org/10.3390/en14082250

[10] Almohaimeed, S. A. and Abdel-Akher, M. "*Power Quality Issues and Mitigation for Electric Grids with Wind Power Penetration*", Appl. Sci., Vol. 10, No. 8852, pp.1-24, 2020.
https://doi.org/10.3390/app10248852

[11] Ali, H.H., El Basuony, G.S. and Kamal, N.A. "*Maximum power production operation of doubly fed induction generator wind turbine using adaptive neural network and conventional controllers*", Int. J. Computer Applications in Technology, Vol. 65, No. 2, pp.173–187, 2021.
http://dx.doi.org/10.1504/IJCAT.2021.114984

[12] Ali, H.H., Kamal, N.A. and El Basuony, G.S. "*Two-Level Grid-Side Converter-Based STATCOM and*

Shunt Active Power Filter of Variable-Speed DFIG Wind Turbine-Based WECS Using SVM for Terminal Voltage", Int. J. of Service Science, Management, Engineering, and Technology, Vol. 12, No. 2, pp.169–202, 2021.
https://dx.doi.org/10.4018/ijssmet.2021030110

[13] Akanto, J. M., Hazari, Md. R. and Abdul Mannan, M. "*LVRT and Stability Enhancement of Grid-Tied Wind Farm Using DFIG-Based Wind Turbine*", Appl. Syst. Innov., Vol. 4, No. 33, pp.1-14, 2021.
https://doi.org/10.3390/asi4020033

[14] Alhato, M. M. and Bouallègue, S. "*Direct Power Control Optimization for Doubly Fed Induction Generator Based Wind Turbine Systems*", Math. Comput., Vol. 24, No. 77, pp.1-27, 2019.
https://doi.org/10.3390/mca24030077

[15] Kumar, N., Gaidhane, V.H., Mittal, R.K "*Cloud-based electricity consumption analysis using neural network*", IJCAT, Vol. 62, No. 1, pp.45 – 56, 2020.
https://doi.org/10.1504/IJCAT.2020.103917

[16] Shan, C. "*Computer-based outdoor sport sustainable development using wavelet neural network*", IJCAT, Vol. 61 No. 1/2, pp.112 – 117, 2019.
https://doi.org/10.1504/ijcat.2019.102108

[17] Sitharthan, R., Karthikeyan, M., Sundar, D.S., Rajasekaran, S. "*Adaptive hybrid intelligent MPPT controller to approximate effectual wind speed and optimal rotor speed of variable speed wind turbine*", ISA Transactions, Vol.96, pp.479-489, 2019.
https://doi.org/10.1016/j.isatra.2019.05.029

[18] Vaidyanathan, S., Pehlivan, I., Dolvis, L.G., Jacques, K., Alcin, M., Tuna, M., Koyuncu, I. "*A novel ANN-based four-dimensional two-disk hyperchaotic dynamical system, bifurcation analysis, circuit realisation and FPGA-based TRNG implementation*", IJCAT, Vol. 62, No. 1, pp.20 – 35, 2020.
https://doi.org/10.1504/IJCAT.2020.103921

[19] Zhong, L. P. "*A new topology and power control of grid-connected photovoltaic array*"", IJCAT, Vol. 61 No. 4, pp.287 – 291, 2019.
https://doi.org/10.1504/ijcat.2019.103292

[20] Qi Wang, Bin Wang, Wanwan Xu and Jiapan Xu . "*Research on STATCOM for reactive power flow control and voltage stability in microgrid*", 13th IEEE Conference on Industrial Electronics and Applications (ICIEA), 2018.
https://doi.org/10.1109/ICIEA.2018.8398126

[21] Priya Singh, S K Parida, Baru Chauhan and Niraj Choudhary. "*Online Voltage Stability Assessment Using Artificial Neural Network considering Voltage stability indices*", 21st National Power Systems Conference (NPSC), 2020.
https://doi.org/10.1109/NPSC49263.2020.9331954

[22] Zhou, Z., Liu, B., Wang, W., Wang, H. "*Research on grid-connected photovoltaic inverter based on quasi-PR controller adjusting by dynamic diagonal recurrent neural network*", IJCAT, Vol. 61, No. 3, pp.220 – 228, 2019.
https://doi.org/10.1504/ijcat.2019.102846

[23] Mohamed A. Ali. "*Hybrid technique for testing IEC 61850 based IEDs of distance protection*", Nineteenth International Middle East Power Systems Conference (MEPCON), 2017.
https://doi.org/10.1109/MEPCON.2017.8301205

[24] Sagar S. Patil, R. A. Metri and Omkar K. Shinde. "*Shunt active power filter for MV 12-pulse rectifier using PI with SMC controller*", International Conference on Circuit, Power and Computing Technologies (ICCPCT), 2017.
https://doi.org/10.1109/ICCPCT.2017.8074260

[25] Seyed Abbas Taher, Mohammad Hosein Alaee and Zahra Dehghani Arani . "*Model predictive control of PV-based shunt active power filter in single phase low voltage grid using conservative power theory*", 8th Power Electronics, Drive Systems & Technologies Conference (PEDSTC), 2017.
https://doi.org/10.1109/PEDSTC.2017.7910332

[26] Harsha Vanjani, U. K. Choudhury, Meha Sharma and Bhavesh Vanjani. "Takagi-sugeno *(TS)-type fuzzy logic controller for three-phase four-wire shunt active power filter for unbalanced load*", IEEE 7th Power India International Conference (PIICON), 2016.
https://doi.org/10.1109/POWERI.2016.8077227

[27] Azar, A.T., Serrano, F.E., Flores, M.A., Vaidyanathan, S., Zhu, Q. "*Adaptive neural-fuzzy and backstepping controller for port-Hamiltonian systems*", IJCAT, Vol. 62, No. 1, pp.1 – 12, 2020.
https://doi.org/10.1504/IJCAT.2020.103894

REAL-TIME IMPLEMENTATION OF A SINGLE-PHASE ASYNCHRONOUS MOTOR DRIVE FEEDING WITHIN AN OPEN ENERGY SOURCE

Essamudin A. EBRAHIM **and** **Emad SWEELM**
Power Electronics and Energy Conversion Department, Photovoltaic Department,
Electronics Research Institute (ERI)
Joseph Tito Street, Huckstep, Qism El-Nozha, Cairo Governorate, P. O. Pox 16222, Cairo, Egypt
essamudin@eri.sci.eg, emadsweelem@eri.sci.eg

Abstract: *A modified nanogrid (MnG) is a very small scalable grid with a low power single-input multi-output (SIMO) inverter. This inverter simultaneously produces both AC and DC currents, such as the switched boost inverter (SBI) and the z-source inverter. These inverters are suitable for low-power loads such as home appliances that use fractional horse-power motors as single-phase asynchronous drives. Thus, this article proposes a single-phase induction motor powered from a modified nanogrid that involves multiple types of inverters such as a SBI and a ZS inverter. The modified nanogrid is mainly dependent on photovoltaic (PV) as a renewable resource. Thus, this manuscript involves a full design for this proposed grid with its maximum power point tracking (MPPT) and the mathematical models for motor drive with both a SBI and a ZSI. Time-varying speed trajectories are proposed to test the robustness of the proposed drives relative to the fluctuation of PV-parameters like its irradiance. Test results are obtained using the Matlab/ Simulink software package and a comparison with the traditional sinusoidal pulse width modulation (SPWM) inverter as a single-input single-output inverter (SISOI). The results indicate that the proposed single-input multi-output inverters are suitable for driving these motors through start-up and operation, although the DC-link voltage is minimized. Furthermore, the proposed system is experimentally implemented with OPAL RT-4510v real-time hardware in the loop (HIL), rapid control prototyping, OP-8660 HIL controller and data acquisition platform.*

Key words*: DC-modified nanogrids (DC-MnG), Open Energy Source (OES), Real-time simulator (RTS), Single-phase asynchronous motor (SPAM), Switched Boost Inverter (SBI),* Z-Source Inverter (ZSI),

1. Introduction

Induction motors are still widely used in most industrial, commercial and electrical household applications. They are robust, cost-effective, maintenance-free, and have a high power-to-weight ratio [1]-[3]. In contrast, single-phase fractional horsepower induction motors are widely used in a variety of household appliances such as refrigerators, washing machines, and water pumping [4]-[7].

There are several types of these motors are classified according to their starting such as: capacitor starting, capacitor-starting capacitor running, split-phase and shaded pole induction motors [8].

In the past and to date, many efforts have been made to improve and enhance the performance of these motors as variable speed drives. These proposed techniques use a field-oriented vector control for speed tracking such as in [9]-[13].

However, these motors can be powered from the main grid or from an open energy source (OES). The open energy source is a combination of a huge number of DC-nano-grids (DCnGs) that have connected to one another via a DC-link. They contain renewable resources – such as PV, wind, fuel cells, batteries – which are used to power both the DC and AC loads through converters. The traditional nano-grid involves a two-stage converter. It is known as a single-input single output (SIMO) converter. This type uses many components and requires many circuitry to protect [14]-[15]. On the other hand, the DCMnGs involve single-input multi-output converters that simultaneously produce both the DC and AC currents [16],[17]. However, the DC input voltage to the inverter plays a significant rule on its AC output voltage. If the DC-nanogrid is a standalone/ off-grid connection, its AC-output voltage must be well controlled to ensure the sufficient voltage value needed to control the speed and torque of these motors. Most renewable energy sources such as PVs produce a variable DC-voltage based on their irradiation. This DC-voltage is directly proportional to the input radiation. Therefore, if it is cloudy or dark, the AC output voltage will be reduced. Depending, the performance of the asynchronous motor will be

affected during starting and running. Thus, it should increase the AC-input voltage to maintain the torque and speed with proper values keeping the motor running safe with the load. The SBI and ZSI can do that [18]-[23]. Thus, this article introduces a single-phase induction motor (SPIM) with starting capacitor - powered from an open energy source through a single input multi-output inverter (SIMOI). The voltage/ frequency control technique is offered to maintain the internal torque constant through speed change. A robust DC-link voltage controller is provided to maintain the DC-link voltage of the SBI constant. In addition, z-source inverter will be compared with the SBI and the conventional (SPWM) as a single-input single-output (SISO) inverter. The best will be implemented in real-time with the help of OPAL RT-hardware in the loop (HIL) with rapid control prototyping platform. This real-time emulator will be connected through OPAL OP8660 HIL controller and data acquisition module. The real time results are also obtained with the help of the Matlab/ Simulink program for a gradual speed trajectory with different PV-supplies dependent on their insolation. This manuscript is organized a long the following lines: section 1 is introduction. The proposed system with SIMO inverters and the mathematical model of the motor are elaborated in sec. 2. Section 3, provides an explanation for both SBI and z-source inverter. The proposed master and slave controllers for both speed and maximum power point tracking (MPPT) are detailed in sections 4 and 5 respectively. A comparison with the simulation results for the proposed inverter and other systems is conducted in section 6. Real-time emulation of the developed and selected system is implemented using OPAL- RT in section 7. Finally, Section 8 summarizes the research and its conclusion.

2. The proposed SPAM-drive control system

The proposed system comprises SPAM with its two windings, the open energy system (OES), and the controller (as shown in Figure 1). In the following sections, each subsystem will be explained in some detail.

2.1. Single phase asynchronous motor model

This machine is equipped with two windings: main and auxiliary. There are four modes of operation as: split-phase, capacitor starting, capacitor-starting capacitor-running, and main and auxiliary winding mode. In this study, a capacitor-starting single-phase induction motor (SPIM) is used.

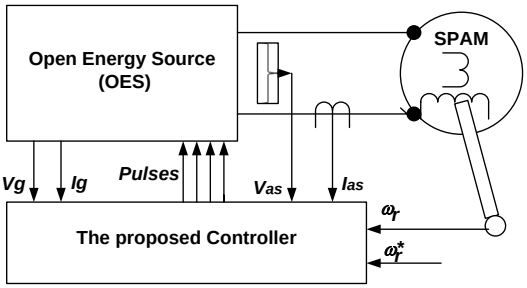

Fig. 1 the proposed SPAM- drive fed from an OES

2.1.1. The mathematical model of SPIM

The dq-reference frame equations for the electrical model for both stator and rotor of SPIM are [24]:

$$V_{sd} = (R_{sd} + pL_{sd}).i_{sd} + pL_{md}.i'_{rd} \quad (1)$$

$$V_{sq} = \left(R_{sq} + pL_{sq}\right).i_{sq} + pL_{mq}.i'_{rq} \quad (2)$$

$$0 = (p.L_{md}).i_{sd} - (\frac{N_d}{N_q}.\omega_r.L_{mq}).i_{sq} + (R'_{rd} + pL'_{rd}).i'_{rd} - (\frac{N_d}{N_q}.\omega_r.L'_{rq}).i'_{rq} \quad (3)$$

$$0 = \left(p.L_{mq}\right).i_{sq} - (\frac{N_q}{N_d}.\omega_r.L_{md}).i_{sd} + \left(R'_{rq} + pL'_{rq}\right).i'_{rq} - (\frac{N_q}{N_d}.\omega_r.L'_{rd}).i'_{rd} \quad (4)$$

Where, $L_{sd} = L_{lsd} + L_{md}$ (5)

$$L_{sq} = L_{lsq} + L_{mq} \quad (6)$$

$$L'_{rd} = L'_{lrd} + L'_{md} \quad (7)$$

$$L'_{rq} = L'_{lrq} + L'_{mq} \quad (8)$$

The instantaneous electro-magnetic internal torque of the motor can be computed as:

$$T_e = \frac{P}{2}.\frac{N_d}{N_q}.L_{mq}.(i_{sq}.i'_{rd} - i_{sd}.i'_{rq}) \quad (9)$$

The dynamic equation is:

$$p.\omega_r = \frac{1}{J_m}.(T_e - T_l) \quad (10)$$

Where, V_{sd}, V_{sq} are the stator voltage in dq-axis frame, R_{sd}, R_{sq} are the stator resistance in dq-axis frame. $L_{sd}, L_{sq}$are the stator inductance in dq-reference frame, p is the differential operator (d/dt), i_{ds}, i_{qs} are the stator currents in dq-frame, L_{md}, L_{mq} are the mutual inductances in dq-frame, N_d, N_q are the effective turns in dq-frame, R'_{rd}, R'_{rq} are the rotor resistance referred to stator in dq-frame, i'_{rd}, i'_{rq} are the rotor current referred to stator in dq-frame, $L'_{rd}, L'_{rq}$are the rotor inductance referred to stator in dq-frame, ω_r is the rotor angular speed, L'_{lrd}, L'_{lrq} are the leakage inductance of rotor in dq-frame, L_{lsd}, L_{lsq} are the leakage inductance of stator in dq-frame, T_e is the motor electrical internal torque, P is the number of pair pole of the motor, and J_m is the motor inertia.

In the above equations, the auxiliary winding represents d-axis components and the main winding represents the q-axis components. So, the supply voltage V_{supply} equal to V_{sq} as:

$$V_{supply} = V_{sq} \quad (11)$$

$$V_{sd} = V_{supply} - \frac{1}{C}\int i_{sd}dt \quad (12)$$

Where, C is the capacitor connected for starting.

2.2. An Open Energy Source (OES)

OES consists of several huge nanogrids that are connected to each other through a DC-link. These interconnected nanogrids are controlled with a smart system to manage the flow of power to each other. Each nanogrid has a power converter to produce both DC and AC supplies. The classical nanogrid uses a two-stage converter-inverter set. But, the modified nano-grid contains a SIMO-inverter. There are two types of SIMO-inverters: switched boost inverter (SBI) and z-source inverter (ZSI). For this study, the PV is selected as a renewable source used to power all grids. An array of PV is arranged as number of series N_s and parallel N_p modules are connected with each other to provide the required power with the appropriate terminal voltage. In this case, the SunPower SPR 305WHT (appendix A) module is used. Also, we selected 2 in series and 10 in parallel to supply about 6 KW.

3. Single input multi-output inverter (SIMOI)

Through the following lines, both the SBI and ZSI with some detail will be explained. Furthermore, a comparison between SIMOI and SISOI (such as the sinusoidal PWM inverter) will performed. Thus, SISOI will also be brief explained.

3.1. Switched boost inverter (SBI)

As shown in Figure 2, SBI consists of five IGBTs, 2-diodes, one coil, and one capacitor to transmit the power from the PV-source to the motor. It depends on two modes of operation: the shoot-through and non-shoot through techniques to turn-on and off switches. This technique protects all switches from short-circuit current and there is no need to dead-time delay circuit to avoid overlapping between two IGBTs on the same inverter leg. Its output can be controlled directly to upward or downward the DC and /or AC voltage values. Thus, when it is supplied from the PV-intermittent source, it increases its AC-output voltage to sufficient value that produces the torque required to start-up the motor with a pre-scribed speed.

In the non-shoot through state, $t_{off} = (1\text{-}D)\times T_s$, the switch S is turned off and the inverter bridge is represented by a current source. Where, t_{off} is the turn off time for the switch S, D is the duty ratio, and T_s is the periodic time for switch S equal ($t_{off} + t_{on}$) and t_{on} is the turn-on time. Now, the voltage of the renewable source (i.e., PV)(V_g), and the energy stored in the inductor L together will supply the inverter and the capacitor through diodes D_a and D_b.

The inductor current in this interval equals the capacitor charging current added to the inverter input current. Note that the inductor current is assumed to be sufficiently high for the continuous conduction of diodes D_a and D_b for the entire interval. The inductor current (I_L) will exceed linearly to a value equal to that of the capacitor charging current added to the DC load current and the inverter input current (assuming continuous conduction mode) for the interval $((1\text{-}D)\times T_s)$. The SBI utilizes the shoot-through interval of the H-bridge to appeal to the boost operation. So, the traditional PWM control technique of the traditional voltage source inverter (VSI) should be modified to incorporate the shoot-through state to be suitable for the SBI [25].

The PWM scheme for SBI is developed based on the traditional sine-triangle PWM with voltage switching level. This technique has been illustrated during positive and negative half cycles of the sinusoidal modulation signal v_m(t) and is given in details in [26]-[28]. However, the DC-output voltage of SBI can be computed as:

$$\frac{V_{DC}}{V_g} = \frac{1-D}{1-2D} \quad (12)$$

Where, V_{DC} is the DC-link voltage of the inverter. It should be noted that the shoot-through state of the inverter bridge will not affect the harmonic spectrum of the inverter's output voltage if the sum of shoot-through duty ratio (D) and the modulation index (M) is less than or equal to unity.

$$M + D \leq 1 \quad (13)$$

Hence, the values of M and D are chosen according to the peak value of the AC output voltage $\tilde{V}_{AC}$ that is given by:

$$\tilde{V}_{AC} = M.V_{DC} = M.\frac{1-D}{1-2D}.V_g \quad (14)$$

3.2. Z-Source inverter

As shown in Figure 3, it contains more passive elements than SBI. It implies two identical coils and capacitors – for symmetrical one – to prevent short-circuit current when the switches are conducting and 4- IGBTs as a classical inverter and one diode to block reverse current. There are three modes of

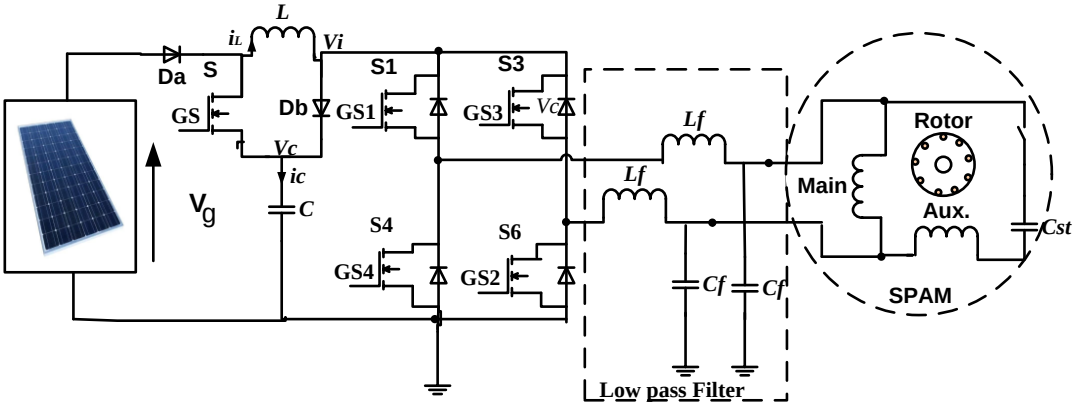

Fig. 2 SPAM fed from PV-array via a SBI

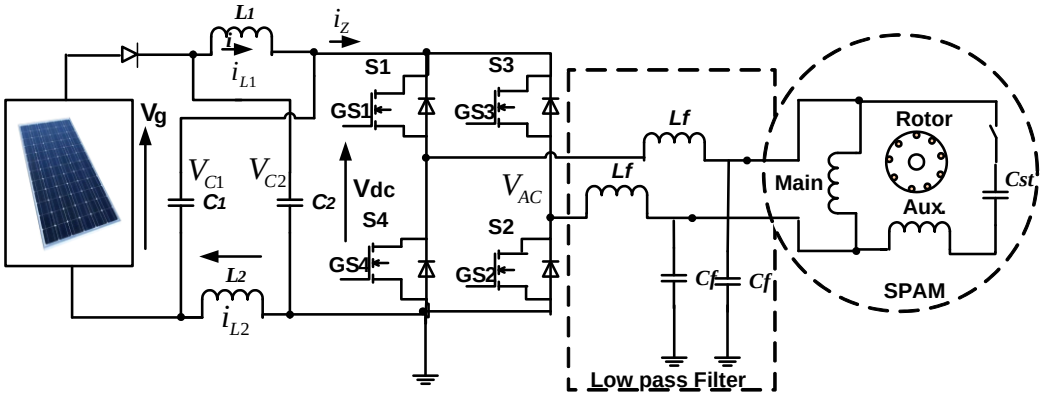

Fig. 3 SPAM fed from PV-array via a ZSI

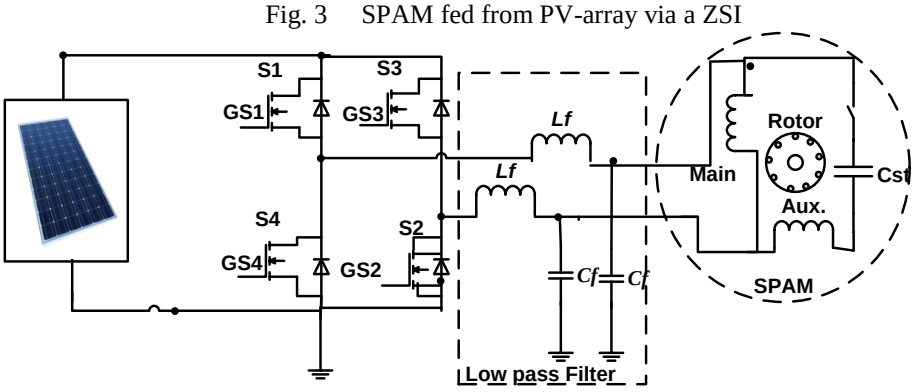

Fig. 4 SPAM fed from PV-array via a SISO inverter

Table 1. Switching modes of z-source inverter operation

Switching States (Modes)	S_1	S_4	S_3	S_2	Output voltage
Active state	1	0	0	1	Finite Voltage
	0	1	1	0	
Zero state	1	0	1	0	Zero
	0	1	0	1	
Shoot-through state	1	1	S_3	S_2	Zero
	S_1	S_4	1	1	
	1	1	1	1	

operation for z-source inverter: the active state, zero state, shoot-through zero state. Table 1 describes these operating states.

The voltage across each capacitor is equal and the current through each coil is also equal. So, in shoot-through state, $V_Z = 0$, if the duty ratio D_Z is equal to (T_S/T), where T_s is the total shoot-through time through one cycle and T is the periodic time, then, applying Kirchhoff's Lows:

$$\begin{cases} v_{L1} = v_{C1} = v_{L2} = v_{C2} \\ i_{C1} + i_{L1} = i_{C2} + i_{L2} = 0 \\ i_Z = i_{L1} - i_{C2} = i_{L2} - i_{C1} \end{cases} \quad (15)$$

$$\begin{cases} v_{L1} = v_{L2} = V_g - v_{C1} = V_g - v_{C2} \\ V_{dc} = 2.v_{C1} - V_g \\ i_{L1} = i_{C2} + i_Z \\ i_{L2} = i_{C1} + i_Z \end{cases} \quad (16)$$

$$\frac{d}{dt}\begin{bmatrix} i_{L1}(t) \\ i_{L2}(t) \\ v_{C1}(t) \\ v_{C2}(t) \end{bmatrix} = \begin{bmatrix} 0 & 0 & \frac{(2.D_Z-1)}{L_Z} & 0 \\ 0 & 0 & 0 & \frac{(2.D_Z-1)}{L_Z} \\ \frac{-D_Z}{C_Z} & \frac{1-D_Z}{C_Z} & 0 & 0 \\ \frac{1-D_Z}{C_Z} & \frac{-D_Z}{C_Z} & 0 & 0 \end{bmatrix} \cdot \begin{bmatrix} i_{L1}(t) \\ i_{L2}(t) \\ V_{C1}(t) \\ V_{C2}(t) \end{bmatrix} + \begin{bmatrix} \frac{1-D_Z}{L_Z} \\ 0 \\ \frac{1-D_Z}{L_Z} \\ 0 \end{bmatrix} . V_g + \begin{bmatrix} \frac{D_Z-1}{C_Z} \\ \frac{D_Z-1}{C_Z} \end{bmatrix} . i_Z \quad (17)$$

The steady state parameters can be obtained by setting equation (17) to zero:

The state-space equation for the Z-inverter can be written as follows:

$$\begin{cases} v_{C1} = v_{C2} = \frac{1-D_Z}{1-2.D_Z} . V_g = V_{dc} \\ V_{dcp} = \frac{1}{1-2.D_Z} . V_g \\ i_{L1} = i_{L2} = \frac{1-D_Z}{1-2.D_Z} . i_Z \end{cases} \quad (18)$$

According to the equation (18), the AC- peak output voltage of the inverter can be determined as:

$$\hat{V}_{AC} = \frac{\hat{V}_m}{\hat{V}_{Car}} . \bar{V}_{dc} = m_a . \left(\frac{D_Z-1}{2.D_Z-1}\right) . \bar{V}_{dc} \quad (19)$$

Where, $\hat{V}_m$ is the peak value of the modulation wave (i.e., sine wave), $\hat{V}_{Car}$ is the peak value of the carrier wave (i.e., triangular wave), m_a is the modulation index of the inverter, $\bar{V}_{dc}$ is the dc-link voltage of the inverter. For more details about two-level z-source inverter, it can be referred to [29]-[32].

3.3. THE SINUSOIDAL PWM-SISOI

The sinusoidal-PWM inverter is considered as a single-input single-output inverter which has only one DC-input voltage and only one AC-output voltage. It can be supplied directly from the DC-source such as PV or battery bank as shown in Figure 4.

4. THE MASTER SPEED CONTROL AND MPPT ALGORITHM

The block diagram for the master speed controller is shown in figure 5. The controller strategy depends on the variation of both voltage and frequency with the same rate – as a scalar value – to keep the motor internal torque constant. The reference frequency and voltage can be computed according to the following equations:

$$f_r = \frac{PN_r}{60} \quad (20)$$

$$e(t) = (f_r^* - f_r) \quad (21)$$

Where P is the number of pair-poles, f_r^*, f_r is the rotor reference and actual frequency and e is the error signal. The output of the PI-controller is the slip-frequency f_{slip}:

$$f_{slip} = K_p.e(t) + K_i \int e(t)dt = K_p.(f_r^* - f_r) + K_i \int (f_r^* - f_r)dt \quad (22)$$

Then, the reference synchronous frequency f_s^* of the motor can be computed as:

$$f_s^* = f_r + f_{slip} \quad (23)$$

The reference voltage peak- value V_m^* :

$$V_m^* = K_{vf}.f_s^* \quad (24)$$

Where, K_{vf} is a constant depends on flux and selected according to the rated frequency and voltage of the machine. For this work, this value is equal 2.4 for the test machine.

The main purpose of this control is to generate the modulation signal required to produce IGBTs gating signals for all inverters. So, the sinusoidal signal can be computed – according to the block diagram of Fig. 6-a as:

$$v_m(t) = V_m^*.Sin\ \theta_r^* \quad (25)$$

Where, θ_r^* is the reference position angle and can be computed from the reference frequency as:

$$\theta_r^* = \int \omega_r^* . dt = \int 2.\pi.f_r^* . dt \quad (26)$$

This modulated signal is compared with the triangle signal according the modulation index M as:

$$M = \frac{V_m^*}{V_P^*} \quad (27)$$

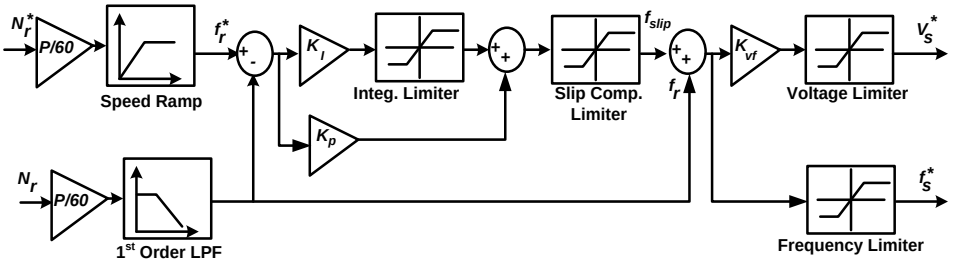

Fig.5 The master controller (sequence of scalar speed control V/f block diagram)

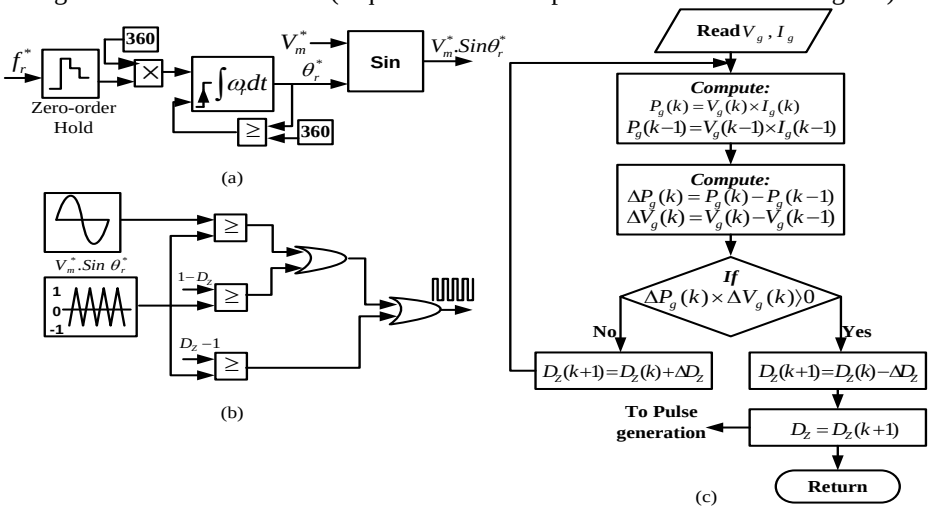

Fig. 6 Slave control: (a) MPPT flow chart (b) modulator-signal generation
(c) modified sine triangle PWM generation

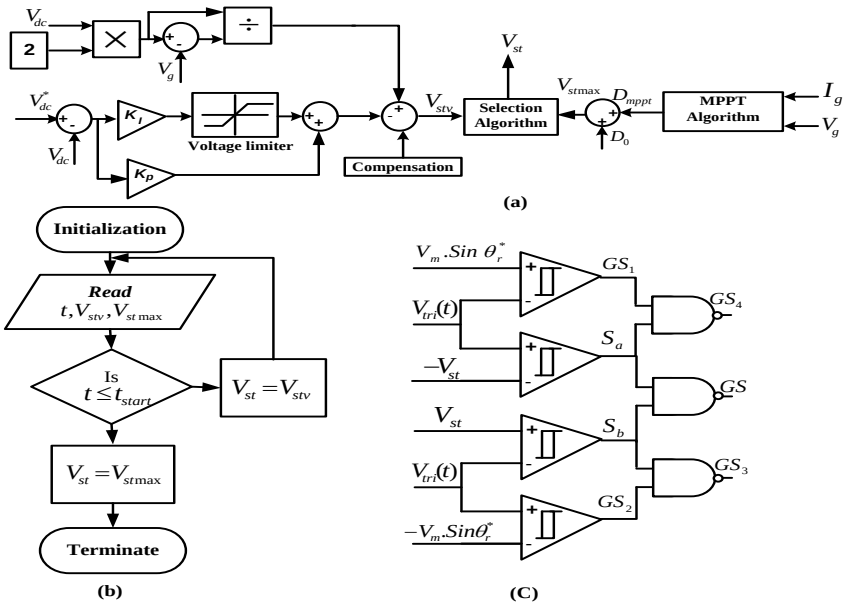

Fig. 7 SBI-Voltage control (a) DC-link voltage control (b) starting algorithm (c) logic gating signals

Table 2 the main parameters for both Z-source and SBI inverters

SBI parameters [16]			ZSI-parameters [33]		
parameter	value	unit	parameter	value	unit
Inductance of main inductor (L)	5	mH	Inductance of main coils ($L_1 = L_2$)	1	mH
Capacitance of main capacitor (C)	1500	μF	Capacitance of main capacitors ($C_1 = C_2$)	1300	μF
Inductance of filter inductor (L_f)	1	mH	Inductance of filter inductor (L_f)	1	mH
Capacitance of filter capacitor (C_f)	150	uF	Capacitance of filter capacitor (C_f)	150	uF

Where, V_P^* is the peak value of the carrier-triangular wave – as shown in Fig. 6-b.This technique is used for speed control for all compared inverters. But, for SIMOIs, another parameter is used with the combination of *M* to control the voltage of DC-link and this will directly affect the motor speed and torque. This parameter is the duty ratio *D*, this can be controlled according to the maximum power point tracking (MPPT) for the PV-array. In this research, the hill-climbing algorithm is used as a MPPT. The flow chart for this algorithm is shown in fig. 6-c. The same MPPT algorithm is used for both z-source and SBI inverters. In z-source inverter the duty ration D_z is used in shoot-through period to control the DC-link voltage as shown in Fig. 6-b. But, in the SBI, a proposed DC-link voltage controller is used.

5. DC-LINK VOLTAGE CONTROLLER OF SBI

The block diagram of the DC-link voltage of SBI is depicted in fig. 7-a. This block produces the voltage level control signal (V_{ST}) that is needed for shot-through signals controlling the switch (*S*).The control algorithm depends on introducing a mathematical model for the actual value of V_{ST} that can be computed as follows [16]:

From the strategy and analysis of the SBI, $+V_{ST} = V_p\,(1-D)$, $-V_{ST} = -\,V_p\,(1-D)$, so:

$$D = 1 - \frac{V_{ST}}{V_P} \quad (28)$$

If $V_P = 2$, by substituting in eqn. 28,

$$D = 1 - \frac{V_{ST}}{2} \quad (29)$$

By substituting in eqn. 12 from 29,

$$V_{ST} = \frac{2*V_{dc}}{2*V_{dc}-V_g} \quad (30)$$

The block diagram for this model is drawn as a reference according to Eqn. 30. Also, its output is added to the output of the PI-controllers used for voltage control loop with compensation - as shown in Figure 7-a. Two operating modes are offered. The first one is proposed through starting to keep the voltage of DC-link constant. This increases the voltage to its maximum value and the second algorithm achieves MPPT as shown in Fig. 6-c. The output control signal of the voltage control is denoted by V_{stv}. On the other hand, the control signal in case of MPPT is denoted by V_{stmax}.The flow chart of this algorithm is shown in Fig. 7-b. This algorithm depends mainly on the starting time t_s. If the time is less than or equal to the motor start-up time, the controller maintains the motor voltage constant through start-up. After this, the operation time increases to more than start-up time, thus activating the MPPT algorithm. The digital logic gates required to generate the 5-control gating signals for the IGBTs of the SBI is shown in Fig. 7-c. For more details referred to [15],[16].

6. Simulation results and discussion

To test the robustness of the proposed system, a comparison between the SIMO and SISO inverters is performed. Two SIMO inverters are tested (i.e., z-source and SBI). The SISO inverter is the sinusoidal PWM which is compared to the other two types. The same motor-speed controller – proposed in Section 4 is used for all types with the same parameters. The gain parameters for PI-speed controller are: $K_p = 3,$ and $K_i = 10$. The name plate date of the fractional-horse power test single-phase induction motor and its main parameters are included in appendix B [8]. The PV-array consists of two modules in series and ten in parallel with irradiance varies from 200 to 1000 w/m² at 25° C. The parameters of PI-controller for DC-link voltage control of SBI is: K_p =0.00001 and $K_i = 0.00005$ with limiting block values ∓ 2. All parameters are selected according to Ziegler-Nichols Formula. The main parameters for both z-source and SBI inverters are presented in Table 2. The switching frequency for all inverters equal 10 KHz. All systems are implemented using the Matlab/Simulink software package (ver. R2018a) [33]. To test the robustness of the proposed system against the DC-link input variation for all inverters, several cases are investigated. The first case is designed using a constant battery input voltage with a value of 126 V. The second case, when all inverters are supplied from a PV-array with a constant irradiance (1000 w/m²) with a 126V output. The third case, is the study of the effect of irradiation on the motor performance when its value is reduced from 1000 to 200 w/m² by starting the motor. Furthermore, the robustness of the controller is also tested by starting, accelerating, and decelerating of the motor. The speed trajectory is considered initially as a ramp with acceleration to increase the motor speed linearly to 1500 rpm across 1 second of start time. Then, the motor reaches to steady state with a constant speed for another second and after that the motor decelerates to 750 rpm over the period (2 to 2.5 seconds). Finally, the motor reaches a speed of 750 rpm and continues to operate at this speed as a steady-state value. The test machine is a single-phase staring-capacitor induction motor. The starting capacitor is used during start-up until the motor reaches to 80 % of its nominal speed (i.e., 1800 rpm).

6.1. Case 1: The motor is powered by a battery bank through the inverters

In this case, the motor is powered by a battery bank - with a constant value equal to 126V- through the aforementioned three inverters. Fig. 8 illustrates the proposed speed trajectory for motor power across all inverters. As can be seen, they all showed a good response with some overshooting compared to the reference speed trajectory. In addition, it can be noted that the speed trajectory with SBI is under damping with minimum overshooting in comparison with the other two types. Figure 9 demonstrates the total stator currents with all inverters. At 80 % of the synchronous speed (i.e., 1440 rpm) the capacitor is cut off. The waveform of internal electric torque of the motor is illustrated as an instantaneous value given in Fig. 10. At start-up, the motor torque is increased until the motor reaches steady state and then decreases to a nominal value.

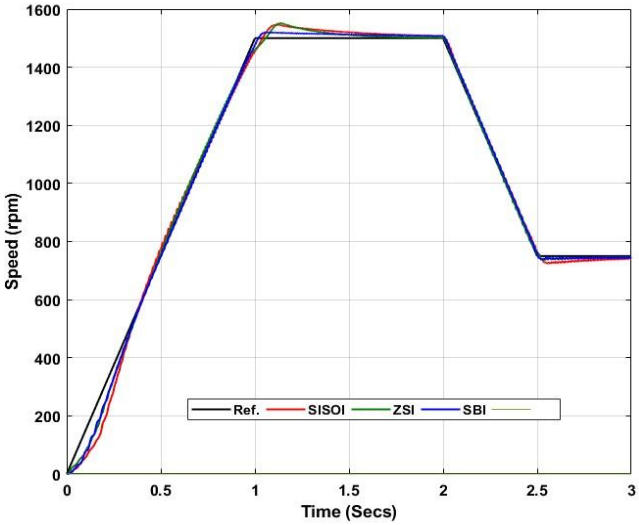

Figure 8 actual and reference forward speed trajectories for inverters with battery bank

6.2. Case 2: The motor is powered by a PV-array without shade

In this case, the motor is delivered by a PV-array through the selected inverters. In this case the PV-irradiance is assumed to be constant without shade and equal to 1000 W/m² - as shown in Figure 11-a.

Figures 11-b and c illustrate the voltage of PV-terminal and the power profiles of this radiation. As stated, at the start the voltage value is roughly constant and equal to 126 V. Then, while starting, its value is affected by switching the load and inverter. It therefore varies slightly according to the motor current and power. The motor speed trajectory is shown in Fig. 12. Due to oscillations in the PV-output voltage, the speed trajectory is also affected accordingly,

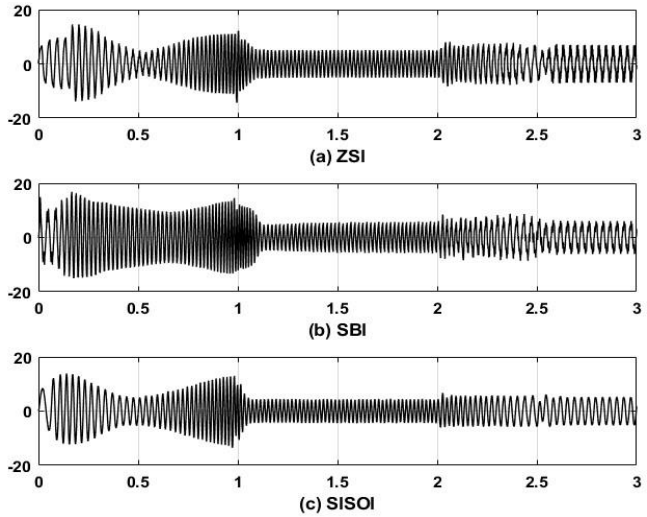

Fig. 9 The total stator currents with all inverters

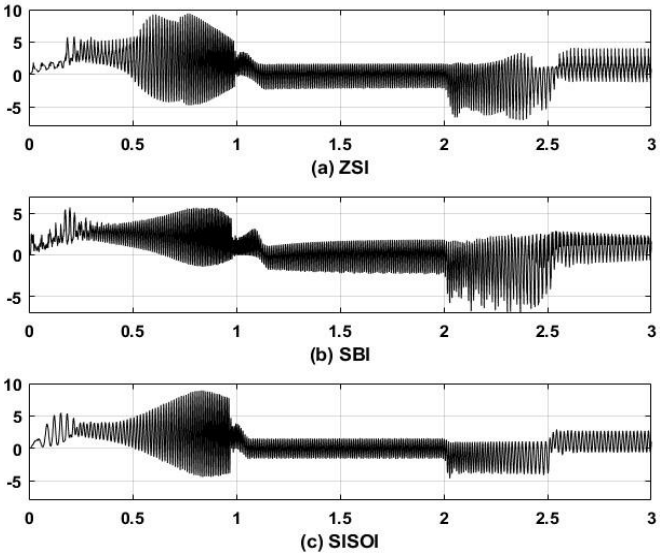

Fig. 10 Motor internal electric torque

especially with the SISO-inverter due to absence of the first stage (i.e., converter). However, both two-stage inverters almost follow the refernce speed trajectory. But, the best drive is that of SBI due to the robust controller offered. In addition, z-source inverter is tracking with a slight deflection. Figure 13 demonstrates the stator total currents. As shown, when starting the current will increase and then decrese in steady state. As shown, when the motor reaches to 80% of the nominal speed, the capcitor circuit is open. It depends on the temporal response of each proposed system based on its controller and the voltage of the DC-link. Likewise, SBI is much faster than others with minimum overshot. Accordingly, the internal electrical torque, shown in Figure 14, is also affected by the DC-link input voltage of the inverter.

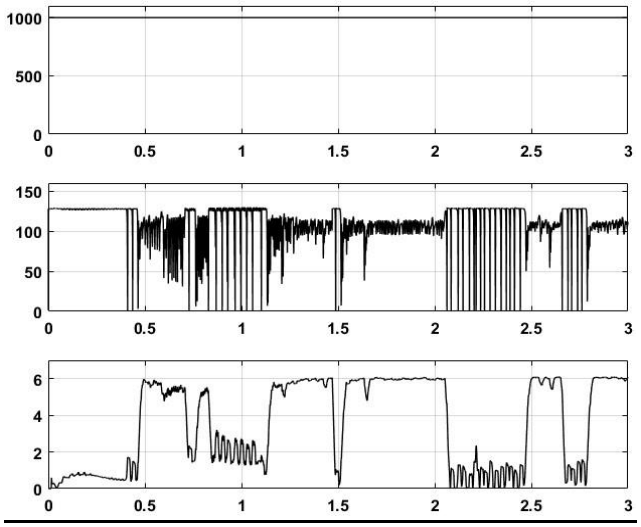

Fig. 11 PV-array (a) irradiance (b) voltage (c) power

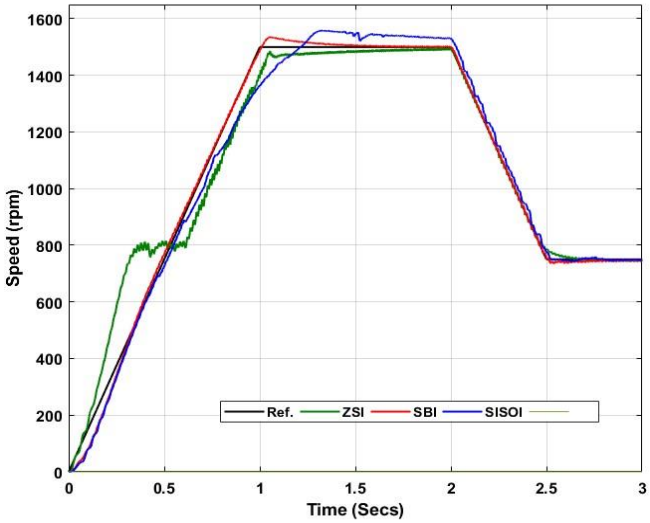

Figure 12 actual and reference forward speed trajectories for inverters without PV-shadow

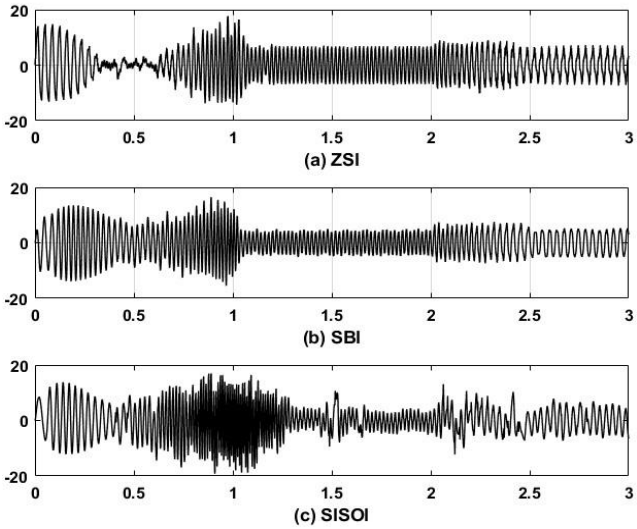

Fig. 13 The total stator currents for all inverters

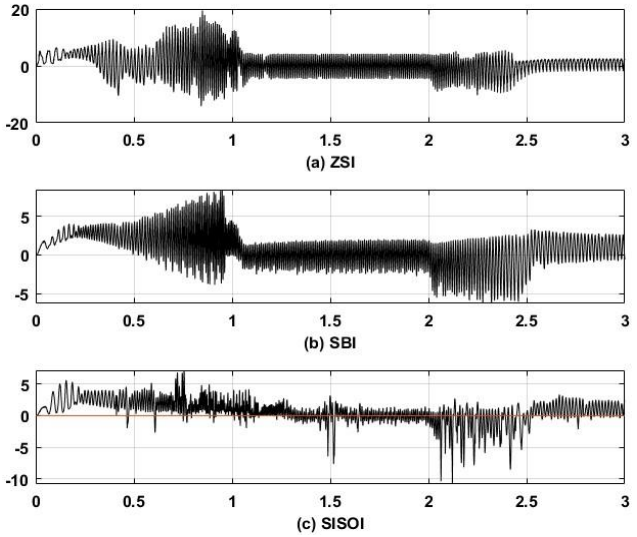

Fig. 14 Motor internal electrical torque

The motor torque gradually increases at start-up and then decreases with the current steady state. As shown, the SISO inverter provides low-starting torque comapred to other two inverter types.

6.3. Case (3): The motor is powered by a PV-array with shade

In this case, the shadow for the PV-array shall be considered. At t-0.5 to 0.6, the insolation is reduced from 1000 W/m² to 200 W/m² during this period as shown in Fig. 15a. Accordingly, the terminal voltage and generated power are shown in Figures 15-b and c. The reference and actual speed trajectories of all compared inverter systems are shown in the Fig. 16. As illustrated, the SBI with the help of the proposed voltage controller and its strategy, succeeded to follow the trajectory through start-up. Although the insolation was reduced to its minimum value, the DC-link voltage is increased to a sufficient value.

Moreover, the z-source inverter also followed the trajectory with a time delay and a maximum overshot at startup. The SBI and z-source inverters followed the speed trajectory through the deceleration without error. However, the SISO-inverter system took more delay time without deviation of the speed trajectory through starting period. Furthermore, it could not follow the deceleration of speed trajectory. Figure 17 illustrates the stator current. At starting, the motor with both SBI and z-source inverters consumes fewer power than the SISO inverter. This can be illustrated clearly through the internal electrical torque of the motor as shown in Fig. 18. The motor exerted more torque for the SBI and z-source inverters but SISO-inverter produces a bit of torque due to the lake of input DC-voltage.

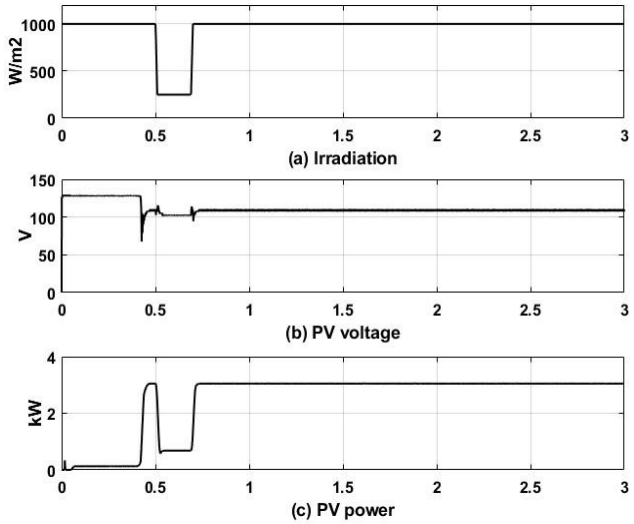

Fig. 15 PV- (a) irradiance (b) terminal voltage (c) output power

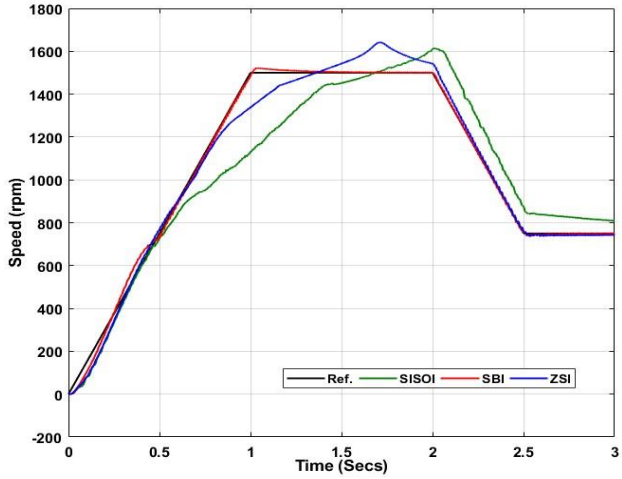

Fig. 16 actual and reference forward speed trajectories for inverters with PV-shadow

7. Real-time implementation for the SIMO-inverter systems

In power systems and drives, real time simulator (RTS) is used to design, test control, and protect equipment performance before installation on actual state. So, in this work, the combination of OP4510 real-time hardware-in the loop (HIL) and rapid-control prototype (RCP) [34] and OP8660 HIL-controller and data acquisition interface [35] platforms are used to implement the proposed drive.

According to simulation results, the SPIM-drive based on SBI will be only implemented to overcome the parameter variations of the PV-fluctuations. The overall practical system is shown in figure 19. All output parameters of the drive such as speed, torque, capacitor voltage, and currents are measured as real signals through the analog port of the HIL and its

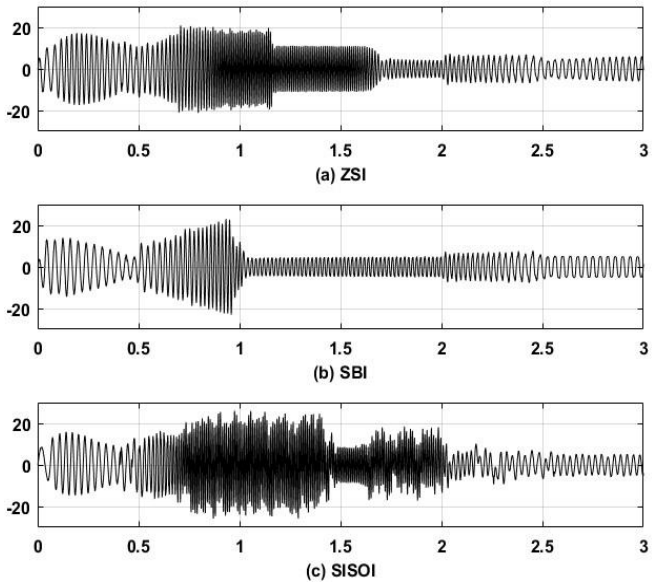

Fig. 17 The total stator currents for all inverters

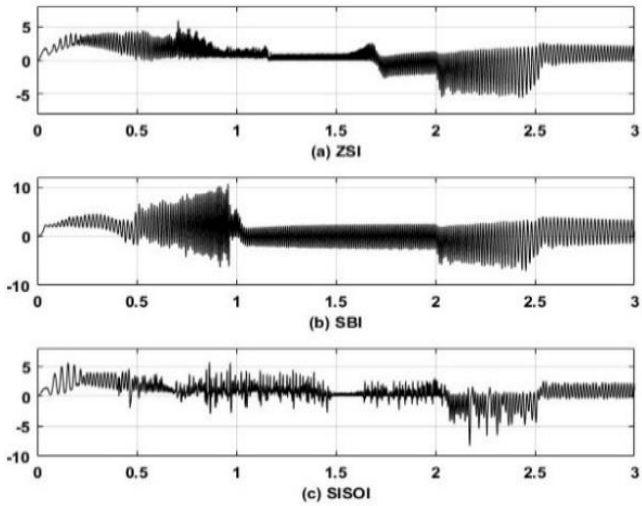

Fig. 18 Motor electric internal torques with all inverters

controller. The speed trajectory is scaled down through the Simulink platform by 1000. So, as shown in fig. 20-Chs. B and C, the actual and reference speed trajectories are nearly identical with real scale 1000 rpm/ div. In addition, the electrical internal torque is scaled down by 20 and channel scale is 500mv/div, so as shown in fig. 20-Ch. A, the real-scale value is 5 N.m. /div. The total stator current, main, and auxiliary winding currents are also the real scale is 10 A/div. As illustrated in fig. 21 Chs. A, B, and C, at starting the motor currents are increased and then decreased after steady-state. This can be clearly depicted as shown in fig. 21. The starting capacitor voltage ensures the starting process as illustrated through Ch. D with real-scale 200V/div.

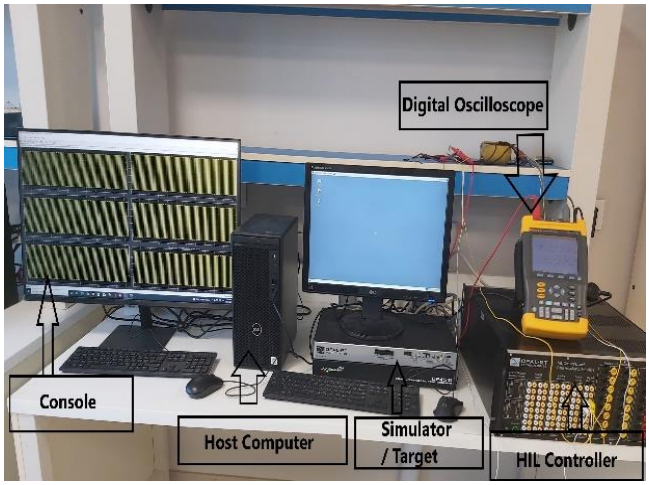

Fig. 19 Experimental rig

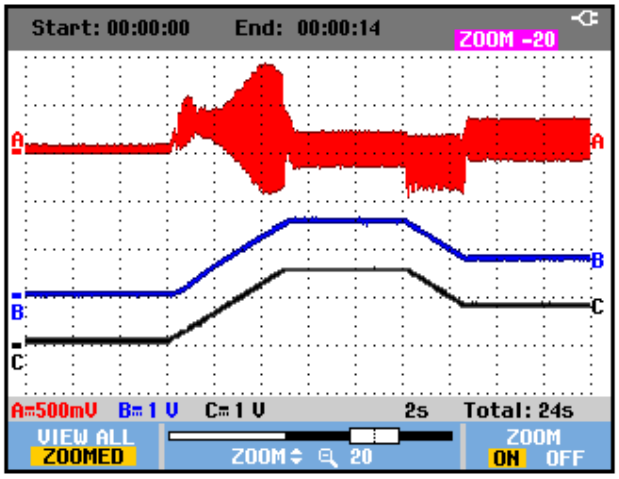

Fig. 20 Ch. A: internal torque, Ch. B and C reference and actual speed

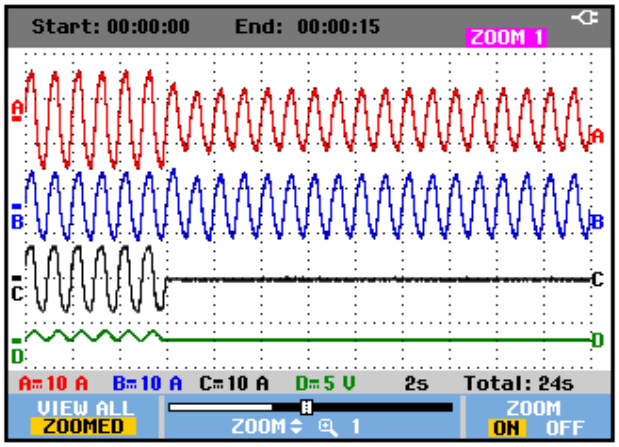

Fig. 21 Ch. A: total stator current, Ch. B main winding, Ch. C: Auxiliary winding currents, and Ch. D capacitor voltage (starting moment)

8. Conclusion

This article has examined the performance and behavior of a single phase induction motor when fed from an intermittent voltage source, such as a solar cell via SIMO- SBI and z-inverters. This manuscript suggested a scalar voltage/frequency as the master controller for the motor speed. In addition, another slave controller was proposed for DC-link voltage control and MPPT algorithm. This controller contributed to keep the DC-link voltage of the SBI constant to a certain value when the PV-array has a low radiation due to shade or cloudy weather. This value is sufficient to ensure the torque and current of the motor leads to better performance during starting and running. SIMO inverters are the best solution to ensure the best performance for SPIM drives with these intermittent sources compared to the SISO inverters. The proposed system was implemented in a real time. Thus, in the near future, it can be easily deployed as a true physical prototype.

APPENDIX A

PV-Module Specifications

P_{STC} = 305W, P_{PTC} = 208.6W, P (I_{max}) = 5.58A, V (P_{max}) = 54.7V, I_{SC} = 5.96A, V_{OC}=64.2V, N_{cell}=96, V_{max}=600V.

APPENDIX B

The motor data: $P_{rated} = 0.25$ HP, $P = 4$, $V_{rated} = 110$ V, f_{rated}=60 Hz, $R_{sm} = 2.02\ \Omega$, $X_{lsm} = 2.79\ \Omega$, $X_M = 66.8\ \Omega$, $R_{sa} = 7.14\ \Omega$, $X_{lsa} = 3.22\ \Omega$, $R_{cap.} = 2.15\ \Omega$, $C_{st.} = 255\ \mu$F, $R'_{lr} = 4.12\Omega$, $X'_{lr} = 2.12\ \Omega$

REFERENCES

[1] E. A. Ebrahim,: *A novel approach of adaptive neuro-PI vector controller fed IM servo drives*, 2002 IEEE/RSJ Int. Conf. , Switzerland, October 2002, pp. 2181-2186.

[2] E. A. Ebrahim and N. Hammad,: *Fault analysis of current-controlled PWM-inverter fed induction motor drives*, 7th Int. Conf. on Properties and Applications of Dielectric Materials, Japan, 2003, pp. 1065-1070.

[3] E. A. Ebrahim and A. A. Metwaly,: *Performance and tracking control of three-phase induction-motor drive fed from a DC-modified nano-grid*, WSEAS Transaction on Power Systems, Vol. 16, pp. 8-22, 2021.

[4] N. Ahmed et. al.: *AC chopper voltage controller-fed single-phase induction motor employing symmetrical PWM control technique*, Electric Power Systems Research, Vol. 55, pp. 15–25, 2000.

[5] E. Ribisi and P. Freere,: *Reduced starting current for single phase capacitor induction motors while maintaining starting torque*, 2019 IEEE AFRICON, Ghana, Sep. 2019.

[6] M. Almani et. al.: *An improved technique for energy-efficient starting and operating control of single phase induction motors*, IEEE Access, Vol. 9, pp. 12446-12462, 2021.

[7] S. Wang, J. Kang, and J. Noh,: *Topology optimization of a single-phase induction motor for rotary compressor*, IEEE Transactions on Magnetics, Vol. 40, No. 3, pp. 1591-1596, MAY 2004.

[8] I. Poldea and S. Nasar,: *The induction machines design hand book*, CRC Press, 2010.

[9] M. Corrêa et. al.: *Rotor-flux-oriented control of a single-phase induction motor drive*, IEEE Transactions on Industrial Electronics, Vol. 47, No. 4, pp. 832-841, 2000.

[10] F. Gbaden, et. al.: *Design and implementation of speed adjustment for single phase induction motor*, IOSR Journal of Electrical and Electronics Engineering , Volume 16, Issue 2, PP 09-17, 2021.

[11] A. Nied et. al.: *Single-phase induction motor indirect field oriented control under nominal load*, PEDS2009, Taiwan, pp. 789-793, 2-5 Nov. 2009.

[12] P. Kumbhar, S. *Lokhande,: Embedded based compact fuzzy system to speed control of single phase induction motor*, IOSR Journal of Electrical and Electronics Engineering, Volume 9, Issue 5,PP 56-59, 2014.

[13] V. Vodovozov, N. Lillo, Z. Raud,: *Variable-speed single-phase induction motor drive for vehicular applications*, Electrical Engineering Research, Volume 2, pp. 18-24, 2014.

[14] E. A. Ebrahim, et. al.,: *DC-Based interconnected-modified nano-grids with an open energy distributed system*, (CIRED'19), Madrid, pp. 1-5, 3-6 June 2019.

[15] E. A. Ebrahim, et. al.,: *Photovoltaic Based Interconnected Modified DC Nanogrids within an open energy distribution system*, (ACCS) & (PEIT) IEEE Egypt Section, Cairo, pp. 253-258, 2019.

[16] E. A. Ebrahim, et. al.,: *Closed-loop control of a single-stage switched-boost inverter in modified DC-interconnected nano-grids*, IET, the Journal of Engineering, Vol. 2020, Iss. 10, pp. 843-853, 2020.

[17] E. A. Ebrahim, et. al.,: *Open energy distribution system-based on photo-voltaic with interconnected-modified DC-nanogrids*, (ASTESJ) Journal, Vol. 6, No. 1, pp. 982-988, 2021.

[18] A. Rajaei, et. al.: *Single-phase induction motor drive system using z-source inverter*, IET Electric Power Applications, Vol. 4, Iss. 1, pp. 17– 25, 2010.

[19] S. Rahman et. al.: *Design and implementation of cascaded multilevel qZSI powered single phase induction motor for isolated grid water pump application*, IEEE Transactions on Industry Applications, Vol. 56, Issue 2, pp. 1907-1917, 2020.

[20] B. Ge, et. al.,: *Novel energy stored single-stage photovoltaic power system with constant DC-link peak voltage*, IEEE Transactions on Sustainable Energy, vol. 5, no. 1, pp. 28-36, Jan. 2014.

[21] D. Sun, B. et. al.: *An energy stored quasi-Z-Source cascade multilevel inverter-based photovoltaic power generation system*, IEEE Transactions on Industrial Electronics, vol. 62, no. 9, pp. 5458-5467, Sept. 2015.

[22] A. Ahmad, et. al.: *Switched boost modified Z-source inverter topologies with improved voltage gain capability*, IEEE Journal of Emerging and Selected Topics in Power Electronics, Vol. 6, Issue 4, pp. 2227-2244, Dec. 2018.

[23] M. Nguyen and T. Tran: *A single-phase single-stage switched-boost inverter with four switches*, IEEE Transactions on Power Electronics, Vol. 33, Issue 8, pp. 6769-7681, Aug. 2018.

[24] P. Krause, et. al.: *Analysis of electric machinery and drive systems*, Third Edition, IEEE Press, 2013.

[25] V. Karthik, and S Kottayil,: *An improved PWM control of quasi-switched-boost inverter with reduced ripple magnitude and increased ripple frequency input current*, 2017 IEEE (TAP Energy) , India, pp. 1-6, 21-23 Dec., 2017.

[26] R. Adda, S. Mishra and A. Joshi,: *A PWM control strategy for switched boost inverter*, 2011 IEEE Energy Conversion Congress and Exposition, Phoenix, AZ, USA, pp. 991-996, 17-22 Sept. 2011.

[27] V. Anusree and P. Saifunnisa,: *Closed loop control of switched boost inverter*, IEEE 2016 (ICEEOT), India, pp. 3040-30443, 3-5 Mar 2016.

[28] S. Mishra, R. Adda, and A. Joshi,: *Inverse Watkins–Johnson topology-based inverter*, IEEE Transactions on Power Electronics, Vol. 27, Issue 3, pp. 1066-1070, March 2012.

[29] Y. Siwakoti, F. Blaabjerg and P. Loh,: *Z-source converters*, Book chapter of: *Power electronic converters and systems: frontiers and applications*, A. M. Trzynadlowski, Ed. Stevenage, U.K.: IET Press, pp. 205–243, Dec. 2015.

[30] L. Huang, M. Zhang, L. Hang, W. Yao, and Z. Lu,: *A family of three-switch three-state single-phase Z-source inverters*, IEEE Transactions on Power Electronics, Vol. 28, Issue 5, pp. 2317-2329, May 2013.

[31] Y. Liu, B. Ge, H. Abu-Rub, and F. Blaabjerg,: *Single-phase Z-source/ quasi-Z-source inverters and converters*, IEEE Industrial Electronics Magazine, Vol. 12, Issue 2, pp. 6-23, June 2018.

[32] W. Xu, et. al.,: *A series of new control methods for single-phase Z-source inverters and the optimized operation*, IEEE Access, Vol. 7, pp. 113786-113800, 2019.

[33] T Vijay Muni,: *Z-Source Inverter*, MATLAB Central File Exchange. Retrieved January 6, 2022.

[34] https://www.opal-rt.com/simulator-platform-op4510/

[35]https://www.opal-rt.com/resource center/document/?resource=L00161_0362

Using Separately Excited DC Motor in Railway Vehicles Systems

Ashraf Mohamed [1], Ahmed Abdolkhalig [2], Fatihe Abusief [3]
[1,2,3] *Electrical Engineering Department, Tobruk University*
([1]a.mohamed@tu.edu.ly, [2]ahmed@tu.edu.ly, [3]fatihe.abusief@tu.edu.ly)

Abstract— Like most road running vehicles, a railway traction power system provides mechanical power that can be converted into kinetic and potential energy and can be used to overcome resistance to motion.For every successful train traction system, there are certain general requirements which should be met such as The capability to start and haul a prescribed load over its specified routes whilst maintaining the timetable and a sufficiently long service lifetime with minimal non-availability due to maintenance and standby. Three typical railway traction systems are used in railway system: electric, diesel electric and hybrid. DC and AC electric traction systems are commonly deployed in the railway industry. A separately excited DC motor is adopted in this paper. The electric vehicle power train system and the components are modelled in details and all the simulation models has been done designed and evaluated with Matlab programming environment.

Keywords: Railway System, SEDM, Electric Vehicle, Driveline, Powertrain.

I. INTRODUCTION

The first railways were powered by steam engines. Although the first electric railway motor came on the scene halfway through the 19th century, the high infrastructure costs meant that its use was very limited. The first Diesel engines for railway usage were not developed until halfway through the 20th century. The evolution of electric motors for railways and the development of electrification from the middle of the 20th century meant that this kind of motor was suitable for railways. Nowadays, practically all commercial locomotives are powered by electric motors (Faure, 2004; Iwnicki, 2006)[1,2].Figure(1) illustrates a flow diagram for the different types of rail engines and motors most widely used throughout their history. The first Diesel locomotives with a mechanical or hydraulic drive immediately gave way to Diesel locomotives with electrical transmission[3,4]. These locomotives are really hybrids equipped with a Diesel engine that supplies mechanical energy to a generator, which, in turn, supplies the electrical energy to power the electric motors that actually move the drive shafts. Although this may appear to be a contradiction in terms, it actually leads to a better regulation of the motors and greater overall energy efficiency.

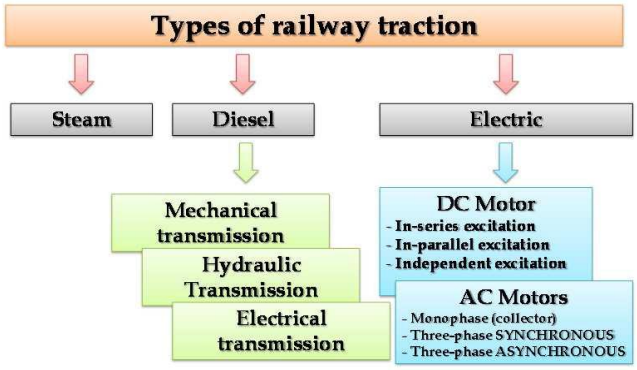

Figure.1. Railway engine and motor types.

The major drawback of electrical traction is the high cost of the infrastructure required to carry the electrical energy to the point of usage[5,6]. This requires constructing long electrical supply lines called *"catenary"*, (Figure 2).

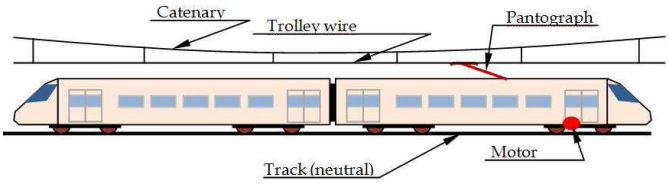

Figure. 2. Electric railway traction: General outline, catenary and pantograph.

In addition, the locomotives need devices that enable the motor to be connected to the catenary: the most common being "pantographs" or the so-called "floaters". In its favour, electrical traction can be said to be clean, respectful of the

environment and efficient, as an optimum regulation of the motors can be achieved. In this work, we will only focus on the functioning and regulation of the most widely used types of electric motors.

The most widely used electric motors for railway traction are currently of three basic types:

1. Direct current electric motors with in-series excitation.
2. Direct current electric motors with independent excitation.
3. Alternating current electric motors.

The induction motor has long been regarded as a suitable final drive for railway traction systems due to its inherent capability for regeneration and steep speed and torque characteristics[7,8]. However, the widespread introduction of induction motors could only be realised after modern power electronics became available [9]. The two reasons for this are as follows:

- Speed control of the induction motor is achieved by changing the input frequency and voltage of the input power supply;
-The difficulty of obtaining the proper three-phase supply from a DC or single phase AC traction line should be solved by power electronics techniques.

The development of power electronics relies on advancement of semiconductor devices [10,11]. In the 1960s, the development of the power thyristor gave rise to trials of several experimental inverter-fed induction motor locomotive drives. The main drawback of this type of device is the lower current and voltage level which it could withstand which limits its application in high power fields. In the 1970s, the development of a high-power force-commutated thyristor led to the deployment of the Current Source Inverter (CSI) in DC-fed metro traction drives. Later, the large power Gate-Turn-O_ (GTO) thyristor realised the Voltage Source Inverter (VSI) in railway applications. Until very recently, the Insulated Gate Bi-polar Transistor (IGBT), which has a lower operation current and higher switching speed has taken the place of the GTO. In the 1980s, the pulse converter was developed, which is a four-quadrant AC-DC line converter that enables three-phase VSI-Induction Motor drives on single-phase AC supplied railways. There are two commonly applied types of AC motor: induction and asynchronous motor[12].

Direct current electric motors usually work under a 3 kV supply and alternating current motors under 25 kV[13]. Direct current motors are gradually becoming obsolescent in favour of alternating current motors. This is mainly due to maintenance problems with the direct current motor collectors and the better technological progress of alternating current motors.

The most common DC traction motors used in the railway industry are series and separately-excited machines[14,15]. In series motor, the field winding is connected in series with the armature, resulting in the field being determined by the armature current. The series field forms a protection to ensure that no current flows in the motor without a corresponding field having already been established. The field becomes non-linear when iron saturation occurs at a higher current. For any series traction motor with a steady terminal voltage, "wheel-slip correction" can be inherently realised with a high starting torque followed by a constant power operation regime with increasing speed. This is a very attractive feature for stable operation. Speed control for a series DC machine can be achieved by varying the terminal voltage at the starting stage and the field through the diverter resistor at a greater speed which is usually referred to as a "field weakening operation". However, the insertion of a series resistor into the motor circuit is regarded as wasteful of power and of limited use. In a camshaft controlled train, the series resistance is varied to give the overall characteristic shown in Figure.3. At the beginning, both armature and field current are both maintained constant to generate a constant torque. With the increase of rotating speed, the output power is increased until the base speed. Subsequently, field current is reduced and bring down the output toque. This operation called field weakening operation. After the rotating speed is over the transition speed, the armature current begins to drop and further bring down the torque. The motor then goes into a weak field operation.

For the separately-excited motor, the field excitation circuit is independent from the field circuit. Speed control is also realised through varying the armature voltage or the field current. This type of motor with its separately excited field can be used for regenerative braking. In Figure.3, three control regimes have been identified with different characteristics in terms of torque, current, speed and power [16,17].

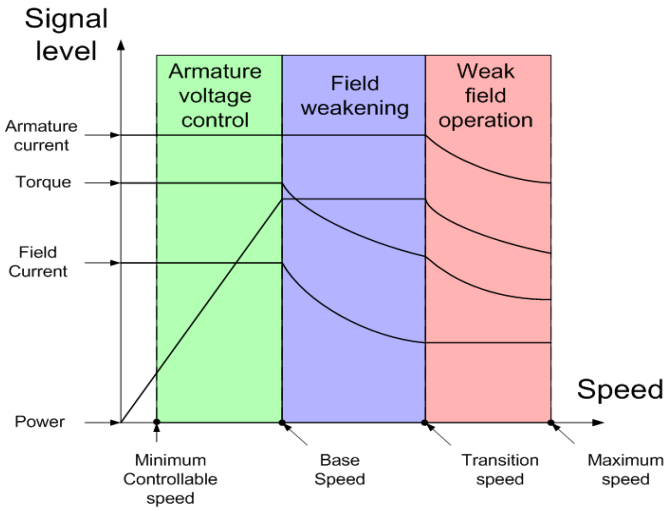

Figure3. Characteristics curve of separately excited DC motor

II. SEPARTELY EXCITED DC MOTOR MODELLING

The equivalent circuit of separately excited DC motor shown in figure(4) [18,19]. The armature voltage equation is given by:

$$V_a = I_a R_a + L_a \frac{dI_a}{dt} + E_b \qquad (1)$$

Where (V_a) is the armature voltage, (I_a) is the armature current, (R_a) is the armature resistance, L_a is the armature inductance, (E_b) is the back emf.

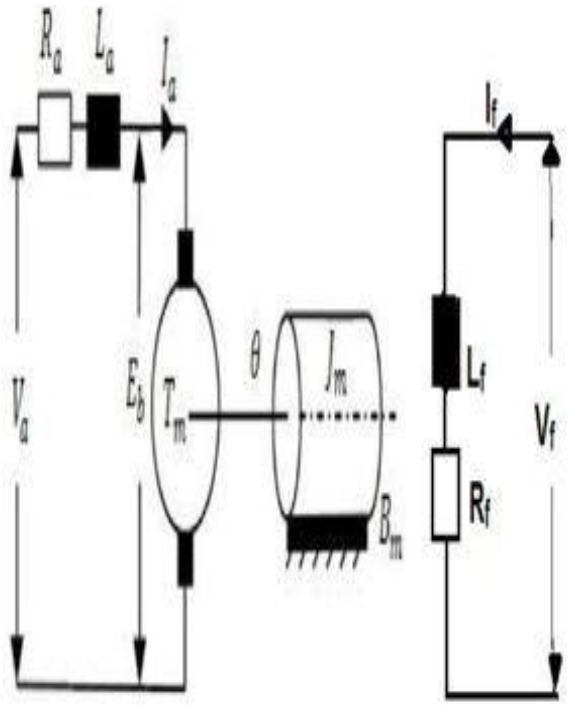

Figure4. Equivalent circuit of separately excited DC motor.

When the armature conductors carry current, forces are exerted on them due to the interaction of this current with the steady air gap flux (Φ), which consists of the field current component(Φ_f).The resulting instantaneous electromechanical torque(*Te*) developed by D.C motor is given by:

$$T_e(t) = K_t \Phi I_a \qquad (2)$$

Rotation of the armature conductors in the flux field causes an electro motive force. to be induced in the armature circuit of such polarity as to oppose the flow of armature current. This induced e.m.f. is usually known as the reverse e.m.f. or back e.m.f., which in terms of instantaneous variables is given by:

$$E_b = K_E \Phi \omega \qquad (3)$$

Where (ω) is the instantaneous speed. In the international system units, the torque and voltage constants (K_t) and (K_E)are equal and have the dimensions of Newton meters per Weber ampere and volt second per Weber radian.

The electromechanical torque developed by the drive has to supply the torque demand of the externally applied load (T_L), overcome the friction, windage effects and accelerate the inertial mass of the rotor during speed increases. If the polar moment of the inertia of the load and drive machine is (*Jm*) and the friction consists of a coulomb friction torque (T_f) plus a viscous friction term(*Bm*) then the dynamic mechanical part is implemented by the following equation for an adjustable speed drive is given by :

$$T_e = J_m \frac{d\omega}{dt} + T_f + B_m \omega + T_L \qquad (4)$$

Mathematical model for the dynamic simulation of the dc motor has been developed. This model has been verified by simulation using Matlab. Looking at the DC motor output shaft position(θ), and choosing the state variable to be the motor shaft output position (θ), velocity (ω) and armature current (I_a).

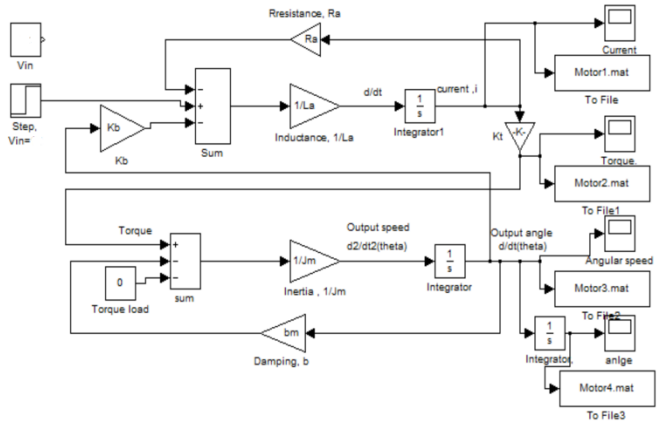

Figure5.Dynamic model of separately excited DC motor

III.DRIVELINE MODELLING

A typical driveline model consists of motor, spring-damper, gearbox and the wheel in series. The purpose of using a torsional damper is to keep engine torque peaks as well as operational irregularities away from the powertrain and connected units. If the forces operating in the powertrain area were not countered, driving comfort would be noticeably reduced and the powertrain components would also show considerably higher levels of wear.For the system the equations of motion can be derived as:

$$J_m \ddot{\theta}_m = T_m - K(\theta_m - n\theta_\omega) - c(\dot{\theta}_m - n\dot{\theta}_\omega) \qquad (5)$$

Where $\theta_m, \dot{\theta}_m, \ddot{\theta}_m$ are the angular ,angular speed and angular acceleration of the motor respectively, and $\theta_\omega, \dot{\theta}_\omega, \ddot{\theta}_\omega$ are the angular ,angular speed and angular acceleration of the wheel respectively . (*K*) and(c) are coefficient and coefficient of viscous friction of spring damper (*n*) is the gear ratio.

$$\ddot{\theta}_\omega = \frac{nK}{j_e}(\theta_m - n\theta_\omega) + \frac{nc}{J_e}(\dot{\theta}_m - n\dot{\theta}_\omega) - \frac{FR}{J_e}\dot{\theta}_\omega + \frac{FV_s}{J_e} \qquad (6)$$

$$J_e = J_\omega + n^2 J_g \qquad (7)$$

$$\dot{V}_s = \frac{FR^2}{M_v}\dot{\theta}_\omega - \frac{FR}{M_v}V_s - \frac{B}{M_v}V_s \quad (8)$$

Where:
(V_s), $(\dot{V}_s)$ are the vehicle speed and acceleration respectively. (J_ω) is the Wheel inertia, and (J_g) is Transmission gear inertia refer to motor.*(F)* is vehicle running resistance, (M_v) is the vehicle mass and *(R)* is the wheel radius.

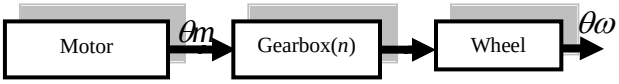

Figure(7).Driveline model

n

IV.SIMULATION RESULTS AND DISCUSION

n

To analyze the performance of the separately excited DC motor when it is used in powertrain system, the following modeling parameters are adopted:

Motor &driveline system	
Armature resistance (Ra)	0.04 Ω
Armature inductance (La)	0.4mH
DC supply	1500V
Nominal armature current	75A
Motor constant (Kt)	4.28
Power	112.5KW
Armature inertia(Jm)	11Nm/rad.s^2
Torque max	317N.m
Damping ratio of motor shaft(Dm)	0.003
Transmission gear inertia(Jg) refer to motor	0.6
Motor windage &viscous friction(Bm)	0.12
Corner speed of the motor	350rad/sec
Wheel inertia(Jw)	250Nm/rad.s^2
Wheel radius(R)	0.45m
Gear ratio(n)	5.68
Spring coefficient (K)	10000KNm/rad
Coefficient of viscous friction(C)	100KNms/rad
Vehicle running resistance(f)	10000KN
Train &track parameters	
Vehicle Mass(Mv)	6000000Kg
Rolling resistance coefficient,(Fr)	0.001
Air density, (ρ)	1.2Kg/m^3
Aero dynamic drag coefficient,(CD)	0.653
Front area, (Af)	2m^2
Track gradient,(i)	1%
Vehicle acceleration(a)	0.5m/s^2
Average electrical accessory load	30KW

The current demand input to the system is shown in figure 8.With the help of MATLAB programming , the performance of separately excited DC motor connected to drive line system in time domain was obtained and the results are shown in figure 9,10,11.
It is clear that the relation between the vehicle acceleration is equal to the wheel acceleration multiplied by the wheel radius(R=0.45m) .
The characteristic curve of the motor can be divided into three regions:
First region (0-1sec):In this region the motor starts from zero position until the current reaches 75A,and the torque at this point is equal to 317Nm.
Constant torque re region (1-23.6sec): In this region the armature and the current torque are constants, while the speed is increasing until reaching the corner speed(ω_c =350rad/sec) at the time of 23.6sec.
Constant power region($\omega>\omega_c$):It can be seen that in this region the armature torque and current are decreasing with the increasing of the motor speed. So the power (P=Tω)remain constant, and the motor works naturally.

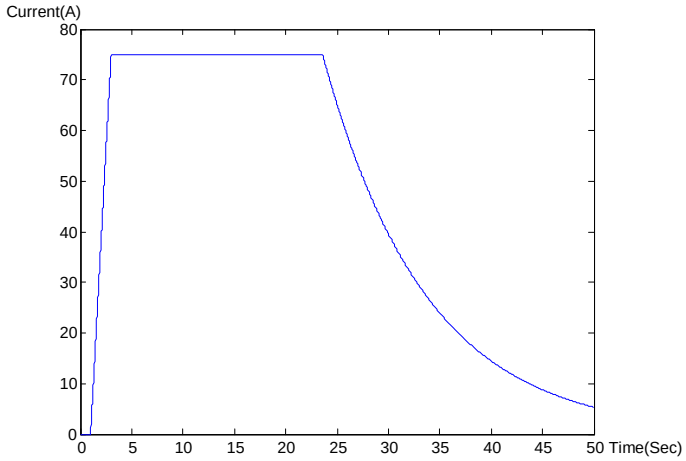

Figure(8).Current demand input to the system

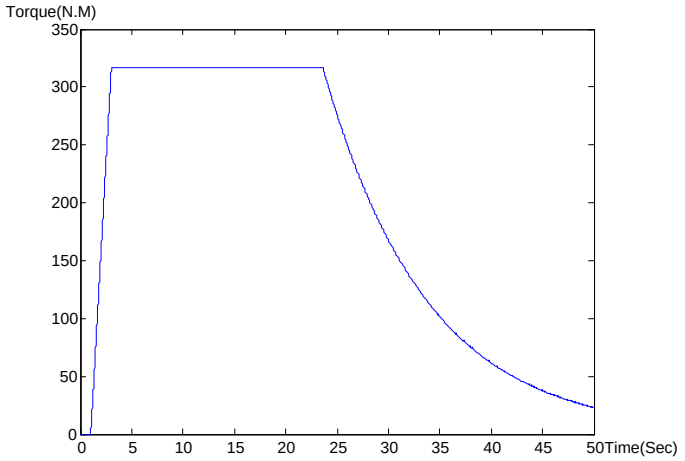

Figure(9).Torque versus time of the motor

The motor torque during starting is very high and gradually decreases as the angular velocity of the motor increases. Consequently, during starting, the current intensity needs to be limited to avoid the circuits burning out and to limit the motor torque, thereby preventing the adhesion limits being exceeded in the wheel-rail contact.

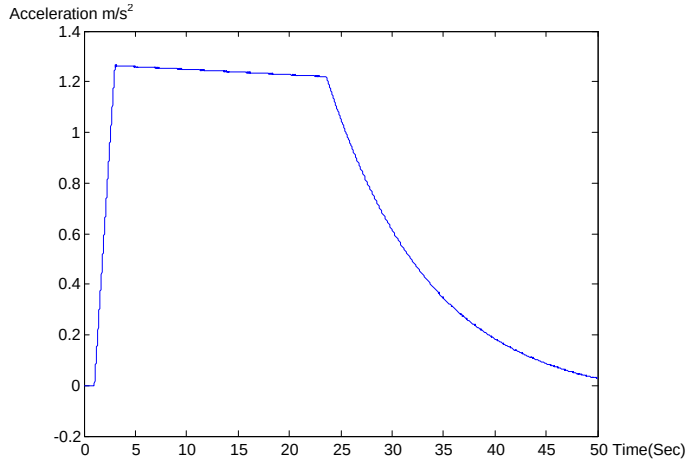

Figure(10). Vehicle acceleration versus time

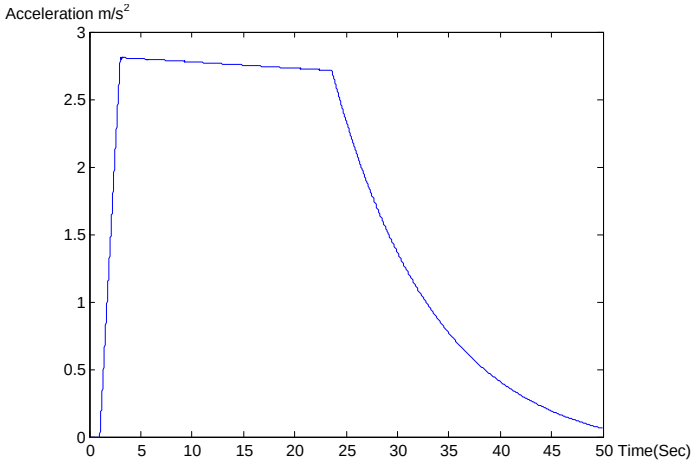

Figure(11). Wheel acceleration versus time

V. CONCLUSTION

There are different types of electric motors which are commonly used in the drive train. Choice of the electric motor depends on several factors such as speed and torque characteristics, physical size ,weight differences, material cost and efficiency. Because of its high starting torque, and it can operate in stable conditions with any field excitation, separately excited DC motor is adopted in this paper. The electric vehicle power train system and the components are modelled in details and all the simulation models has been done designed and evaluated with Matlab programming environment. The results show that the performance of separately excited DC motor when it is used in powertrain systems was confirmed to be satisfactory because its wide range of speed control.

REFERENCES

[1] R. Liu and L. M. Golovitcher, "Energy-efficient operation of rail vehicles,"Transportation Research Part A: Policy and Practice, vol. 37, no. 10, pp. 917–932, 2003.

[2] T. K. Ho and T. H. Yeung, "Railway junction control by heuristic methods," IEEE Proceedings- Electric Power Applications, vol. 148, no. 1, pp. 77–84, 2001.

[3] Y.-H. Chou, Distributed approach for rescheduling railway traffic in the event of disturbances. PhD, School of Electronic, Electrical and Computer Engineering, The University of Birmingham, 2009.

[4] G. J. Hull, "Simulation of energy efficiency improvements on commuter railways, "Master of Philosophy, School of Electronic, Electrical and Computer Engineering, the University of Birmingham, Dec. 2009.

[5] H.-S. Hwang, "Control strategy for optimal compromise between trip time using genetic algorithms," IEE Proceeding -Electric Power Applications, vol. 144, no. 1, pp. 65–73, 1997.

[6] Y. V. Bocharnikov, A. M. Tobias, C. Roberts, S. Hillmansen, and C. J. Goodman,"Optimal driving strategy for traction energy saving on DC suburban railways," Electric Power Applications, IET, vol. 1, no. 5, pp. 675–682, 2007.

[7] H.-J. Chuang, C.-S. Chen, C.-H. Lin, C.-H. Hsieh, and C.-Y. Ho, "Design of optimal coasting speed for saving social cost in mass rapid transit systems," in Third International Conference on Electric Utility Deregulation and Restructuring and Power Technologies, pp. 2833–2839, 2008.

[8] T. Albrecht, Railway timetable & traffic: analysis, modeling and simulation. Energy-Efficient Train Operation, pp. 83–105. Eurailpress | DVV Rail Media (DVV Media Group GmbH), 2008.

[9] P. Howlett, "The optimal control of a train," Annals of Operation Research, vol. 98, pp. 65–87, 2000.

[10] E. Khmelnitsky, "On an optimal control problem of train operation," IEEE transactions on automatic control, vol. 45, no. 7, pp. 1257–1266, 2000.

[11] M. Alaküla, Hybrid Drive Systems for Vehicles: System Design and Traction Concepts, Lund: Lund University of Technology, 2006.

[12] M. Leksell, Electrical Machines and Drives, Stockholm: KTH, 2004.

[13] R. Ottersten, Hybrid Vehicle Drives: Power Electronics, Göteborg: Chalmers University of Technology, 2004.

[14] B. S Fan, "Modeling and Siumulation of a Hybrid Electric Vehicle Using MATLAB/Simulink and ADAMS," University of Waterloo, Waterloo, ON, MASc Thesis 20

[15] Li-Cun Fang and Shi-Yin Qin, "Concurrent Optimization for Parameters of Powertrain and Control System of Hybrid Electric Vehicle Based on Multi-Objective Genetic Algorithm," in *SICE-ICASE International Joint Conference*, Busan, Korea, 2006, pp. 2424-2429. 2006.

[16] Y. Ding, F.-m. Zhou, Y. Bai, T.-k. Ho, and Y.-f. Fung, "Parallel computing for multi-train movement simulation on electrified railway," in Second International Conference on Information and Computing Science, vol. 4, pp. 280–283, 21-22, 2009.

[17] Y. Cai, M. R. Irving, and S. H. Case, "Iterative techniques for the solution of complex DC-rail-traction systems including regenerative braking," IEEE Proceedings-Generation Transmission and Distribution, vol. 142, no. 5, pp. 445–452, 1995.

[18] A.K. Mishra, V.K. Tiwari, R. Kumar, "Speed control of dc motor using artificial bee colony optimization technique," IEEE International Conference on Control, Automation, Robotics and Embedded Systems (CARE 2013), Jabalpur, 2013.

[19] J. Sriram, K. Sureshkumar, "Speed Control of BLDC Motor Using Fuzzy Logic Controller Based on Sensorless Technique," IEEE International Conference on Green Computing Communication and Electrical Engineering (ICGCCEE), Coimbatore, 2014.

vol 22 / 2022

University "Politehnica"
Timișoara Romania
Faculty of Electrical and Power
Engineering

"Politehnica" Publishing House
ISSN 1582-4594

No 1